Fracture of ultra-soft hydrogels probed by puncture and cavitation

Yuanyuan Wei

PSL UNIVERSITÉ PARIS

THÈSE DE DOCTORAT
DE L'UNIVERSITÉ PSL

Préparée à l'Ecole Supérieure de Physique et de Chimie Industrielles de la ville de Paris (ESPCI Paris)

Fracture d'hydrogels ultra-mous sondée par insertion d'aiguille et cavitation

Fracture of ultra-soft hydrogels probed by puncture and cavitation

Soutenue par
Yuanyuan WEI
Le 5 octobre 2022

Ecole doctorale n° 397
Physique et chimie des Matériaux

Le Laboratoire de Sciences et Ingénierie de la Matière Molle (SIMM)

Spécialité
Physico-chimie

Confidentielle jusqu'au 31/12/2023

ESPCI PARIS PSL

Composition du jury :

Président du jury Laurent CORTE Chercheur de CNRS ESPCI Paris - PSL	*Examinateur*
Laurence RAMOS Directeur de recherche CNRS Université de Montpellier	*Rapporteur*
Esther AMSTAD Professeure associée EPFL	*Examinateur*
Robert STYLE Group leader ETH Zurich	*Rapporteur*
Tetsuharu NARITA Chargé de recherche CNRS ESPCI Paris - PSL	Co-*Directeur de thèse*
Costantino CRETON Directeur de recherche CNRS ESPCI Paris - PSL	*Directeur de thèse*

Acknowledgment

Upon the completion of this thesis, I would like to express my gratitude to those who have given me encouragement and support during my Ph.D. study.

First of all, profound gratitude goes to my supervisors, Costantino Creton and Tetsuharu Narita who allowed me to pursue my Ph.D. degree in ESPCI Paris. Costantino, you always help me to overcome the difficulties that I encountered in my research projects and pointed me in the right direction with your profound knowledge in the field of polymer mechanics. Thank you for offering me plenty of opportunities to be involved in international conferences and letting me grow. You will always be my role model as a professor, who is very conscientious, modest, and open-minded. Tetsu, thank you for helping me to enrich my experimental setup skills and for your generosity to spend a lot of time discussing the unexpected results with me. You always encourage me and trust me to discover new things in my projects and spare no effort to help me pursue my research career. I wouldn't be able to accomplish this work without your support, patience, and encouragement.

Also, I sincerely express my thanks to my collaborators: Professor Alfred J Crosby and Dr. Christopher W Barney from the University of Massachusetts Amherst, who helped me with the puncture and cavitation setup development and results analysis. Thanks to Professor Rong Long and his student Xingwei Yang from the University of Colorado, who helped me with the analytical work of puncture force field construction. Thanks to Professor Matteo Ciccotti from the SIMM lab of ESPCI, for the guidance on mechanics. Thanks to Dr. Jianzhu Ju for the help in developing the optical setup and mechanical experiments.

I would like to thank all the jury members: Professor Laurent Corte, Laurence Ramos, Esther Amstad, and Robert Style. I appreciate their evaluations for my thesis manuscript.

I feel very lucky to be able to work with all the SIMM members. We are a big family with various kinds of activities: wine and cheese tasting, beer tasting, concerts, marathon racing, lab weekend, after-work bars, etc. All these events will be unforgettable moments in my life. I would like to thank all the students/colleagues in the SIMM lab, especially: Donghao, Lily, Lazare, Julie, Flora-maud, Anusree, Victoria, Malak, etc. Thanks for your accompany and sharing all the interesting things both in research and life, making the lab time enjoyable. Thanks to my friends

Wenqing, Jianxun, Yichang etc. in Paris and Tiantian, Chunxian, Chuan etc. in China who are always there for me as best friends to encourage me and inspire me in many aspects!

Meanwhile, I would like to extend my deep gratitude to my family. Thanks to my parents and my brother for your endless and selfless love, support, and encouragement. Your love is my source of strength to overcome all the difficulties and courage to explore the world.

Finally, I would like to thank CSC (Chinese scholarship council) for financial funding for my Ph.D.

Thank you all for making my four-year Ph.D. life wonderful in Paris!

General introduction

Hydrogels are good candidates for biological applications such as tissue engineering, artificial cartilage, vessels, prosthetic joints, soft contact lenses, etc[1]. Some of the human tissue or organs (such as the brain, breast, and lung) exhibit a very low stiffness and modulus, ~ tens Pa. Recently, with the prominent development of medical robotics and surgical tactile sensors in medical application[8-10], a knowledge of the deformation and fracture behavior of ultra-soft materials, to mimic how soft tissues react on the medical device under loading conditions, is of remarkable importance.

Ultra-soft materials deform and fracture distinctly compared to commonly named soft materials. First, the surface tension can play an important role in the large deformation and presumably in the fracture behavior of soft solids. The surface tension-induced deformation is related to the elasto-capillary length which is defined as the ratio of the surface tension to the shear modulus, $l_{ec} = \gamma/G'$. When the stiffness of the gel is low, l_{ec} could be comparable to specimen size, in which the capillarity or surface tension dominates elasticity. Then, the structural heterogeneity of hydrogels, which is more prominent for ultra-soft hydrogels at low crosslinking levels, could largely affect their fracture properties under extreme loading conditions. In addition, highly compliant and elastic materials can sustain large deformations exceeding their linear elastic range, in which the large deformation or strain-induced structural rearrangements such as chain orientation and crystallization may result in substantially different fracture behavior. Importantly, the ultra-soft nature of the specimen makes it difficult to manipulate and perform mechanical tests with conventional geometry, since the sample might not even support its weight under the influence of gravity to a specific dimension[4]. Puncture and cavitation provide solutions for fracture properties characterization of ultra-soft materials. Here are some open questions that remain:

- How surface tension influences the deformation and fracture behavior of ultra-soft hydrogels at elasto-capillary length scale?
- What is the role played by structural heterogeneity in linear elasticity, large deformation, and fracture properties for ultra-soft hydrogels?
- Is there any structural anisotropy structure introduced by large deformation, such as chain orientation and strain-induced crystallization, that locally governs the fracture behavior of soft hydrogels?

To bring some answers to these questions, the present manuscript is divided into 7 chapters.

The first chapter is devoted to reviewing the present work on hydrogels, with emphasis on the challenges faced by ultra-soft hydrogels on their distinct deformation and fracture behavior as well as their mechanical property characterizations.

In Chapter 2 we will investigate the rheological and puncture behavior of (chemically cross-linked) polyacrylamide hydrogel, poly(dimethyl siloxane) (PDMS), and (physically cross-linked) carrageenan hydrogel at elasto-capillary length scale.

In Chapter 3, we will focus on the fracture behavior of poly(vinyl alcohol) (PVA) hydrogel with a low hydrolysis degree. The fracture resistance of hydrogels with different structural heterogeneity will be revealed.

In Chapter 4, we will report the extreme large strain-induced crystallization (SIC) during the puncture test in PVA hydrogel with a high hydrolysis degree. The resultant above-needle-tip crack phenomenon and reinforcement of SIC will be discussed.

In Chapter 5, we will detail the effect of molecular weight and the addition of surfactant in PVA hydrogel to study their effect on fracture resistance.

In Chapter 6, we will put forward a new optical technique – photon correlation imaging to quantitatively visualize the 3D deformation mapping of the deep indentation process.

In Chapter 7, we will investigate the needle-insertion-induced crystallization in cavitation and elucidate its role in controlling cavity morphology. The fracture energy estimated by cavitation and pure shear test of PVA at a large range of crosslinking levels will be discussed.

1. Chapter 1：Introduction

1.1. Hydrogels

Hydrogels are hydrophilic polymeric networks swollen in water where the water molecular can be tightly bound to the polymer network or free to move within the polymer network[1]. The high water content feature of hydrogels (typically ~ 70 – 99%) leads to unique liquid-like attributes including swelling properties, permeability to a wide range of chemical and biological molecules, and high transparency to optical and acoustic waves[2]. On the other hand, the polymer network in hydrogels, serving as porous "solid" results in solid-like behavior such as elasticity, deformability, and fracture of the sample[3]. Thanks to their high water contents and biocompatibility, hydrogels are good candidates for biomedical applications in tissue engineering, such as artificial cartilage, vessels, prosthetic joints, and soft contact lenses, in which the hydrogels intimately interact with biological organisms of the human body[1, 4]. Current research works on hydrogels for future use demonstrate that they have great potential in the biomedical field including cell encapsulation, nanoparticle coatings, and diagnostic micro-devices such as microfluidics[5, 6]. More recently, intensive efforts have been devoted to investigating their applications in machines and devices such as hydrogel actuators[4, 7], soft robots[8, 9], electronic devices[10], ionic devices[11], and underwater adhesives[12, 13,] etc.

The stiffness of human tissue and organs varies considerably corresponding to its inherent function[14]. More specifically, the mechanically static organs (brain, breast, and lung) exhibit sufficient low modulus ~ tens Pa, whereas load-bearing organs, such as bone joints, possess a modulus several orders of magnitude larger as shown in **Figure 1.1**. The mechanical properties of hydrogels to the survival and wellbeing of the living body are markedly significant and crucial to realizing the application in the above-mentioned situations. The high-water content in hydrogel usually renders

it poor mechanical properties when compared to the commonly used engineering material, such as plastic and rubber. Numerous studies have been employed to investigate the mechanical properties, including the elasticity, toughness, and fracture resistance, of hydrogels oriented to overcome the disadvantage of hydrogel in mechanical performance and develop robust materials, like bone and muscle in the human body, to realize such specific biological application. The advance in the development of medically surgical devices such as surgical robots and disease diagnosis raise demands in understanding the interactions between tissue and device in terms of the deformation and fracture properties of the material with a wide range of toughness, especially the ultra-soft tissue/organs such as breast, brain, and lung, which is poorly understood and addressed in the current research.

In this section, we will review the work on hydrogels chemistry, fabrication, and challenges in mechanical characterization with an emphasis on the ultra-soft hydrogel.

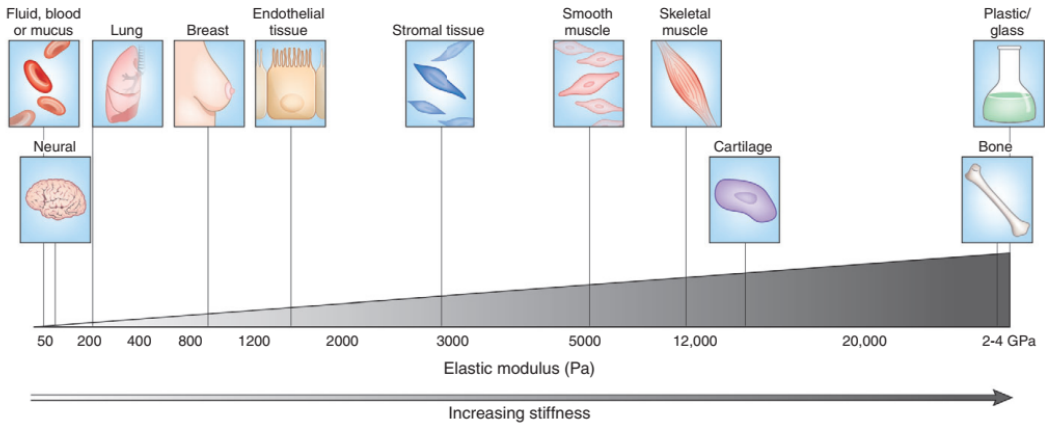

Figure 1.1. The variations of stiffness (elastic modulus) in human tissue. The biomechanical properties of tissue in terms of elastic modulus vary significantly between organs and tissues according to their function[13, 14].

1.1.1. Hydrogels compositions

Hydrogels can be broadly categorized into three classifications according to the nature of the polymeric materials: (1) synthetic polymer; (2) natural polymer; and (3) hybrid materials with both synthetic and natural components. Synthetic polymers have been widely used for the design and fabrication of hydrogels formed by copolymerization of monomers, cross-linkers, or by reactions of synthetic polymers, macromers, and cross-linkers. The chemical structure of common synthetic polymers for hydrogels including poly (acrylic acid) (PAA)[15], poly(2-hydroxyethyl methacrylate) (PHEMA)[16], poly(vinyl alcohol) (PVA)[17], poly(ethylene glycol) (PEG)[18], polyacrylamide[19], silicone[20] are shown in **Figure 1.2A**.

Hydrogels made from naturally derived polymers usually have biocompatibility due to the similarity in their compositions. Natural polymer hydrogels (**Figure 1.2B**) include those of proteins, such as collagen[21] and silk[22], denatured proteins, such as gelatin[23], and polysaccharides, such as hyaluronic acid[24] and alginate[25]. The degradability and biocompatibility in biological tissue of natural sourced polymeric hydrogels make it a very attractive material in recent research on tissue engineering.[26]

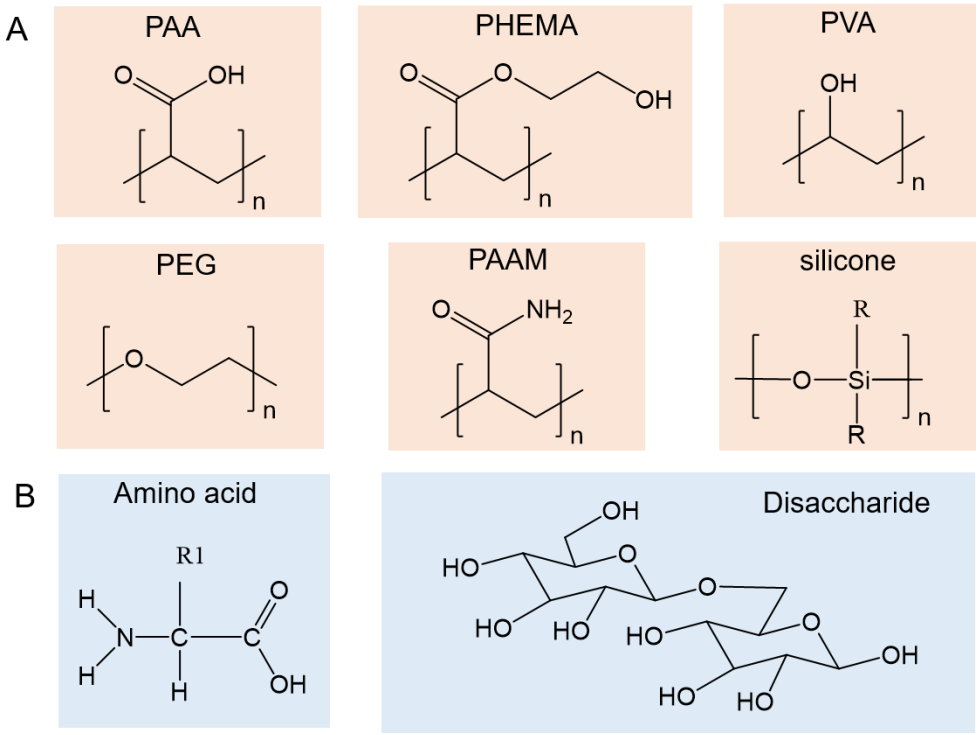

Figure 1.2. Examples of common synthetic polymer and natural polymer for hydrogels. (A) Synthetic polymers: poly(acrylic acid) (PAA); poly(2-hydroxyethyl methacrylate) (PHEMA); poly(vinyl alcohol) (PVA); poly(ethylene glycol) (PEG); polyacrylamide; silicone. (B) Natural polymers. Left: an amino acid, the repeating unit of a protein; Right: a disaccharide, the repeating unit of a polysaccharide.

1.1.2. Crosslinking types

Based on the nature of the crosslinking junctions to fabricate the networks, hydrogels can also be commonly categorized into chemically cross-linked and physically cross-linked hydrogels.[27] Chemically crosslinked networks have permanent crosslinks where strong chemical bonds connect polymer chains in the network. **Figure 1.3 a-d** illustrates a series of chemical hydrogel in which the network can be (a) ideally chemically bonded; (b) non-ideally chemically bonded, with polymer chain self-loops and free ends; (c) a double network in which there are two distinct networks, each only covalently linked to chains and making an interpenetrating network structure, or (d) a non-conventional slidable crosslinking network.

Physical networks could be formed by transient crosslinks due to (a) polymer chain entanglements, (b) helix formation, (c) ions bridging between adjacent chains, or (d) crystalline domain ((**Figure 1.3 e-h**))[28].

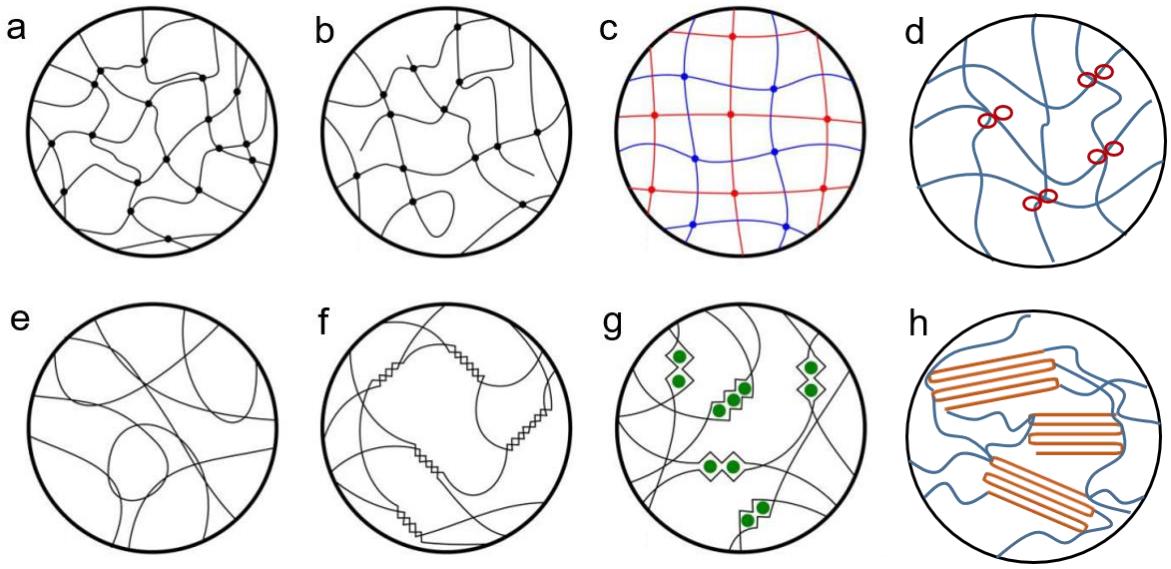

Figure 1.3. Schematic microstructure of gels to define types of cross-linking. (a) ideal cross-linked network with all tetra-functional linkages. (b) non-ideal cross-linked network including molecular ends and loops. (c) ideal cross-linked double network gel. (d) slidable crosslinks network. (e) physically entangled network. (f)

physically entangled network with helix formation. (g) alginate-like network with divalent calcium ions forming local bridges between adjacent chains[25]. (h) crystalline domain cross-linked network.

The nature and strength of the cross-link points are fundamentally distinct when comparing chemical and physical gels. Chemical crosslinks are relatively immobile with high bond energy, for example, that for permanent covalent bond varies from 200 – 600 kJ mol^{-1}, while the physical bond is weaker with lower bond energy as shown in **Figure 1.4**.[27]

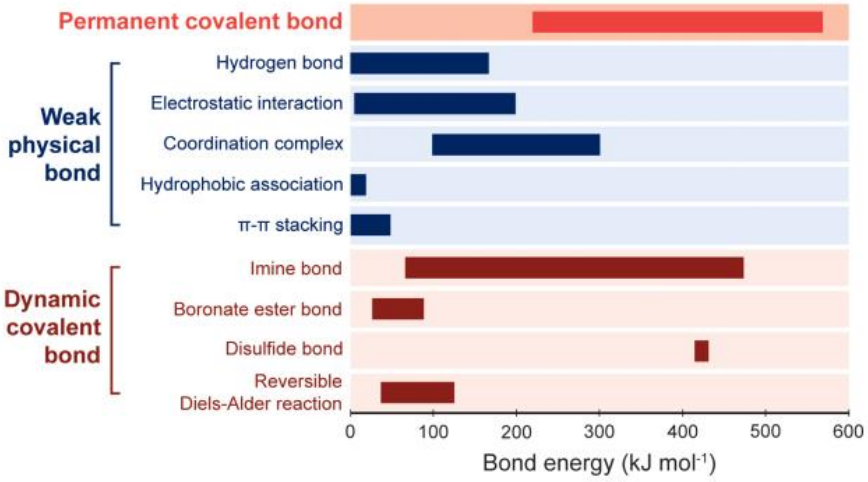

Figure 1.4. Bond energies of various types of permanent covalent cross-links, weak physical cross-links and dynamic covalent cross-links.[27]

1.1.3. Toughening of hydrogels

Simple chemically crosslinked hydrogels are typically brittle, in that they break under moderate stresses, making them unsuitable for industrial applications requiring a certain mechanical toughness. The poor mechanical properties of the hydrogels are mainly due to a lack of energy dissipation mechanism and heterogeneity of the network structure. To overcome such shortcomings of hydrogels, various reinforcement strategies in hydrogels are carried out over the past

decades. The toughness and fracture resistance of hydrogels are markedly improved by introducing sacrificial bonds in double networks[29], synthesizing the ideal network with uniform mesh size[30], and introducing crystallite[31].

In 2003, Gong et al. first reported double network hydrogels with extremely high mechanical strength[29]. The structure illustration of this double network system is as shown in **Figure 1.3c** in which it consists of a second polymer network implanted within a first network. The first network is highly cross-linked and made of poly (2-acrylamido-2-methylpropanesulfonic acid) (PAMPS) by UV-initiated polymerization which is then swollen in a solution containing a very small amount of cross-linker and a high concentration of the second network polymer, acrylamide (AAm). It is demonstrated that the brittle first network breaks upon large deformation and dissipates energy, while the interpenetrated second network keeps the integrity of the gel. **Figure 1.5**. (A) The compression of PAMPS single network (left) and PAMPS-PAAm double network (right). (B) Uniaxial compression stress-strain curves for the single networks (PAMPS and PAAm), and the double network of PAMPS-PAAm hydrogel.[29] **Figure 1.5A** shows the photographs of how the (brittle) PAMPS single network and (tough) PAMPS-PAAm double network react to the compression: the double network shows no visible damage after 90 % compression. Correspondingly, it is obvious that the double network has a good performance on both deformation and stiffness compared to either single PAMPS or PAAM gel as illustrated in the stress-strain curve (**Figure 1.5B**).

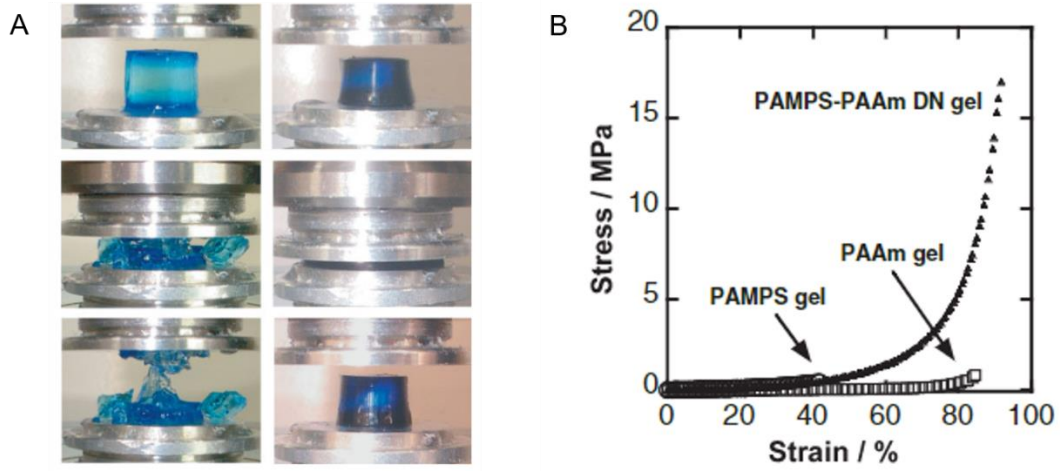

Figure 1.5. (A) The compression of PAMPS single network (left) and PAMPS-PAAm double network (right). (B) Uniaxial compression stress-strain curves for the single networks (PAMPS and PAAm), and the double network of PAMPS-PAAm hydrogel.[29]

Another strategy to achieve tough hydrogels is to introduce a well-defined mesh size with fixed crosslinks in the gel network. Sakai et al. [30] developed Tetra-PEG hydrogels by combining two symmetrical four-arm star-shaped macro monomers with the same chain length: tetra-NHS-glutarateterminated PEG (TNPEG) and tetra-amine-terminated PEG (TAPEG). These two materials are schematically represented in **Figure 1.6**, with the functional groups at the end of their arms. The obtained hydrogels have fewer network defects than usually chemical hydrogels, and the stress concentration at the weakest chains is prevented. The tetra-PEG gel demonstrates both higher fracture strain and stress compared to acrylamide gel and agarose gel as shown in **Figure 1.6C** due to the homogeneous structure of the network.

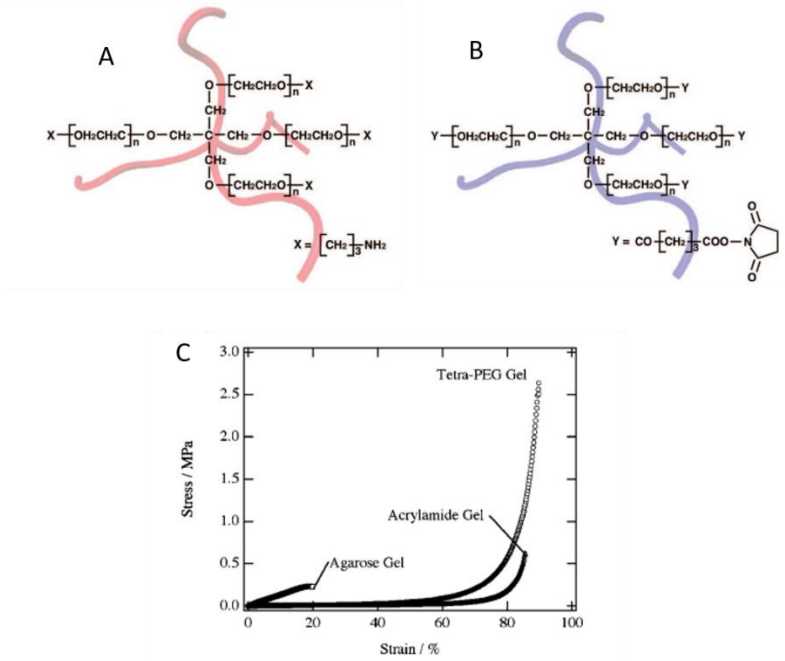

Figure 1.6. Molecular structure of TAPEG (A) and TNPEG (B); (C) Stress-strain curves of agarose gel, acrylamide gel, and tetra-PEG gel.[30]

Another effective way to reinforce the mechanical properties of hydrogels by introducing crystalline domains in the gel network will be discussed in detail in Chapter 4.

1.2. The challenges in ultra-soft hydrogels

1.2.1. Structural heterogeneity

The practical application of hydrogels is strongly limited when their macroscopic properties are impacted due to structural heterogeneity. An inhomogeneous network gives rise to localized stresses on certain chemical bonds at the molecular level and facilitates the initiation of larger defects that can propagate into cracks, therefore strongly decreasing the stress and strain at the break of hydrogels.

According to the work of Shibayama et al.[32], there are three classifications of gel inhomogeneities as shown in **Figure 1.7**: (1) spatial inhomogeneities, (2) topological

inhomogeneities, and (3) connectivity inhomogeneities. It is concluded that the spatial inhomogeneities stem from uneven distributions of crosslinks. The topological inhomogeneities rely on the topology of the network related to elastically inactive crosslinking including loops, trapped entanglements, and dangling chains. The connectivity inhomogeneities are linked to the size and spatial distributions of clusters which could be dominated at the gelation threshold in terms of the percolation problem.[33, 34]

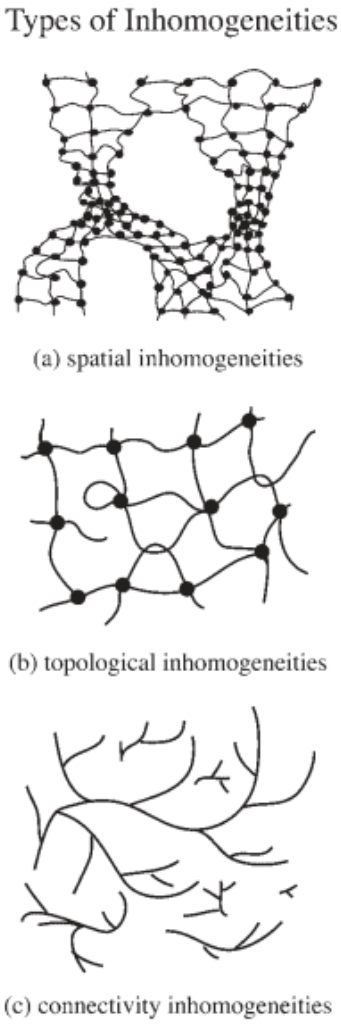

Figure 1.7. Inhomogeneities in gels.[32]

Small-angle X-ray and neutron scattering are well-recognized techniques to characterize structural heterogeneity in polymer gels. It is reported that the scattering of homogenous polymer gels is mainly from the fluctuation of the polymer chains and can be analyzed with the Ornstein-Zernike model[35]. On the contrary, the presence of the heterogeneous structure brings significant excess scattering intensity[35].

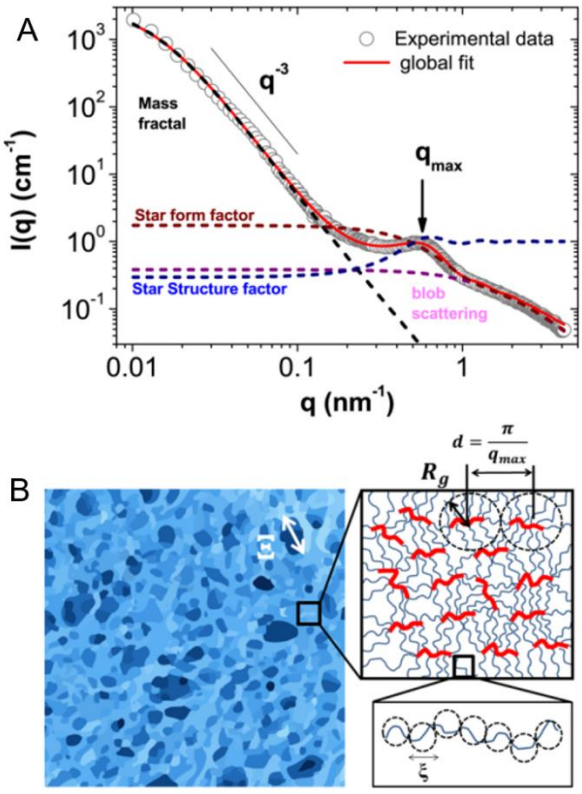

Figure 1.8. (A) Scattering intensity of a hydrogel PEGDA at ∅=0.2 showing all contributions to the global fit. (B) Schematic representation of a hydrogel of stars arranged into a fractal structure. In the insets, red lines represent acrylic backbones and blue lines represent PEG macromers.[36]

Helgeson et.al.[36] investigated the heterogeneity and its influence on the mechanical properties of poly(ethylenene glycol) diacrylate (PEGDA) hydrogel by small-angle neutron scattering technique over a large range of molecular weights and volume

fractions. The scattering data is well-described by the Guinier-Porod model by assuming spherical cross-links between PEG chains and acrylic crosslinking backbones in which a star-like polymer structure rather than a mesh chain is proposed in PEGDA gel as shown in **Figure 1.8**. As such, both the PEG chains and the acrylic backbones contribute to the elasticity modulus and the equilibrium swelling properties of PEGDA hydrogel. They conclude that the heterogeneity arises not from defects in the crosslinking network but rather from a heterogeneous distribution of polymer concentration, in which the heterogeneity structure results in the significant loss of elasticity.

1.2.2. The effect of surface tension

The elastic modulus of elastomers is generally in the order of megapascals. In that case, the engineering analysis of the deformation of material conventionally ignores the effect of gravity and surface tension which is remarkably important in the microfabrication of devices such as microfluidic channels[37]. Gravity loading is very important for large structures like buildings and dams. However, when the gel modulus is quite low, the surface tension could be the dominant driving force behind the shape change.

1.2.2.1. Deformation of soft materials on solid substrate

Recently, the highly stretchable DNA hydrogel (metagel) with a modulus in the order of only a few pascals has been developed[38]. As shown in **Figure 1.9**, the opaque DNA hydrogel emerged in water with a specific shape that can be stained by the DNA dye in green. The higher elastic modulus (< 10 Pa) than viscous modulus (< 1 Pa) over a large range of frequency further confirms the formation of the gel.

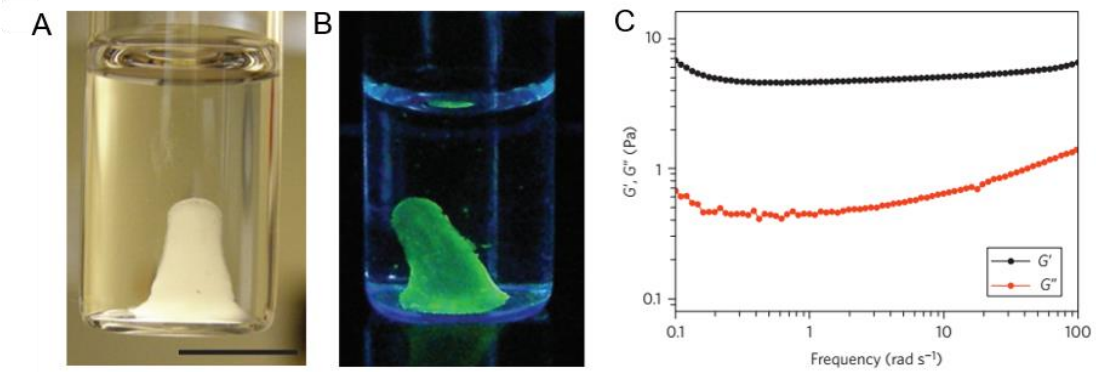

Figure 1.9. Characterization of the DNA hydrogel[38]. (A) Photograph of the hydrogel. Scale bar is 10 mm. (B) Hydrogels stained with GelGreen, a DNA-specific dye. (C) Elastic modulus and viscous modulus as a function of frequency from a rheometer measurement.

Figure 1.10 shows the shape change of a DNA Metahydrogel. Since the gel consists mostly of water, the loading due to gravity and surface tension is relatively small when the gel is submerged in water in which the gel could keep a well-defined shape as shown in **Figure 1.10A**. Then when water is removed from the vial, gels immediately deform to a pancake shape due to the influence of gravity and surface tension (**Figure 1.10B**); Interestingly, they recover to their original shape when reintroducing the water into vials (**Figure 1.10C**). As seen in **Figure 1.10D**, the gel with D-shape presents shape recovery within 15 s which is considered the elasticity of the gel network since the characteristic time for the swelling of the gel sample is in the order of hours. This memory effect of metagel interacting with water is potentially applied in the electric circuit using water as a switch[38].

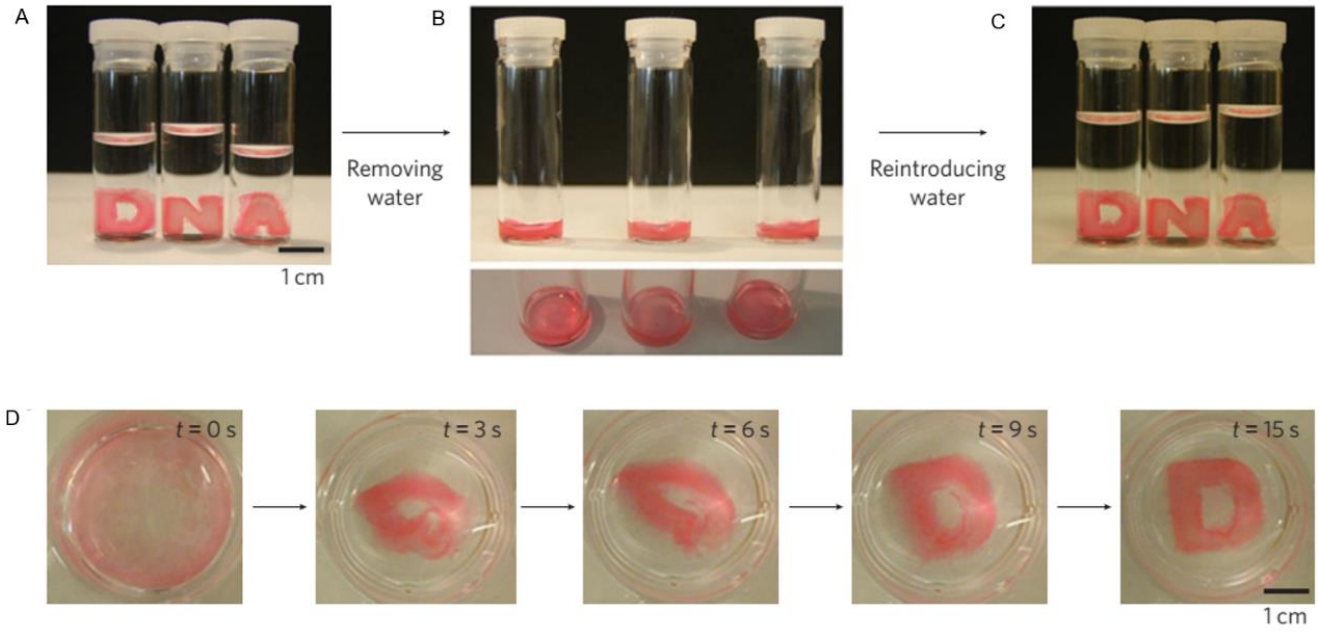

Figure 1.10. Shape change of a DNA Metahydrogel[38]. (A) D-, N- and A-shaped hydrogel. (B-F) Series of photographs showing the process of DNA hydrogel returning to its original shape after reintroducing water. The gel continues to transform back to its original shape, gradually and smoothly until the final D shape with 15 s.

To illustrate the relative importance of the role of elasticity, surface tension, and gravity in defining the shape of a soft material, Hui et. al.[39] proposed a 2D deformation map as shown in **Figure 1.11**. Two key strain parameters α and β are given from this plot. $\alpha = \gamma/\mu d$ denotes the average strain of the cube sample with a side length of d due to the surface tension, where γ is the surface tension and μ is the elastic modulus of the sample. $\beta = \rho g d/\mu$ denotes the average strain driven by the gravity of the sample, where ρ is the mass density and g is the acceleration of gravity. Considering the role of elasticity, surface tension, and gravity for an elastic solid, the deformation map could be divided into five distinct regions: (1) small strain regime E; (2) gravity-dominated regime G; (3) surface tension dominant

regime S; (4) gravity and surface tension dual action regime (G/S), and (5) gravity, surface tension, and elasticity triple-action regime (G/S/E).

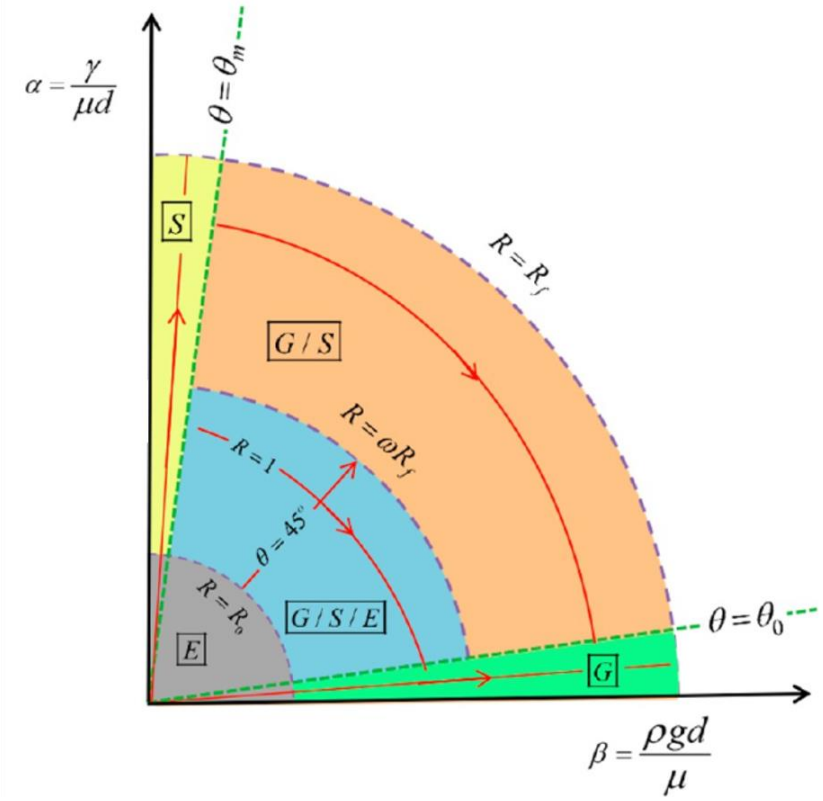

Figure 1.11. Deformation map of a soft material considering the role of elasticity, surface tension and gravity[39]. (1) small strain regime E; (2) gravity-dominated regime G; (3) surface tension dominant regime S; (4) gravity and surface tension dual action regime (G/S), and (5) gravity, surface tension, and elasticity triple-action regime (G/S/E).

Based on the work of DNA metahydrogel[38], the FEM simulation results of the deformation map for the gravity-dominant regime G using a neo-Hookean model are shown in **Figure 1.12A** and **Figure 1.12B**. The shape change of the sample is more evident for the sample with a larger gravity-driven average strain β = 80 compared to that with β = 20, indicating that the role of gravity to compress (change the shape) the sample is more significant for softer materials. Similarly, in the surface, tension-

driven deformation regime S, the deformation of the sample is larger for the sample with higher surface tension strain α = 100 ($\gamma \gg \mu d$, surface tension dominates to elasticity) compared to that with α = 1 where the role of surface tension is comparable to the elasticity ($\gamma = \mu d$) as shown in **Figure 1.12C** and **Figure 1.12D**. All of the above-mentioned experiments and simulation analyses demonstrate that the role of surface tension and gravity needs to take into account when dealing with mechanical problems especially the deformation of ultra-soft materials.

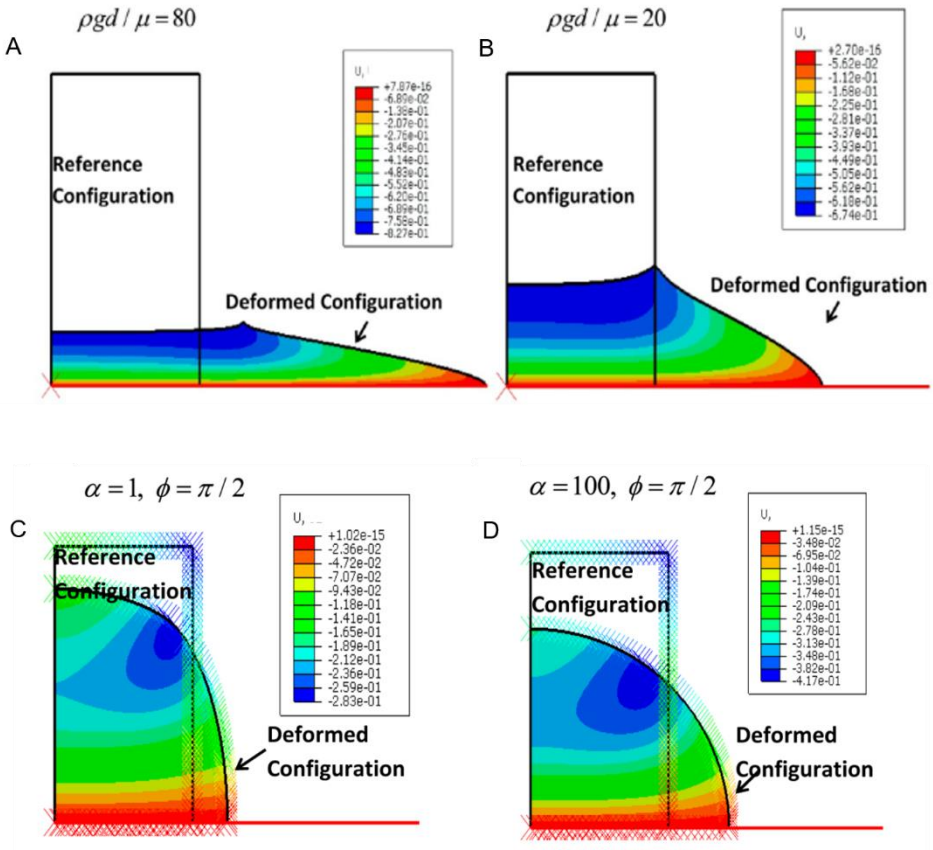

Figure 1.12. (A) FEM simulation results for the gravity-dominant regime using a neo-Hookean model with initial and deformed shapes at β = 80. (B) initial and deformed shapes at β = 20. (C) FEM simulation results for the surface tension dominant regime: comparison of deformed shape with initial shape for α = 1. (D) comparison of deformed shape with initial shape for α = 100.[39]

1.2.2.2. Indentation contact with soft materials

When a rigid solid is indented into a soft substrate, the surface tension in the contact line could be dominant to the elasticity of the material and determines its deformation behavior, as has been recently pointed out by Style et.al.[40] As shown in **Figure 1.13A**, the surface deformation of silicone gel to a spherical silica particle increases with decreasing gel modulus. The vertical deformation for a gel with E = 3 kPa is ~ 18 μm, comparable to the particle size a = 15 μm, while that for a gel with E = 500 kPa is negligible[40]. This deformation is relative to the elasto-capillary length which is defined as the ratio of the surface tension to the shear modulus, $l_{ec} = \gamma/E$. As shown in **Figure 1.13B,** when large particle contact with the stiff substrate (contact radius a is much larger than l_{ec}), the contact is described by the Johnson-Kendall-Roberts (JKR) theory, which balances adhesion and elastic stresses, and the surface tension contribution is negligible. On the contrary, when a small particle contacts with the soft substrate ($a < l_{ec}$), surface tension dominates to the contact mechanics and adhesion mimics adsorption on a fluid interface in which the elastic forces are negligible (**Figure 1.13C**).

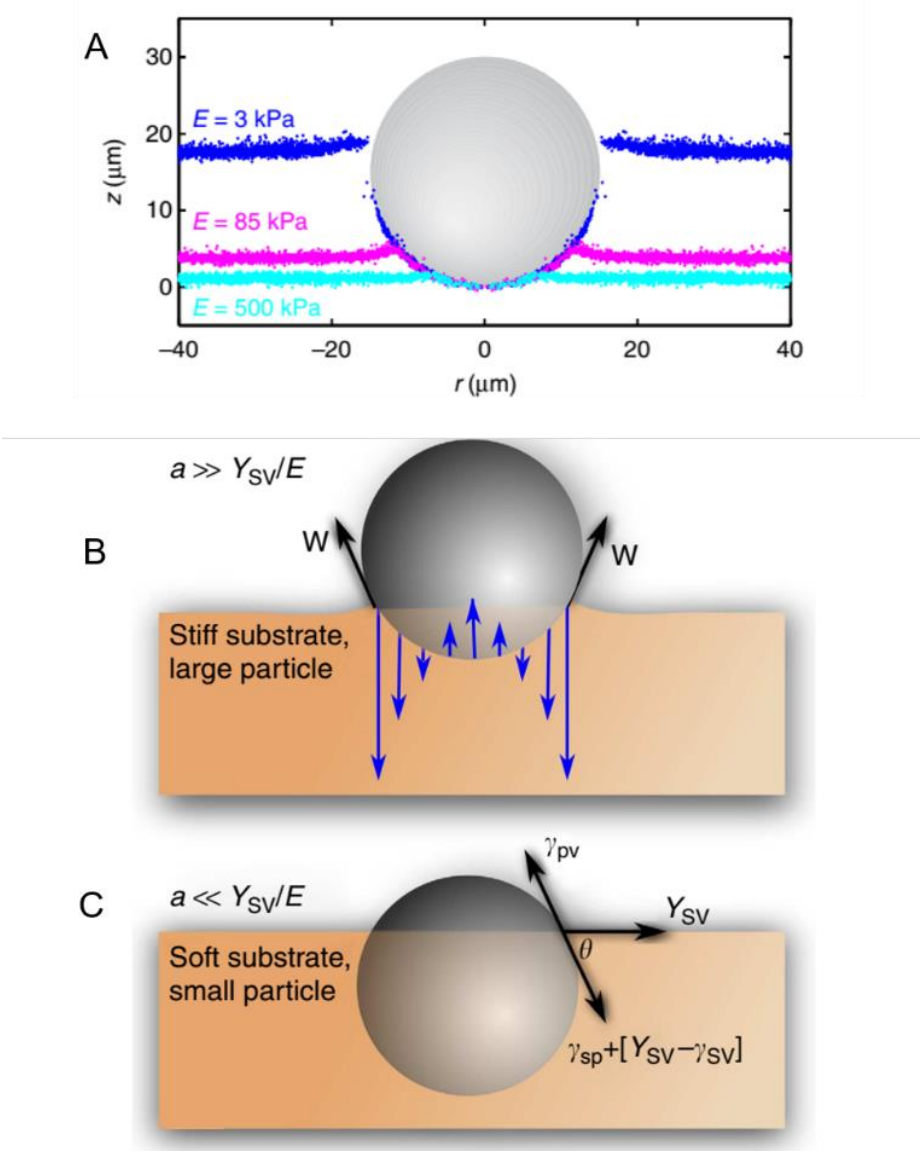

Figure 1.13. (A) Surface indentation profile of silicone substrates (E = 3, 85, and 500 kPa) on adhesion to spherical silica particles with a radius of 15 μm. (B) Contact of a large particle to a stiff substrate. (C) Contact of a small particle to a soft substrate.[40]

When the elastic modulus of the solid is low, the surface tension can induce deformation, and the size scale over which is explained by the elasto-capillary length. The deformation amplitude caused by surface tension would thus vary from atomic dimensions to several microns or millimeters according to the stiffness of

materials. For some materials with a large modulus, such as metal with modulus ~ 100 GPa, the effect of surface tension is insignificant and can be ignored as the l_{ec} is quite small. For elastomers with a modulus in the order of 10 – 100 kPa, the value of l_{ec} can be micrometric, and it has been reported that the surface tension can cause a shape change of soft solids, such as flattening a sharp corner surface and close a crack inflated by hydrostatic pressure.[41-43]

1.3. Mechanical characterization techniques for hydrogels

The proper measurement of the mechanical properties of hydrogel in their own right is important as the mechanical properties of gels are relatively poor compared to engineering materials. Hydrogels exhibiting low mechanical strength also pose a challenge to the mechanical characterization in which the specimen can be difficult to "grip" for testing. Next, we will introduce briefly how the mechanical properties of gels in terms of stiffness ranging from ultra-soft to commonly recognized tough, can be properly tested.

1.3.1. Universal test frame

The most common technique used for the mechanical characterization of materials is the universal test frame, capable of carrying out a wide variety of experimental tests. Uniaxial and biaxial instruments are included in this frame in which the tension and compression testing could be performed. For the tension test of hydrogels, one difficulty to execute the experiment is to properly grip the sample in the geometry as the gel specimen is often compliant and hydrated. Solutions for addressing this challenge include the use of glue, double-sided tape, and cardboard tabs to assist in fixing the hydrogels[44]. For both tension and compression testing, the load-displacement data are converted into a commonly used stress-strain curve using

simple geometrical relations, in which Young's modulus and failure strength are inferred. This universal test frame is appropriate to measure the mechanical properties of gels with modulus in kPa to mega-Pa where a well-defined shape of the specimen is possible to be gripped in the testing geometries.

1.3.2. Indentation

When the stiffness of gels is quite low, as discussed above the ultra-soft sample cannot even support its weight when free standing due to the gravity effect, the gripping of such compliant sample into a regular (tensile or compressive testing) specimen geometry is practically impossible. New testing geometry is required to complete the mechanical characterization in such soft material system.

In indentation, a rigid probe of known geometry is brought into contact with the material surface. With the increasing indentation depth, fracture (breakup of the material surface) occurs, which is generally named as "puncture" test – the main tool to investigate the fracture properties of ultra-soft hydrogels in this thesis. Technically speaking, the indentation test is a local compression test, where the sample is compressed by a small probe instead of the across the entire surface, in which the load-displacement data is recorded. It is straightforward to keep hydrogel samples hydrated in the container throughout the indentation test and capable of probing the local inhomogeneity of graded or patterned gels using a mapping technique across the sample surface.[45] This technique can be used to study hydrogels at a highly adaptable length scale from ~mm to ~nm or ~μm. The atomic force microscopes (AFMs) is a good example of the nano-indentation which is attractive to probe the stiffness of cells.[46]

Recently, puncture has been widely used in probing the fracture properties in soft materials, especially in biological tissues at a relatively small length scale.[47-49] Crosby et.al.[47] investigated the influence of polymer volume fraction on fracture

initiation at elasto-capillary length scale via puncture for self-assembled triblock copolymer gels (**Figure 1.14**). They found that the fracture initiation energy Γ_0 from puncture scales as $\Gamma_0 \sim \phi_v$ while the fracture energy release rate scale with the volume fraction by $G_c \sim \phi_v^{2.2}$ showing great agreement with the classical Lake-Thomas model. This result indicates that the role played by different fundamental mechanisms governs fracture initiation in soft gels.

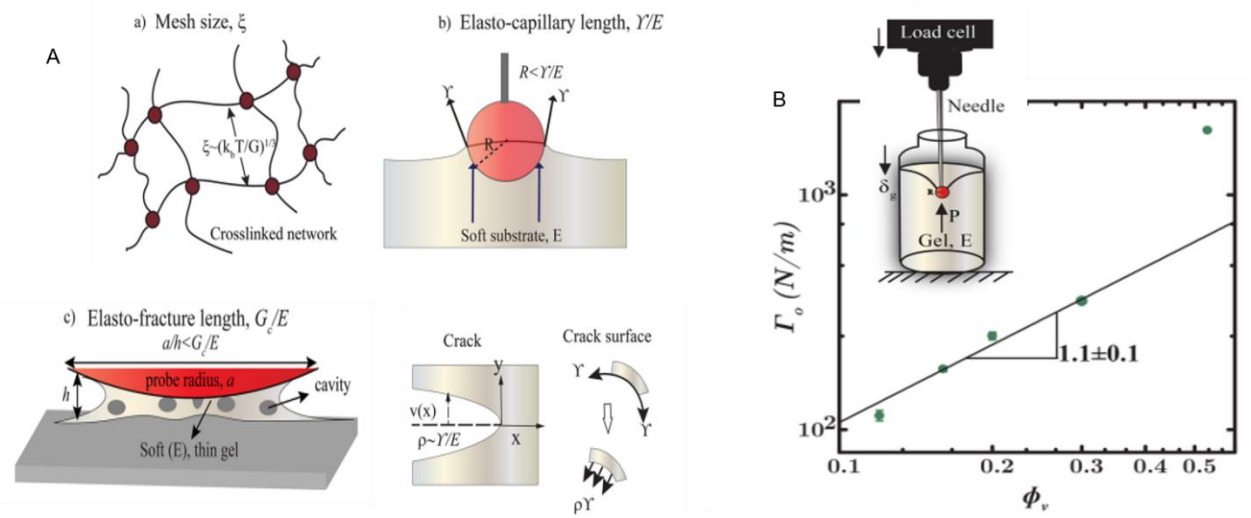

Figure 1.14. (A) Schematic depicting various characteristic length scales: (a) mesh size of the network ξ, (b) the elasto-capillary length γ/E, and (c) the elasto-fracture length G_c/E. (B) The fracture initiation energy as a function of gel volume fraction.[47]

1.3.3. Cavitation

The cavitation rheology or needle-induced cavitation (NIC) enables spatially localized probing of nonlinear elastic and fracture behavior for soft materials that are often difficult to manipulate with traditional mechanical characterization geometries[50, 51]. The technique involves inducing a cavity by pressurizing the air into soft materials at the tip of a syringe needle in an arbitrary position. Recently, it has been extensively employed to measure the in vivo and ex vivo mechanical response

of various polymer gels and biological networks, exhibiting tremendous potential applications in the biomedical and biological field[52]. For example, the anisotropic mechanical properties of bovine eye lenses were measured using cavitation rheology over a range of length scales (**Figure 1.15A**)[51]. It was also utilized to probe the stiffness of brain tissue in different regions (such as grey matter and white matter) to potentially predict the possible related diseases in the living body (**Figure 1.15B**)[53].

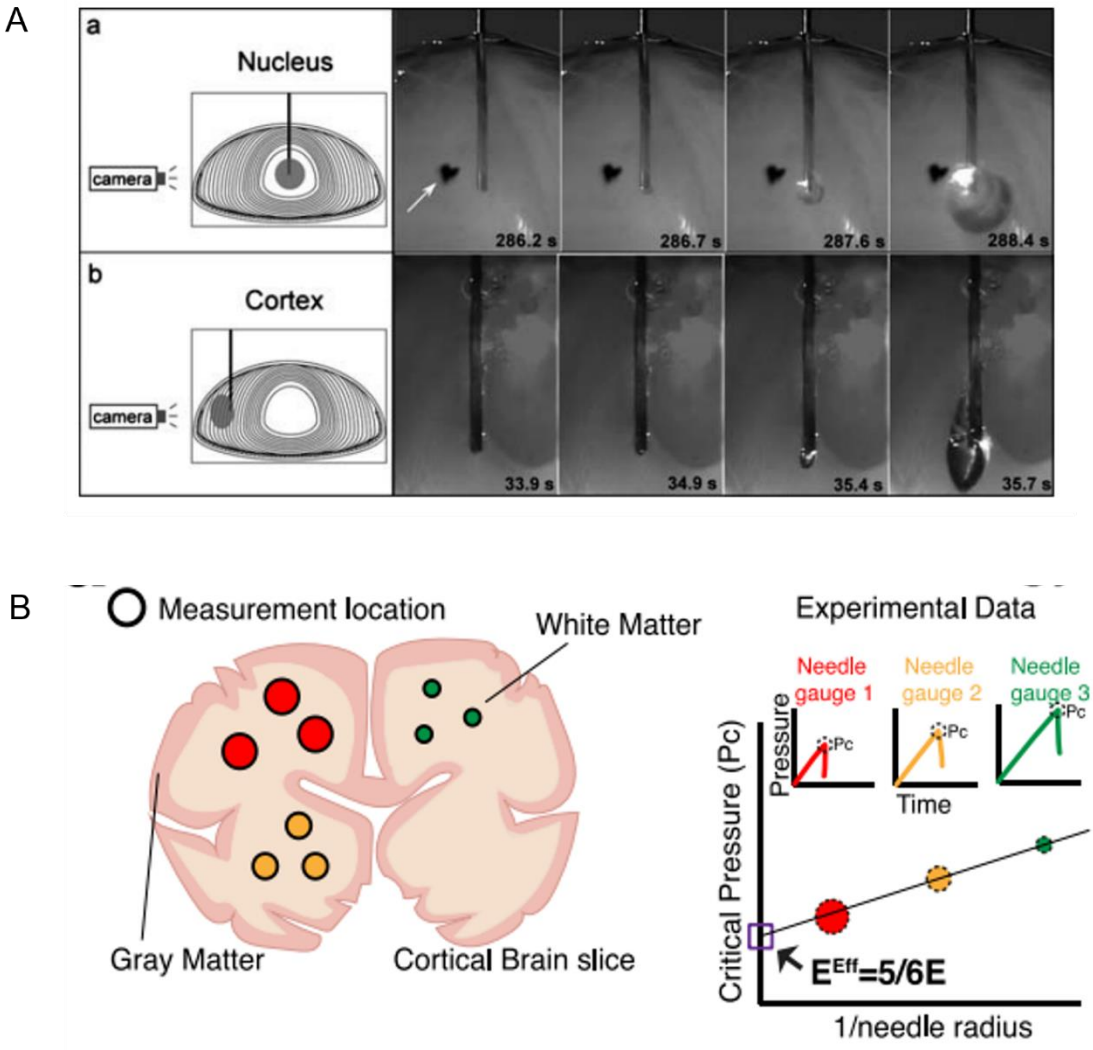

Figure 1.15. (A) Micrographs of initiation and propagation of cavities in the regions of nucleus (top) and cortex (bottom)[51]. (B) Schematic of cavitation in brain

tissue (left) and the critical pressure against needle radius to calculate Young's modulus of the brain tissue[53].

1.4. The objective of this thesis

As described in this chapter, ultra-soft material exhibits different mechanical (deformation and fracture) characteristics compared to common soft material, and as such put forward an open and fascinating research area.

However, ultra-soft hydrogels received rather limited research attention despite the great importance of application in tissue engineering and biomedical use. In this thesis, we focus on the characterization of unique deformation and fracture behavior of ultra-soft hydrogel, as a model of soft organs in the human body, through puncture and cavitation techniques accompanied by optical methods, aiming to provide fundamental mechanical insight into the fracture-associated phenomena of ultra-soft material in medical and surgical science.

The experimental part of this thesis is organized according to the following plan:

1. **Chapter 2** is dedicated to describing the rheological and puncture behavior of polyacrylamide hydrogel, poly(dimethyl siloxane) (PDMS), and carrageenan hydrogel at elasto-capillary length scale.
2. **Chapter 3** focuses on the fracture behavior of poly(vinyl alcohol) (PVA) hydrogel with low hydrolysis degree. The fracture resistance of hydrogels with different structural heterogeneity will be investigated.
3. **Chapter 4** reports the extreme large strain-induced crystallization in PVA hydrogel with high hydrolysis degree as well as the resultant above-needle-tip crack phenomenon due to the localized reinforcement effect.
4. **Chapter 5** details the effect of molecular weight and surfactant in PVA hydrogel on their fracture resistance.

5. **Chapter 6** deals with the quantitative 3D visualization of deformation of the deep indentation process by photon correlation imaging technique.

6. **Chapter 7** reports the needle-insertion-induced crystallization in cavitation. The cavitation morphology and fracture energy for PVA in the presence and absence of crystalline domain with a wide range of crosslinking level will be studied.

1.5. References

1. Zhao, X., Multi-scale multi-mechanism design of tough hydrogels: building dissipation into stretchy networks. *Soft matter* **2014,** *10* (5), 672-687.
2. Li, J.; Mooney, D. J., Designing hydrogels for controlled drug delivery. *Nature Reviews Materials* **2016,** *1* (12), 1-17.
3. Hong, W.; Zhao, X.; Zhou, J.; Suo, Z., A theory of coupled diffusion and large deformation in polymeric gels. *Journal of the Mechanics and Physics of Solids* **2008,** *56* (5), 1779-1793.
4. Yuk, H.; Lin, S.; Ma, C.; Takaffoli, M.; Fang, N. X.; Zhao, X., Hydraulic hydrogel actuators and robots optically and sonically camouflaged in water. *Nature communications* **2017,** *8* (1), 1-12.
5. Deligkaris, K.; Tadele, T. S.; Olthuis, W.; van den Berg, A., Hydrogel-based devices for biomedical applications. *Sensors and Actuators B: Chemical* **2010,** *147* (2), 765-774.
6. Brandl, F.; Sommer, F.; Goepferich, A., Rational design of hydrogels for tissue engineering: impact of physical factors on cell behavior. *Biomaterials* **2007,** *28* (2), 134-146.
7. Beebe, D. J.; Moore, J. S.; Bauer, J. M.; Yu, Q.; Liu, R. H.; Devadoss, C.; Jo, B.-H., Functional hydrogel structures for autonomous flow control inside microfluidic channels. *Nature* **2000,** *404* (6778), 588-590.
8. Li, T.; Li, G.; Liang, Y.; Cheng, T.; Dai, J.; Yang, X.; Liu, B.; Zeng, Z.; Huang, Z.; Luo, Y., Fast-moving soft electronic fish. *Science advances* **2017,** *3* (4), e1602045.
9. Kim, Y. S.; Liu, M.; Ishida, Y.; Ebina, Y.; Osada, M.; Sasaki, T.; Hikima, T.; Takata, M.; Aida, T., Thermoresponsive actuation enabled by permittivity switching in an electrostatically anisotropic hydrogel. *Nature materials* **2015,** *14* (10), 1002-1007.
10. Liu, Y.; Liu, J.; Chen, S.; Lei, T.; Kim, Y.; Niu, S.; Wang, H.; Wang, X.; Foudeh, A. M.; Tok, J. B.-H., Soft and elastic hydrogel-based microelectronics for localized low-voltage neuromodulation. *Nature biomedical engineering* **2019,** *3* (1), 58-68.
11. Kim, C.-C.; Lee, H.-H.; Oh, K. H.; Sun, J.-Y., Highly stretchable, transparent ionic touch panel. *Science* **2016,** *353* (6300), 682-687.
12. Rose, S.; Prevoteau, A.; Elzière, P.; Hourdet, D.; Marcellan, A.; Leibler, L., Nanoparticle solutions as adhesives for gels and biological tissues. *Nature* **2014,** *505* (7483), 382-385.
13. Yuk, H.; Varela, C. E.; Nabzdyk, C. S.; Mao, X.; Padera, R. F.; Roche, E. T.; Zhao, X., Dry double-sided tape for adhesion of wet tissues and devices. *Nature* **2019,** *575* (7781), 169-174.
14. Cox, T. R.; Erler, J. T., Remodeling and homeostasis of the extracellular matrix: implications for fibrotic diseases and cancer. *Disease models & mechanisms* **2011,** *4* (2), 165-178.
15. Elliott, J. E.; Macdonald, M.; Nie, J.; Bowman, C. N., Structure and swelling of poly (acrylic acid) hydrogels: effect of pH, ionic strength, and dilution on the crosslinked polymer structure. *Polymer* **2004,** *45* (5), 1503-1510.
16. Sefton, M.; May, M.; Lahooti, S.; Babensee, J., Making microencapsulation work: conformal coating, immobilization gels and in vivo performance. *Journal of Controlled Release* **2000,** *65* (1-2), 173-186.
17. Peppas, N. A.; Merrill, E. W., Development of semicrystalline poly (vinyl alcohol) hydrogels for biomedical applications. *Journal of biomedical materials research* **1977,** *11* (3), 423-434.

18. Ostuni, E.; Chapman, R. G.; Holmlin, R. E.; Takayama, S.; Whitesides, G. M., A survey of structure− property relationships of surfaces that resist the adsorption of protein. *Langmuir* **2001,** *17* (18), 5605-5620.
19. Yang, C.; Yin, T.; Suo, Z., Polyacrylamide hydrogels. I. Network imperfection. *Journal of the Mechanics and Physics of Solids* **2019,** *131*, 43-55.
20. Tighe, B. J., A decade of silicone hydrogel development: surface properties, mechanical properties, and ocular compatibility. *Eye & contact lens* **2013,** *39* (1), 4-12.
21. Knapp, D. M.; Barocas, V. H.; Moon, A. G.; Yoo, K.; Petzold, L. R.; Tranquillo, R. T., Rheology of reconstituted type I collagen gel in confined compression. *Journal of Rheology* **1997,** *41* (5), 971-993.
22. Nagarkar, S.; Nicolai, T.; Chassenieux, C.; Lele, A., Structure and gelation mechanism of silk hydrogels. *Physical Chemistry Chemical Physics* **2010,** *12* (15), 3834-3844.
23. Hudson, C. B., Gelatine—relating structure and chemistry to functionality. In *Food Hydrocolloids*, Springer: 1994; pp 347-354.
24. Burdick, J. A.; Prestwich, G. D., Hyaluronic acid hydrogels for biomedical applications. *Advanced materials* **2011,** *23* (12), H41-H56.
25. Donati, I.; Holtan, S.; Mørch, Y. A.; Borgogna, M.; Dentini, M.; Skjåk-Bræk, G., New hypothesis on the role of alternating sequences in calcium− alginate gels. *Biomacromolecules* **2005,** *6* (2), 1031-1040.
26. Zhang, Y. S.; Khademhosseini, A., Advances in engineering hydrogels. *Science* **2017,** *356* (6337), eaaf3627.
27. Zhao, X.; Chen, X.; Yuk, H.; Lin, S.; Liu, X.; Parada, G., Soft materials by design: unconventional polymer networks give extreme properties. *Chemical Reviews* **2021,** *121* (8), 4309-4372.
28. Oyen, M., Mechanical characterisation of hydrogel materials. *International Materials Reviews* **2014,** *59* (1), 44-59.
29. Gong, J. P.; Katsuyama, Y.; Kurokawa, T.; Osada, Y., Double-network hydrogels with extremely high mechanical strength. *Advanced materials* **2003,** *15* (14), 1155-1158.
30. Sakai, T.; Matsunaga, T.; Yamamoto, Y.; Ito, C.; Yoshida, R.; Suzuki, S.; Sasaki, N.; Shibayama, M.; Chung, U.-i., Design and fabrication of a high-strength hydrogel with ideally homogeneous network structure from tetrahedron-like macromonomers. *Macromolecules* **2008,** *41* (14), 5379-5384.
31. Lin, S.; Liu, X.; Liu, J.; Yuk, H.; Loh, H.-C.; Parada, G. A.; Settens, C.; Song, J.; Masic, A.; McKinley, G. H., Anti-fatigue-fracture hydrogels. *Science advances* **2019,** *5* (1), eaau8528.
32. Ikkai, F.; Shibayama, M., Inhomogeneity control in polymer gels. *Journal of Polymer Science Part B: Polymer Physics* **2005,** *43* (6), 617-628.
33. De Gennes, P.-G., On a relation between percolation theory and the elasticity of gels. *Journal de Physique Lettres* **1976,** *37* (1), 1-2.
34. Stauffer, D., Introduction to Percolation Theory, Francis & Taylor. London: 1985.
35. Matsunaga, T.; Sakai, T.; Akagi, Y.; Chung, U.-i.; Shibayama, M., SANS and SLS studies on tetra-arm PEG gels in as-prepared and swollen states. *Macromolecules* **2009,** *42* (16), 6245-6252.
36. Malo de Molina, P.; Lad, S.; Helgeson, M. E., Heterogeneity and its Influence on the Properties of Difunctional Poly (ethylene glycol) Hydrogels: Structure and Mechanics. *Macromolecules* **2015,** *48* (15), 5402-5411.

37. McDonald, J. C.; Whitesides, G. M., Poly (dimethylsiloxane) as a material for fabricating microfluidic devices. *Accounts of chemical research* **2002,** *35* (7), 491-499.
38. Lee, J. B.; Peng, S.; Yang, D.; Roh, Y. H.; Funabashi, H.; Park, N.; Rice, E. J.; Chen, L.; Long, R.; Wu, M., A mechanical metamaterial made from a DNA hydrogel. *Nature nanotechnology* **2012,** *7* (12), 816-820.
39. Xu, X.; Jagota, A.; Peng, S.; Luo, D.; Wu, M.; Hui, C.-Y., Gravity and surface tension effects on the shape change of soft materials. *Langmuir* **2013,** *29* (27), 8665-8674.
40. Style, R. W.; Hyland, C.; Boltyanskiy, R.; Wettlaufer, J. S.; Dufresne, E. R., Surface tension and contact with soft elastic solids. *Nature communications* **2013,** *4* (1), 1-6.
41. Jagota, A.; Paretkar, D.; Ghatak, A., Surface-tension-induced flattening of a nearly plane elastic solid. *Physical Review E* **2012,** *85* (5), 051602.
42. Hui, C.; Jagota, A.; Lin, Y.-Y.; Kramer, E., Constraints on microcontact printing imposed by stamp deformation. *Langmuir* **2002,** *18* (4), 1394-1407.
43. Liu, T.; Long, R.; Hui, C.-Y., The energy release rate of a pressurized crack in soft elastic materials: effects of surface tension and large deformation. *Soft Matter* **2014,** *10* (39), 7723-7729.
44. Normand, V.; Lootens, D. L.; Amici, E.; Plucknett, K. P.; Aymard, P., New insight into agarose gel mechanical properties. *Biomacromolecules* **2000,** *1* (4), 730-738.
45. Constantinides, G.; Chandran, K. R.; Ulm, F.-J.; Van Vliet, K., Grid indentation analysis of composite microstructure and mechanics: Principles and validation. *Materials Science and Engineering: A* **2006,** *430* (1-2), 189-202.
46. Kloxin, A. M.; Kloxin, C. J.; Bowman, C. N.; Anseth, K. S., Mechanical properties of cellularly responsive hydrogels and their experimental determination. *Advanced materials* **2010,** *22* (31), 3484-3494.
47. Rattan, S.; Crosby, A. J., Effect of polymer volume fraction on fracture initiation in soft gels at small length scales. *ACS Macro Letters* **2019,** *8* (5), 492-498.
48. Fakhouri, S.; Hutchens, S. B.; Crosby, A. J., Puncture mechanics of soft solids. *Soft Matter* **2015,** *11* (23), 4723-4730.
49. Rattan, S.; Li, L.; Lau, H. K.; Crosby, A. J.; Kiick, K. L., Micromechanical characterization of soft, biopolymeric hydrogels: stiffness, resilience, and failure. *Soft matter* **2018,** *14* (18), 3478-3489.
50. Kundu, S.; Crosby, A. J., Cavitation and fracture behavior of polyacrylamide hydrogels. *Soft Matter* **2009,** *5* (20), 3963-3968.
51. Cui, J.; Lee, C. H.; Delbos, A.; McManus, J. J.; Crosby, A. J., Cavitation rheology of the eye lens. *Soft Matter* **2011,** *7* (17), 7827-7831.
52. Jansen, L. E.; Birch, N. P.; Schiffman, J. D.; Crosby, A. J.; Peyton, S. R., Mechanics of intact bone marrow. *Journal of the mechanical behavior of biomedical materials* **2015,** *50*, 299-307.
53. Mijailovic, A. S.; Galarza, S.; Raayai-Ardakani, S.; Birch, N. P.; Schiffman, J. D.; Crosby, A. J.; Cohen, T.; Peyton, S. R.; Van Vliet, K. J., Localized characterization of brain tissue mechanical properties by needle induced cavitation rheology and volume controlled cavity expansion. *Journal of the Mechanical Behavior of Biomedical Materials* **2021,** *114*, 104168.

2. Chapter 2: Puncture of ultra-soft gels

2.1. Introduction

The stiffness of human organ tissues varies considerably corresponding to its inherent function. More specifically, the mechanically static organs (brain, breast, and lung) exhibit sufficient low modulus ~ tens Pa, whereas load-bearing organs, such as bones or joints, possess a modulus several orders of magnitude larger[1]. The mechanical features of hydrogel based tough materials with potential use in human tissue engineering have been extensively investigated [2-3]. However, the mechanism of common low-moduli soft tissues which may virtually exhibit strikingly large deformability and fracture resistance is far less known.

The challenges of characterizing the fracture properties of very soft solids lie in three aspects. First, the ultra-soft nature of the sample makes it difficult to manipulate and perform mechanical tests, since the sample might not even support its weight under the influence of gravity to a specific dimension[4]. Conventional fracture characterization tests such as a pure shear tests commonly used for harder solids is difficult to apply, and an appropriate geometry/technique for fracture measurement is necessary. Secondly, highly compliant, elastic materials can sustain large deformations exceeding their linear elastic range. Consequently, linear elastic fracture mechanics (LEFM)[5-6], well-established to investigate fracture for conventional hard solids, could no longer predict the failure behavior of such compliant systems without initial defect.

Thirdly fracture behavior in soft materials is reported to be sensitive to several characteristic length scales[7]. For instance, the mesh size of the material network ξ ($\sim(k_{\mathrm{B}}T/G')^{1/3}$, where k_{B} is the Boltzmann constant, T is temperature and G' is the elastic modulus)[8]; the electrocapillary length γ/G',[9-11] given by the solvent surface tension γ over the material elastic modulus G', as well as the elasto-fracture length

G_c/G',[7] determined by the ratio of the critical energy release rate for crack propagation G_c to elastic modulus G'.

Moreover, it should be noted that the surface tension can play an important role in the large deformation and presumably in the fracture behavior of soft solids. When the elastic modulus of the solid is low, the surface tension can induce deformation, and the size scale over which this capillary effect is important is explained by the elasto-capillary length. The deformation amplitude caused by surface tension would thus vary from atomic dimensions to several microns or millimeters according to the stiffness of materials. For some materials with an exceptionally large modulus, such as metal with modulus ~ 100 GPa, the effect of surface tension is insignificant and can be ignored as the l_{ec} is infinitely small. For elastomers with a modulus in the order of 10 – 100 kPa, the value of l_{ec} can be micrometric, and it has been reported that the surface tension can cause a shape change of soft solids, such as flattening a sharp corner surface and close a crack inflated by hydrostatic pressure[12-14]. Hui et al.[15] revealed that surface tension could resist crack growth by lowering the applied energy release rate. Various capillarity-induced deformation has been reported in the last 10 years. For the ultra-soft gels having G' ~ 10 Pa, l_{ec} can be of the order of 1 mm, approaching the sample size. In this case, surface tension would play a significant role in the mechanical properties.

Puncture experiments, allowing to detect the large local deformation and failure in soft solids, have been employed in characterizing the fracture behavior recently[16-18]. This technique involves inserting a long and sharp indenter into the soft material and record the puncture force as a function of indenter displacement during the puncture process. The point where the puncture force sharply drops corresponds to the failure of the material, where the indenter pierces the sample's surface. Fakhouri et al. studied the resistive force and failure of acrylic triblock copolymer gel with a

modulus above several kPa on large deformation and revealed two failure regimes: stress-limited and energy-limited by applying a process zone model of fracture[17]. Rattan et al. investigated the effect of polymer volume fraction on fracture initiation in acrylic triblock copolymer indented by a spherical-tipped indenter over length scales around the elasto-capillary length[16]. However, access to a length scale below the elasto-capillary length is beset with difficulties due to the specificity of the indenter geometry and the softness of the specimen. The fracture properties of soft solids below the elasto-capillary length scale are not well understood, justifying the necessity to clarify the role of surface tension on the fracture mechanisms at this specific length scale.

Thus, this work aims to explore the role played by capillarity in the fracture properties of ultra-soft hydrogels at the elasto-capillary length scale. In this chapter we show puncture mechanics of three model soft polymeric solids. Chemically crosslinked polyacrylamide (PAAM) hydrogels are commonly used neutral chemical hydrogels of flexible polymer chains. Poly(dimethylsiloxane) (PDMS) is an elastomer well characterized in the literature for the mechanics of soft solids. We also test κ-carrageenan. Carrageenan is a linear sulfated polysaccharide extracted from red seaweeds consisting of 1,3 linked β-D-galactopyranose (G) and 1,4 linked 3,6-anhydro α-D-galactopyranose (AG)[19]. There are three types of carrageenan:κ-, ι- and λ-carrageenans which are widely used in food industries as gelling, thickening, and stabilizing agents. The κ-carrageenan contains more sulfated groups than the others and exhibits a stronger gelling ability. The gelation mechanism for carrageenan was believed to be the coil-to-helix conformation transition in the presence of certain cations followed by the aggregation of double helices to form a stiff network during the cooling process[20]. By puncture experiments, these three model systems with a modulus range of 100 – 3000 Pa are studied.

2.2. Experimental section

2.2.1. Gels preparation

2.2.1.1. Synthesis of Polyacrylamide (PAAM) hydrogels

The synthesis of Polyacrylamide chemical gels was performed by conventional free radical polymerization. In brief, acrylamide (AAM) monomer (C_{AAM} = 4 – 10 wt%) was dissolved in water, in the presence of chemical crosslinker (*N*,*N*'-methylenebisacrylamide, MBA) (C_{MBA}= 0.18 mol%) radical initiator potassium peroxydisulfate (KPS) (C_{KPS} = 1 mol%) and catalyzer *N*,*N*,*N*',*N*'-tetramethyl ethylenediamine (TEMED) (C_{TEMED} = 1 mol%). The synthesis was done under air atmosphere considering the necessity to produce a large batch of samples for puncture test. To compensate the possible consumption of free radicals by O_2 during the polymerization process, an excess amount of initiator KPS was added in the system.

2.2.1.2. Synthesis of PDMS elastomer

A commercially available Sylgard 527 PDMS elastomer was prepared with a variable ratio of PDMS component A to component B as W_A/W_B: 0.8, 1, 1.1, 1.25, respectively. The two components were then stirred for 5 min to be homogenously mixed and then poured into a mold (cylindrical glass vial with diameter 25 mm) cured at 90 ℃ for 12 h.

2.2.1.3. Synthesis of the Carrageenan hydrogel

Carrageenan with a polymer concentration of 0.5 – 1.5 wt% was dispersed in water with the presence of KCl solution (adjusted to C_{KCl} = 10 mM) in a cylindrical glass vial and stirred vigorously with a magnetic bar for 30 min. Then the homogenously dispersed carrageenan solution was heated in the heating stage at 70 ℃ for 30 min and then further heated at 90 ℃ for 20 min following the procedure detailed in

reference[19]. The hot sample solution was placed at room temperature to cool down and complete the gelation process.

2.2.2. Puncture experiment

Puncture tests were performed on a custom apparatus consisting of a motorized stage, flat-end indenter, and force sensor. A balance with a precision of 0.1mg was placed at the bottom of the sample and used as a force sensor to measure the puncture loading force. As indenters, flat-end metal needles (obtained from Hamilton Company) with a radius of 0.13 – 0.31 mm were used. They were backfilled with epoxy resin and fixed to the adapter in the actuator (motorized stage). The inserting velocity of the indenter was 0.25 mm/s in this study. The loading force as a function of time and displacement can be recorded during the puncture process. For puncture test, all the samples were gelled in a cylindrical glass container with a diameter of ~ 25 mm and height of ~ 50 mm.

2.2.3. Rheology

Rheological measurements were carried out on a strain-controlled rheometer (ARES, TA Instruments, USA) with a steel cone-plate geometry (25 mm in diameter, 0.053mm in the gap). A fresh gel mixture solution before gelation was loaded for time sweep measurement to track the gelation behavior of the PAAM sample at 25 ℃. PDMS was placed in the cone-plate geometry and kept 60 ℃ for 6h to finish the gelation. Hot carrageenan solution was loaded to the rheometer at 90 ℃ and gelation was monitored during the cooling process. Then Frequency sweep with an angular frequency range of 0.1-100 rad/s at a linear strain of 2 % and strain sweep with amplitude ranging 0.1-1000 % at a fixed frequency of 1 Hz were performed successively for the sample at 25 ℃. For each measurement, the exposed surface of the sample was covered with a thin layer of low-viscosity silicone oil to avoid water evaporation.

2.3. Results and Discussion

2.3.1. Linear-mechanical response characterization via Rheology

To explore the linear mechanical response of PAAM hydrogels, we performed oscillatory shear rheology. **Figure 2.1**A shows the frequency ω dependence of PAAM hydrogel made from a monomer (AAM) solution of concentration of 4 – 10 wt%. A well-defined elastic plateau was observed for each of the samples, with a viscous modulus *G*'' two orders of magnitude smaller than *G*'. The elastic modulus *G*' was found to increase with the AAM concentration, and it is nearly independent of the applied frequency, indicating the purely elastic character of the PAAM hydrogel. In **Figure 2.1**B, the strain sweep was performed at a fixed frequency of 6.28 rad/s for PAAM hydrogel. For each of the samples, a large linear viscoelastic regime was observed with increasing applied strain, followed by the decrease of both elastic modulus and viscous modulus at a large critical strain value until the gel network was ruptured. While a linear dependence of *G*' with polymer concentration is expected from the theory of rubber elasticity ($G' = \nu kT$, where ν is the number of elastically effective chains per unit volume), we found that the elastic modulus of PAAM increases with AAM concentration. In **Figure 2.1**C the AAM concentration dependence of the plateau modulus is shown. The scaling argument for entangled polymer networks in a good solvent predicts $G' \sim \emptyset_v^{2.2}$, as indicated by a solid line. Our result exhibits a stronger concentration dependence, suggesting that at the lower AAM concentration, the network is close to the percolation limit and has a lower modulus than predicted value. Here we define the rupture strain γ^* of the PAAM gel as the strain at which *G*' starts to decrease. γ^* was plotted as a function of elastic modulus in **Figure 2.1**D, from which γ^* decreases with elastic modulus, presumably linked to the limited chain extensibility of the gel network.

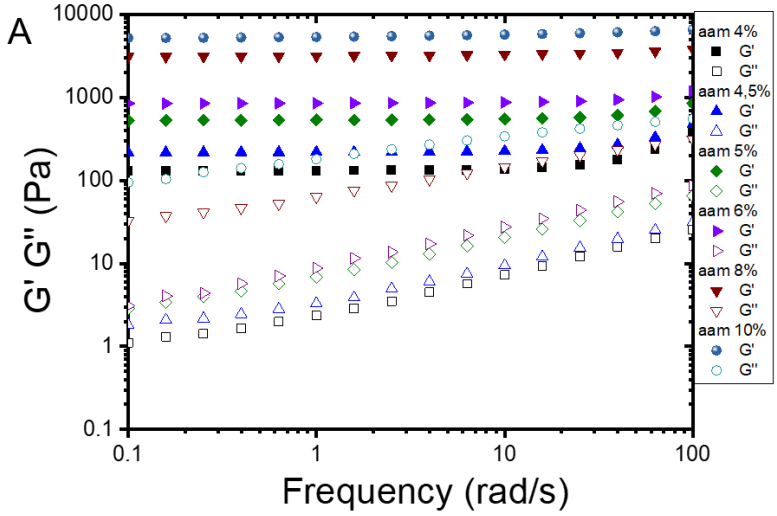
A
G' G" (Pa)
Frequency (rad/s)
10000
1000
100
10
1
0.1
0.1
1
10
100
aam 4%
G'
G"
aam 4,5%
G'
G"
aam 5%
G'
G"
aam 6%
G'
G"
aam 8%
G'
G"
aam 10%
G'
G"

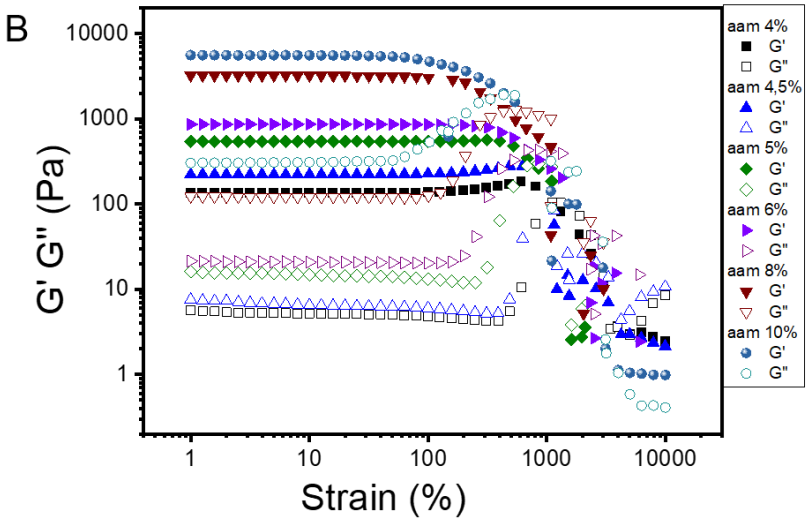
B
G' G" (Pa)
Strain (%)
10000
1000
100
10
1
1
10
100
1000
10000
aam 4%
G'
G"
aam 4,5%
G'
G"
aam 5%
G'
G"
aam 6%
G'
G"
aam 8%
G'
G"
aam 10%
G'
G"

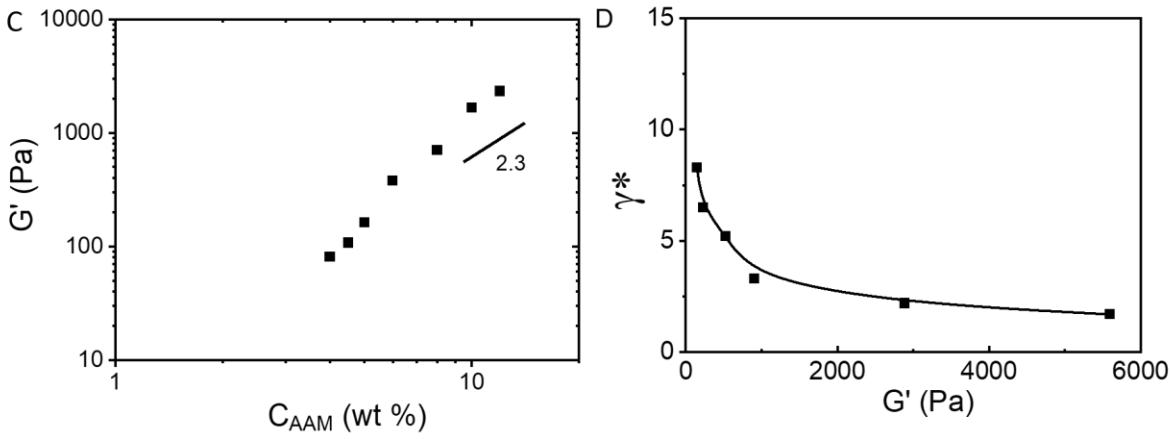

Figure 2.1. (A) Frequency sweep of PAAM hydrogel with AAM concentration varying from 4 to10 wt %. (B) Elastic modulus and viscous modulus as a function of strain for PAAM hydrogel. (C) Elastic modulus against AAM concentration, with the solidline indicating the scaling relation $G' \sim C^{2.3}$. (D) Rupture strain γ^* as a function of elastic modulus.

Figure 2.2 shows the frequency and strain dependence of the modulus for PDMS with the weight ratio of components A and B equal to 1 and 1.25, respectively. In **Figure 2.2A**, for PDMS with component $W_A/W_B = 1$, the elastic modulus is almost independent of the frequency but the viscous modulus increases significantly with frequency becoming even comparable to the elastic modulus at ω ~100 rad/s. The elastic modulus and viscous modulus are nearly overlapped and present a strong frequency dependence (increase with ω) for PDMS with component $W_A/W_B = 1.25$. This result indicates that PDMS shows a distinct viscoelastic characteristic. A large linear viscoelastic region is observed for both PDMS with $W_A/W_B = 1$ (G' ~ 800 Pa) and $W_A/W_B = 1.25$ (G' ~ 150 Pa) in **Figure 2.2B**, until the rupture of the material at critical strain $\gamma^* \sim$ 1000%, exhibiting the great deformability of PDMS polymer chain.

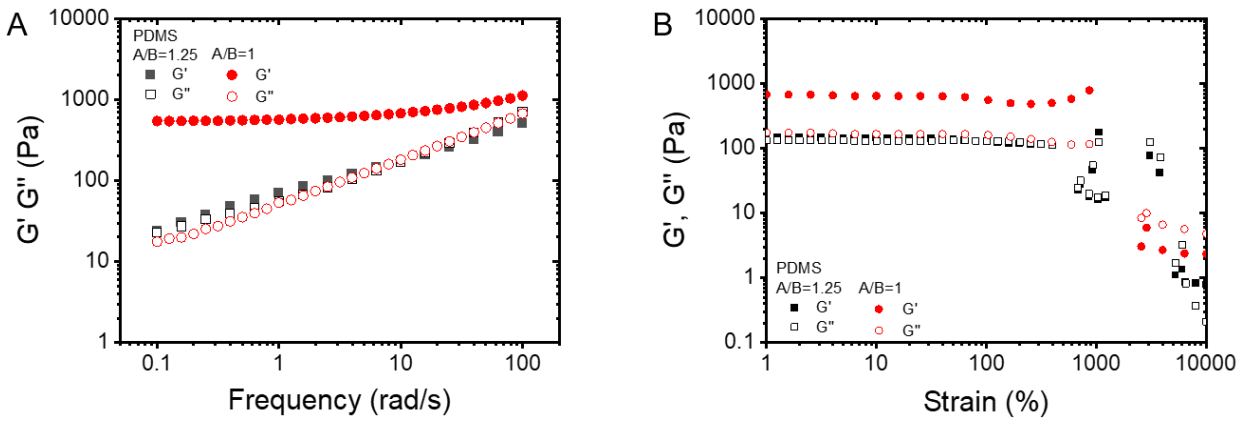

Figure 2.2. (A) Frequency dependence and (B) Strain dependence of modulus for PDMS with the weight ratio of component A and component B $W_A/W_B = 1$ and $W_A/W_B = 1.25$.

We performed also small amplitude oscillatory shear measurements of carrageenan. Especially for higher carrageenan concentrations, it is difficult to load a hot solution sample to the geometry before quick cooling and gelation of the sample take place. **Figure 2.3A** shows the frequency dependence of the modulus for carrageenan with polymer concentration 0.8 wt%, where the elastic modulus and viscous modulus are both independent of frequency, showing obvious elastic features. **Figure 2.3B** shows the strain sweep of the carrageenan in comparison to PAAM. Interestingly, the carrageenan and PAAM present quite similar elastic and viscous modulus values in the linear viscoelastic strain region. However, the rupture strain γ^* for carrageenan is about 10 % while that value for PAAM can reach ~ 1000 %, due to the stiffness of the carrageenan polymer chain.

In order to complete the modulus measurements of all the samples, we used a small displacement indentation force measurement during the puncture tests. The results obtained with this method are shown in the next section.

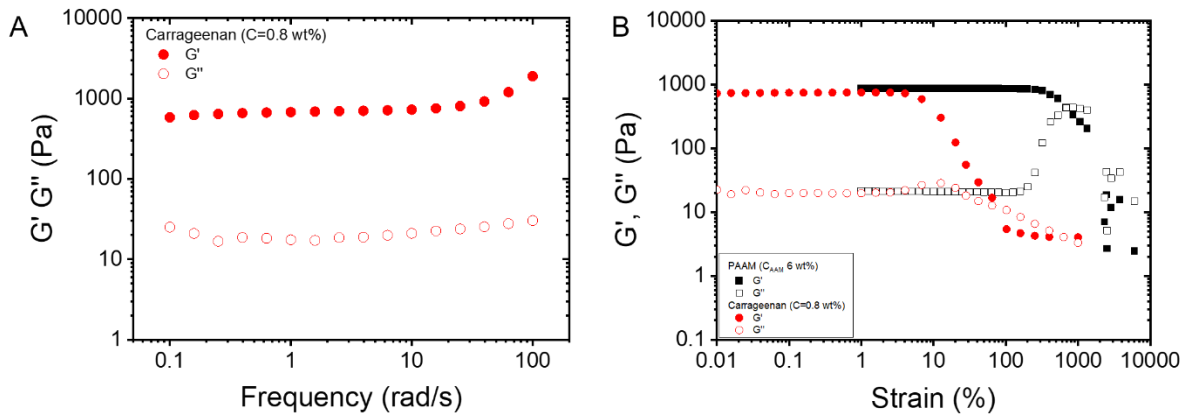

Figure 2.3. (A) Frequency dependence and (B) Strain dependence of modulus of Carrageenan at the polymer concentration C = 0.8 wt%, with the comparison of PAAM (C_{AAM} = 6 wt%). The elastic modulus of Carrageenan and PAAM is in the same level G'~ 900 Pa.

2.3.2. Puncture

2.3.2.1. Puncture loading-unloading curve

Figure 2.4A shows the schematic of the puncture setup. The needle is inserted into the gel with a constant velocity (0.25 mm/s) and penetrates the surface of the gel-fracturing material. Here we describe the needle insertion as a sharp transition between two needle-specimen configurations, namely, indentation and penetration.

The displacement of needle d (starting from the contact position of needle and gel surface) as a function of time is illustrated in **Figure 2.4A**. In **Figure 2.4B**, the loading force as a function of displacement can be recorded during the puncture process, from which the critical puncture force F_c (the peak force in the loading curve), and D_c the critical displacement can be extracted. After the critical puncture point, the force drops immediately and then continues to increase until the maximum indentation depth is reached as the needle keeps penetrating the material. Then the

unloading curve corresponds to the retraction process of the needle from the sample, reflecting the friction between the needle and the material.

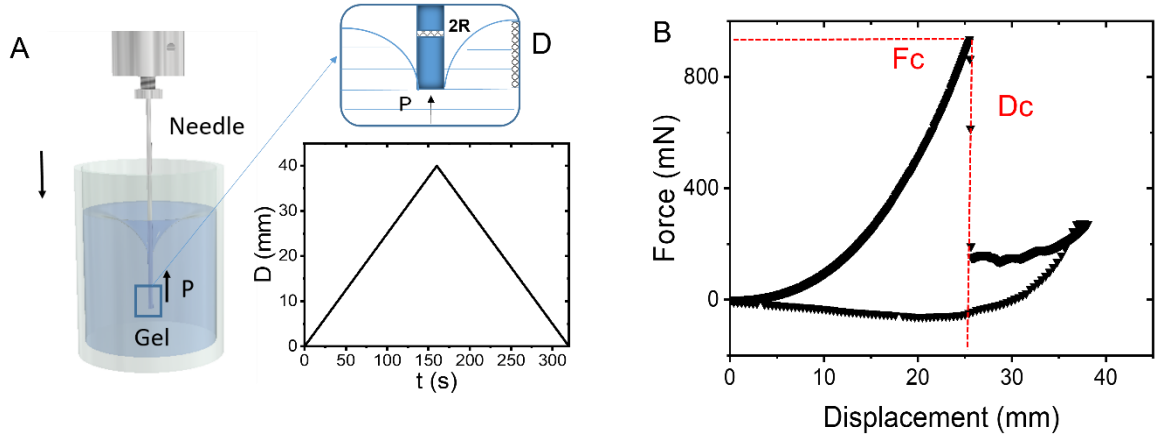

Figure 2.4. (A) Schematic of puncture apparatus and (B) representative puncture loading curve: puncture force as a function of puncture displacement, with critical force marked as F_c and critical displacement as D_c for PAAM hydrogel with C_{AAM} = 6% wt.

In **Figure 2.5**, typical loading-unloading curves for the three model systems tested in this chapter are shown. The shape of the curves strongly depends on the system. For the PAAM gel, during the loading, the force increases linearly then nonlinearly. The critical displacement D_c at the puncture fracture point is very large, above 20 mm. After the catastrophic fall of the force (fracture), the increase in the force is small during further indentation. This result suggests that upon fracture the stress is elastically released, and that the friction between the gel and the PAAM gel is weak. The stress release is also confirmed from the video taken during the test. Upon fracture the deformed surface of the gel quickly moved up toward the original position. During the unloading, the force gradually decreased to reach negative values, the hysteresis is not large, indicating again that the friction is weak.

The response of the PDMS during loading before fracture seems similar to that of the PAAM gel: the loading force nonlinearly increases to D_c whose value (~12 mm) is lower than that of the PAAM gel. After the fracture point, the decrease in the force is limited, and for this example a second peak is identified. During the unloading, the force decreases below zero, and the absolute value of the force is as large as those during the loading, resulting in a very large hysteresis. This result suggests that the friction of the PDMS against the indenter is stronger than that of the PAAM hydrogel.

Finally, for the carrageenan gel, the behavior is further different. During the loading the force increases practically linearly while fracture occurs at a very short D_c, about 2 mm. After this first peak, at every about 1 mm, fracture repeatedly occurs, showing the brittle nature of the gel. During the unloading, the force stays practically zero, no sign of friction and residual stress. The muti-peak phenomenon during the loading process was reported previously for polyacrylamide hydrogel where each peak is believed to correspond to a cone-shape crack initiation[21]. The low friction of PAAM/carrageenan and needle could be attributed to the high content of water in hydrogels as previously reported for PAAM hydrogels[22] while the PDMS as an elastomer adheres to the needle and shows more friction. In this work, we further characterize the loading process and the fracture behavior.

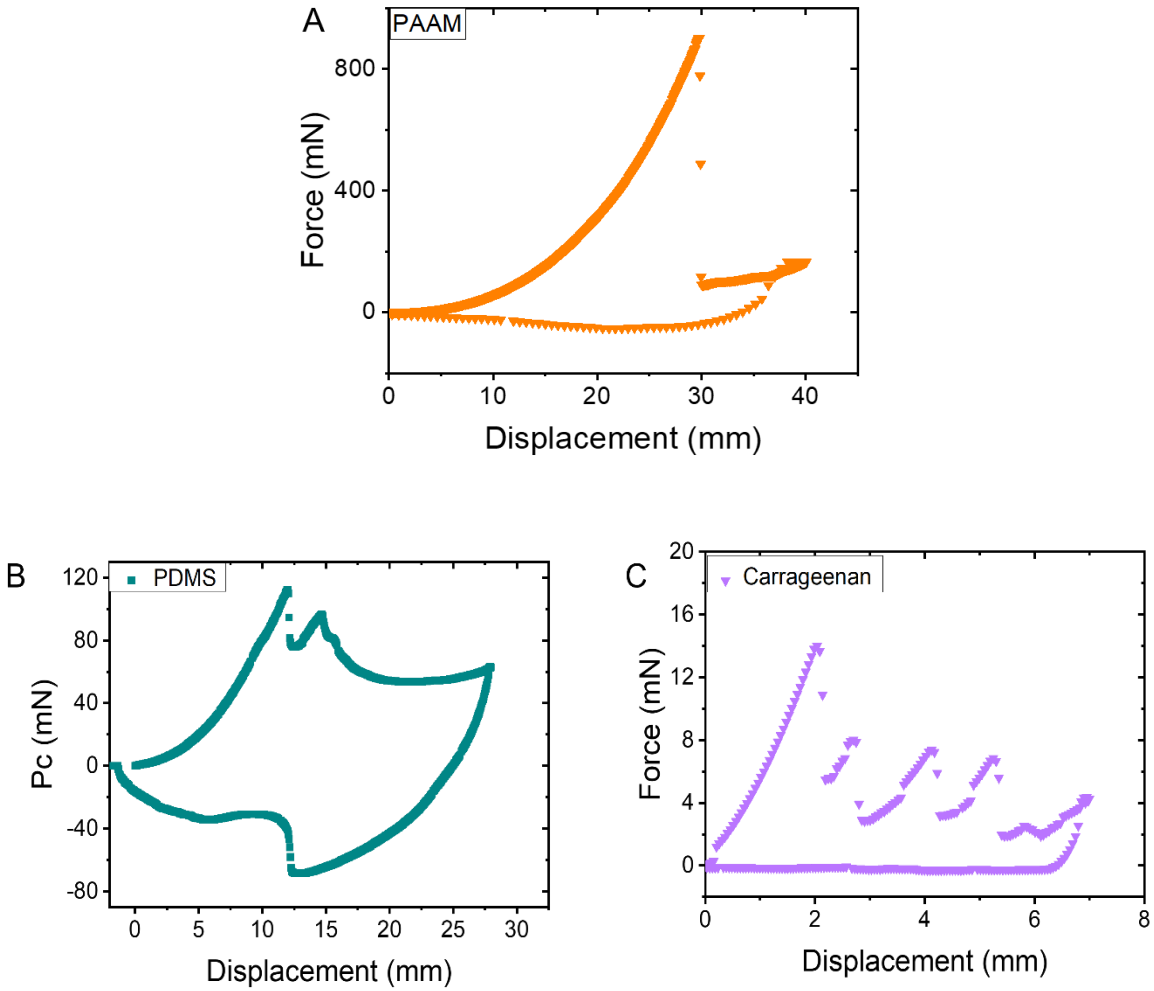

Figure 2.5. (A) Puncture loading and unloading curves for PAAM with elastic modulus 900 Pa (B) Puncture loading-unloading curve for PDMS with elastic modulus 900 Pa. (C) Carrageenan hydrogel with elastic modulus 1500 Pa. Needle size R = 0.23 mm.

2.3.2.2. Neo-Hookean model and modulus measurement

In a practical case, the stiffness of the soft tissue is measurable by contacting a flat-end indenter with the tissue surface during minimally invasive surgery. As the tissue abnormalities are often stiffer than the surrounding organs, a surgeon or a surgical robot can precisely localize the abnormalities by analyzing the force profile. This

method has been reported to be utilized in identifying the embedded (stiffer) tumors in the lung [23] and shows great potential in advancing the medical robotics design and robot tactile sensing system[24].

In the following section, we focus on the mechanical response obtained from the loading curve. The Neo-Hookean model is employed here to describe the loading behavior of the puncture process[17],

$$P = k'Ed^2 + k''ERd$$

Where P is the puncture force, E is the Young′s modulus of the material, d is the displacement of the indenter tip, k' is an empirical coefficient, and k'' is a constant depending on indenter tip geometry from Hertzian contact mechanics ($k'' = 8/3$ for flat-end indenters). For a PAAM hydrogel, we measured the modulus from the small strain contact. As shown in **Figure 2.6**A, for small strains where displacement is comparable to needle radius (d~R), the force-displacement behavior of flat-end indenters is found linear with displacement. From the linear term of the Neo-Hookean model above, P~8/3ERd, the elastic modulus (assuming for incompressible gel samples a Poisson's ratio v = 0.5 and E=2G'(1+ v)) can be derived by fitting the data of the puncture loading curve in the linear region to this equation. The elastic modulus estimated from the puncture method was plotted as a function of that measured from the shear rheometer in **Figure 2.6**B. It needs to be noted that the G' from puncture is smaller than G' from the rheometer for the PAAM hydrogels. This is because the elastic modulus of the gel near its surface and its average bulk modulus may be different as the polymerization process was performed under the air atmosphere in which the O_2 may consume some free radicals on the gel surface and lower the crosslinking efficiency thus causing a modulus gradient. Since the puncture method reflects more the local surface stiffness of the small contact region of the needle and sample, it reasonably yields a smaller elastic modulus when

compared to that from the rheometer where the average bulk modulus is measured for the whole sample. However, when the sample is basically considered homogenous, we observe a good agreement between elastic modulus measured from puncture and rheological method, as detailed in Chapter 3 for poly (vinyl alcohol) hydrogels. The values of elastic modulus of PDMS with different component ratios (A/B) and carrageenan with various polymer concentrations, measured by this method are shown in **Figure 2.7**.

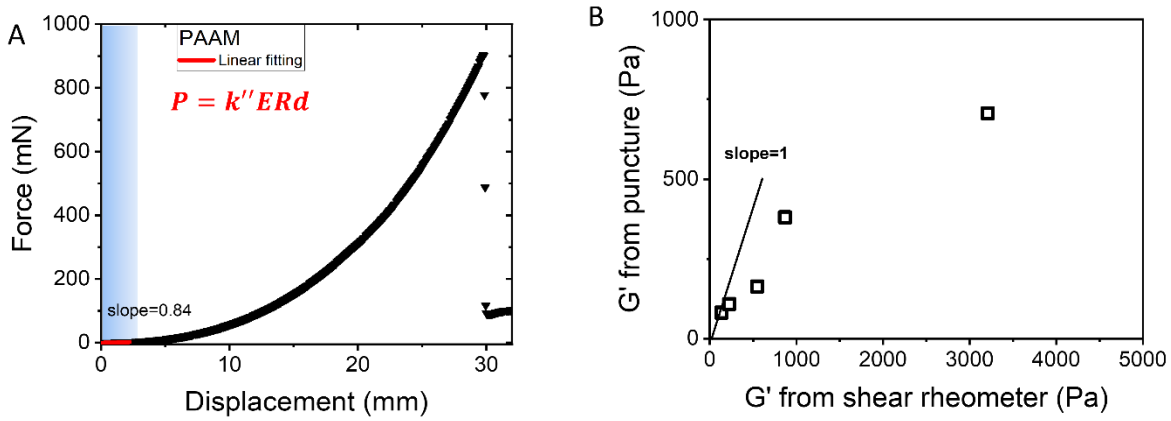

Figure 2.6. (A) Loading curve of PAAM (C_{AAM} = 6 wt%, R = 0.23 mm) with indicated linear region in blue shadow (the red line shows linear fitting of Neo-Hookean model). (B) Elastic modulus extracted from puncture experiment against that from shear rheometer.

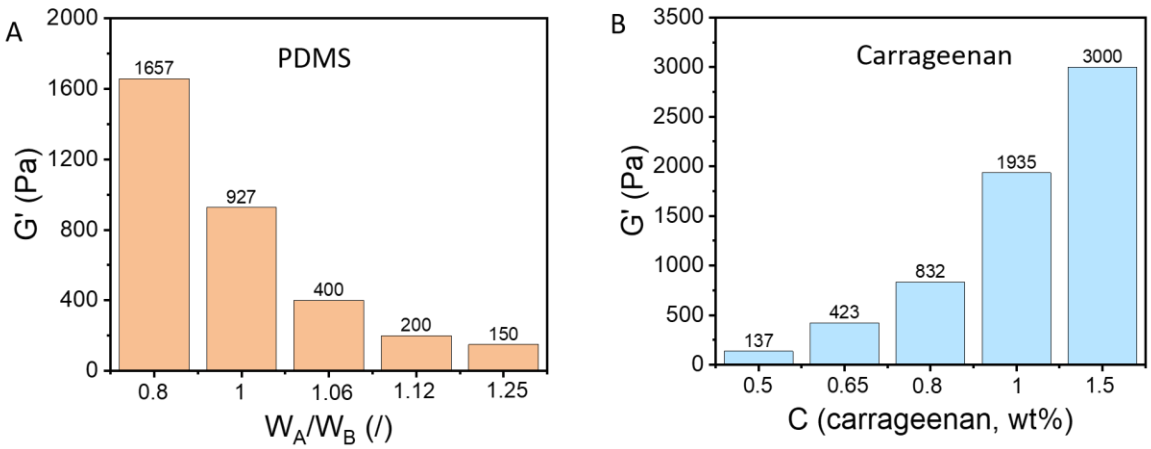

Figure 2.7. (A) Elastic modulus as a function of component A and B ratio for PDMS. (B) Elastic modulus of carrageenan hydrogel as a function of polymer concentration.

At large strain contact region, where we fit the loading curve prior to the fracture point to the Neo-Hookean model by setting $k'' = 8/3$, and $k'E$ as a fitting parameter, the resulting values of $k'E$ are plotted as a function of the linear elastic modulus. $k'E$ is a measure of the large-strain response (effective modulus at failure point) of materials. It has been reported to correlate well with small deformation modulus from conventional mechanical measurement techniques[16, 17]. In **Figure 2.8**, the plot of $k'E$ against the low strain modulus gives a good linear fit, with a slope of 0.28, 0.37, and 0.14 for PAAM, PDMS, and carrageenan, respectively. This empirical parameter consistent with the previous studies where the k' value ranges from 0.26 ~ 0.37 [16-17, 25] for elastomers, suggesting that our result for the PAAM and PDMS is reasonable. The evaluation of the nonlinear properties for the rigid carrageenan with a very low value of D_c might not be very accurate, resulting in the relatively low value of k''.

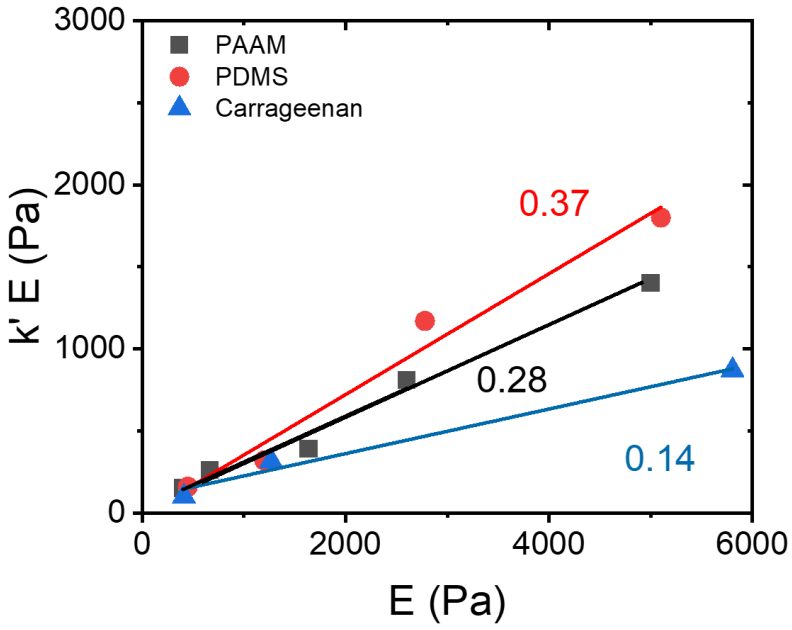

Figure 2.8. Empirical determination of the coefficient *k'E* from the Neo-Hookean model represents the effective large strain response to the point of puncture as a function of low strain elastic modulus for PAAM, PDMS and carrageenan hydrogel, respectively.

2.3.3. Large strain response and critical depth at puncture

Figure 2.9 shows the systematic measurement of loading-unloading curves for PAAM hydrogels with a polymer concentration varying from 4 – 8 %wt. From the loading curve up to the critical displacement D_c and critical force F_c, the large strain response of the material prior to fracture can be characterized.

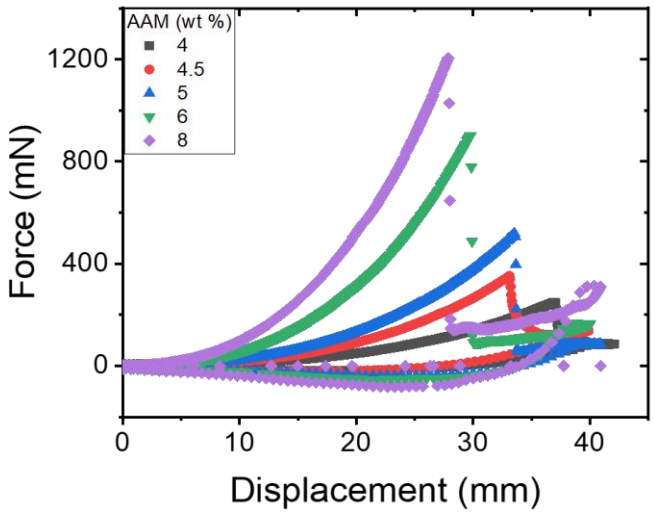

Figure 2.9. Puncture loading and unloading curves: force as a function of displacement for PAAM with varying monomer concentration (C_{AAM} = 4 - 8 wt%). Needle size R = 0.23 mm.

In **Figure 2.10A**, the critical displacement D_c was found to decrease with increasing PAAM modulus when $G' < 1000$ Pa and reaches a plateau value above this modulus. In addition, the smaller needle size yields a lower D_c. In **Figure 2.10B**, the critical force F_c increases with the gel modulus.

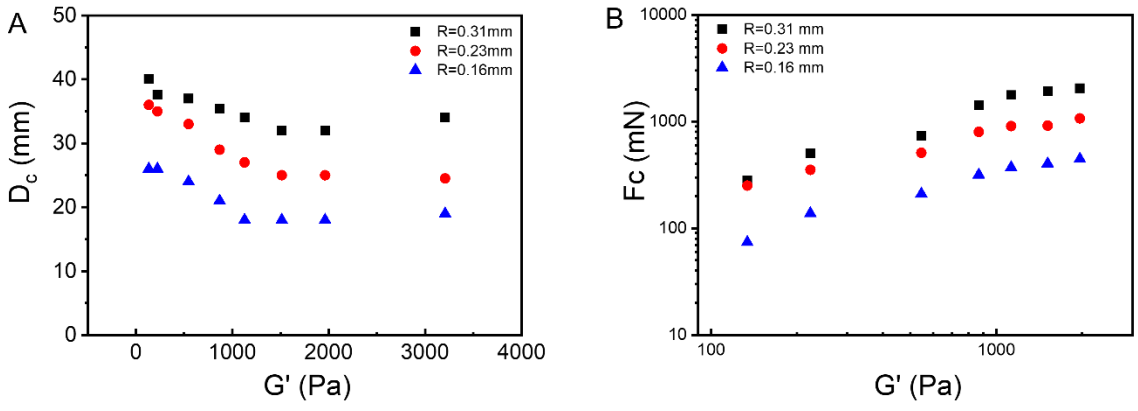

Figure 2.10. (A) Critical puncture displacement D_c and (B) critical puncture force F_c for PAAM hydrogel.

Similar to the PAAM hydrogel, D_c for PDMS increases with decreasing gel modulus when $G' < 400$ Pa and approaches a constant D_c when $G' > 400$ Pa, i.e., $D_c = 16$ mm when $R = 0.31$ mm, and $D_c = 11$ mm when $R = 0.23$ mm. Also, the critical force was found to increase with the gel modulus (**Figure 2.11**).

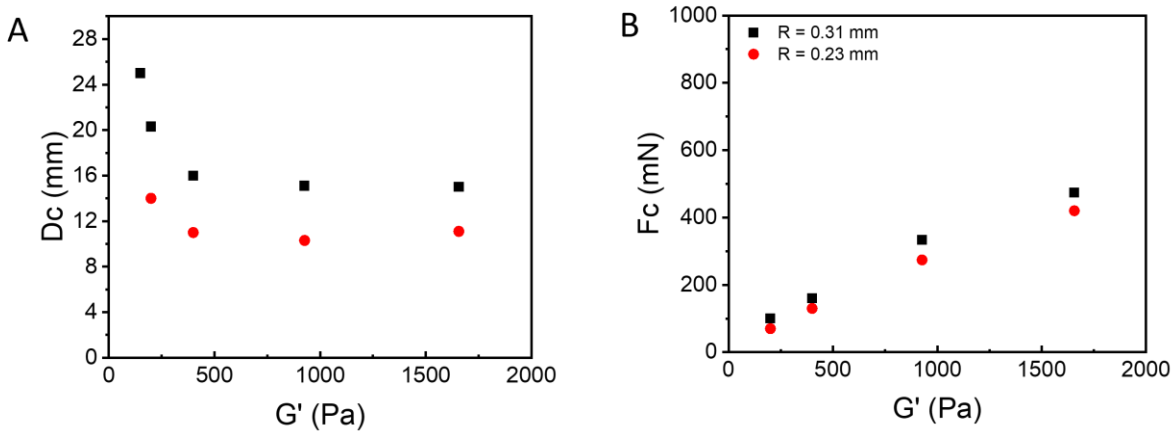

Figure 2.11. (A) Critical puncture displacement D_c and (B) critical puncture force F_c for PDMS gel.

However, the D_c for carrageenan hydrogel differs from that for PAAM hydrogel and PDMS. Firstly, D_c was only about 1~3 mm for carrageenan over a wide modulus range (100 - 3000 Pa), indicating that this kind of hydrogel is quite weak and brittle and could be easily fractured by the needle (**Figure 2.12**). Then, D_c shows almost no dependence on gel modulus. Correspondingly, the critical force F_c is much lower compared to that for PAAM and PDMS. This is due to the limited chain extensibility of the stiff carrageenan polymer chain.

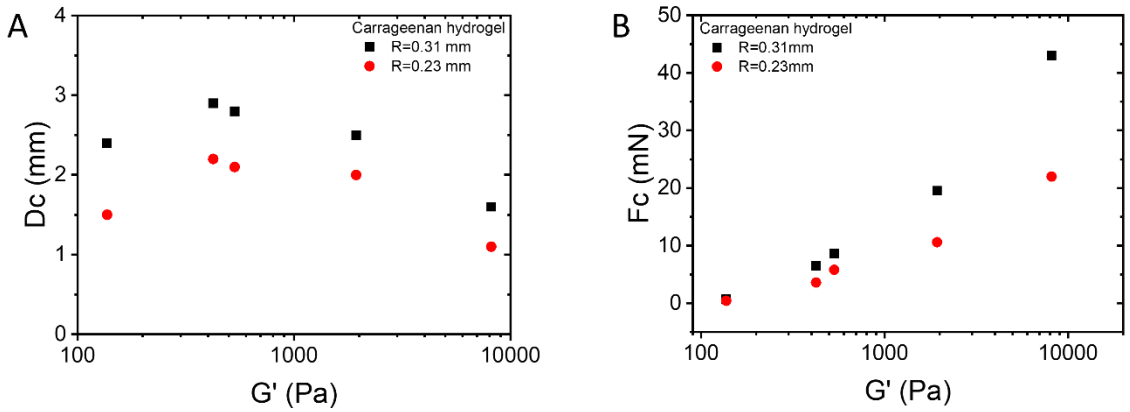

Figure 2.12. (A) Critical puncture displacement D_c and (B) critical puncture force F_c for Carrageenan hydrogel.

2.3.4. Fracture resistance

As the surface tension is expected to play a role in fracture properties at small length scale, we normalized the needle radius R by the elastocapillary length γ/G' as RG'/γ. The surface tension value of PDMS and PAAM is taken as γ~23 mN/s and γ~50 mN/s, respectively, from literature [26-27]. A rough estimation of γ~72 mN/s is adopted for carrageenan hydrogel as the polymer concentration is low in this gel system. The plot of the fracture resistance σ_c/G' as a function of the normalized radius by the elasto-capillary length is shown in **Figure 2.13**. The critical nominal stress, $\sigma_c=F_c/\Pi R^2$, represents the maximum average stress that can be sustained by the gel. The dimensionless parameter σ_c/G' is indicative of the fracture initiation resistance of soft materials[17]. $\sigma_c/G' \sim 150$ for triblock polymers with modulus above several thousand Pascal was reported by Fakhouri et al. [17]

For the PAAM hydrogels, a fracture resistance of $\sigma_c/G' \sim 3000 - 10000$ is somehow surprising, suggesting a considerable fracture resistance in the puncture geometry. Notably, while the σ_c/G' is almost a constant value of 3000 for large indenters above the elastocapillary length (R/l_{ec}~2), we observe an increase in fracture resistance

below this critical length scale demonstrating the excellent fracture resistance ability of ultra-soft gels. For PDMS, the fracture resistance value σ_c/G' is ranging from 1000 – 3000, lower than PAAM hydrogels which suggests differences in the material's intrinsic fracture properties. But also, there is an increasing trend for an increasing fracture resistance at smaller length scales. While the PAAM and PDMS both present a considerable fracture resistance where the nominal stress could surpass their elastic modulus by 3 orders of magnitudes, we found that the value for carrageenan is only below 100, approaching the value reported for triblock polymers. Still, at a smaller length scale, the fracture resistance improved for carrageenan. Since both the critical nominal stress and needle size are normalized by the elastic modulus, we think that the fracture resistance plateau at large length scale is linked to the elasticity-dominated fracture mechanism where the fracture behavior can be predicted by considering the elasticity of the material. However, whengoing to the small length scale (below the elastocapillary length), the surface tension starts to play a role, instead of elasticity alone, the capillarity is expected to dominate the fracture, resulting in an improved fracture resistance σ_c/G' value of the material at smaller length.

However, it’s worth noting that the chemically crosslinked gel including PAAM and PDMS shows 1 – 2 orders of magnitudes higher fracture resistance compared to the physically crosslinked carrageenan hydrogel. For the former, the fracture occurs when covalent chemical bonds break, while for the latter, it is believed that the chain-pull-out mechanism accounts for the fracture behavior which lowers the energy barrier.

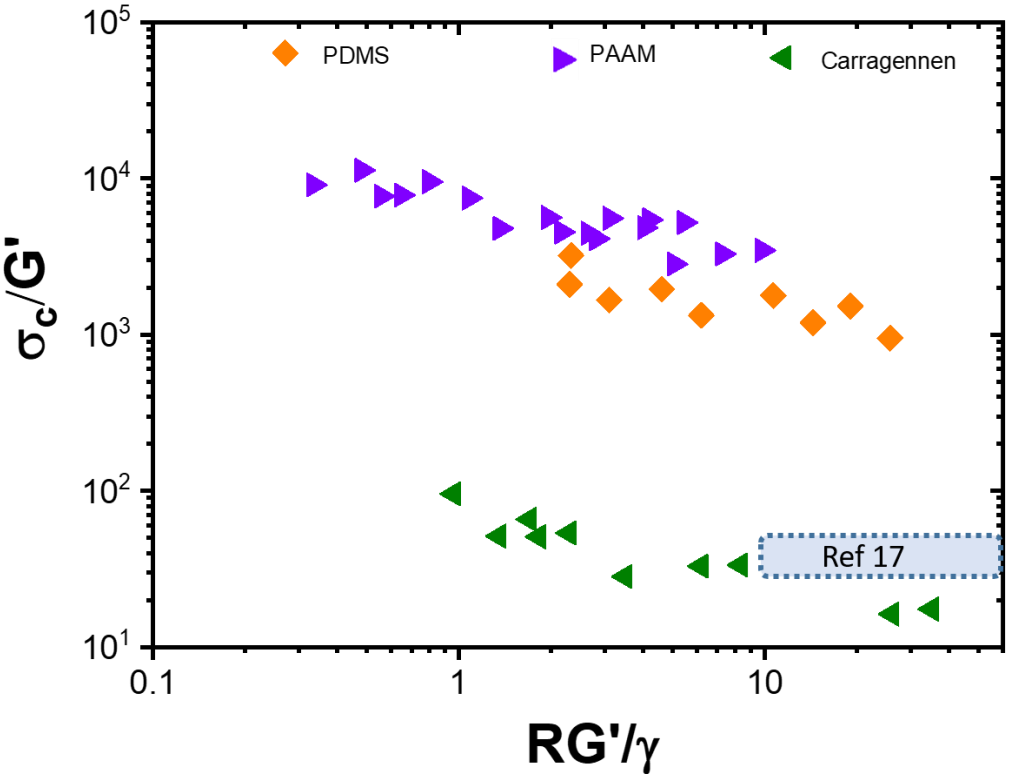

Figure 2.13. Critical nominal stress normalized by modulus, σ_c/G', as a function of indenter radius R normalized by elastocapillary length γ/G' for PAAM hydrogel, PDMS, and carrageenan hydrogel. (Constant surface tension value γ=50 mN/s, 23 mN/s, and 72 mN/s for PAAM, PDMS, and carrageenan hydrogel were adopted from the reference, respectively.) The normalized fracture resistance for the acrylic triblock copolymer gel in reference[17] is indicated as blue area.

2.4. Conclusions

The deformation and puncture behavior of ultrasoft gels of PAAM, PDMS, and carrageenan are investigated in this work. Using the puncture test at small indentation depth, the low strain elastic modulus of the gels could be estimated by the Neo-Hookean model. The effective modulus $k'E$ at large strain prior to fracture point is found to vary with the material, among which k' is 0.28, 0.37 and 0.14 for PAAM, PDMS, and carrageenan, respectively.

The critical displacement D_c of PAAM and PDMS was found to increase with decreasing gel modulus, which can reach several tens of millimeters for the gel with a modulus ~ 100 Pa. However, D_c for carrageenan is only about 1 - 3 mm. Correspondingly, the fracture resistance σ_c/G' for PAAM and PDMS is one order of magnitude larger than that of carrageenan. While above the elastocapillary length scale, fracture resistance is dominated by the nonlinear elasticity and fracture energy of the material, capillarity must play a role in the onset of fracture by puncture below this length scale since σ_c/G' is improved at smaller length scales.

The three systems tested in this chapter exhibited specificities and certain limitations when we characterize the puncture mechanics. The PAAM hydrogels have a slightly different network structure at the interface with the air due to the free radical polymerization. The viscoelasticity of PDMS needs to be further evaluated. Carrageenan hydrogel is too brittle presenting a very small fracture displacement. In the next chapter, we use another elastic hydrogel made from a neutral polymer, poly (vinyl alcohol).

2.5. References

1. Guimarães, C. F.; Gasperini, L.; Marques, A. P.; Reis, R. L., The stiffness of living tissues and its implications for tissue engineering. *Nature Reviews Materials* **2020,** *5* (5), 351-370.

2. Sun, J.-Y.; Zhao, X.; Illeperuma, W. R.; Chaudhuri, O.; Oh, K. H.; Mooney, D. J.; Vlassak, J. J.; Suo, Z. J. N., Highly stretchable and tough hydrogels. **2012,** *489* (7414), 133-136.

3. Gong, J. P. J. S., Materials both tough and soft. **2014,** *344* (6180), 161-162.

4. Xu, X.; Jagota, A.; Peng, S.; Luo, D.; Wu, M.; Hui, C.-Y., Gravity and surface tension effects on the shape change of soft materials. *Langmuir* **2013,** *29* (27), 8665-8674.

5. Lawn, B., TR Wilshaw Fracture of Brittle Solids. Cambridge, University Press: 1975.

6. Griffith, A. A., VI. The phenomena of rupture and flow in solids. *Philosophical transactions of the royal society of london. Series A, containing papers of a mathematical or physical character* **1921,** *221* (582-593), 163-198.

7. Creton, C.; Ciccotti, M., Fracture and adhesion of soft materials: a review. *Reports on Progress in Physics* **2016,** *79* (4), 046601.

8. Tsuji, Y.; Li, X.; Shibayama, M., Evaluation of mesh size in model polymer networks consisting of tetra-arm and linear poly (ethylene glycol) s. *Gels* **2018,** *4* (2), 50.

9. Andreotti, B.; Bäumchen, O.; Boulogne, F.; Daniels, K. E.; Dufresne, E. R.; Perrin, H.; Salez, T.; Snoeijer, J. H.; Style, R. W., Solid capillarity: when and how does surface tension deform soft solids? *Soft Matter* **2016,** *12* (12), 2993-2996.

10. Roman, B.; Bico, J., Elasto-capillarity: deforming an elastic structure with a liquid droplet. *Journal of Physics: Condensed Matter* **2010,** *22* (49), 493101.

11. Style, R. W.; Jagota, A.; Hui, C.-Y.; Dufresne, E. R., Elastocapillarity: Surface tension and the mechanics of soft solids. *Annual Review of Condensed Matter Physics* **2017,** *8*, 99-118.

12. Jagota, A.; Paretkar, D.; Ghatak, A., Surface-tension-induced flattening of a nearly plane elastic solid. *Physical Review E* **2012,** *85* (5), 051602.

13. Hui, C.; Jagota, A.; Lin, Y.-Y.; Kramer, E., Constraints on microcontact printing imposed by stamp deformation. *Langmuir* **2002,** *18* (4), 1394-1407.

14. Liu, T.; Long, R.; Hui, C.-Y., The energy release rate of a pressurized crack in soft elastic materials: effects of surface tension and large deformation. *Soft Matter* **2014,** *10* (39), 7723-7729.

15. Hui, C.-Y.; Liu, T.; Schwaab, M.-E., How does surface tension affect energy release rate of cracks loaded in Mode I? *Extreme Mechanics Letters* **2016,** *6*, 31-36.

16. Rattan, S.; Crosby, A. J., Effect of polymer volume fraction on fracture initiation in soft gels at small length scales. *ACS Macro Letters* **2019,** *8* (5), 492-498.

17. Fakhouri, S.; Hutchens, S. B.; Crosby, A. J., Puncture mechanics of soft solids. *Soft Matter* **2015,** *11* (23), 4723-4730.

18. Rattan, S.; Li, L.; Lau, H. K.; Crosby, A. J.; Kiick, K. L., Micromechanical characterization of soft, biopolymeric hydrogels: stiffness, resilience, and failure. *Soft matter* **2018,** *14* (18), 3478-3489.

19. Geonzon, L. C.; Bacabac, R. G.; Matsukawa, S. J. F. h., Network structure and gelation mechanism of kappa and iota carrageenan elucidated by multiple particle tracking. **2019,** *92*, 173-180.

20. Du, L.; Brenner, T.; Xie, J.; Matsukawa, S. J. F. H., A study on phase separation behavior in kappa/iota carrageenan mixtures by micro DSC, rheological measurements and simulating water and cations migration between phases. **2016,** *55*, 81-88.

21. Muthukumar, M.; Bobji, M.; Simha, K. J. S. M., Cone cracks in tissue-mimicking hydrogels during hypodermic needle insertion: the role of water content. **2022,** *18* (18), 3521-3530.

22. Kundan, K. K.; Laha, S.; Ghatak, A. J. E. M. L., Vibration assisted puncturing of a soft brittle solid. **2019,** *26*, 26-34.

23. McCreery, G. L.; Trejos, A. L.; Naish, M. D.; Patel, R. V.; Malthaner, R. A., Feasibility of locating tumours in lung via kinaesthetic feedback. *The International Journal of Medical Robotics and Computer Assisted Surgery* **2008,** *4* (1), 58-68.

24. Liu, H.; Li, J.; Song, X.; Seneviratne, L. D.; Althoefer, K., Rolling indentation probe for tissue abnormality identification during minimally invasive surgery. *IEEE Transactions on Robotics* **2011,** *27* (3), 450-460.

25. Rattan, S.; Crosby, A. J., Effect of far-field compliance on local failure dynamics of soft solids. *Extreme Mechanics Letters* **2018,** *24*, 14-20.

26. Tian, Y.; Ina, M.; Cao, Z.; Sheiko, S. S.; Dobrynin, A. V., How to measure work of adhesion and surface tension of soft polymeric materials. *Macromolecules* **2018,** *51* (11), 4059-4067.

27. Al-Sabagh, A.; Kandile, N.; El-Ghazawy, R.; El-Din, M. N.; El-Sharaky, E., Solution properties of hydrophobically modified polyacrylamides and their potential use for polymer flooding application. *Egyptian Journal of Petroleum* **2016,** *25* (4), 433-444.

3. Chapter 3: The effect of structural heterogeneity on fracture properties of Poly (vinyl alcohol) hydrogel at elasto-capillary length scale

3.1. Introduction

3.1.1. General introduction

Hydrogels are networks of cross-linked polymer chains swollen in water. Thanks to their high water contents and biocompatibility, hydrogels are good candidates for biomedical applications such as tissue engineering, artificial cartilage, vessels, prosthetic joints, soft contact lenses, etc[1]. The growing demand for hydrogel enhances the importance of understanding their mechanical properties, especially fracture resistance properties for stress-bearing applications. Tough hydrogels have been extensively investigated recently, either for covalently cross-linked[2-3], physically cross-linked[4-6], or double network (DN) hydrogel[7]. With these tough hydrogels having a modulus typically in the order of kPa, several different mechanisms to prevent crack initiation and/or crack propagation have been proposed. However, some of the human organs (brain, breast, and lung) exhibit a very low stiffness, and modulus ~ tens Pa. With the notable advances in medical robotics and surgical tactile sensors application[8-10], understanding the deformation and fracture behavior of such ultra-soft materials, or how soft tissues react on the medical device on loading conditions, is of remarkable importance.

The difficulties encountered in characterizing the fracture behavior of ultra-soft materials have been introduced in detail in Chapter 2. To elucidate the role of capillarity on the fracture properties, a material system with a quite low modulus is required to access such small length scales, in which the structure's architecture (such as imperfections of the network, chain entanglements, and loops) of the sample could also significantly influence its mechanical properties. The practical application of hydrogels is strongly limited when their macroscopic properties are impacted due to structural heterogeneity. An inhomogeneous network gives rise to localized stresses on certain chemical bonds at the molecular level and facilitates the initiation

of larger defects that can propagate into cracks, therefore strongly decreasing the stress and strain at break of hydrogels.

In polymer networks, there are generally three types of heterogeneity[11]: (1) structural heterogeneities stemming from the inhomogeneous spatial distribution of crosslinks and (2) topological defects including dangling chain ends, loops, etc. (3) connectivity heterogeneity. While the topological defects were reported to have less impact on the network structure of polymers, the spatial inhomogeneity of crosslinking is widely recognized as an important role to account for reducing the mechanical strength of hydrogel[12-13]. When the polymer networks cannot behave cooperatively because of the inhomogeneity, the fracture tends to start from the weakest crosslinks, thus the crosslinking heterogeneity is of particular significance in deformed gels. While the elasticity is taken into account, yet the influence of structural heterogeneity of soft hydrogels on their deformation and fracture behavior at a small length scale is poorly understood.

This chapter focuses on the effect of the structural heterogeneity of poly (vinyl alcohol) (PVA) hydrogels on their deformation and fracture behavior at the elasto-capillary length scale. PVA hydrogels were prepared following two different paths by either varying the polymer concentration or varying the crosslinker concentration to obtain a comparable elastic modulus: 80 – 1700 Pa. Conventional rheology was employed to study the basic linear properties and elasticity dependence on composition (cross-linker or polymer concentration). The structural heterogeneity of the gels prepared from two paths was first elucidated by dynamic light scattering. Then, puncture experiments were used to characterize the deformability and fracture properties of gels with a comparable elastic modulus, but made from these two paths and therefore with a distinct structural heterogeneity at the elasto-capillary length scale.

3.1.2. Dynamic light scattering (DLS)

Dynamic light scattering (DLS) is a powerful tool to study the dynamic properties of polymers such as colloidal particles, suspensions, and solutions. DLS consists in analyzing the temporal fluctuations of the refractive index when coherent light propagates through heterogeneous media inside samples. In detail, monochromatic laser light is sent to a 10 mm-diameter test tube containing a sample, in which the concentration gradients of polymer chains evolve with time over a time scale associated with the polymer chain length and interactions. When the scattering objects are moving around an equilibrium location (e.g. Brownian motion), the motion of the polymer chain will be reflected in the fluctuation of the scattered light intensity. By analyzing the scattered light intensity evolving with time, the movement or dynamics of the polymer chains can be investigated.

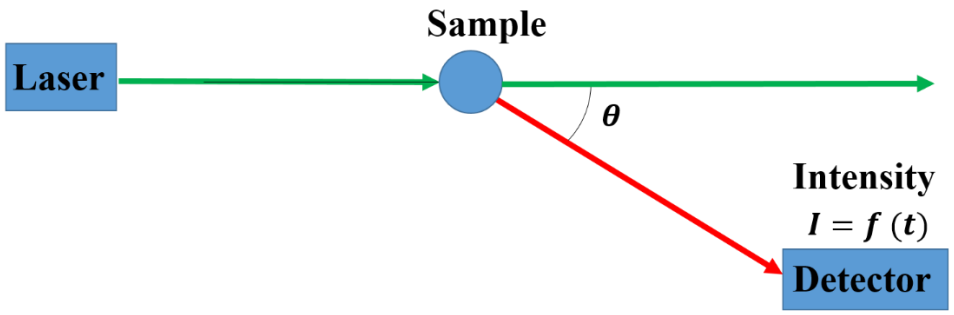

Figure 3.1. Schematics of dynamic light scattering experiment.

Figure 3.1 shows the protocol of the DLS measurement. The light intensity $I = f(t)$ from a direction with a scattering angle of θ from the incident direction was detected at a scattering vector q defined as:

$$q = \frac{4\pi n}{\lambda} sin\frac{\theta}{2} \quad 3.1$$

where n is the refractive index, λ is the wavelength of the light and θ is the scattering angle.

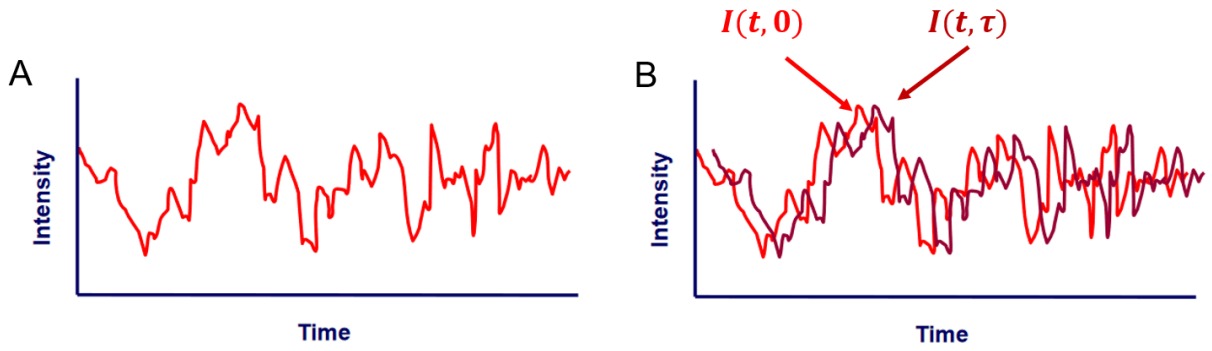

Figure 3.2. (a) Scattered light intensity as a function of time. (b) Correlation between $I(t)$ and $I(t+\tau)$.

As long as the temporal intensity is known, the time-averaged normalized intensity autocorrelation function $g^{(2)}$ is generated as a function of the correlation time τ:

$$g^{(2)} = \frac{\langle I(t) \cdot I(t+\tau) \rangle_t}{\langle I(t) \rangle_t^{\,2}} \qquad 3.2$$

Here $\langle \dots \rangle_t$ indicates time averaging. In **Figure 3.2B**, when $\tau = 0$, the original curve $I(t)$ and itself $I(t+\tau)$ overlap and the correlation between them will give the maximum correlation value of 1. While with increasing time τ, the correlation will be progressively reduced and eventually fully lost, thus $g^{(2)}(t)$ is always a decreasing function of time and the time scale τ is the decay time of the auto-correlation function. The time the auto-correlation function is then converted to the field auto-correlation function $g^{(1)}$ to simplify the modelling with the Siegert relation:

$$g^{(2)}(t) = 1 + \beta\left[g^{(1)}(t)\right]^2 \qquad 3.3$$

For ergodic samples, such as polymer solutions, it is possible to detect the scattering information over the whole space in the course of the experimental time at a fixed sampling position as long as the duration of acquisition is long enough compared to the slowest characteristic time of the sample system. In this case, the time-averaged autocorrelation function is sufficiently precise compared to the ensemble-averaged one where we commonly yield an amplitude plateau from the autocorrelation function when $t = 0$, and it progressively reduces to zero ultimately at a long time scale.

Gels are generally considered non-ergodic samples due to their topologically frozen structures. The concept of non-ergodicity of gels was first pointed out by Pusey and van Megen, leading to the significant development of relevant methods to analyze the dynamic properties of gels[14]. The dynamics of a non-ergodic sample depend on the spatial position of the speckles in the system since the static concentration gradient is associated with the presence of frozen disorder. In this case, the time averaging is not equivalent to the ensemble averaging when the scattered light is restricted to one fixed position where the other possible configurations of the system out of a plane would be important but are neglected. In order to overcome such a downside, the sample cell needs to be vertically translated steadily during the time averaging (more than 3600 s). Thus $g^{(2)}$ coincides with the ensemble-averaged autocorrelation function, up to a boundary decay time decided by the sample translation speed (having here a characteristic time of around 10 s). The stretched exponential equation with one or two relaxation times is commonly used to practically fit the obtained field correlation functions.

3.2. Experimental section

3.2.1. Materials

Poly (vinyl alcohol) (PVA) with a degree of hydrolysis: 88 % (named as PVA88), and molecular weight: 67000 g/mol, glutaraldehyde (GA, 25% aqueous solution), and hydrochloric acid (HCl) were purchased from Sigma-Aldrich and used as received.

3.2.2. Gel preparation

A PVA88 stock solution at a concentration of 8.8 wt% (or 2 M for repeating unit) was prepared by dissolving the PVA88 powder in deionized water at 90 ℃ and stirring vigorously over four hours. Chemically cross-linked PVA88 hydrogels were prepared by crosslinking PVA88 with the cross-linker GA in the presence of HCl (0.05 mM). In order to vary the elastic modulus and structure, the PVA88 and GA concentrations were systematically varied following two paths. In path 1, the PVA88 concentration was adjusted to 6.6 wt% (or 1.5 M for the repeating unit), and the GA concentration was varied between 4 and 10 mM. In path 2 the PVA88 concentration varied from 3.3 to 11 wt% (or 0.75 – 2.5 M) with a fixed GA concentration of 7 mM. The system was gelled in a cylindrical glass vial with a diameter of 25 mm and used for measurement after more than 12 h.

3.2.3. Puncture experiment

Puncture tests were performed on a custom apparatus consisting of a motorized stage, flat-ended indenter, force sensor, and camera. A balance with a precision of 0.1mg was placed at the bottom of the sample and used as a force sensor to measure the puncture loading force. As indenters, flat-end metal needles (obtained from Hamilton Company) with a radius of 0.13 – 0.31 mm were used. They were backfilled with epoxy and fixed to the adapter in the actuator (motorized stage). The

inserting velocity of the indenter was 0.25 mm/s in this study. The displacement and loading force as a function of time were recorded during the puncture process, and the camera captured corresponding images.

3.2.4. Rheology

Rheological measurements were carried out on an ARES strain-controlled rheometer (TA Instruments, USA) with a steel cone-plate geometry (25 mm in diameter, 0.053mm in the gap) having a roughened surface. A fresh gel mixture solution before gelation was loaded for a time sweep measurement to track the gelation behavior of the PVA sample. A frequency sweep test with an angular frequency range of 0.1 – 100 rad/s at a linear strain of 2 % was performed, followed by a strain sweep with amplitude ranging from 0.1 – 1000 % at a fixed frequency of 1 Hz. For each measurement, the exposed surface of the sample was covered with a thin layer of low-viscosity silicone oil to avoid water evaporation.

3.2.5. Dynamic light scattering

Dynamic light scattering (DLS) was performed with an ALV CGS-3 goniometer system (ALV, Langen, Germany), equipped with a cuvette rotation/translation unit (CRTU) and a He-Ne laser (22 mW at λ = 632.8 nm). The time-averaged autocorrelation function of the scattered light intensity at a scattering vector q was measured. PVA gels for DLS measurement were prepared in a glass tube (10 mm in diameter) with a pre-gel solution volume of 5 ml. A syringe filter of 0.22 micron was used to pre-filter the pre-gel solution.

3.3. Results and Discussion

3.3.1. The phase diagram

Figure 3.3 shows the experimental phase diagram of PVA88 hydrogels with two different measurement paths. The red line indicates the gelation limit of PVA88, determined by the so-called "tilting-a-tube" method[15], or observation of the flowability of the inverted sample in a small vial. Below this gelation limit line, the system is in a liquid state with either a low crosslinker concentration and/or a low polymer fraction and above that, the system demonstrates solid-like behavior.

For a gel system, we studied two different gelation paths as shown in **Figure 3.3** to investigate the role of structure architecture in its dynamic, deformation, and fracture properties. In path 1, with a fixed polymer concentration (C_{PVA} = 6.6 wt%) the cross-linker concentration varied from 4 to 10 mM. In path 2, the same modulus range was obtained by changing the polymer concentration from 0.75 to 2.5 M with a constant GA concentration (C_{GA} = 7 mM). Path 1 corresponds to "bond percolation", or there are sufficient amounts of binding sites to crosslink (here diols on PVA chains), and the distance from the percolation points is determined by bond formation probability, or by the amounts of bonds (crosslinks, adjusted by the GA concentration). Path 2 corresponds to "site percolation", or with a sufficient bond formation probability, the site probability (concentration of the sites, here PVA concentration) determines the distance from the percolation point[11, 13].

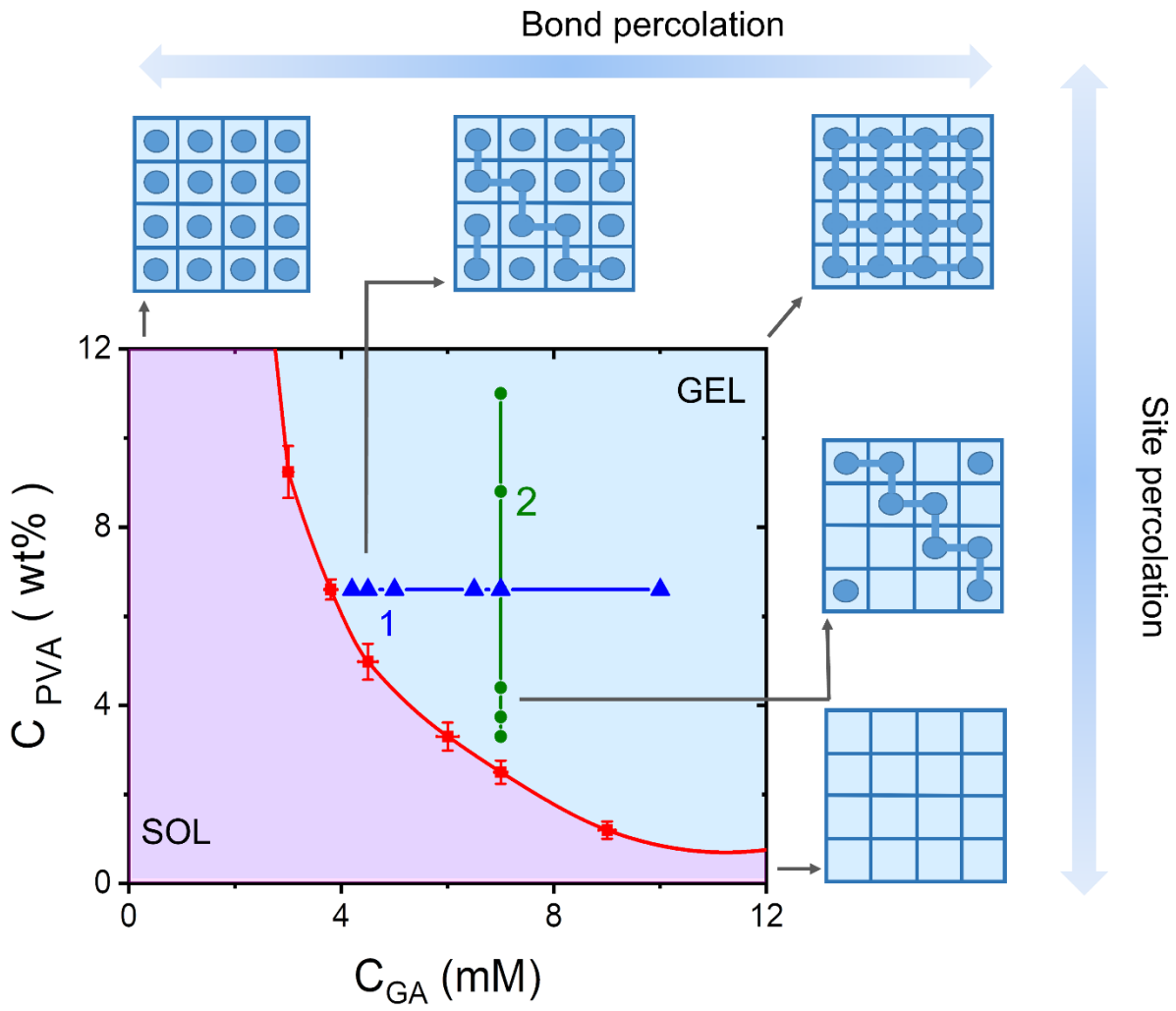

Figure 3.3. The experimental sol-gel phase diagram of PVA88 hydrogels shows the two measurement paths (path 1 and path 2) used in this work. The grids describe bond-percolation and site-bond percolation theory with ordinate and abscissa denoting bond probability and site probability, respectively.

3.3.2. Rheology

Figure 3.4A shows the representative frequency sweep curves of PVA88 hydrogels from Path 1 with C_{GA} = 4.2 and 10 mM. For both of the gel samples, the elastic modulus *G'* is independent of the applied frequency, yielding a well-defined elastic plateau of about 60 Pa (for C_{GA} = 4.2 mM) and about 1700 Pa (for C_{GA} = 10 mM), respectively. The viscous modulus *G"* is far lower than *G'*, little dependent on the

crosslinker concentration. This result indicates that the chemically cross-linked gel system can be considered purely elastic with a negligible viscous component.

The strain sweeps of PVA88 hydrogels with different crosslinker concentrations of C_{GA} at a fixed frequency of 6.28 rad/s are shown in **Figure 3.4B**. The linear elastic modulus was found to increase with C_{GA}, indicative of the increasing crosslinking density n according to rubber elasticity where $G' = nkT$ (k is the Boltzmann constant and T is the temperature). In the linear strain region, the elastic modulus G' is plotted as a function of C_{GA} (**Figure 3.4C**). The elastic modulus scales with the crosslinker concentration in $G' \sim C_{GA}^{2.74}$ when $C_{GA} > 5$ mM, while at the lower concentration G' does not follow the scaling, decreasing rapidly with decreasing C_{GA}. This strong dependence on the crosslinker concentration and the decrease are presumably due to the presence of defects of the topological structure at a low crosslinking ratio close to the gelation limit. In **Figure 3.4D**, the rupture strain γ^* of the PVA88 gel, defined as the strain value at which G' starts to decrease was plotted as a function of elastic modulus. $\gamma^*$was found decrease with elastic modulus. We attribute the modulus dependence of rupture strain to its chain stretch limit λ_m that will be discussed in the following sections.

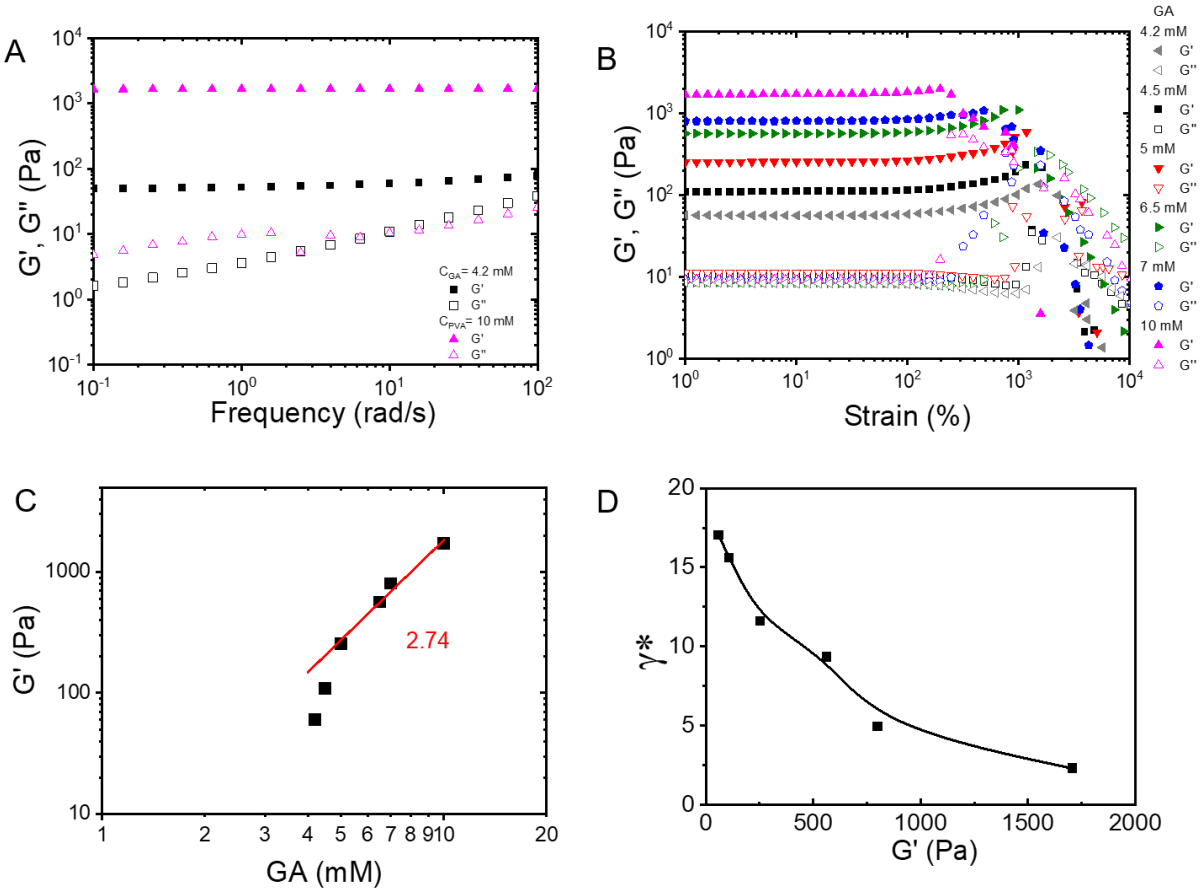

Figure 3.4. (A) Frequency sweep of PVA hydrogel from Path 1 with C_{GA} = 4.2 and 10 mM, respectively. (B) Strain sweep of PVA hydrogel with varied crosslinker concentration (C_{GA}: 4 – 10 mM). (C) Plateau modulus versus GA concentration. (D) Critical rupture strain versus elastic modulus.

Figure 3.5A shows the frequency dependence of the modulus for PVA88 hydrogels from Path 2 with C_{PVA} = 3.3 and 8.8 wt%, respectively. Similar to the result from Path 1, the elastic modulus shows nearly no dependence on frequency even with G'~ 100 Pa, demonstrating a purely elastic characteristic of the chemical gel system. The elastic and viscous moduli as a function of strain for PVA88 hydrogel with different polymer concentrations are shown in **Figure 3.5B**. With the increase in crosslinker concentration, the elastic modulus increases. The elastic modulus was found to scale with polymer concentration as $C^{2.38}$ (**Figure 3.5C**), in good agreement with the

scaling behavior of entangled polymer solutions in a good solvent[16]. It is interesting to note that even though the elastic modulus range is quite similar to Path 1, the critical rupture strain is almost independent of the modulus with a relatively constant value of ~ 5 (**Figure 3.5D**), while this critical strain value can reach 3 times higher for gels with low modulus in Path 1.

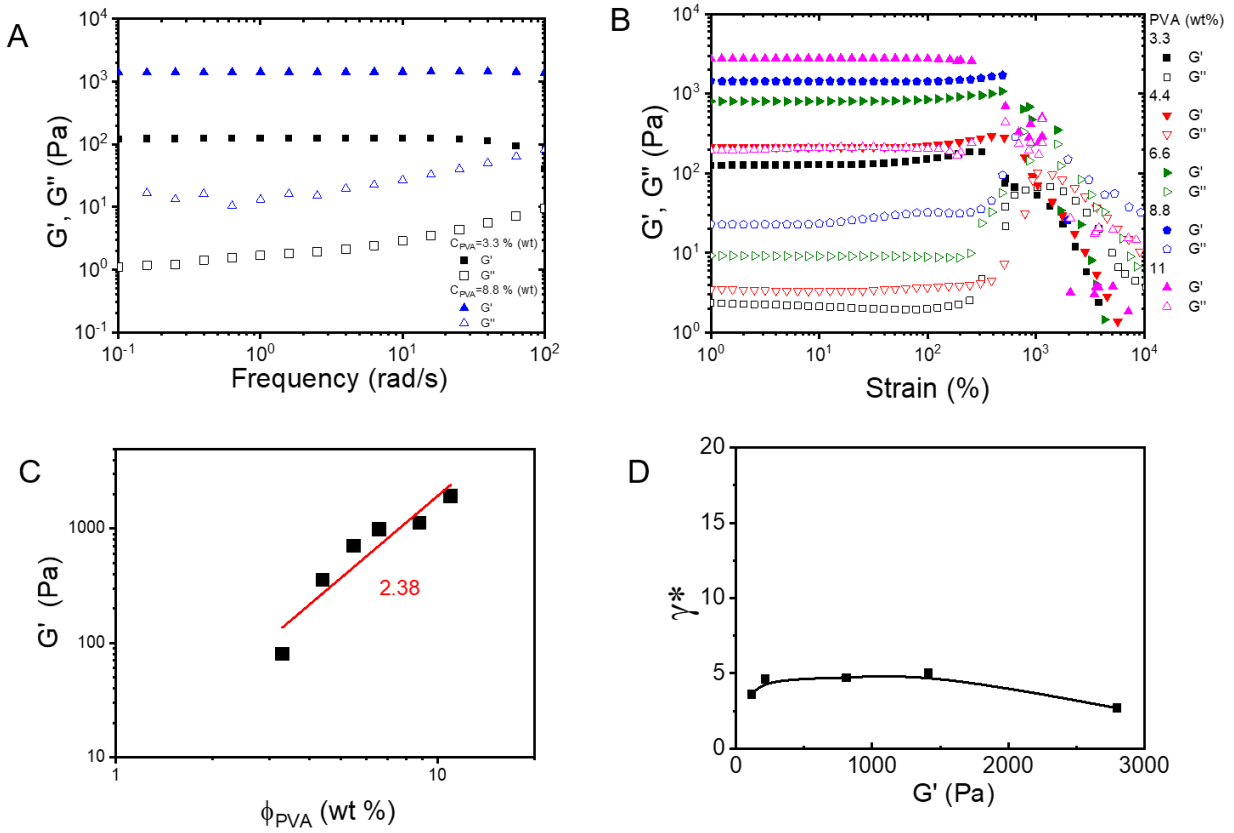

Figure 3.5. (A) Frequency sweep of PVA88 hydrogels from Path 2 with C_{PVA} = 3.3 and 8.8 wt%.. (B) Strain sweep of PVA hydrogel with varying polymer concentration (C_{PVA}: 3.3 – 11 wt%). (C) Plateau modulus versus PVA concentration. (D) Critical rupture strain versus elastic modulus.

3.3.3. Structural heterogeneity investigated via dynamic light scattering

DLS measurement is performed for PVA88 hydrogels from two different experimental paths. The representative normalized ensemble-averaged intensity

autocorrelation function $g^{(2)} - 1$ of the PVA88 gel at the crossover point of the two paths (C_{PVA} = 4.4 wt% and C_{GA} =7 mM) at a scattering angle of 90° is shown in **Figure 3.6**. The autocorrelation function decays at about 0.1 ms, to reach a plateau. The fast decorrelation is the so-called gel mode, which is linked to the collective motion of polymer chains in the network[17]. Generally, this is the only relaxation mode observed in a chemical gel. The fact that the auto-correlation function does not fully decorrelate to zero but shows a plateau indicates that a part of the scattered light intensity does not fluctuate with time which can be attributed to the spatially frozen concentration gradient in the polymer network due to the permanent crosslinking. To quantify the respective contribution of the fluctuation from the polymer network and of the frozen-in structure to the scattered light intensity, the amplitude of the two contributions was determined. As shown in **Figure 3.6**, a_f represents the decorrelation amplitude of the autocorrelation function and a_u is the plateau amplitude, and we have $a_f + a_u = 1$ in the normalized $g^{(2)} - 1$ function. The scattered light intensity I_{total} is the sum of the intensity from the fluctuating structure I_f and from the un-fluctuating (or frozen-in) structure I_u, i.e., $I_{\text{total}} = I_f + I_u$. Consequently, we can separately calculate the scattered light intensity of them, $I_f = a_f I_{\text{total}}$, and $I_u = a_u I_{\text{total}}$.

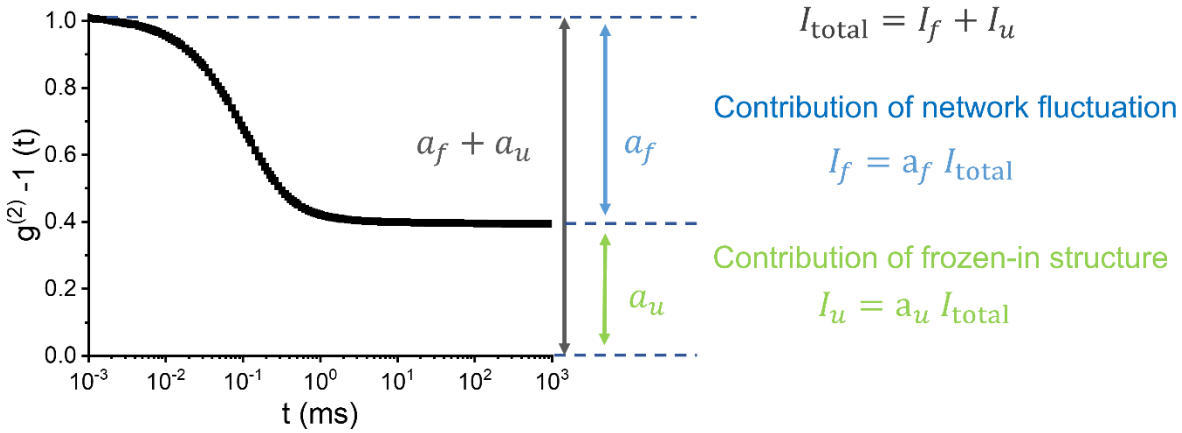

Figure 3.6. Normalized ensemble-averaged intensity autocorrelation function $g^{(2)}$ – 1 measured at an angle of 90°, for the PVA88 gel with a PVA concentration of 6.6 wt% and GA 7 mM.

I_u tells the structural heterogeneity in the polymer network. In **Figure 3.7A**, the contribution of the un-fluctuating structure to the scattered light I_u is plotted as a function of the gel modulus for the two paths. It is interesting to note that the value of I_u increases with increasing modulus for the gel from Path 1 (changing C_{GA}) but it decreases for the gel from Path 2 (changing C_M). Also, the value of I_u for gel in Path 2 at the low modulus is higher than those of the gels from Path 1. This result indicates that the sample from Path 2 has a strong imperfect polymer network that does not fluctuate the scattered light as a spatially frozen structure. **Figure 3.7B** gives schematic illustrations of the proposed network structure of gels from the two paths. Although a similar density of elastically active chains (elasticity) is expected considering the comparable modulus of these two paths, the network architecture could be affected by the different synthesis routes. In path 1, a fixed polymer concentration C_{PVA} = 6.6 wt% is involved and limited crosslinker points are distributed in the system for low modulus sample (bond-percolation), resulting in a relatively homogenous network structure. On the contrary, at low polymer

concentrations with a high crosslinker concentration (site-percolation), polymer chains are supposed to form densely crosslinked zones as the crosslinking can locally increase the polymer concentration and increase the crosslinking reaction rates, resulting in the unevenly distributed crosslinks which contribute more to the un-fluctuating component than to the fluctuating one. This connectivity heterogeneities in gels become predominant at the gelation threshold as the percolation problem.[18-19] Thus the strong scattering light due to such inhomogeneous structure is reflected by the high plateau value a_u and by the great value of I_u in **Figure 3.7A**.

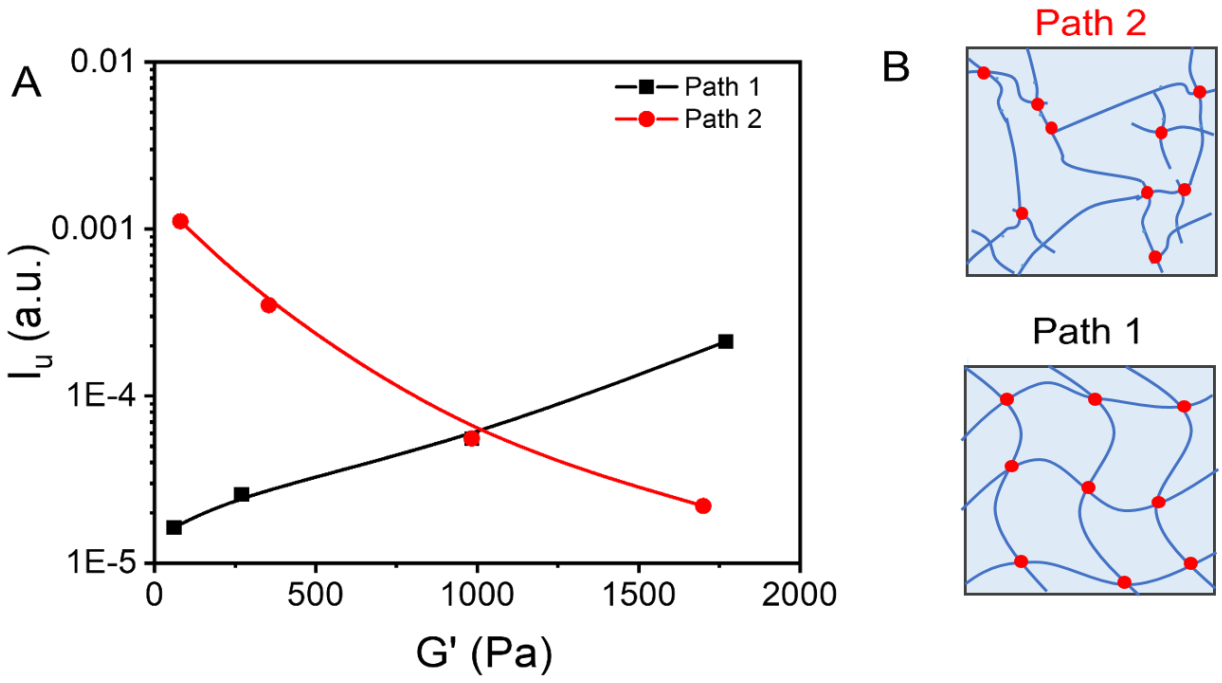

Figure 3.7. (A) The intensity contribution from an inhomogeneous structure I_u as a function of gel modulus for two experimental paths. (B) The proposed gel structure of two paths where a heterogeneous structure of path 2 is expected and a relatively homogenous network is proposed for gel from path1 at low modulus region.

We further evaluated the dynamics of the gel networks. The normalized ensemble-averaged field autocorrelation functions $g^{(1)}$ are plotted as a function of time for the

PVA88 gels from path 1 and path 2 in **Figure 3.8**. The field autocorrelation function of the chemical gel can be empirically well fitted by the stretched exponential function:

$$g^{(1)} = a \cdot exp[-(t/\tau)^{\alpha}] + b \qquad 3.4$$

where a is the amplitude of the decorrelation mode, b is the value of the plateau ($b = 1 - a$), τ is the characteristic time of the decorrelation and α is the stretch exponent which represents the distribution of characteristic times around the mean value τ.

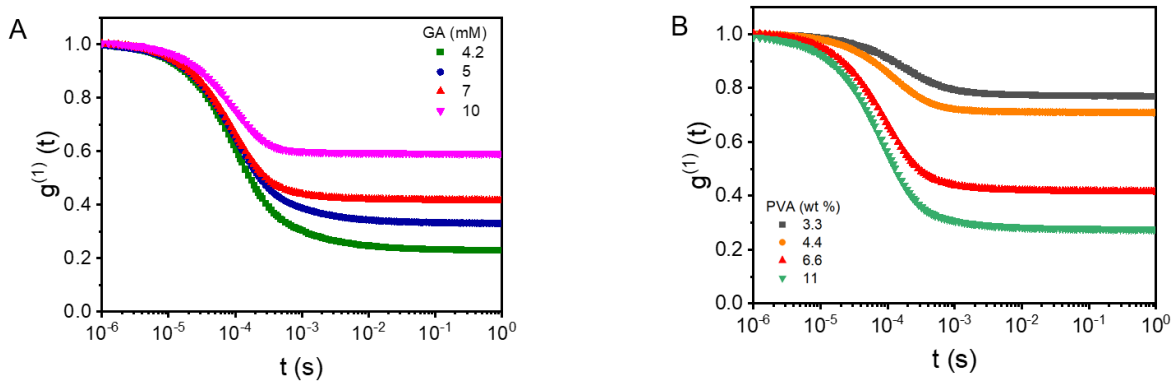

Figure 3.8. Normalized ensemble-averaged field autocorrelation function $g^{(1)}$ measured at an angle of 90°, for the PVA88 gels from Path 1 (A) and Path 2 (B).

To confirm the nature of this mode, we studied the scattering vector dependence of the characteristic times: the experiment was carried out at different scattering angles θ, thus varying the scattering vector q (see Eq. 3.1). The obtained values for τ are then plotted as a function of the scattering vector, in **Figure 3.9Error! Reference source not found.**. Generally, a theoretical scaling exponent $\tau \sim q^{-2}$ is expected, interpreted as the collective fluctuations of the entangled or crosslinked chains characterized by the diffusion coefficient $D_c = (\tau q^2)^{-1}$. A scaling behavior of $\tau \sim q^{-1.91}$ is observed for the gel with C_{PVA} = 6.6 wt%, C_{GA} =7 mM, close to the theoretical value (–2).

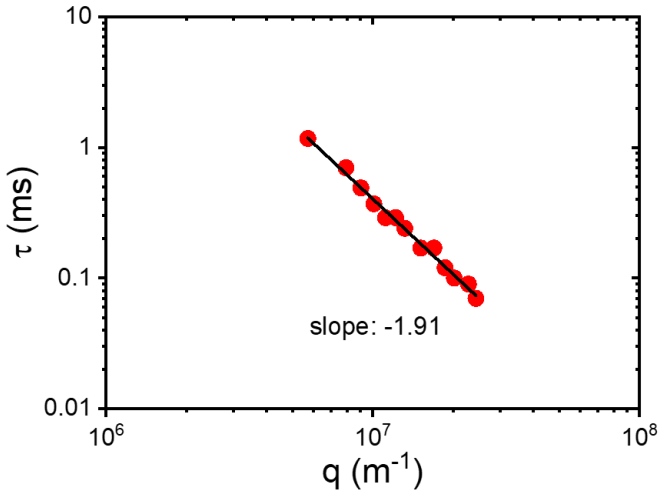

Figure 3.9. Characteristic decorrelation time observed in the PVA88 gel (C_{PVA}=6.6 wt%, C_{GA} = 7 mM) (light blue circles), as a function of the scattering vector $q = \frac{4\pi n}{\lambda} sin\frac{\theta}{2}$.

The network dynamics were further characterized to correlate them with the structure. In **Figure 3.10A** and **Figure 3.10B**, the decorrelation time τ at 90° was plotted against cross-linker concentration C_{GA} (for Path 1) and polymer concentration C_{PVA} (for Path 2), respectively. For comparison, that of the corresponding PVA88 solutions is also plotted. As seen in **Figure 10A**, the value of τ for the solution (red circle) is about 0.1 ms. The gels have a similar value (black squares), while with the decrease in crosslinker concentration it slightly increases. In **Figure 3.10B** the PVA88 concentration dependence of τ is shown. In solution, τ does not strongly depend on the concentration in the studied range, the value of it is about 0.1 ms. That of the gel exhibits a stronger concentration dependence, especially at low PVA concentrations. These results suggest that the decorrelation time increases when the gel approaches the gelation limit, where the network structure is fractal. The gels synthesized from the two paths can be compared by plotting the decorrelation time as a function of the modulus (**Figure 3.10C**). τ

monotonously increases with decreasing modulus, and the softest gel of Path 2 has a particularly large value.

From the decorrelation time a characteristic length, correlation length, can be further analyzed. It is defined as $\xi_c = k_B T \tau q^2/(6\pi\eta_s)$, where $k_B T$ is the thermal energy, η_s is the viscosity of the solvent (water), q is the scattering vector. This relation is valid when τ scales with q as $\tau \sim q^{-2}$, thus the dynamics are diffusive, and the collective diffusion coefficient is $D = \frac{1}{(\tau q^2)}$. Thus, the shorter correlation length shows faster dynamics. The values of ξ_c for the gels are plotted as a function of the average mesh size ξ of the gel, estimated from the elastic modulus of the sample $\xi \sim (k_B T/G')^{1/3}$(**Figure 3.10D**). The correlation length is shorter than the mesh size, ranging between 9.4 and 14 nm for Path 1, 9.4 and 22 nm for Path 2. Those for the solutions range between 6.9 and 9.5 nm (data not plotted in the figure). This observation well agrees with the structure proposed from the scattered light intensity (**Figure 3.7B**): the soft gels from Path 2 (by site-percolation) has larger and slower fluctuating network strands connecting densely crosslinked domains contributing to the higher un-fluctuating intensity.

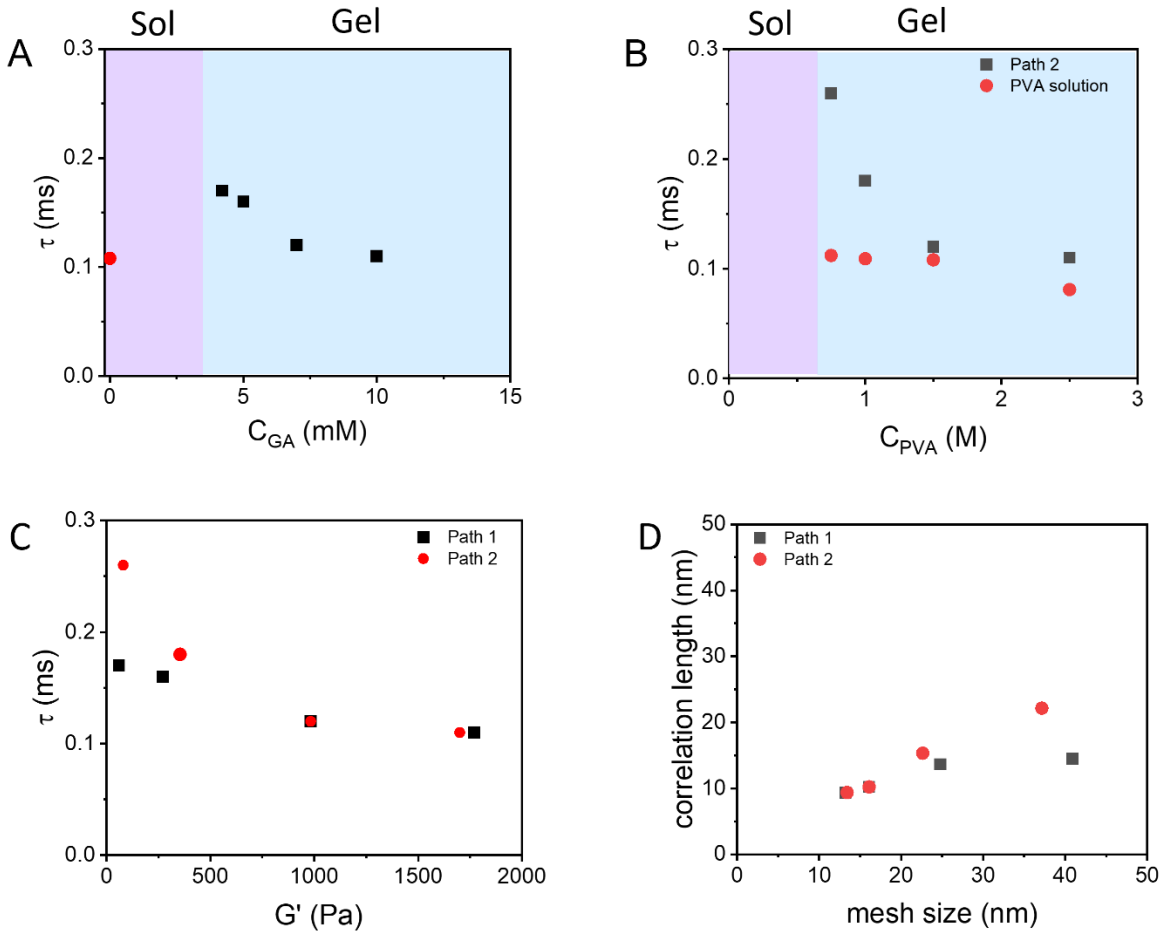

Figure 3.10. (A) Characteristic decorrelation time τ as a function of crosslinker GA concentration in Path 1. (B) τ as a function of PVA88 concentration in Path 2. (C) τ as a function of gel modulus. (D) Correlation length estimated from fast mode versus mesh size for gel from Path 1 and Path 2.

3.3.4. Puncture

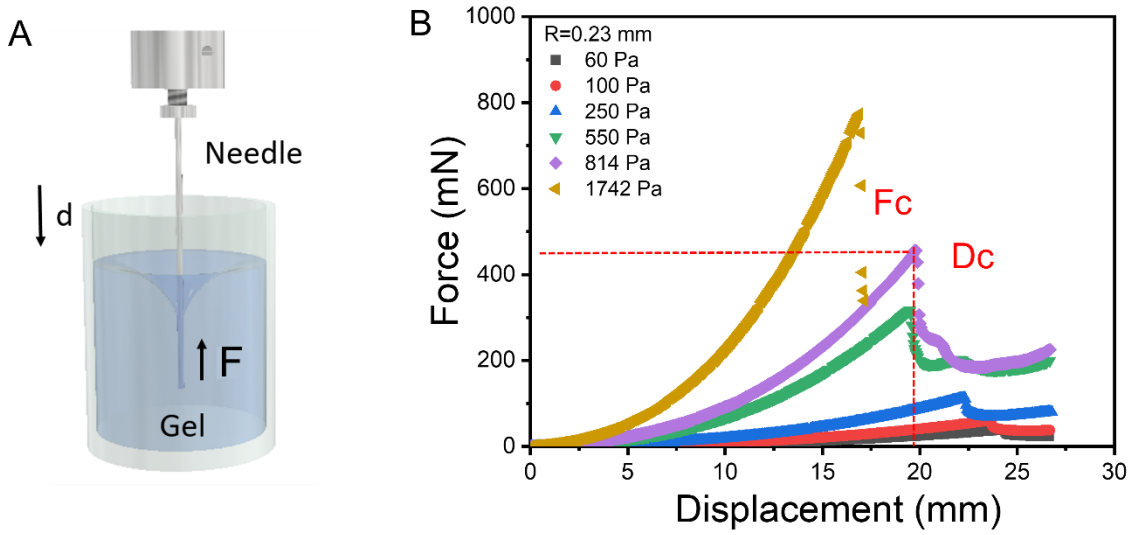

Figure 3.11. (A) Schematic of puncture apparatus and (B) representative puncture loading curve for PVA88 hydrogel from Path 1: puncture force as a function of puncture displacement, with critical force marked as F_c and critical displacement as D_c.

The loading force as a function of displacement can be recorded during the puncture process, from which the critical puncture force F_c is the peak force in the loading curve, and D_c is the critical displacement, as shown in **Figure 2.4**. With a fixed needle radius, F_c increases with gel modulus while D_c, tends to decrease with gel modulus. The role of needle size on fracture behavior will be detailed in the following section. In this section, we take the PVA88 gel from path 1 as a representative to illustrate the validity of the puncture experiment.

3.3.4.1. Neo-Hookean model and modulus measurement

As mentioned in Chapter 2, the Neo-Hookean model is employed here to describe the loading behavior of the puncture process[20],

$$P = k'Ed^2 + k''ERd$$

Where P is the puncture force, E is the Young′s modulus of the material, d is the displacement of the indenter tip, k' is an empirical coefficient, and k'' is a constant depending on indenter tip geometry from Hertzian contact mechanics ($k'' = 8/3$ for flat-end indenters). At small strain contact (**Figure 3.12A**), the elastic modulus can be estimated. Further, the comparison of modulus from small strain contact of puncture experiment and conventional rheology is shown in **Figure 3.12B** for the data of **Figure 11**. The data from the two measurement methods agree well with each other, with a slope of ~1.07, indicating that the elastic modulus can be effectively and accurately measured from the small contact condition of puncture process.

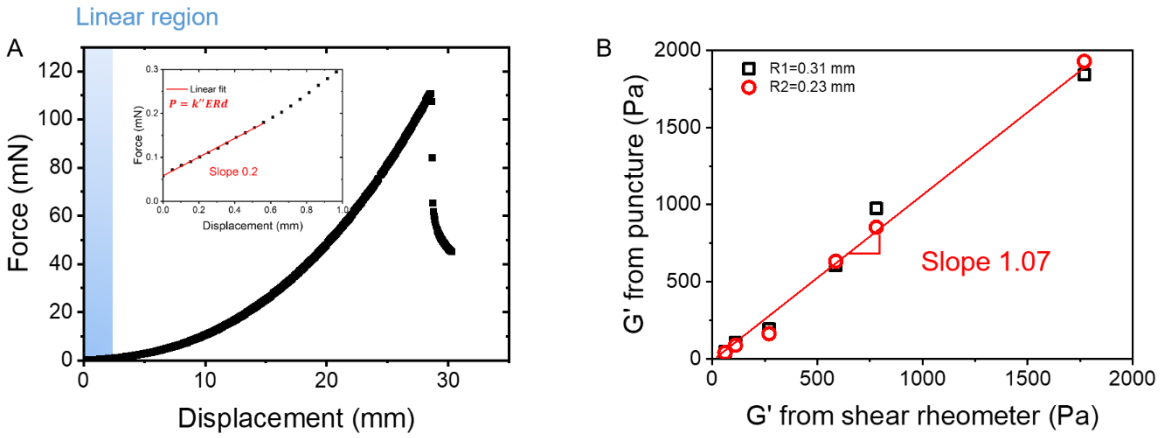

Figure 3.12. (A) Loading curve of PVA88 hydrogel from Path 1 (G' = 250 Pa and R = 0.23 mm) with an indicated linear region in blue shadow (the inset shows the linear fitting of the Neo-Hookean model). (B) Comparing elastic modulus from puncture experiment (with indenter R = 0.31 mm and R = 0.23 mm for examples) and rheology.

At the large strain contact region (**Figure 3.13A**), where we fit the loading curve before the fracture point to the Neo-Hookean model by setting $k'' = 8/3$, and $k'E$ as a fitting parameter, the resulting values of $k'E$ are plotted as a function of elastic modulus measured from shear rheology (**Figure 3.13B**). $k'E$ is a measure of the

large-strain response (effective modulus closer to the failure point) of materials. It has been reported to correlate well with the small deformation modulus from conventional mechanical measurement techniques, like rheology. The plot gives an excellent linear fit, with a slope of 0.45, while an empirical parameter consistent with the previous studies where the k' value ranges from 0.26~0.37 [20-22].

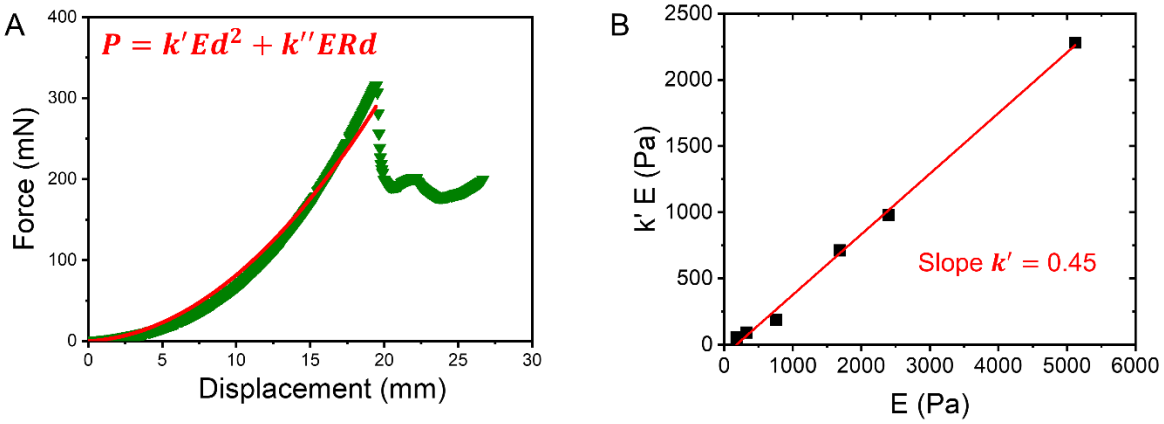

Figure 3.13. (A) Loading curve of PVA88 from Path 1 (G' = 550 Pa and R = 0.23 mm) fitting with the Neo-Hookean model. (B) Empirical determination of the coefficient k' of Neo-Hookean model in PVA88 hydrogel of various modulus.

3.3.4.2. Effect of indentation velocity

Substantial work has been placed on the rate-dependent fracture behavior of chemical and physical gels. It was reported that the failure processes of chemical gels, such as crack propagation and interfacial separation, are rate-dependent which is linked to the kinetic theory of bond dissociation and viscoelastic dissipation.[23-25] The local dynamic failure of physical gels is tightly associated with the dissipative phenomena including bulk viscoelasticity, and viscous dissipation owing to the solvent flow relative to the network.[26]

In an attempt to investigate the effect of the indentation velocity to fracture initiation, the puncture experiment was performed with the indentation velocity of 0.05, 0.25,

1, 5, and 10 mm/s, respectively (**Figure 3.14**). The loading curves prior to fracture with v = 0.05 - 5 mm/s nearly overlap yielding identical critical fracture force values F_c ~ 350 mm/s (**Figure 3.14B**). This result is consistent with the rheological result of the PVA gel in **Figure 3.4A** where the elastic modulus is insensitive to the applied frequency in such a purely elastic material system and the range of experimentally accessible strain rates.

Earlier studies on fracture of soft materials proposed two possible fracture mechanisms after the chain segments between entanglements crossing a plane have been fully extended: chain pull-out and chain scission.[27-28] The chain pull-out is governed by a time scale whereas chain scission is less sensitive to the applied time or velocity. For example, Seitz et al. concluded that the fracture energy release rate G_c scales with the loading velocity by an exponent of 0.4.[28] Crosby et al.[22] reported the rate-dependent fracture properties of physically crosslinked acrylic triblock gels where $F_c \sim v^{0.2}$, which have been attributed to the viscous drag between solvent and the network since chains are pulled out of the gel network during failure[28]. The rate-independency of fracture initiation in our experiment further confirmed that the fracture of chemically crosslinked PVA is induced by the chain scission crossing the plane.

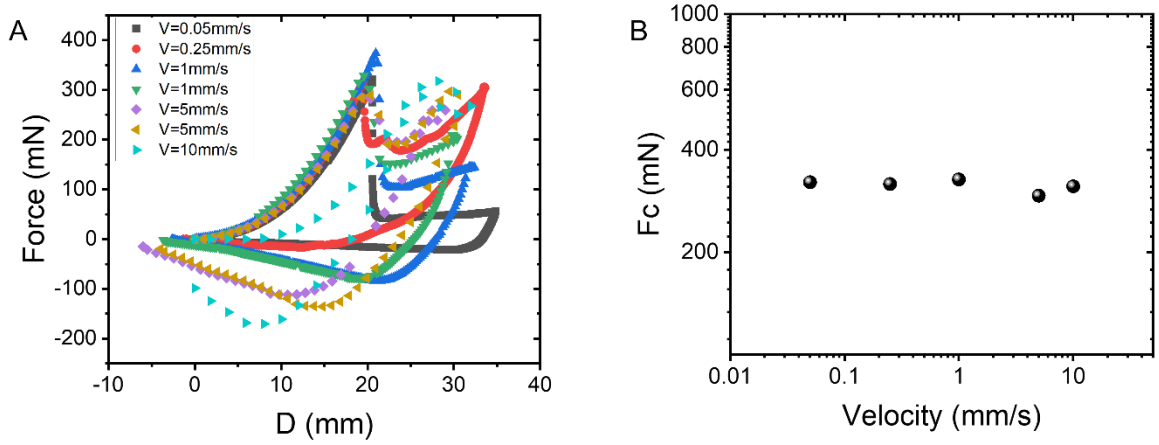

Figure 3.14. (A) The force curve of puncture with different indentation velocity for PVA88 hydrogel from Path 1 (G' ~ 600 Pa). (B) Critical fracture force F_c as a function of velocity.

3.3.5. Nonlinear response prior to fracture

In the previous sections, we have shown that the two series of soft PVA hydrogels having a similar range of moduli but with different spatial heterogeneity were successfully prepared. In this section, we characterized their fracture mechanics by puncture tests.

3.3.5.1. Large critical deformation

For PVA88 hydrogels prepared from Path 1 and Path 2, the critical puncture displacement D_c was measured by varying the indenter radius R and is plotted as a function of the plateau modulus G' in **Figure 3.15**. For gels from Path 1, D_c is found to increase with increasing indenter size and decreasing gel modulus (**Figure 3.15A**). Further, when the D_c is normalized by needle size R, D_c/R could reach above 100 times for the softest gel (**Figure 3.15B**). Compared to previous work where D_c is about 13 times R for acrylic triblock copolymer gels with modulus ranging from 2 kPa to 13 kPa [20], here D_c/R ~ 100, demonstrating different mechanics for these ultra-soft gels.

For gels from Path 2, D_c is also found to increase with the increase in indenter size, consistent with the result found for gel from Path 1 (**Figure 3.15C**). But D_c shows a limited dependence on gel modulus, consistent to the previous study that D_c is practically independent in gel modulus[20]. Notably, D_c/R for the softest gel is around 60, much lower than that for gel from Path 2 in a comparable modulus level (**Figure 3.15D**).

The stretch limit of the polymer chains λ_m in the dry polymer network containing *n* polymer chains per unit volume can be expressed as:[29]

$$\lambda_m = \frac{Nb}{\sqrt{N}b} = N^{1/2} \tag{3.5}$$

Where *N* is the number of Kuhn monomers between two successive covalent cross-links, and b is the Kuhn monomer length. Nb and $\sqrt{N}b$ are the end-to-end distance of a polymer chain at the relaxed state and stretched state, respectively. The shear modulus (or elastic modulus) of the network under initial deformation by assuming the affine network model is: [29]

$$G'=nk\mathrm{T} \tag{3.6}$$

Where *k* is the Boltzmann constant and *T* is the absolute temperature. Also, we have $Nnv=1$, where *v* is the volume of a Kuhn monomer.

According to the Lake-Tomas model, the fracture energy required to fracture a single layer of polymer chains per unit area is:

$$\Gamma = n\sqrt{N}bNU_f = nbN^{3/2}U_f \tag{3.7}$$

Where $n\sqrt{N}b$ is the number of the polymer chains per unit area, NU_f is the energy to fracture a polymer chain, and U_f is the energy to fracture a single Kuhn monomer.

Combing eq. 3.5-3.7, the mechanical properties of the hydrogel are coupled through the following relation:[30-31]

$$\lambda_m \sim \Gamma \sim G'^{-1/2} \tag{3.8}$$

The energy release rate $\mathcal{G}$ is proportional to the elastic energy and scales with $G'\lambda^2$. At the fracture point $\mathcal{G} = \Gamma$. Therefore one would expect that λ_m(L-T) ~ $G'^{-3/4}$, a stronger scaling than the one predicted by the single linear chain.[31]

The stretch limit of the bulk hydrogel (or D_c/R in puncture) scales with the stretch limit λ_m. But it also depends on the polymer network architecture as reported.[32] For the gel from Path 1 with a relatively homogenous network structure, D_c/R reasonably increases with decreasing modulus G', while the stretch limit of gel from Path 2 is highly affected by its structural heterogeneity as revealed by DLS.

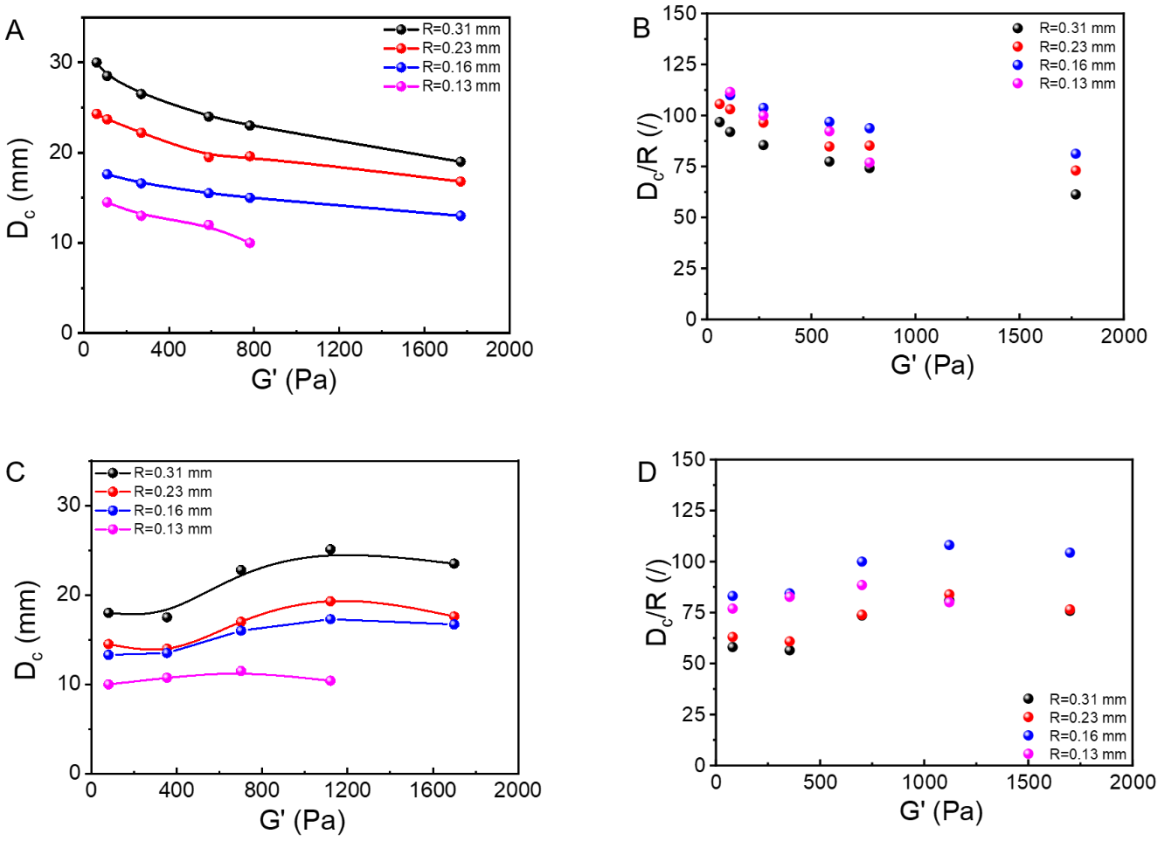

Figure 3.15. (A) Critical puncture displacement D_c as a function of gel modulus G' for PVA88 hydrogel from Path 1; (B) Normalized D_c by indenter size R versus G' for PVA88 hydrogel from Path 1. (C) Critical puncture displacement D_c as a function of gel modulus for PVA88 hydrogel from Path 2; (D) Normalized D_c by indenter size versus G' PVA88 hydrogel from Path 2.

3.3.5.2. Critical puncture force

For a chemical bond to fail by chain scission due to the applied external stress, the bond must first be subjected to critical stress. For gel from Path 1 and Path 2, the critical puncture force F_c was found to increase with the gel modulus and needle size (**Figure 3.16A** and **Figure 3.16C**). Although the stress field is highly inhomogeneous spatially we can define a critical nominal stress σ_c calculated as F_c normalized by the cross-sectional area of the needle, $\sigma_c=F_c/\Pi R^2$, characteristic of

the fracture point by puncture, and plotted as a function of gel modulus. In **Figure 3.16B**, the critical nominal stress σ_c was found to basically increase with gel modulus but, surprisingly, σ_c values superpose for gels with one fixed modulus and various needle size. This phenomenon indicates that the mechanism of fracture of gels from Path 1 is insensitive to the needle size or initial defect size. However, the σ_c of gel from Path 2 shows a clear dependence on the needle size: practically the smaller the needle size, the higher the nominal stress.

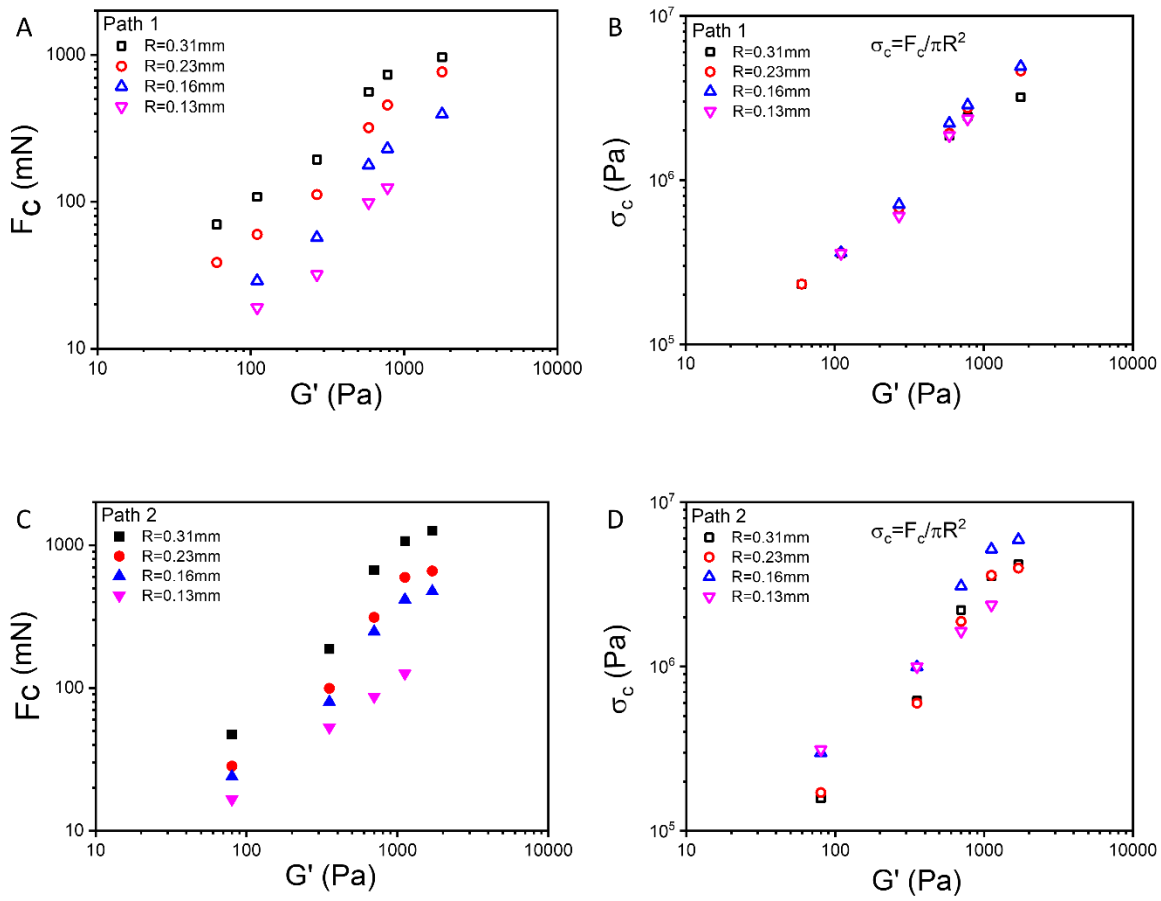

Figure 3.16. (A) Critical puncture force F_c versus modulus for PVA88 hydrogel from Path 1. (B) Critical nominal stress σ_c versus modulus for PVA88 hydrogel from Path 1. (C) F_c versus modulus for PVA88 hydrogel from Path 2. (D) σ_c versus modulus for PVA88 hydrogel from Path 2.

3.3.6. Fracture resistance

Before discussing the fracture resistance of gels with different structural heterogeneity, here we listed the characteristic lengths of PVA88 hydrogels to illustrate the experimental length scale where the fracture occurs. **Table 1** shows the summary of the gel modulus *G*', physical mesh size, and elasto-capillary length, for the gel with varied crosslinker GA concentrations in Path 1. As we discussed above, the ideal stretch limit scales with the modulus by $\lambda_m \sim G'^{-3/4}$ which partially explains the increase of critical fracture distance D_c for gels with lower modulus. The surface tension may start to play a role when approaching the elasto-capillary length scale. Thus, we calculated the elasto-capillary length l_{ec} according to the gel modulus (γ = 42 mN/m obtained from surface tension measurement for 6.6 wt% PVA solution). The value of l_{ec} is ranging from 716 – 24 μm for the modulus varying 60 – 1770 Pa. Notably, the needle size we applied in this indentation experiment is 130 – 310 μm, which is comparable to the l_{ec}, indicating that we are able to approach a quite small and adjustable length scale well below and above the l_{ec}. Similarly, the gel modulus *G*', mesh size, and elasto-capillary length evolution when varying the PVA polymer concentration (Path 2) are listed in Table 2. By increasing the polymer concentration from 3.3 to 11 wt%, the elastocapillary length of the gel system decreases from 537 to 25 μm, obtaining a comparable length range to needle size.

Table 1. Summary of modulus and characteristic length scales for gels in Path 1.

C_{GA}	Elastic modulus	Mesh size	Elasto-capillary length
		$\xi \sim (k_b T/G')^{1/3}$	$l_{ec} = \gamma/E$
(mM)	(Pa)	(nm)	(μm)
4.2	60	40.9	716.7
4.5	110	33.4	390.9

5	270	24.8	159.3
6.5	587	19.1	73.3
7	780	17.4	55.1
10	1770	13.2	24.3

Table 2. Summary of modulus and characteristic length scales for gels in Path 2.

C_{PVA} (wt %)	Elastic modulus (Pa)	Mesh size $\xi \sim (k_b T/G')^{1/3}$ (nm)	Elasto-capillary length $l_{ec} = \gamma/E$ (μm)
3.3	80	37.1	537.5
4.4	354	22.6	121.5
6.6	701	18.0	61.3
8.8	1120	15.4	38.4
11	1700	13.4	25.3

As the surface tension is expected to play a role in the fracture properties below the elasto-capillary length, we plot the fracture resistance σ_c/G' as a function of the radius normalized by the elasto-capillary length in **Figure 3.17**. Critical nominal stress, $\sigma_c = F_c/\Pi R^2$, characterizing the nucleation of a crack, was surprisingly found to surpass the modulus by 3 orders of magnitude, whereas $\sigma_c/G' \sim 150$ was previously reported for triblock polymers [20]. The dimensionless parameter σ_c/G' is indicative of the resistance to fracture initiation of soft materials[20]. The value of $\sigma_c/G' \sim 2000 – 4000$ is somehow surprising, suggesting the considerable fracture-resistant ability for ultra-soft PVA hydrogel. Notably, while the σ_c/G' is almost a constant value of 3000 when above the elasto-capillary length ($R > l_{ec}$), we observe an increase

of fracture resistance when below this critical length scale where σ_c/G' scales with the normalized length scale in -0.16, demonstrating the excellent fracture resistance ability for ultra-soft gels. This result indicates different fracture mechanisms, namely elasticity-dominated fracture and capillary-dominated fracture, respectively.

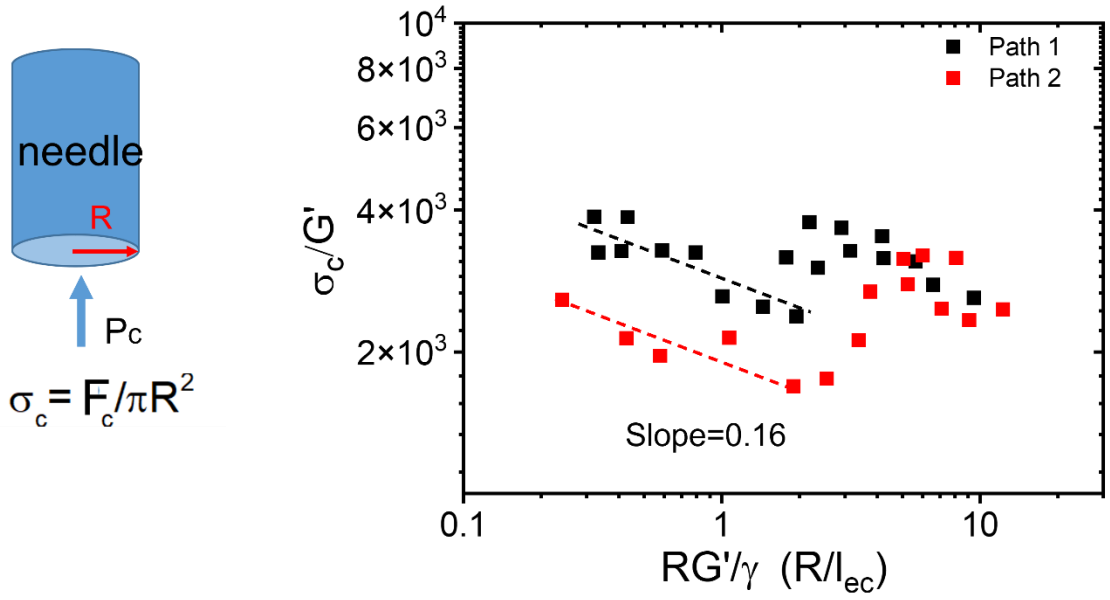

Figure 3.17. Critical nominal stress normalized by modulus, σ_c/G', as a function of indenter radius R normalized by elasto-capillary length γ/G'.

From **Figure 3.17**, it is obvious that even if the samples from both Path 1 and Path 2 show quite similar scaling behavior in fracture resistance below the elasto-capillary length scale, differences exist between the gels prepared by the two paths. The gels from Path 1 exhibit a higher σ_c/G' than those from Path 2. Based on the analysis of the structural heterogeneity via DLS, we attribute the difference in the fracture resistance of the gels from two paths to their structural heterogeneity. Generally, the fracture resistance of synthetic soft materials is largely affected by the inhomogeneous network structure created by cross-linking. When the networks cannot be deformed affinely because of the inhomogeneous network structure, the

crack tends to initiate from the weakest crosslinking. As presented in **Figure 3.18**, the gel from Path 1 possesses a relatively homogeneous network structure, in which the network could sustain large deformations by evenly distributing the applied stress and delaying crack nucleation involving chain scission. On the contrary, the network structure of gel prepared from Path 2 is spatially heterogenous, therefore the externally applied stress tends to concentrate on localized overstressed chains, nucleate larger defects and result in the catastrophic failure of the material. Consequently, we attain a lower critical deformation and fracture resistance of the inhomogeneous gel when compared to the homogenous one.

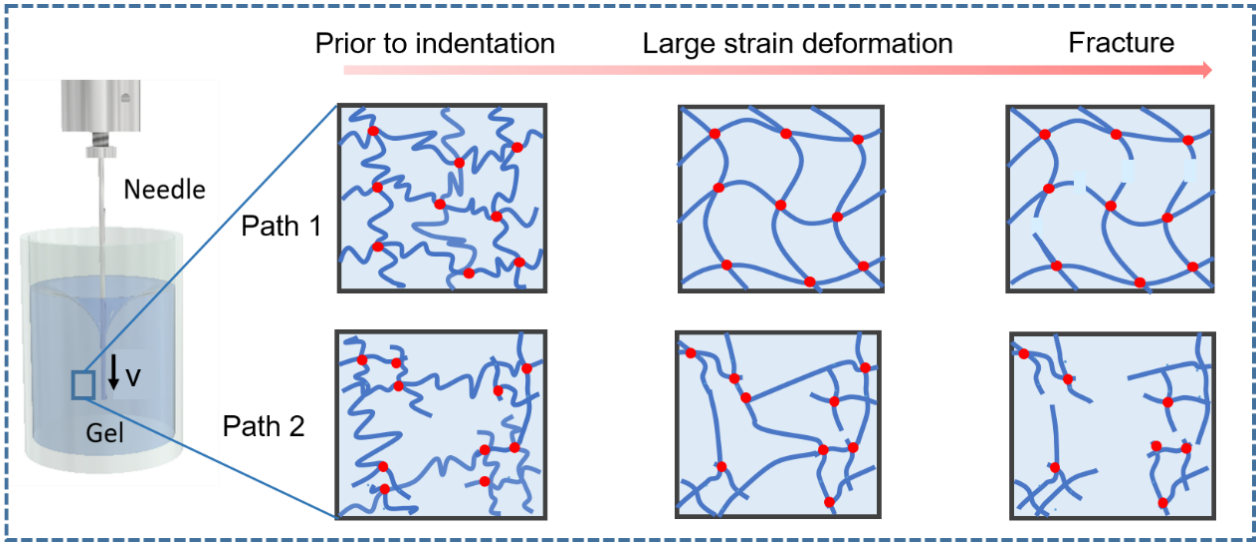

Figure 3.18. Schematic of the PVA88 hydrogel (form Path 1 and Path 2) network evolution under needle tip at different stages: prior to indentation, large strain deformation, and the point of fracture. Gels from Path 2 present high structure inhomogeneity compared to gels from Path 1 and sustain less large deformation when polymer chains cannot behave cooperatively to applied stress.

3.4. Conclusions

In this chapter, we investigated the impact of the structural heterogeneity of PVA hydrogels on their deformation and fracture behavior at the elastocapillary length scale. According to the phase diagram of PVA gelation, PVA hydrogels with modulus ranging from 80 – 1700 Pa were synthesized by varying the crosslinker GA concentration at fixed PVA content (Path 1) and by varying the PVA fraction with a fixed crosslinker concentration (Path 2). Through the rheological experiments, we found that the elastic modulus of PVA hydrogels from both paths shows limited frequency dependence even at a quite low stiffness range, indicating the purely elastic characteristic of the gel system. This result was confirmed by the puncture tests where the fracture point is independent of the applied indentation velocity. For gel from Path 1, the critical rupture strain was found to decrease with the increasing gel modulus, while that value is almost independent of gel modulus for sample from Path 2, indicating that the deformation and rupture of PVA hydrogel depend not only on its elastic modulus. The structural heterogeneity of gel formed by site-percolation (Path 2) is more prominent compared to that of gel formed by bond-percolation (Path 1) revealed by DLS. In puncture tests, we found that the critical fracture displacement D_c of gels from Path 1 decreases with gel modulus, while D_c of gel from Path 2 shows no dependence on gel modulus, associated with the stretch limit and structure architecture. The fracture resistance σ_c/G' was found to increase when the needle radius was smaller than the elasto-capillary length scale for gels made from both paths because of surface tension. However, σ_c/G' was reduced for gel from path 2 indicating that the strong structural heterogeneity favors crack nucleation at lower average stress.

3.5. References

1. Lee, K. Y.; Mooney, D. J., Hydrogels for tissue engineering. *Chemical reviews* **2001,** *101* (7), 1869-1880.
2. Livne, A.; Ben-David, O.; Fineberg, J., Oscillations in rapid fracture. *Physical Review Letters* **2007,** *98* (12), 124301.
3. Livne, A.; Cohen, G.; Fineberg, J., Universality and hysteretic dynamics in rapid fracture. *Physical review letters* **2005,** *94* (22), 224301.
4. Barrangou, L. M.; Daubert, C. R.; Foegeding, E. A., Textural properties of agarose gels. I. Rheological and fracture properties. *Food Hydrocolloids* **2006,** *20* (2-3), 184-195.
5. Bonn, D.; Kellay, H.; Prochnow, M.; Ben-Djemiaa, K.; Meunier, J., Delayed fracture of an inhomogeneous soft solid. *Science* **1998,** *280* (5361), 265-267.
6. Kong, H. J.; Wong, E.; Mooney, D. J., Independent control of rigidity and toughness of polymeric hydrogels. *Macromolecules* **2003,** *36* (12), 4582-4588.
7. Gong, J. P.; Katsuyama, Y.; Kurokawa, T.; Osada, Y., Double-network hydrogels with extremely high mechanical strength. *Advanced materials* **2003,** *15* (14), 1155-1158.
8. Abolhassani, N.; Patel, R.; Moallem, M., Needle insertion into soft tissue: A survey. *Medical engineering & physics* **2007,** *29* (4), 413-431.
9. Okamura, A. M., Methods for haptic feedback in teleoperated robot-assisted surgery. *Industrial Robot: An International Journal* **2004**.
10. McCreery, G. L.; Trejos, A. L.; Naish, M. D.; Patel, R. V.; Malthaner, R. A., Feasibility of locating tumours in lung via kinaesthetic feedback. *The International Journal of Medical Robotics and Computer Assisted Surgery* **2008,** *4* (1), 58-68.
11. Shibayama, M.; Norisuye, T., Gel formation analyses by dynamic light scattering. *Bulletin of the Chemical Society of Japan* **2002,** *75* (4), 641-659.
12. Shibayama, M., Spatial inhomogeneity and dynamic fluctuations of polymer gels. *Macromolecular Chemistry and Physics* **1998,** *199* (1), 1-30.
13. Shibayama, M., Small-angle neutron scattering on polymer gels: phase behavior, inhomogeneities and deformation mechanisms. *Polymer journal* **2011,** *43* (1), 18-34.
14. Pusey, P. N.; Van Megen, W., Dynamic light scattering by non-ergodic media. *Physica A: Statistical Mechanics and its Applications* **1989,** *157* (2), 705-741.
15. Guenet, J.-M., *Thermoreversible gelation of polymers and biopolymers*. Academic Press: 1992.
16. Rubinstein, M.; Colby, R. H., *Polymer physics*. Oxford university press New York: 2003; Vol. 23.
17. Narita, T.; Mayumi, K.; Ducouret, G.; Hebraud, P., Viscoelastic properties of poly (vinyl alcohol) hydrogels having permanent and transient cross-links studied by microrheology, classical rheometry, and dynamic light scattering. *Macromolecules* **2013,** *46* (10), 4174-4183.
18. De Gennes, P.-G., On a relation between percolation theory and the elasticity of gels. *Journal de Physique Lettres* **1976,** *37* (1), 1-2.
19. Stauffer, D., Introduction to Percolation Theory, Francis & Taylor. London: 1985.
20. Fakhouri, S.; Hutchens, S. B.; Crosby, A. J., Puncture mechanics of soft solids. *Soft Matter* **2015,** *11* (23), 4723-4730.
21. Rattan, S.; Crosby, A. J., Effect of polymer volume fraction on fracture initiation in soft gels at small length scales. *ACS Macro Letters* **2019,** *8* (5), 492-498.

22. Rattan, S.; Crosby, A. J., Effect of far-field compliance on local failure dynamics of soft solids. *Extreme Mechanics Letters* **2018,** *24*, 14-20.
23. Chaudhury, M. K.; Weaver, T.; Hui, C.; Kramer, E., Adhesive contact of cylindrical lens and a flat sheet. *Journal of applied physics* **1996,** *80* (1), 30-37.
24. van Vliet, T., Large deformation and fracture behaviour of gels. *Current Opinion in Colloid Interface Science* **1996,** *1* (6), 740-745.
25. Chaudhury, M. K., Rate-dependent fracture at adhesive interface. *The Journal of Physical Chemistry B* **1999,** *103* (31), 6562-6566.
26. Baumberger, T.; Caroli, C.; Martina, D., Solvent control of crack dynamics in a reversible hydrogel. *Nature materials* **2006,** *5* (7), 552-555.
27. Prentice, P., Influence of molecular weight on the fracture of poly (methyl methacrylate)(PMMA). *Polymer* **1983,** *24* (3), 344-350.
28. Seitz, M. E.; Martina, D.; Baumberger, T.; Krishnan, V. R.; Hui, C.-Y.; Shull, K. R., Fracture and large strain behavior of self-assembled triblock copolymer gels. *Soft Matter* **2009,** *5* (2), 447-456.
29. Rubinstein, M.; Colby, R., Oxford University Press; New York: 2003. *Polymer Physics.[Google Scholar]*.
30. Lake, G.; Thomas, A., The strength of highly elastic materials. *Proceedings of the Royal Society of London. Series A. Mathematical and Physical Sciences* **1967,** *300* (1460), 108-119.
31. Creton, C.; Ciccotti, M., Fracture and adhesion of soft materials: a review. *Reports on Progress in Physics* **2016,** *79* (4), 046601.
32. Boyce, M. C.; Arruda, E. M., Constitutive models of rubber elasticity: a review. *Rubber chemistry and technology* **2000,** *73* (3), 504-523.

4. Chapter 4: Improvement of fracture resistance of highly hydrolyzed PVA hydrogel due to strain-induced crystallization

4.1. Introduction

In Chapter 3, we have elucidated the role of structural heterogeneity on the nonlinear deformation and fracture properties of ultra-soft PVA88 hydrogel (hydrolysis degree, DH ~ 88 %). As an associative polymer, the macromolecular structure of PVA with different DH could significantly affect its melting temperature, structural dynamics, crystallization, and mechanical properties due to varied association strength by the hydrogen bonding between polymer chains[1-4]. Hence, in this Chapter, we adopt highly hydrolyzed PVA99 hydrogel (DH ~ 99 %) fabricated following Path 1 in Chapter 3 with a relatively homogeneous network structure to investigate the fracture behavior with large indentation conditions, aiming to reveal the structure-property relation of this associative polymer regarding the particular strain-induced crystallization in soft hydrogel system.

4.1.1. General introduction of PVA with different hydrolysis degree

PVA is commonly synthesized from poly(vinyl esters) (usually poly(vinyl acetate) (PVAc)) by hydrolysis [2]. The alkaline hydrolysis (saponification) of PVAc results in multiblock copolymers with dominating hydroxyl−hydroxyl interactions, similar to pure poly(vinyl alcohol) (PVA)[5]. The hydrolysis degree (DH) is determined by the mol percent of the -OH (vinyl alcohol (VA-)) groups to the total repeating units, in the PVA polymer chain. For example, the highly hydrolyzed PVA with DH ~ 99 %+ indicates that 99 mol% -OH groups in the PVA chain with less than 1 mol% acetate groups remaining (**Figure 4.1A**). PVA with a low hydrolysis degree, such as DH ~ 88%, has 88 mol% of -OH groups and 12 mol% of acetate groups in the chain (**Figure 4.1B**). The corresponding chemical structure of PVA with different hydrolysis degrees is shown in **Figure 4.1**.

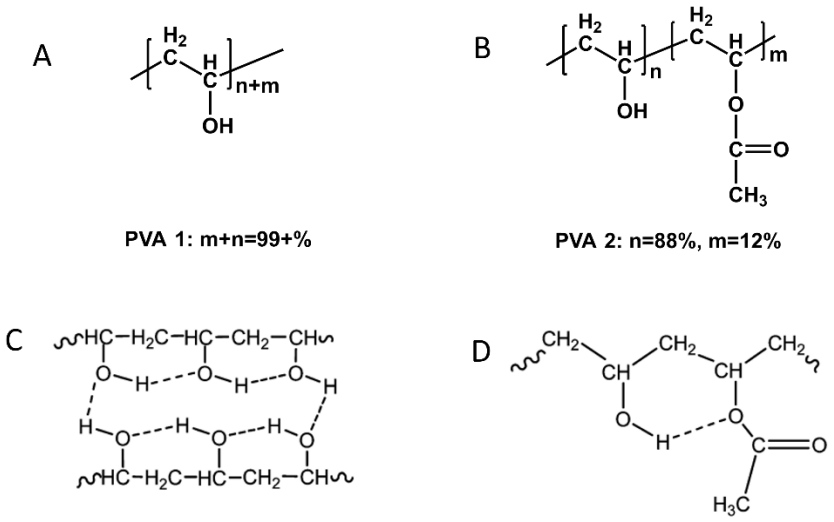

Figure 4.1. Chemical structure of PVA with different hydrolysis degrees. (A) PVA 1 is fully hydrolyzed with the DH ~ 99 % and (B) PVA 2 is less hydrolyzed with DH ~ 88 %. *n* is the number of repeated vinyl alcohol (VA-) groups and *m* is the number of vinyl acetate-(VAc-), in a PVA chain. (C) Hydrogen bonding associations for highly hydrolyzed PVA[3]. (D) Hydrogen bonding associations for partially hydrolyzed PVA[3].

In general, hydrogen bonding can be formed between the -OH groups as indicated in **Figure 4.1C**. If VAc and VA units are chain neighbors, then they can form a hydrogen bond leading to a thermally stable 6-member ring as seen in **Figure 4.1D**. The hydrogen bonding was found to dissociate when heating up to 60 ℃ [3]. In the course of the hydrolysis degree, the glass transition degree T_g increases from 42 °C for pure PVAc to 78 °C for pure PVA. The PVA with a high content of VA units exhibits an ability to crystallize[3].

4.1.2. The overview of the crystallization behavior of PVA

PVA is a semi-crystalline polymer due to the high content of hydrophilic hydroxyl groups in the polymer chains which can form both inter- and intra- molecular hydrogen bonds[1-2]. In a PVA aqueous solution, the coexistence and competition of

hydrogen bonding between PVA/PVA, water/water, and PVA/water complicates its structural dynamics and leads to some particular and interesting phenomena such as crystallization, phase separation, and gelation behavior under different external conditions.

Extensive investigations have been carried out on the crystallization-related behavior of PVA solutions and hydrogels[4, 6]. For PVA aqueous solutions, a sol-to-gel transition at a gelation temperature was observed during the freeze-thaw process, and reversely a gel-to-sol transition during the heating process at a higher gelation temperature was reported by Joshi et al.[7] They concluded that the formation of the microcrystalline domains through hydrogen bonding association between polymer chains accounts for the gelation behavior as shown in **Figure 4.2**. Liu et al. reported the stable flow-induced crystalline precursor in entangled PVA solutions at room temperature 25 ℃ (above the crystallization temperature) which behaves like an associative network, probably due to the disruption of the protective hydration shell around PVA molecules under shear and resultant strong interchain hydrogen bonding[4].

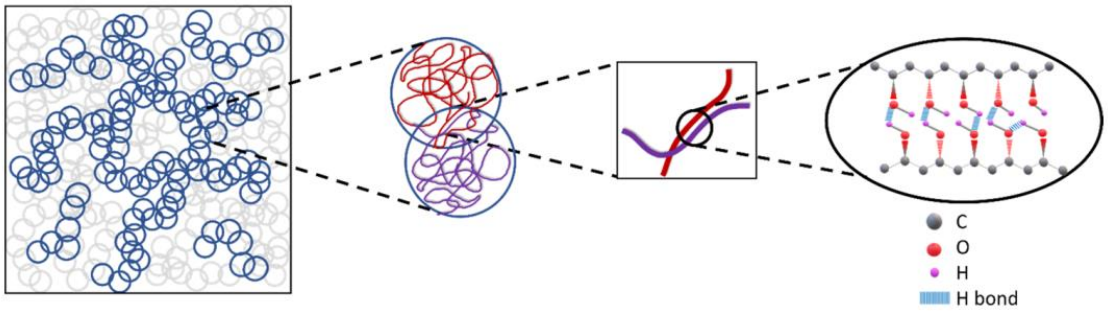

Figure 4.2. Schematic representation of a percolated network formation in PVA solution at the post-gel state. The hydrogen bonding associated segments are responsible for the formation of the micro crystalline domains[8].

Physically crosslinked PVA by the freeze-thaw method has been receiving significant research interest since first reported in 1975 by Peppas.[9] It was noted the viscoelasticity of PVA hydrogel via such method is comparable to that of articular and meniscal cartilage, making it an attractive biomaterial in engineering applications considering its great nontoxicity and biocompatibility[6, 10]. Specifically, this method involves casting of dilute solutions of PVA and then cooling to -20 °C to freeze the sample and thaw it to room temperature for several cycles. It is believed that during the cooling process, PVA is expelled to a polymer-rich region since water freezes, in which the PVA chains come into close contact with neighboring chains and crystallites form through hydrogen bonding. The interactions remain intact during the thawing process and thus a stable hydrogel is produced by the presence of crystalline regions serving as physical crosslinking[6, 11] (seen in **Figure 4.3A**). Several techniques such as solid-state NMR, DSC, and diffraction tools[10, 12] have been utilized to investigate the presence of crystals and crystallinity in freeze-thawed PVA hydrogel. The melting peak or endothermic peak in the DSC curve during the heating process was observed from 46 – 62 °C due to the melting of the crystallites in as-prepared freeze-thawed PVA hydrogel[13]. It has been widely reported that increasing the number of freeze-thaw cycles could significantly improve its mechanical properties by enhancing the crystallization process in the gel system (**Figure 4.3B** and **Figure 4.3C**)[13]. Controlling the processing parameters such as the number of freeze/thaw cycles, and the time and temperature history of the sample enables to tailor the mechanical properties of freeze thawed PVA hydrogel.

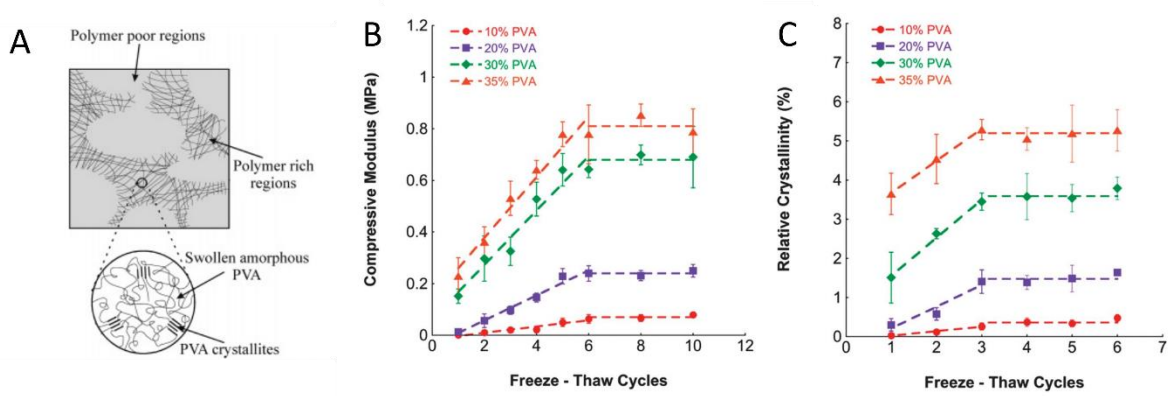

Figure 4.3. (A) Proposed bicontinuous structure of PVA hydrogels via the freeze-thaw method with a PVA-rich phase and a PVA-poor phase. The crystallites forms as additional crosslinking points in polymer-rich region[11]. (B) Compressive modulus and (C) relative crystallinity of 10, 20, 30, and 35 wt% PVA hydrogel with the increasing number of freeze-thaw cycles[6].

PVA can also form crystalline domains through crosslinking amorphous domains by annealing at temperatures above its glass transition temperature owing to the hydrogen bonding interactions of hydroxyl groups in PVA chains[14]. Zhao et.al. [15] reported an anti-fatigue-fracture PVA hydrogel produced via a dry-annealed strategy. Compared to amorphous chemical PVA hydrogel with a low fracture energy Γ_0 ~ 10 J/m^2 and commonly used freeze-thawed PVA hydrogel with low crystallinity, which usually obtains a fatigue energy Γ_0 ~ 23 J/m^2, the hydrogel from dry-annealed could reach Γ_0 ~ 1000 J/m^2 by increasing the crystallinity up to 18.9 wt% (**Figure 4.4**). The fracture resistance was substantially improved due to the introduction of high crystallinity in which the fracture energy required to rupture a crystalline phase is much higher than that for amorphous hydrogel, therefore crystalline domains can also act as intrinsically high-strength phases in the polymer networks.

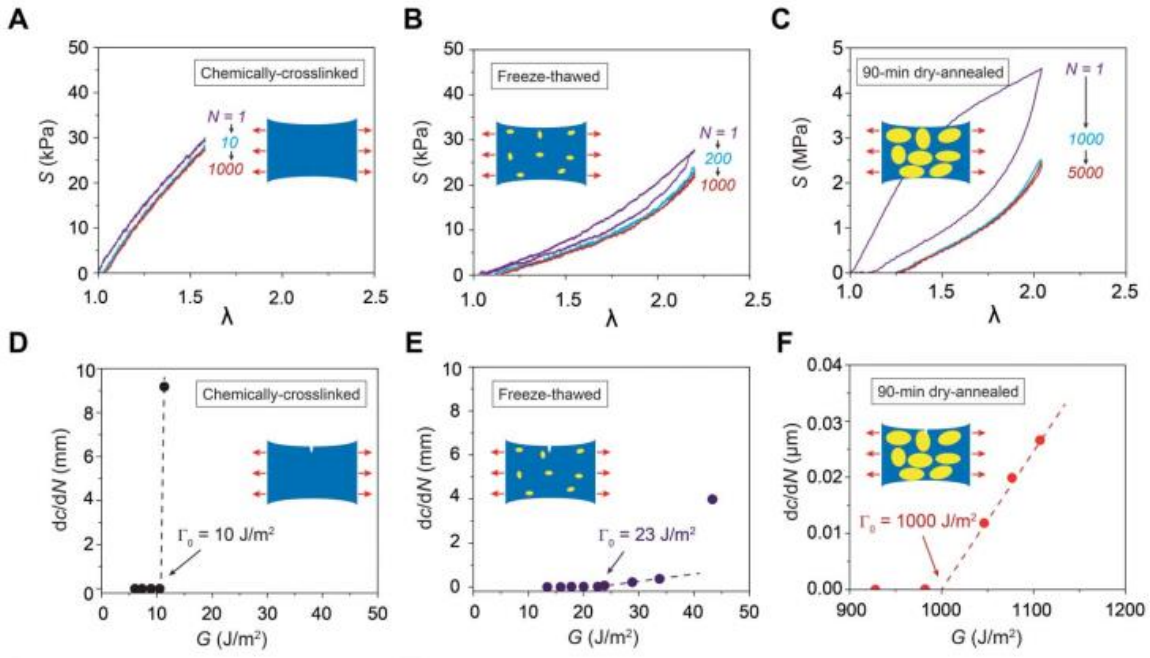

Figure 4.4. Measurement of fatigue thresholds of PVA hydrogels[15]. Nominal stress *S* versus stretch λ curves over cyclic loads for (A) chemically cross-linked hydrogel at an applied stretch 1.6, (B) freeze-thawed hydrogel at an applied stretch 2.2, and (C) 90-min dry-annealed hydrogel at an applied stretch 2. Crack extension per cycle d*c*/d*N* versus applied energy release rate *G* for (D) chemically cross-linked hydrogel, (E) freeze-thawed hydrogel, and (F) dry-annealed hydrogel with annealing time of 90 min.

4.1.3. The strain-induced crystallization (SIC) in soft materials

Strain-induced crystallization is typically found in natural rubber and some biopolymers, such as collagen[16], and spider silk[17]. It is well known that the natural rubber with a relatively high regularity of the chemical structure of cis 1,4 polyisoprene, displays strain-induced crystallization (SIC) and strain-hardening performances under stretch, largely reinforcing the material network around the crack tip and thus improving its fracture resistance[18-20]. It is believed that the SIC in natural rubber is a thermodynamically driven phenomenon triggered by a decrease in entropy of the polymer chain during extension so that it lowers the barrier of

crystal formation[21]. In this case, the higher the deformation of the chains and the lower the temperature, the higher the probability for the chains to crystallize along the stretching direction[22]. Numerous studies have been carried out on the SIC in natural rubber and its dependency on strain, crosslinking, fillers and temperature[23-25]. SIC in natural rubber was found to depend remarkably on filler fraction and temperature[22, 26]. **Figure 4.5A** shows the effect of temperature on tensile properties of an unfilled natural rubber sample (NR0) and a filled sample (NR50)[22]. While the stiffness of the unfilled material appears higher at a high temperature than at a low temperature, consistent with the rubber elasticity, that of the filled material is unaffected by the temperature at low strain but softens significantly at high strain. By comparing the crystallinity index of the filled material NR50 stretched at a different temperatures (**Figure 4.5B**), it was found that crystallinity appears at a higher extensibility for higher temperatures, as reported previously that the crystallization threshold increases with temperature [19].

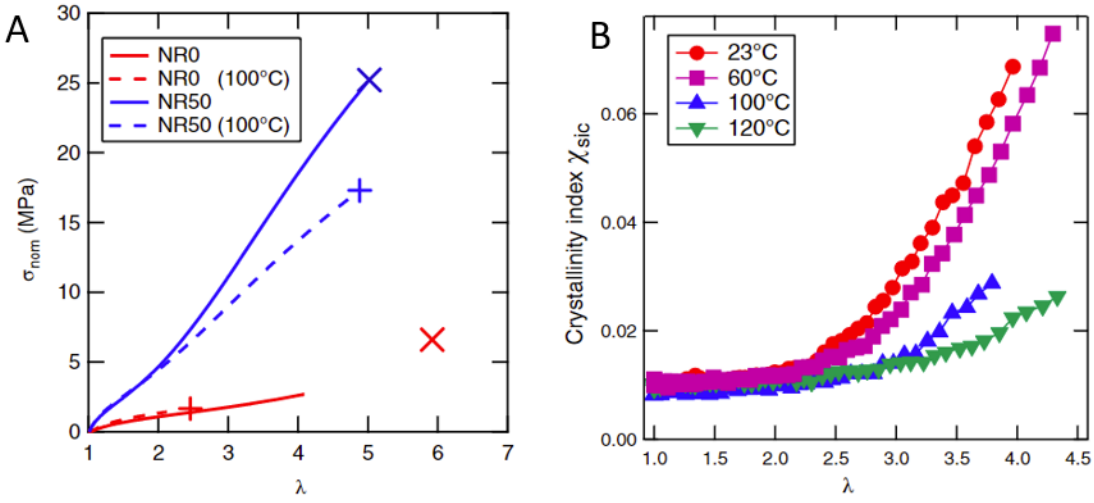

Figure 4.5. (A) Stress vs strain curve of (unfilled) NR0 and (filled) NR50 at 23 and 100 °C. (B) Crystallinity index as a function of stretch at different temperature for the NR50[19].

Toki et al.[26] studied the temperature dependence of stress-strain relation for un-vulcanized/vulcanized natural rubber (NR) and synthetic polyisoprene (IR) at various temperatures from -50 °C to 75 °C. The stress at a lower temperature is higher than that at a higher temperature over the whole strain range, seemingly contrary to the theory of the rubber elasticity (**Figure 4.6**). By using wide angle X-ray diffraction, they confirmed that the SIC occurs at all studied temperature ranges but the onset of SIC increases with temperature and strain as previously reported[26,27]. At higher strain, the SIC serves as the network crosslinking point to bind the polymer chains and thus reduce the limit of extensibility[26].

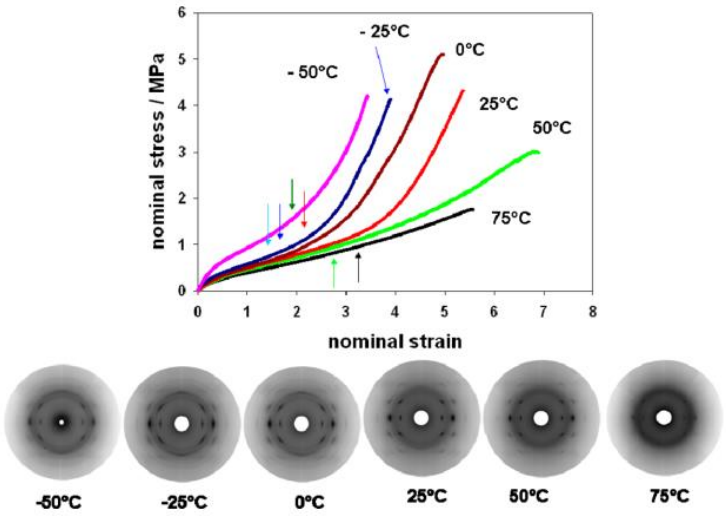

Figure 4.6. Stress-strain relation of vulcanized natural rubber at various temperature. WAXD pictures at largest strain before break. Vertical arrows suggest the onset strain of SIC at various temperature[26].

The sideways crack was studied in elastomers in which cracks propagate perpendicular to their "standard" trajectory due to the crystallization in front of the crack tip[28-29]. During uniaxial stretching in the vertical direction, a crack propagates in the direction of the applied load as seen in **Figure 4.7**. They attributed the side-way crack behavior to structural rearrangements of polymer chains during stretching

in which the chain orientation and crystallites formed at the crack tip. Instead of rupturing a crystalline domain, the crack tends to propagate parallel to the direction of loading to avoid such an energy-expensive route (forward-ways). These sideways cracks stably arrest, thereby allowing the material ahead of the crack to continue to sustain large loads and thus toughening the material[28].

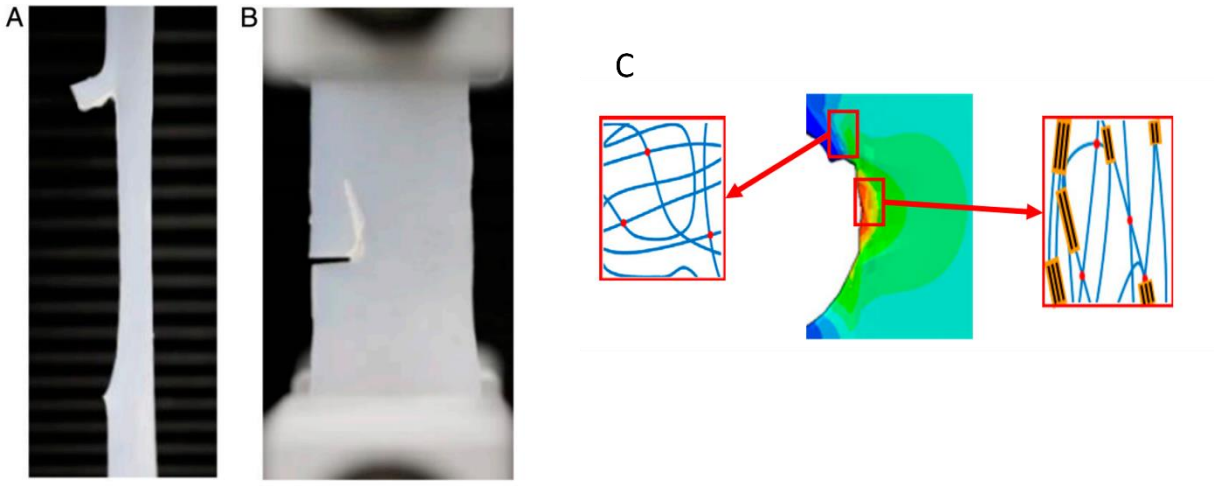

Figure 4.7. Photos of sideways crack propagation from a precut specimen[28]. (A) During uniaxial stretching in the vertical direction, a crack propagates in the direction of the applied load. (B) An image of the crack after unloading, showing the stable propagation of a sideways crack. (C) Hypothesized inhomogeneous distribution of microstructure at two areas of interests near the crack tip.

More recently, the rapid and reversible strain-induced crystallization in the slide-rings poly(ethylene glycol) hydrogel with moderate polymer fraction was reported, resulting in excellent toughness which could be one order of magnitude higher than for homogenously covalently crosslinked PEG hydrogels[30]. The close-packed structure of PEG is formed during stretching and reversibly destroyed during unloading (as shown in **Figure 4.8**), with resultant crystallization, accounting for the excellent toughness of up to 22 MJ/m^3.

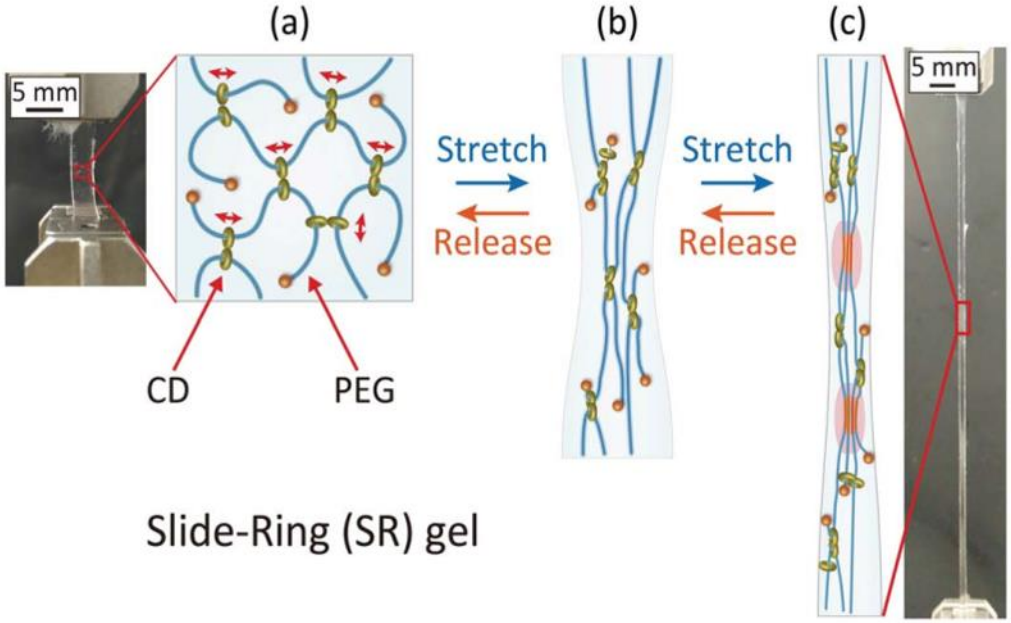

Figure 4.8. Schematic of samples and reinforcement strategy. SR gel with movable crosslinks composed of α-cyclodextrin molecules (CD). The close-packed structure of PEG is formed and destroyed during stretching and releasing[30].

Nevertheless, to the best of our knowledge, the SIC in loosely crosslinked ultra-soft hydrogels has never been reported and its role in fracture properties has remained elusive, especially with the challenge of handling an ultra-soft sample that cannot support its weight under gravity when freestanding[31] and the difficulty to perform fracture tests with the appropriate geometry. In this chapter, we report a novel extremely large strain-induced crystallization in highly hydrolyzed PVA hydrogels observed by birefringence imaging. The impact of the crosslinking ratio (gel modulus), needle size, temperature, and applied strain on its crystallization and fracture behavior is investigated.

4.2. Experimental section

4.2.1. Materials

Poly(vinyl alcohol) (PVA99, molecular weight: 89000 g/mol, degree of hydrolysis: 99 %), Poly(vinyl alcohol) (PVA88, molecular weight: 67000 g/mol, degree of hydrolysis: 88 %), and glutaraldehyde (GA, 25% aqueous solution) and hydrochloric acid were purchased from Sigma-Aldrich and used as received.

4.2.2. Gel preparation

PVA99 stock solution at a concentration of 8.8 wt% (or 2 M of repeating unit) was prepared by dissolving the PVA powder in deionized water at 90 ℃ and under vigorous stirring over four hours. PVA99 hydrogel in this Chapter is fabricated following Path 1 in Chapter 3 to obtain a relatively homogenous network structure. Chemically cross-linked PVA99 hydrogels were prepared by mixing PVA stock solution (adjusted to 6.6 wt%, 1.5 M) and cross-linker GA with various concentrations (3 – 6.5 mM) in the presence of HCl (0.05 mM). The system was gelled in a cylindrical glass vial with a diameter of 25 mm and used for measurement after more than 12 h.

4.2.3. Puncture experiment with birefringence observation

Puncture tests were performed with the custom apparatus described in Chapter 2. Birefringence optics were added to the setup as shown in **Figure 4.9**. Two linear polarizers were placed between the light source (flat LED panel) and the CCD camera. A balance with a precision of 0.1mg was placed at the bottom of the sample and used as a force sensor to measure the puncture loading force. As an indenter, a flat-end metal needle (purchased from Hamilton Company) with a radius of 0.23 – 0.31 mm was used. The needle was backfilled with epoxy and fixed to the adapter

in the actuator (motorized stage). The inserting velocity of the indenter was 0.25 mm/s in this study.

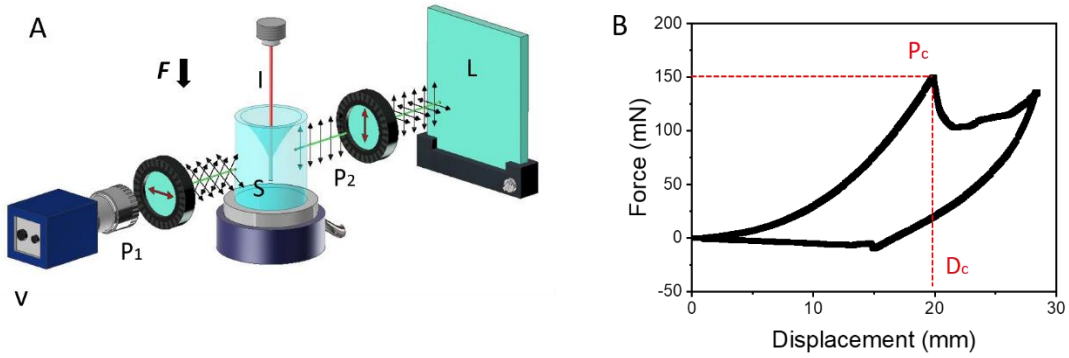

Figure 4.9. (A) Schematic of the custom puncture apparatus for hydrogels incorporated with birefringence optics. L: light source; P1, P2: crossed polarizers; S: sample; I: puncture needle; V: video camera. (B) Representative force profile for a loading and unloading process, with critical fracture force F_c and critical displacement D_c.

4.2.4. Rheology

Rheological measurements were carried out on a stress-controlled rheometer (ARES, TA Instruments, USA) with a steel cone-plate geometry (25 mm in diameter, 0.043 mm in the gap). A fresh gel mixture solution before gelation was loaded for time sweep measurements to track the gelation behavior of the PVA sample. Frequency sweep with an angular frequency range of 0.1 – 100 rad/s at a linear strain of 2 % and strain sweep with amplitude ranging 0.1 – 10000 % at a fixed frequency of 1 Hz were performed successively. For each measurement, the exposed surface of the sample was covered with a thin layer of low-viscosity silicone oil to avoid water evaporation.

4.3. Results and discussion

4.3.1. Rheology

4.3.1.1. Small strain response

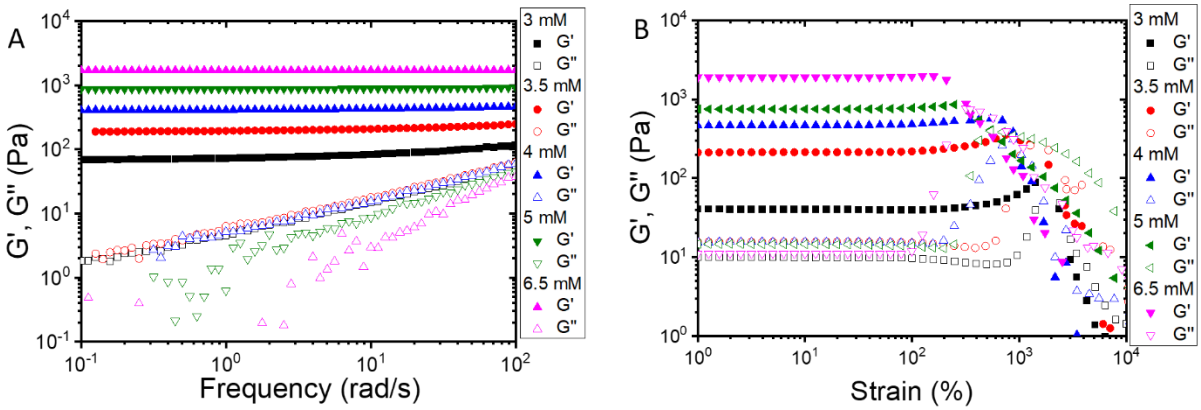

Figure 4.10. (A) Frequency sweep and (B) Strain sweep of PVA99 hydrogel with cross-linker GA concentration ranging from 3 to 6.5 mM.

The elastic properties of the PVA99 hydrogels were varied by changing the chemical crosslinker (glutaraldehyde, GA) concentration, and were characterized by linear rheology. In **Figure 4.10A** the elastic and viscous moduli of the gels are shown as a function of angular frequency. We found that the elastic modulus G' shows practically no frequency dependence for all the gels tested, exhibiting a well-defined elastic plateau with a modulus in a range of about 100 – 2000 Pa. The viscous modulus is much lower than the elastic modulus, and tan δ (G''/G') is calculated to be lower than 0.1 at low frequency. This result confirms the nearly purely elastic feature of the model system. In **Figure 4.10B** the elastic modulus in the linear viscoelastic region increases with the improved crosslinker concentration and a strain hardening (depicted as the increase of elastic modulus) at a large strain region is observed.

4.3.1.2. Large oscillatory amplitude shear (LAOS)

The stress response for a viscoelastic material subjected to a sinusoidal strain of amplitude γ_0, given by $\gamma(t) = \gamma_0 \sin(\omega t)$, can be conventionally described by equation 4.1 if the γ_0 is small enough to satisfy the linearity constraint:

$$\sigma(\mathrm{t}) = \gamma_0[G'(\omega)\sin(\omega t) + G''(\omega)\cos(\omega t)] \qquad 4.1$$

where the G' represents the elastic modulus, G'' is the viscous modulus, and ω is the angular frequency (as shown in **Figure 4.10B**). The strain amplitude γ_0 can be systematically increased to a nonlinear viscoelastic regime, and the G' and G'' are insufficient to capture the complete elastic and viscous behavior. A higher harmonic is needed to describe its viscoelastic behavior under a large amplitude. A Fourier transform could be performed to the strain response of each oscillation cycle to demonstrate the different harmonics composing the strain signal. The original strain response is described as a function of time by Eq. 4.2:

$$\sigma(\mathrm{t}) = \gamma_0 \sum\nolimits_{\mathrm{n:odd}} [G'_n(\omega)\sin(\omega t) + G''_n(\omega)\cos(\omega t)] \qquad 4.2$$

where G_n' and G_n'' represent the viscoelastic moduli at the n-th harmonic. In the linear region, the first harmonic of Eq. 4.2 reduces to Eq. 4.1 with $n = 1$, $G_1' = G'$ and $G_1'' = G''$, respectively, and the stress-strain data, often named as Lissajous−Bowditch (LB) plots, is a well-defined ellipse. At a large strain amplitude, the elliptical shape of the LB curve starts to distort (**Figure 4.11**). Higher-order terms ($n > 1$) of Eq. 4.2 are needed to describe the nonlinearity of the material.

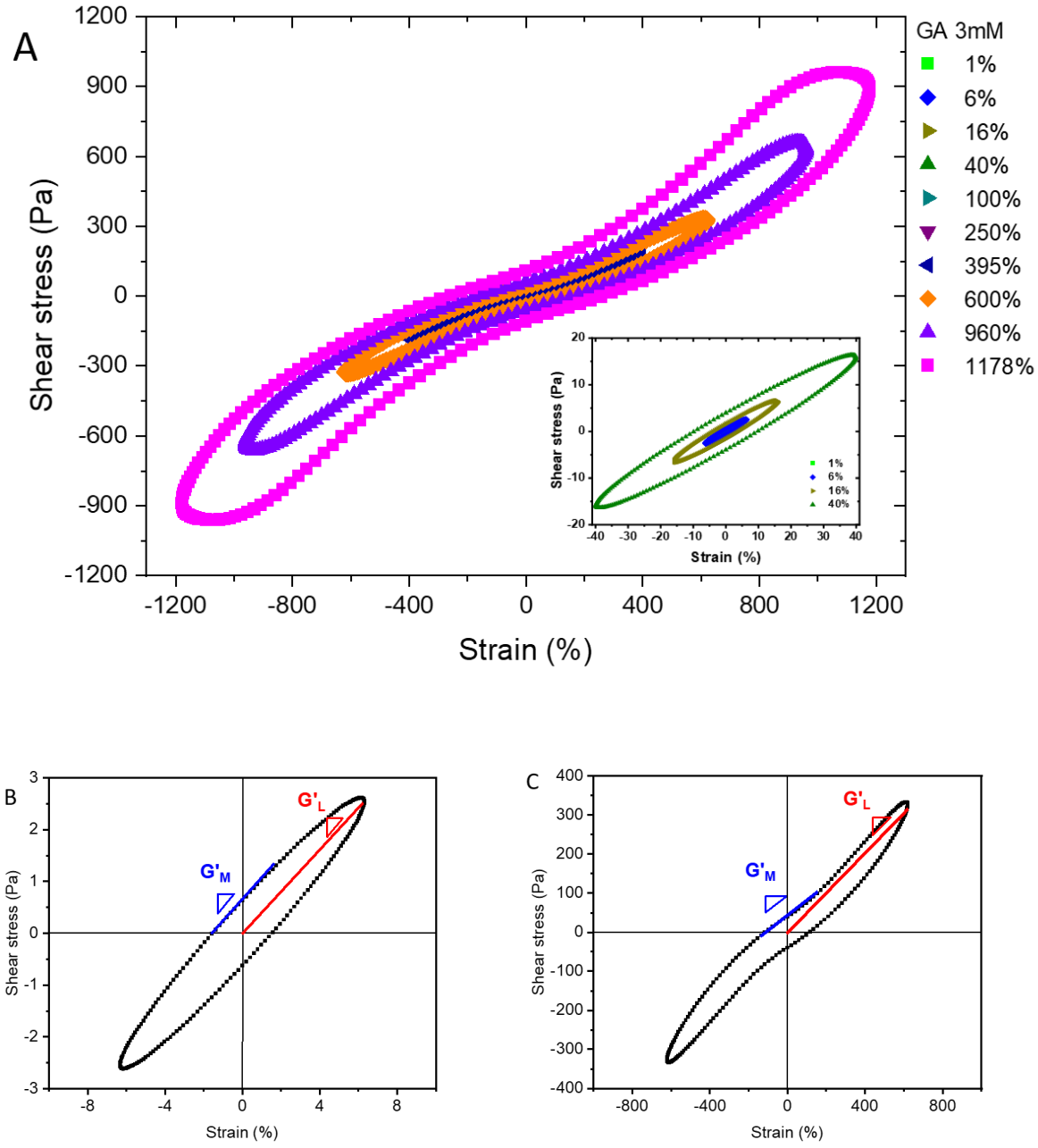

Figure 4.11. (A) The elastic Lissajous−Bowditch curve generated from the stress-strain response of large oscillatory amplitude shear (LAOS) for PVA99 hydrogel with GA concentration of 3 mM. (B) Representative LAOS curve at a strain amplitude of γ_0 = 6 %; (C) at a strain amplitude of γ_0 = 600 % with the indicated large-strain elasticity G_L', and the small-strain elasticity G_M'.

The elastic modulus can be compared to quantify the nonlinearities which distort the linear viscoelastic ellipse in **Figure 4.11B** and **Figure 4.11C**. If the large-strain modulus G'_L is greater than the minimum-strain modulus G'_M, we define the strain-hardening ratio: $S \equiv \frac{G'_L - G'_M}{G'_L}$, where G'_L is the large-strain elasticity $G'_L = (\tau/\gamma)\big|_{\gamma=\pm\gamma_0}$, and G'_M is the small-strain elasticity $G'_M = (d\tau/d\gamma)\big|_{\gamma=0}$, from the LB curve respectively. Here S = 0 indicates a linear elastic response, S>0 indicates intracycle strain hardening and S < 0 is the strain-softening, respectively.

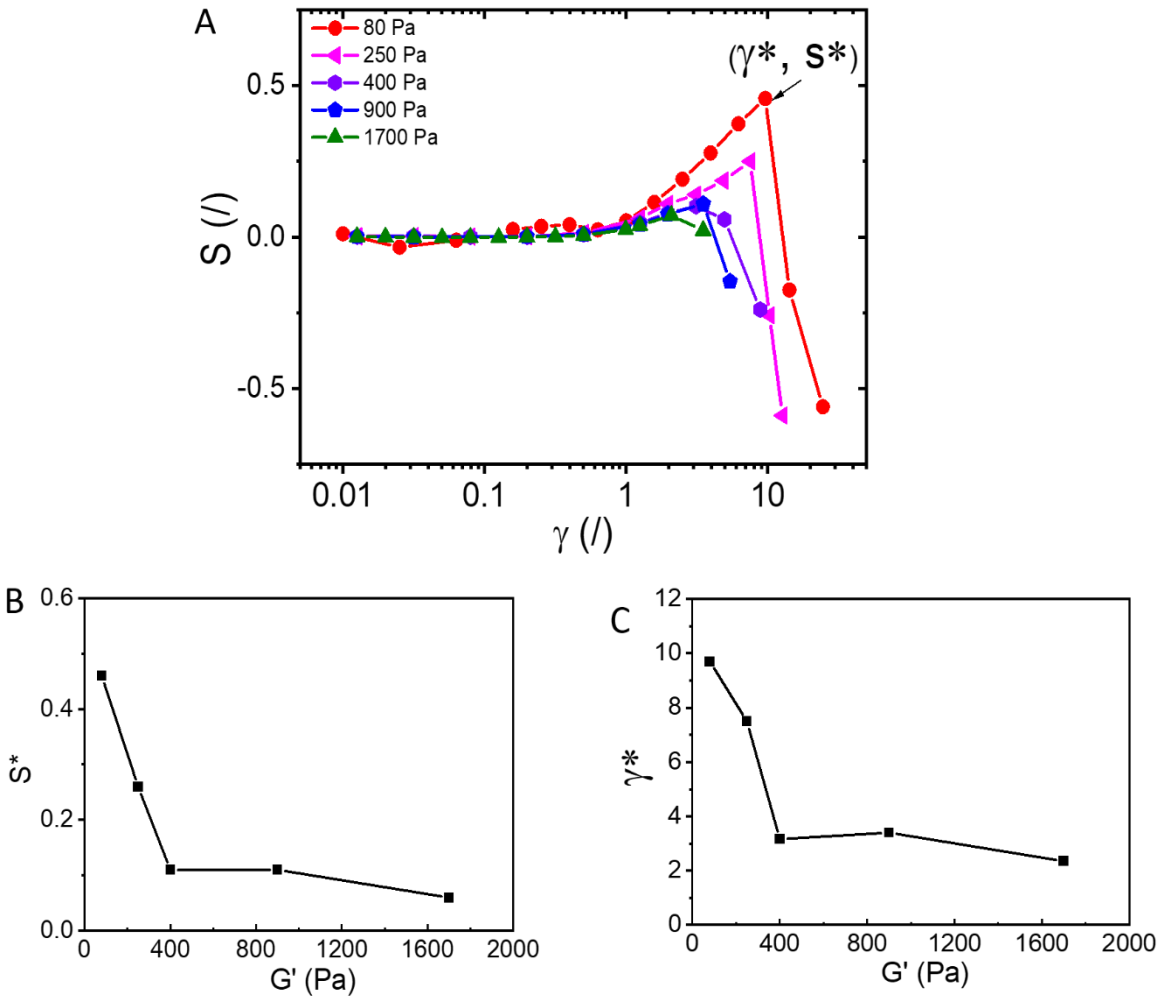

Figure 4.12. (A) Strain hardening index as a function of strain γ from large amplitude oscillation shear for PVA99 gels where the sample shows a strain-

hardening behavior in the large strain regime before rupture. (B) Critical strain-hardening index *S** vs gel modulus. (C) The failure strain γ^* vs gel modulus. (The failure strain γ^* indicates the critical strain after which the material has been destroyed).

We performed the large amplitude oscillation shear (LAOS) measurements for PVA99 hydrogels with varied modulus. In linear response, the LB plot is a well-defined ellipse and deviation from ellipticity is characteristic of nonlinear viscoelastic response[32]. Further, the strain hardening index *S* is plotted as a function of G' in **Figure 4.12A**. In the linear strain region, the strain hardening index *S* is nearly zero, indicating that the large-strain elasticity G'_L and small-strain elasticity G'_M are identical. With the increase of the applied strain, *S* was found to increase at large strain region until the maximum *S*, from which the critical strain hardening *S** and the critical failure strain γ^* are identified. It is interesting to note that the softer the gel, the higher the critical strain hardening index *S** at large deformation, and the larger the critical failure strain γ^*(**Figure 4.12B** and **Figure 4.12C**). A similar strain hardening behavior was also reported in the same analysis protocol for collagen hydrogel[33]. The strain hardening behavior is commonly found either in natural rubber or in biopolymers, such as collagen[16], and spider silk[17]. For the former, it is believed that the strain-induced crystallization mainly accounts for the increase in modulus or strain hardening in elastomers [25]; and for the latter, it's associated with the fibril alignment along extension direction and/or resulting crystallization. For PVA hydrogel with high DH, we assume that the strain hardening may originate from the crystallization under large shear deformation where critical rupture strain γ^* can be up to 1000% for the gel with a modulus G' = 80 Pa.

4.3.2. Puncture

Figure 4.13A presents the loading curves of PVA99 hydrogel having different modulus (R = 0.23 mm). With the rise in the modulus the puncture force increases, thus the critical force where the fracture occurs increases. However, the critical displacement displays the opposite dependence on modulus. When the nominal stress $\sigma = F/\pi R^2$, indicative of the puncture resistance of the gel, was normalized by the elastic modulus, we found that the loading curves for a gel with different moduli display great self-similarity and can surprisingly superpose perfectly until the fracture point as shown in **Figure 4.13B**. Particularly, the loading curve of gel with modulus G' = 80 Pa shows great extensibility and fracture resistance.

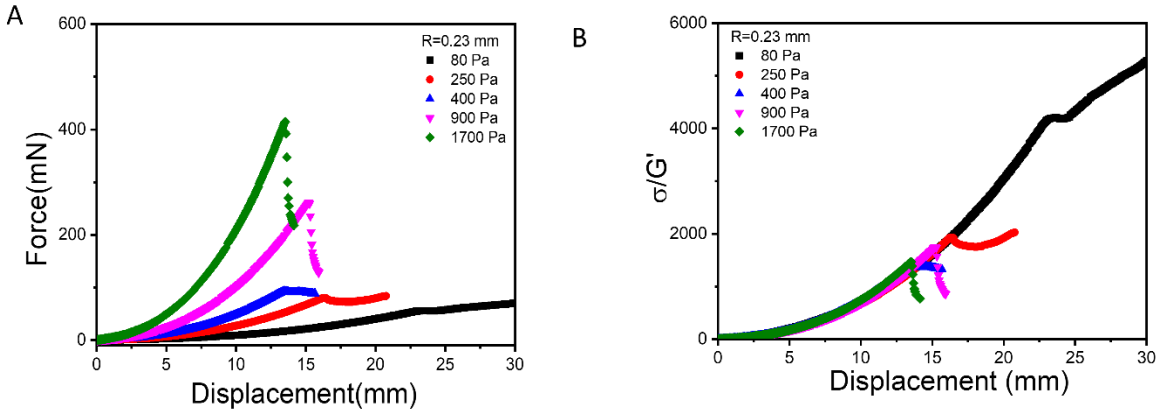

Figure 4.13. (A) Force profile for a loading process for PVA99 hydrogel with the needle size R = 0.23 mm. (B) Nominal stress normalized by elastic modulus σ/G' as a function of displacement.

The values of critical displacement D_c were plotted as a function of G' in **Figure 4.14A**. We found that D_c is quite large compared to R, where D_c/R can reach 50 – 100, indicating that PVA gels are highly deformable. It should be noted that for gels with a modulus higher than 400 Pa, the critical distance D_c is practically independent of the modulus, as reported previously for gels in a kPa range [34]. For the gels with a

modulus lower than 400 Pa, however, D_c increases with the decrease of modulus, $D_c/R \sim 100$ for $G' \sim 80$ Pa, suggesting that the softer gels are more resistant to fracture in puncture.

Figure 4.14B shows the fracture resistance of PVA hydrogels with different moduli. Critical nominal stress for puncture, $\sigma_c = F_c/\pi R^2$, was surprisingly found to surpass the modulus by 3~4 orders of magnitude, whereas $\sigma_c/G' \sim 150$ for triblock polymers as reported[34]. This reflects the large difference in soft gels between the force to break covalent bonds (invariant with modulus) and the shear modulus which depends on the concentration of elastically active chains. The fracture resistance σ_c/G' decreases with the increase in modulus. More specifically, σ_c/G' for gel with a modulus higher than 400 Pa is about 1000, and that value for the softest gel could reach 5000.

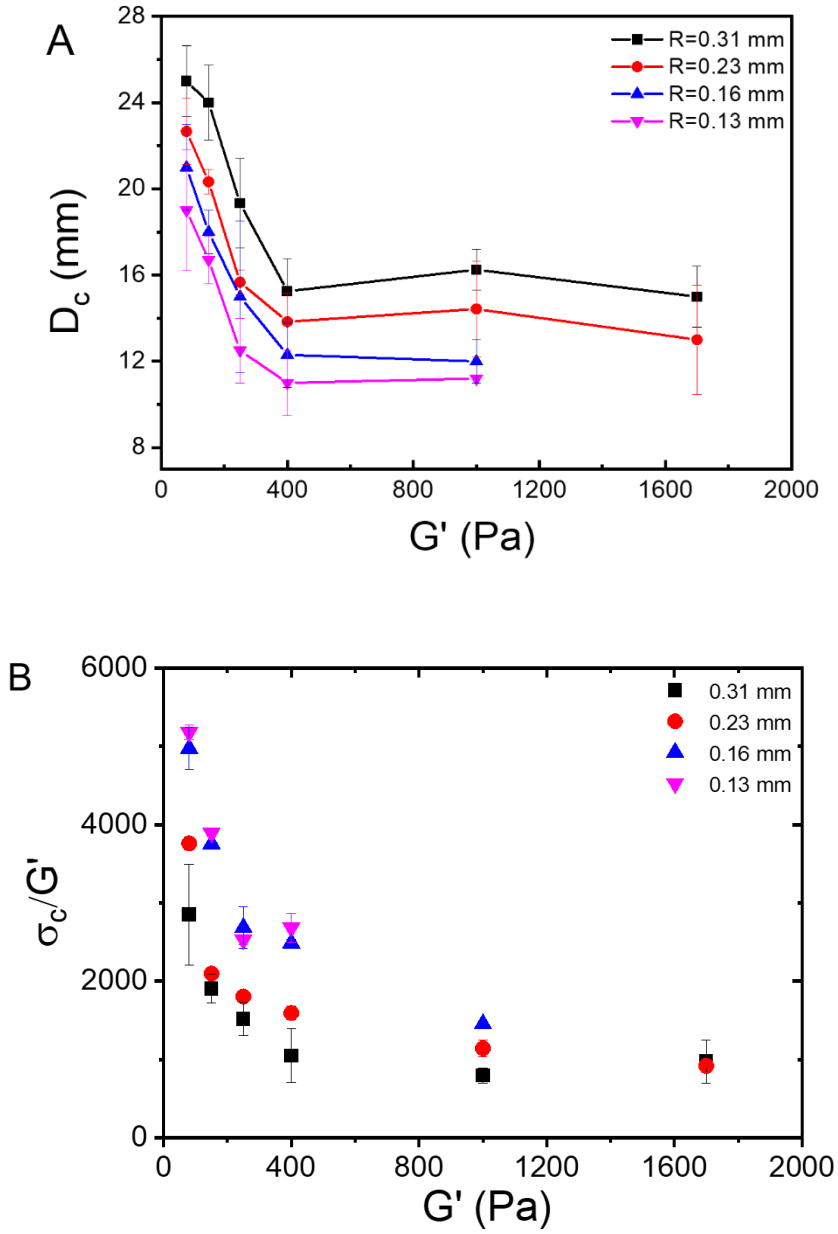

Figure 4.14. Fracture response of PVA99 hydrogel indented by different needle radii as a function of modulus. (A) Critical puncture displacement and (B) fracture resistance σ_c/G'.

4.3.3. Birefringence imaging – above needle tip fracture

To investigate the peculiar fracture behavior of the PVA99 hydrogel, local deformation of the gel during puncture process was investigated by birefringence imaging. **Figure 4.15** shows a series of birefringence images taken at different needle displacements. We confirmed that before indentation no birefringence is observed since the as-prepared hydrogel sample is in an amorphous state (**Figure 4.15**(i)). With the increase of the indentation depth, the birefringence light starts to appear along the indenter, due to the orientation of the polymer chains which are highly stretched in the direction of the indentation (**Figure 4.15** (ii)). At d = 22 mm, the light intensity is further enhanced with the increased displacement (**Figure 4.15** (iii)). When the indenter displacement reaches the critical fracture value (D_c = 24 mm, t = 96 s), the fracture and stress relaxation are expected to occur. However, from the birefringence light intensity (**Figure 4.15** (iv)), we observed the following unexpected results. At d = 24 mm, a zone with lower intensity suddenly appears several millimeters above the indenter tip as indicated by the red arrow. Below and above this low-intensity zone, two bright zones are visible: one at the needle tip is sharp, and the other above the needle tip is broad. While the former seems to follow the displacement of the needle tip, the latter seems to exhibit relaxation, it continues to move upwards (**Figure 4.15**(iv) at d = 26 mm), with a velocity in the order of 1 mm/s. Finally, a v-shaped birefringence pattern is left in the sample when removing the needle from the sample after the puncture process (**Figure 4.15** (vi)).

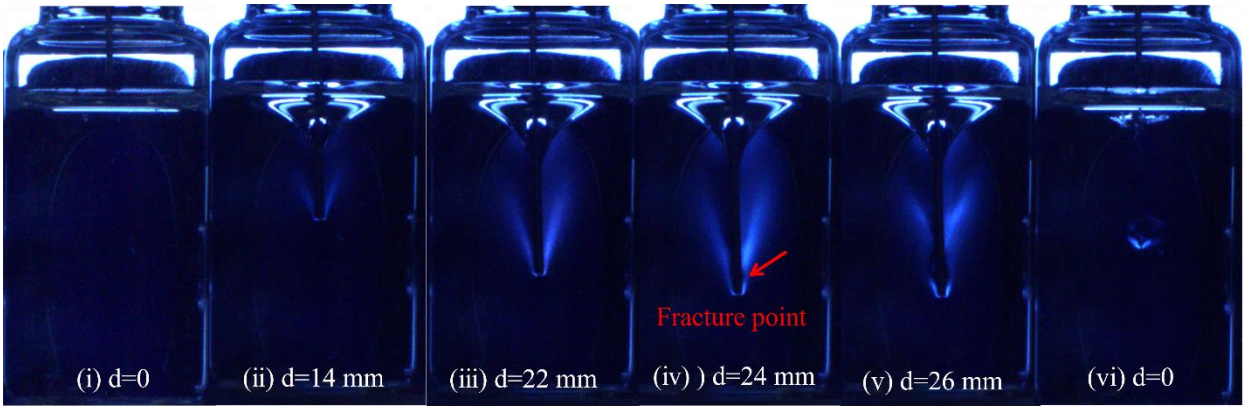

Figure 4.15. Birefringence images under various indentation displacement for PVA99 hydrogel (G' = 400 Pa, R = 0.31 mm) (i) d = 0; (ii) d = 14 mm; (iii) d = 22 mm (before fracture); (iv) d = 24 mm (fracture initiation); (v) d = 26 mm (after fracture); (vi) d = 0 (removal of the needle);

In order to quantitatively analyze the birefringence intensity, the line profile of the intensity along the needle is calculated and plotted in **Figure 4.16**. We extract three values of intensity: (1) at the sharp peak corresponding to the needle tip, I_t, (2) at the broad peak I_s, and (3) at the minimum between the two, I_m. At d = 14 mm (**Figure 4.16**(i)), only the intensity at the needle tip I_t is detectable due to the chain orientations. With increasing d, the intensity continues to increase spreading over a wider range of positions. At d = 22 mm (**Figure 4.16**(ii)), a second peak of the intensity is detected, thus these three characteristic values I_t, I_s, I_m can be well defined. At the fracture point (d = 24 mm, **Figure 4.16**(iii)), the distance between the two peaks increases, and the intensity at the minimum between the two quickly goes to the noise level, which presumably corresponds to the crack initiation in which the polymer chains are ruptured. Meanwhile, the fractured gel surface with an intensity of I_s rapidly moves backward, leaving a broad low-intensity region behind as shown in **Figure 4.15**(iv).

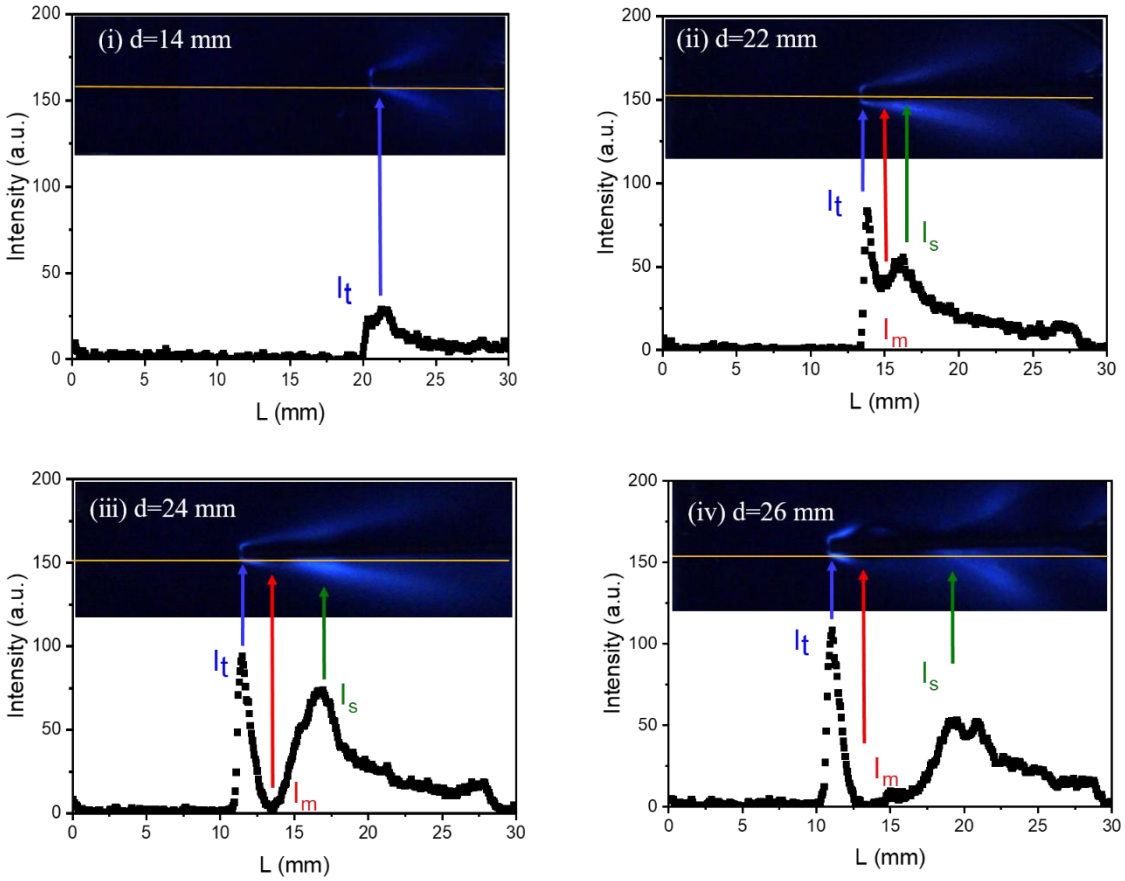

Figure 4.16. Birefringence intensity profile analysis along the needle at different indentation depths for PVA99 hydrogel (I_t: the intensity at needle tip; I_s: the intensity of fractured gel surface; I_m: the intensity of the crack).

The evolution of the values of the intensity from these three positions is shown in **Figure 4.17** as a function of displacement (or time). In the figure, the puncture force is also plotted for comparison. Before the macroscopic fracture from the loading curve, the intensity at the needle tip I_t follows the same trend of the force while I_s and I_m are both undetectable. At the fracture point where the peak of the force is observed, I_s and I_m can be identified and they rapidly decrease with time, approaching zero, however, I_t continues to increase. It is noteworthy that it does not go to zero even after the unloading process and needle pull-out, corresponding to the

anisotropic structure indicated as the "v-shaped" birefringence pattern remains (**Figure 4.15**(v)).

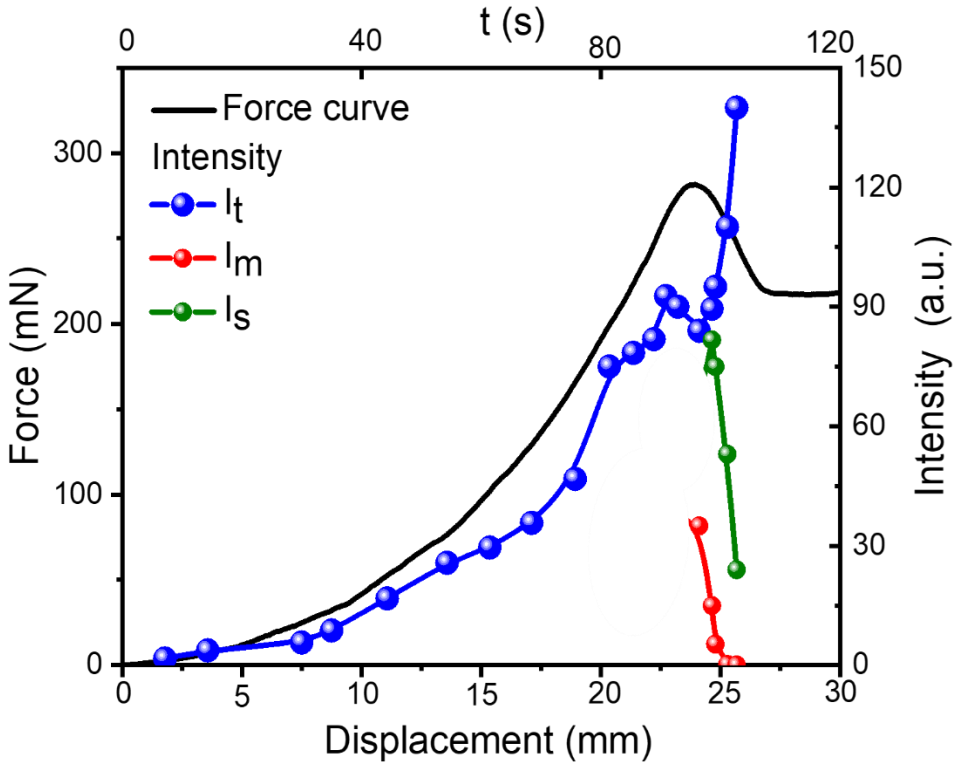

Figure 4.17. Puncture force and critical light intensity I_t, I_s, I_m for PVA99 hydrogel (analyzed from **Figure 4.16**) as a function of displacement/time.

It is counterintuitive that PVA99 hydrogel breaks above the needle tip rather than at the needle tip where stress is highly concentrated. This particular above-needle-tip fracture phenomenon in the PVA99 hydrogel is quite distinct from that typically found and reported in current literature. In most puncture and fracture mechanics analyses, the compressive region below the indenter and the shear region on the sides of the indenter is used to understand its deformation and fracture[35-36]. Barney et. al concluded that the initiation of failure of PDMS was from the compressed region below the tip with a strain mapping from DIC (digital imaging correlation) method[37].

We now compare the puncture behavior of the PVA88 hydrogel with DH of about 88 mol% (the sample used in Chapter 3) to PVA99 with DH ~ 99%. **Figure 4.18** shows a series of birefringence images for PVA88 hydrogel. With the increase in the displacement of the indenter, the birefringence intensity for PVA88 increases near the indenter, but when the fracture occurs at d = 16 mm, the birefringence immediately disappears and there is no sign of above needle tip fracture. Also, after the needle is pulled out, no permanent anisotropic zone is observed. This behavior should be typical for elastic soft solids; we found the same behavior as that for PDMS elastomer or polyacrylamide hydrogels (data not shown), indicating that the PVA99 hydrogel exhibits a particular behavior, mostly due to strain-induced crystallization.

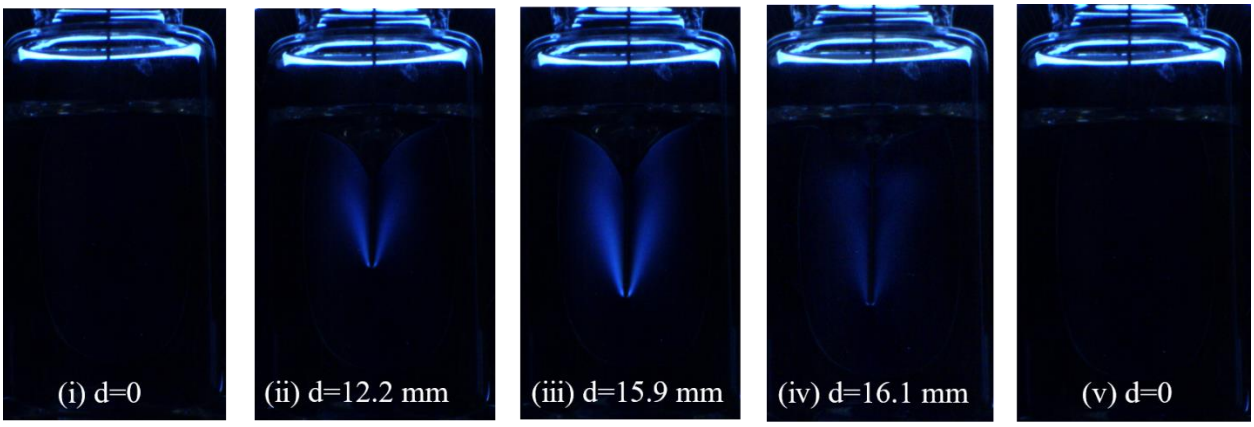

Figure 4.18. Birefringence images under various indentation displacement for PVA88 hydrogel (G' = 600 Pa, R = 0.23 mm). (i) d = 0; (ii) d = 12.2 mm; (iii) d = 15.9 mm; (iv) d = 16.1 mm; (v) d = 0 (needle removed from the sample). The value of D_c = 16 mm.

4.3.4. Origin of the permanent birefringence pattern

Since the above-needle-tip fracture phenomenon is always accompanied by the permanent birefringence pattern after needle pull-out, we investigate the origin of the anisotropic structure in this section. **Figure 4.19** shows the birefringence

morphology of PVA99 hydrogel with different moduli after needle removal. The permanent birefringence intensity is enhanced as the gel modulus increases due to the improved oriented polymer chain density. Interestingly, the v-shaped anisotropic zone is detected for a gel with modulus below 400 Pa while an x-shaped (or two v with inverse direction) anisotropic zone is observed for gels with a higher modulus. For the latter, by imaging the whole puncture process we found that whereas a regular v shape is formed during the loading process, an additional inversed v appears composing a symmetric x shape during the retraction process of the needle. This phenomenon may be attributed to the strong residual stress or stretch of the material below the needle when pulling out the needle from samples.

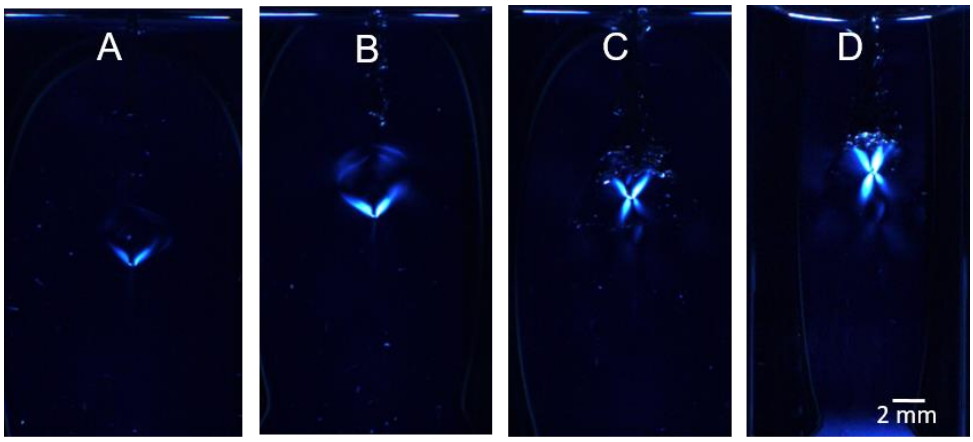

Figure 4.19. The birefringence morphology of PVA99 hydrogel with different moduli after needle removal (R = 0.23 mm). (A) G' = 250 Pa; (B) G' = 400 Pa; (C) G' = 900 Pa; (D) G' = 1700 Pa.

To understand the permanent birefringence pattern seen as the v or x-shaped anisotropic zone formed by the puncture loading process for PVA99 hydrogel, we performed the following characterizations. **Figure 4.20A** shows the morphology photo of the transparent gel after the puncture. The birefringence intensity is permanent at room temperature even after several months, while by heating it can disappear. The effect of temperature on the birefringence intensity is shown in

Figure 4.20B. Compared to the result at room temperature (25 °C), at 40 °C (maintained for 2 hours) the anisotropic zone remains almost the same size, while with further increase in temperature, its size and intensity decrease and it ultimately disappears upon heating to 90 °C for 2 hours. We found also that by the addition of urea (swell the as-prepared hydrogel in urea solution (c = 30 % wt) for one week and then performed the puncture test), the v-shaped birefringence pattern is invisible after puncture. These results strongly suggest that the anisotropic zone is formed by the hydrogen bonding association between the stretched PVA chains.

Figure 4.20C presents the birefringence pattern of the gel sheet after puncture under polarized microscopy, in which the intensity at the right needle tip is highly concentrated. The increase in the local PVA concentration is confirmed by staining the PVA99 hydrogel with Congo red. Congo red is known to form a complex with PVA by hydrogen bonding[38]. After the puncture process, we swell the gel in Congo red solution (**Figure 4.20D**). As indicated by the black arrow in the figure, the red color is more intense at the position of the needle tip, due to the higher PVA concentration in the anisotropic zone.

We hypothesize that this localized anisotropic zone is due to the strain-induced crystallization, or highly stretched PVA chains associated with hydrogen bonding. In fact, as shown in the introduction of this chapter, PVA with a high degree of hydrolysis is known as a semi-crystalline polymer, and even though water is a good solvent for PVA, hydrogen bonding between hydroxyl groups on PVA chains can lead to the formation of microcrystalline domains in aqueous solutions and hydrogels. The crystallization of PVA can melt, and thus the permanent birefringence pattern disappears when heating the sample at a temperature above 60 °C, which is in good agreement with the previous study that the hydrogen bonding was found to dissociate when heating up to 60 °C.[3]

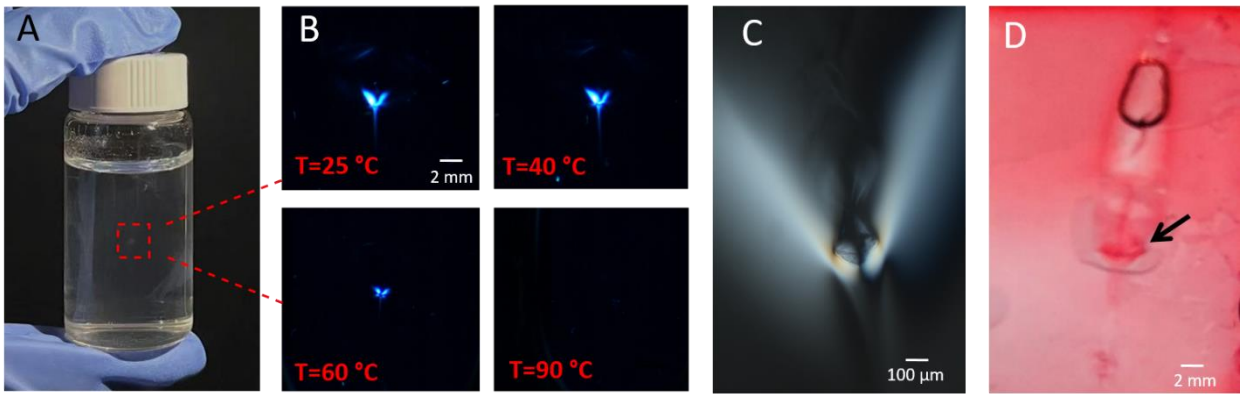

Figure 4.20. (A) The morphology of PVA99 hydrogel (G' = 400 Pa) after needle removal. (B) Birefringence pattern of sample under birefringence at different temperatures, T = 25, 40, 60, and 90 °C. (C) Polarized microscopy photo of gel sheet after puncture. (D) The same sample in (C) swelling in Congo red solution. The black arrow indicates the concentrated red color that signifies the improved polymer concentration and hydrogen bonding associations.

4.3.5. Effects of modulus, indenter size, and temperature on crack initiation

The crack initiates at a zone several millimeters above the needle tip, instead of at the needle tip where stress is highly concentrated. Based on the intensity profile analysis, the exact distance from the needle tip to the crack initiation position ΔL for gels with different moduli is shown in **Figure 4.21A**. ΔL is larger for softer gels. Specifically, $\Delta L \sim 4$ mm for a gel with G' = 80 Pa, and $\Delta L \sim 1$ mm for a gel with G' > 900 Pa. ΔL is independent of the needle size(**Figure 4.21B**). In our puncture tests, the critical displacement D_c where the fracture occurs is large, compared to the radius of the indenter (as discussed above). The larger mesh size of the gel with a smaller modulus enables larger chain (extensibility) deformation, in which the entropy of the polymer chain decreases, and thus facilitates the formation of the crystallization due to its lower energy barrier. Consequently, we observed a larger distance of needle tip to crack position ΔL, signifying a larger volume of crystallite domains serving as additional reinforcement around the needle tip, for softer gel having larger

chain extensibility. The large deformation and increased polymer concentration at the needle tip facilitate the formation of strain-induced crystals before fracture.

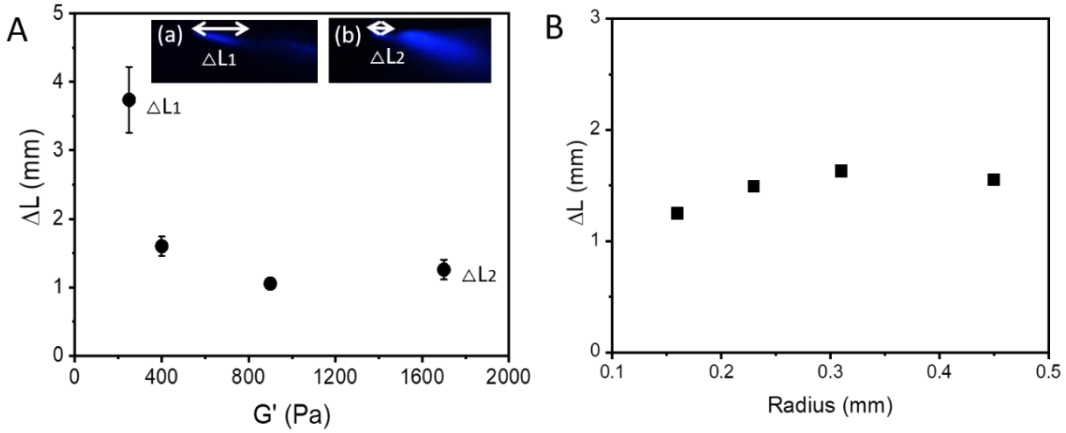

Figure 4.21. (A) The distance of needle tip to crack, Δ*L*, as a function of gel modulus. (B) Δ*L* as a function of needle radius (*G′*=400 Pa).

Then, we performed the puncture test for PVA99 hydrogel with G' = 400 Pa at different temperatures. In **Figure 4.22A**, we observed an obvious softening effect of temperature on its mechanical property. With the increase of temperature, the critical puncture force F_c decreases, and the D_c roughly increases. This phenomenon is in good agreement with what has been reported in natural rubber, where a softening effect was observed attributed to the melting of the strain-induced crystallization[26]. Also, it was reported that for SIC in natural rubber the stress at higher temperatures is lower than that at a lower temperature in the stress-strain relations[26]. Interestingly, Δ*L* decreases from ~2 mm until zero (fracture in the needle tip) with the temperature ranging from 25 °C to 70 °C (**Figure 4.22B**). Meanwhile, the v-shaped birefringence pattern is less visible at high temperatures after puncture. This result indicates that the high temperature could prevent the above-needle-tip fracture behavior and the formation of the anisotropic structure during puncture. Akin to natural rubber, the SIC in PVA hydrogel shows a strong temperature dependence: the increase in

temperature reduces the crystallinity so that the networks at the needle tip can be ruptured without additional reinforcement in that case as indicated by **Figure 4.22B**.

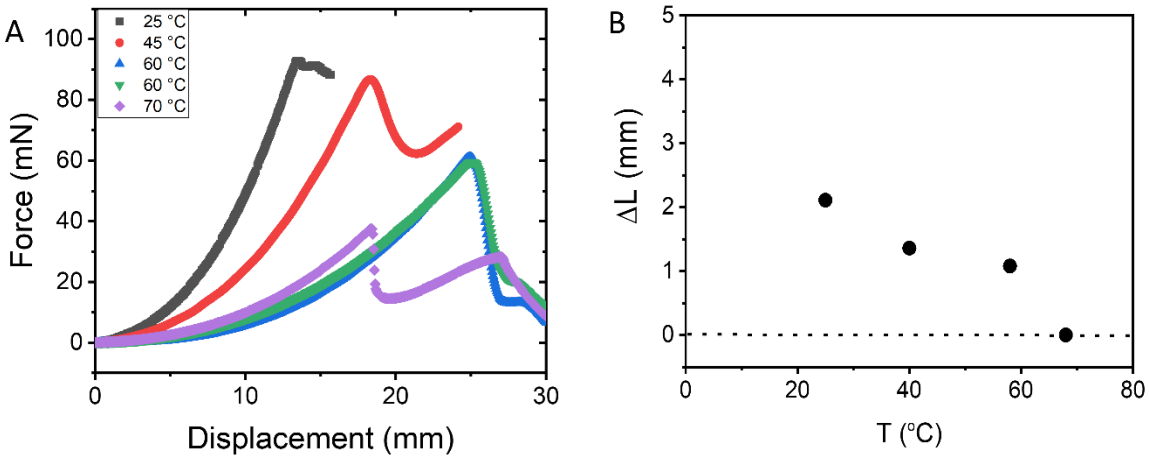

Figure 4.22. (A) The loading curve of PVA99 hydrogel at different temperatures. (B) The distance of needle tip to crack, ΔL, as a function of temperature. G' = 400 Pa, R = 0.23 mm.

4.3.6. Cyclic loading test and Mullin's effect

To investigate the effect of the strain on the occurrence of the anisotropic structure, we performed cyclic puncture testing on PVA99 hydrogels to a sequence of maximum displacements and test the structure evolution during the puncture process. The applied cyclic loading profile is shown in **Figure 4.24**. The maximal displacement D_m of the cycle is increased stepwise and at each maximal displacement, two cycles are applied to evaluate the effects of eventually irreversible damage. At the maximal displacement of 5 mm (**Figure 4.24A**), the loading and unloading curves for the two cycles superpose well, indicating elastic behavior without damage. When the maximal displacement is above 10 mm (**Figure 4.24B, C,** and **D**), a small hysteresis is observed during the first cycle. With the increase of the applied maximum displacement, the hysteresis behavior is progressively

pronounced. The fracture occurs when D_m = 19 mm and a large hysteresis loop is observed (**Figure 4.24E**). Before fracture, the second loading curve does not follow that of the precedent cycle, but rather follows the unloading curve of it. This lower resulting stress for the same applied displacement, or stress-softening, appearing after the first load, is known as Mullin's effect and has been intensively studied for various rubber materials[39] and hydrogels[40]. Generally, Mullin's effect would cause the stress softening in material and various physical interpretations are proposed to account for this phenomenon involving microstructural ruptures and changes (such as physical /chemical bond rupture[41], chain scission[42], molecular slipping[43,] and disentanglement[44]). For PVA99 hydrogel, the unrecoverable hydrogen bonding rupture and reconstitution exist during the first cyclic loading that results in the softening for the second cycle with the same applied maximum displacement before fracture.

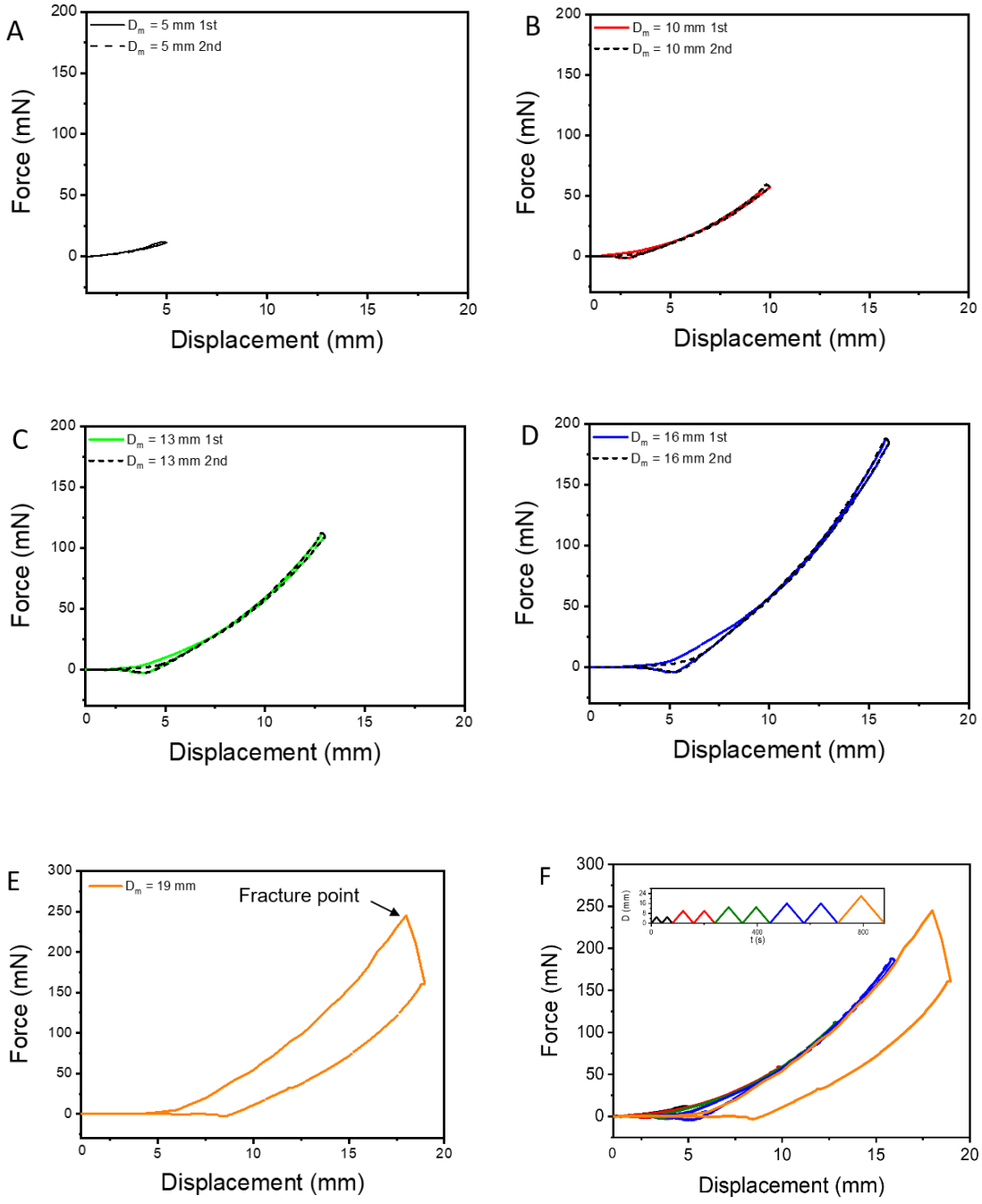

Figure 4.23. Cyclic loading and unloading test of puncture process for PVA99 hydrogel with G' = 400 Pa and R = 0.23 mm at different applied maximum displacement D_m. (A) D_m = 5 mm; (B) D_m = 10 mm; (C) D_m = 13 mm; (D) D_m = 16 mm; (E) D_m = 19 mm; (F) Summary of the cyclic loading-unloading curve. The inset figure indicates the experimental cyclic loading-unloading process.

To figure out the hysteresis behavior in PVA88 hydrogel, we compare the pictures of birefringence intensity after needle pullout at different applied puncture displacements (**Figure 4.24A).** The v-shaped birefringence pattern starts to be visible when the applied displacement is above 10 mm and the signal intensity increases with the applied displacement. The difference in the intensity between the two cycles at the same maximal displacement is minor. The intensity of this permanent birefringence pattern was plotted as a function of the corresponding hysteresis in **Figure 4.24B**, where it scales perfectly with the mechanical hysteresis in a slope of 0.5. Rault et.al. proposed that the mechanical hysteresis resulted only from chain crystallization in vulcanized natural rubber by measuring the crystallinity during cyclic uniaxial tension loading conditions[19, 45]. The interactions between particle fillers and polymer were thought to be the reason for the pronounced first cycle hysteresis which is responsible for the toughening effect in filled rubbers [46]. More similarly, a large hysteresis loop has been observed in slide-ring gel, which was attributed to the recombination of the noncovalent crosslinks in a polymer network on deformation, while the chemical gel shows no hysteresis loop with stable covalent cross-links (no recombination) on deformation[47]. We speculate that in PVA99 hydrogel, the stretched chains under large deformation can associate (crystallize) to form an anisotropic zone which prevents elastic recovery of the chain deformation.

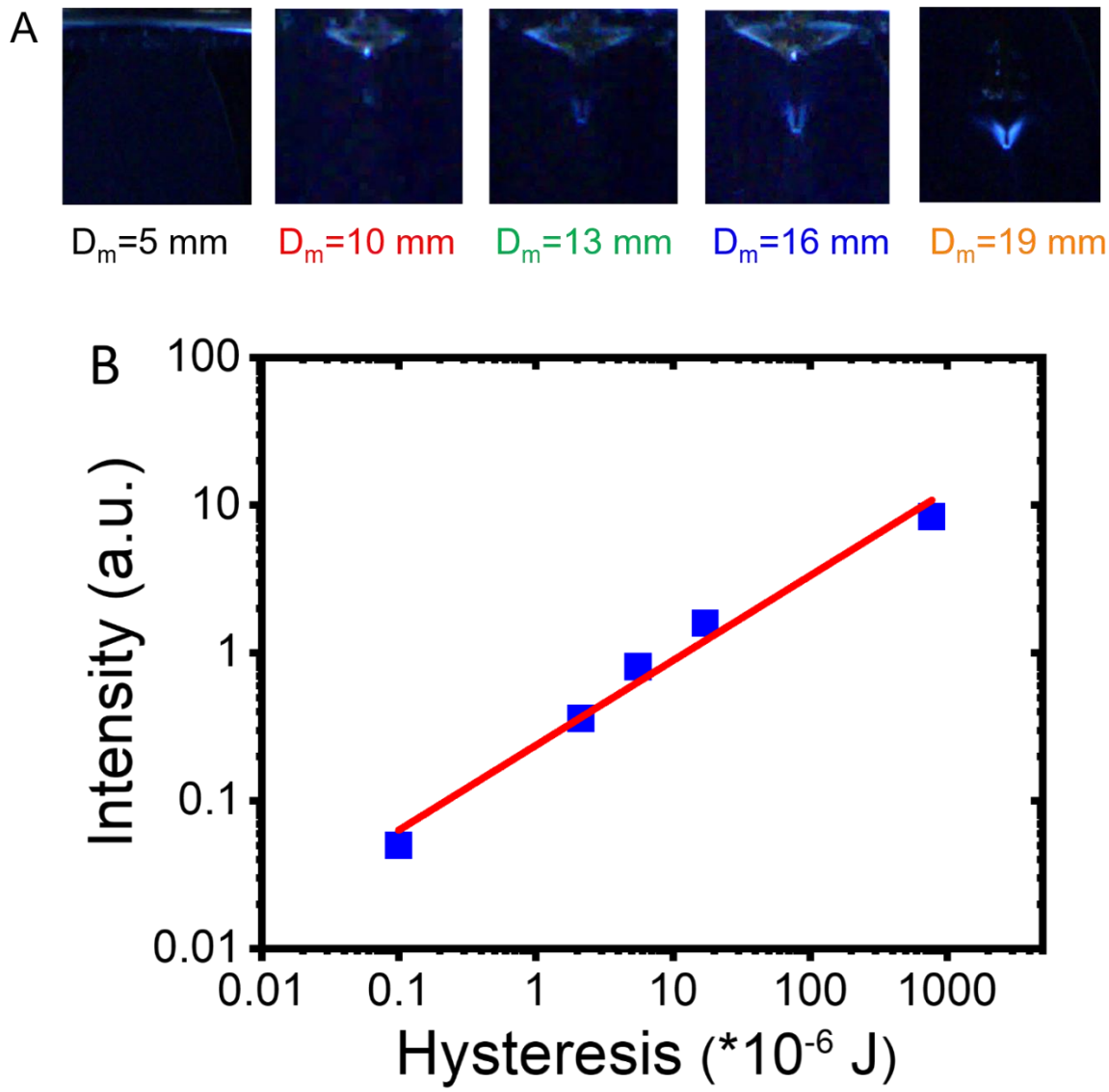

Figure 4.24. (A) Birefringence morphology after pulling out the needle at various applied displacements for PVA99 hydrogel with G' = 400 Pa. (B) The birefringence intensity as a function of hysteresis area from the loading-unloading curve.

4.3.7. Above-needle-tip fracture mechanism

Here we propose an interpretation for the displaced crack initiation mechanism in the PVA99 hydrogel (**Figure 4.25**). Before indentation (**Figure 4.25** (i)), the hydrogel is un-deformed and the chains in the network are not stretched. Under puncture, the indenter needle deforms the chains: they are compressed under the

indenter and sheared along the needle length. Under large puncture deformation (**Figure 4.25** (ii)), the strong association between the stretched chains is formed, and the modulus locally increases, preventing crack initiation at the tip of the needle. Above the needle tip (**Figure 4.25** (iii)), there should be a limit between the crystalline zone and the amorphous zone above the needle tip, and in this limit, the stress concentration occurs, and a crack initiates. The crystalline zone remains after fracture and after needle pullout, leading to the permanent birefringence intensity. This displaced crack initiation is in analogy with the side-way crack propagation observed in natural rubber exhibiting strain-induced crystallization[28-29]. In pure shear tests of natural rubber, in an opened crack, a secondary crack tends to propagate in the direction parallel (side-way) to the stretching direction rather than the perpendicular direction, due to crystallites formed at the crack tip[28]. In the PVA hydrogel with the high degree of hydrolysis studied in this work, the loosely cross-linked polymer network has higher chain extensibility in which the chain entropy is reduced under large deformation, lowering the energy barrier for the formation of microcrystals. Moreover, with the puncture geometry, the polymer network around the needle tip is highly compressed in a confined condition. The locally increased polymer concentration may facilitate the dense association of neighboring chains through hydrogen bonding, further improving the possibility of occurrence of crystallization. While the networks near the needle tip are locally reinforced, thus, the crack takes place from the weakest position of the sample, where it is the boundary layer of the crystalline domain and amorphous domain in PVA hydrogel. With the reinforcement of the SIC, softer hydrogels show a remarkable increase in fracture resistance relative to the stiffer gels (see **Figure 4.14**).

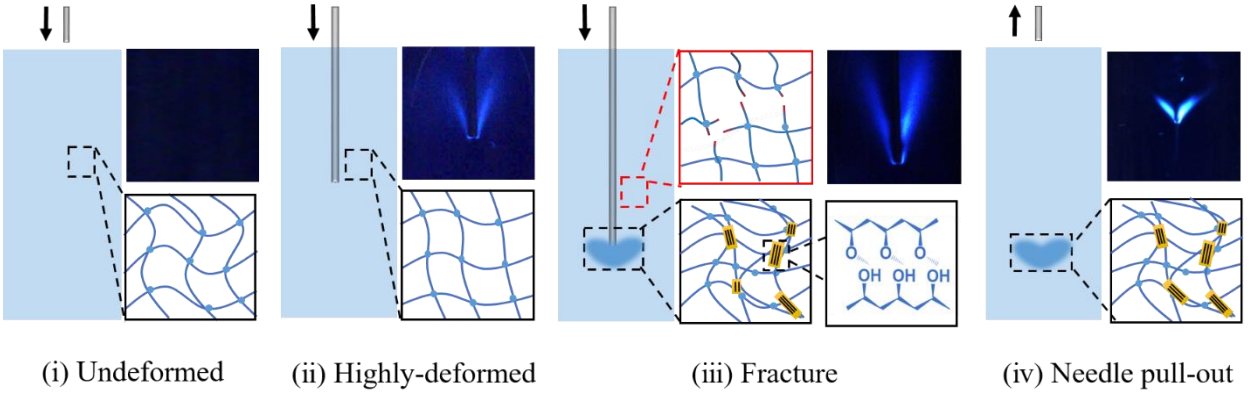

Figure 4.25. Schematic illustration of PVA99 hydrogel structural evolution at different deformed states around needle tip. (i) un-deformed state, (ii) highly deformed state, (iii) fracture at above needle tip, and (iv) needle pullout. Hydrogen bonding association provides additional physical crosslinking which locally reinforced the network as indicated in the blue shadow.

4.4. Conclusions

PVA hydrogel with a high hydrolysis degree (DH = 99%) was chemically crosslinked by varying crosslinker GA concentration 4 – 6.5 mM, which results in an adjustable modulus range of 100 – 2000 Pa. By LAOS experiment, the significant strain hardening behavior was observed for PVA gel system and the exact strain hardening index S was found to increase with the decrease in gel modulus at large strain regime. With puncture test, the critical strain (the ratio of fracture displacement to needle size D_c/R) could reach 5,000 – 10,000%. Consequently, the fracture resistance σ_c/G' for softer gels was improved relative to the stiffer ones, where the critical nominal stress could surpass modulus by 3-4 orders of magnitude. By combining real-time birefringence imaging, we found the failure initiates above the needle tip for several millimeters, rather than needle tip where stress should be highly concentrated. Interestingly, there is always a permanent birefringence pattern remaining after removing the needle from hydrogel, which could be disappeared

when heating to temperature T > 60 ℃. By playing with temperature, we found the distance between needle tip and the position of crack initiation decreases until to zero (needle-tip fracture) when scanning t from 25 to 80 ℃. Also, permanent birefringence was found possible as long as a large indentation depth is reached even before fracture. Considering the high hydrolysis degree of PVA, i.e., high density of –OH groups in the polymer chains, and the above experimental facts, we assume that a strain-induced crystallization (SIC) zone occurs around the needle tip during the indentation process mainly attributed to the hydrogen bonding associations. On the one hand, the SIC displaces the crack initiation point from the needle tip to the edge as the network around the needle tip was physically reinforced by the crystals. On the other hand, the loosely crosslinked sample demonstrates higher fracture resistance compared to the densely crosslinked one, contributing to its high deformability and the resultant larger area of crystalline domain. In our work, the novel strain-induced crystallization phenomenon in highly hydrolyzed PVA hydrogel and resultant above-needle-tip fracture behavior provides insight to understand the improved fracture resistance in associative polymers.

4.5. References

1. Xie, X.; Wittmar, M.; Kissel, T., A Two-Dimensional NMR Study of Poly (vinyl (dialkylamino) alkylcarbamate-co-vinyl acetate-co-vinyl alcohol). *Macromolecules* **2004,** *37* (12), 4598-4606.
2. Briscoe, B.; Luckham, P.; Zhu, S., The effects of hydrogen bonding upon the viscosity of aqueous poly (vinyl alcohol) solutions. *Polymer* **2000,** *41* (10), 3851-3860.
3. Ilyin, S. O.; Malkin, A. Y.; Kulichikhin, V. G.; Denisova, Y. I.; Krentsel, L. B.; Shandryuk, G. A.; Litmanovich, A. D.; Litmanovich, E. A.; Bondarenko, G. N.; Kudryavtsev, Y. V., Effect of chain structure on the rheological properties of vinyl acetate–vinyl alcohol copolymers in solution and bulk. *Macromolecules* **2014,** *47* (14), 4790-4804.
4. Liu, C.; Yu, X.; Li, Y.; Zhao, X.; Chen, Q.; Han, Y., Flow-induced crystalline precursors in entangled Poly (vinyl alcohol) aqueous solutions. *Polymer* **2021,** *229*, 123960.
5. Isasi, J. R.; Cesteros, L. C.; Katime, I., Hydrogen bonding and sequence distribution in poly (vinyl acetate-co-vinyl alcohol) copolymers. *Macromolecules* **1994,** *27* (8), 2200-2205.
6. Holloway, J. L.; Lowman, A. M.; Palmese, G. R., The role of crystallization and phase separation in the formation of physically cross-linked PVA hydrogels. *Soft Matter* **2013,** *9* (3), 826-833.
7. Joshi, N.; Suman, K.; Joshi, Y. M., Rheological behavior of aqueous poly (vinyl alcohol) solution during a freeze–thaw gelation process. *Macromolecules* **2020,** *53* (9), 3452-3463.
8. Joshi, N.; Suman, K.; Joshi, Y. M. J. M., Rheological behavior of aqueous poly (vinyl alcohol) solution during a freeze–thaw gelation process. **2020,** *53* (9), 3452-3463.
9. Peppas, N. A., Turbidimetric studies of aqueous poly (vinyl alcohol) solutions. *Die Makromolekulare Chemie: Macromolecular Chemistry Physics* **1975,** *176* (11), 3433-3440.
10. Hassan, C. M.; Peppas, N. A., Structure and morphology of freeze/thawed PVA hydrogels. *Macromolecules* **2000,** *33* (7), 2472-2479.
11. Auriemma, F.; De Rosa, C.; Triolo, R., Slow crystallization kinetics of poly (vinyl alcohol) in confined environment during cryotropic gelation of aqueous solutions. *Macromolecules* **2006,** *39* (26), 9429-9434.
12. Willcox, P. J.; Howie Jr, D. W.; Schmidt‐Rohr, K.; Hoagland, D. A.; Gido, S. P.; Pudjijanto, S.; Kleiner, L. W.; Venkatraman, S., Microstructure of poly (vinyl alcohol) hydrogels produced by freeze/thaw cycling. *Journal of Polymer Science Part B: Polymer Physics* **1999,** *37* (24), 3438-3454.
13. Ricciardi, R.; Auriemma, F.; Gaillet, C.; De Rosa, C.; Lauprêtre, F., Investigation of the crystallinity of freeze/thaw poly (vinyl alcohol) hydrogels by different techniques. *Macromolecules* **2004,** *37* (25), 9510-9516.
14. Peppas, N. A.; Merrill, E. W., Development of semicrystalline poly (vinyl alcohol) hydrogels for biomedical applications. *Journal of biomedical materials research* **1977,** *11* (3), 423-434.
15. Lin, S.; Liu, X.; Liu, J.; Yuk, H.; Loh, H.-C.; Parada, G. A.; Settens, C.; Song, J.; Masic, A.; McKinley, G. H., Anti-fatigue-fracture hydrogels. *Science advances* **2019,** *5* (1), eaau8528.
16. Münster, S.; Jawerth, L. M.; Leslie, B. A.; Weitz, J. I.; Fabry, B.; Weitz, D. A., Strain history dependence of the nonlinear stress response of fibrin and collagen networks. *Proceedings of the National Academy of Sciences* **2013,** *110* (30), 12197-12202.

17. Du, N.; Yang, Z.; Liu, X. Y.; Li, Y.; Xu, H. Y., Structural origin of the strain-hardening of spider silk. *Advanced Functional Materials* **2011,** *21* (4), 772-778.
18. Candau, N.; Laghmach, R.; Chazeau, L.; Chenal, J.-M.; Gauthier, C.; Biben, T.; Munch, E., Strain-induced crystallization of natural rubber and cross-link densities heterogeneities. *Macromolecules* **2014,** *47* (16), 5815-5824.
19. Trabelsi, S.; Albouy, P.-A.; Rault, J., Crystallization and melting processes in vulcanized stretched natural rubber. *Macromolecules* **2003,** *36* (20), 7624-7639.
20. Zhang, H.; Niemczura, J.; Dennis, G.; Ravi-Chandar, K.; Marder, M., Toughening effect of strain-induced crystallites in natural rubber. *Physical review letters* **2009,** *102* (24), 245503.
21. Flory, P. J., Thermodynamics of crystallization in high polymers. I. Crystallization induced by stretching. *The Journal of Chemical Physics* **1947,** *15* (6), 397-408.
22. Demassieux, Q.; Berghezan, D.; Cantournet, S.; Proudhon, H.; Creton, C., Temperature and aging dependence of strain-induced crystallization and cavitation in highly crosslinked and filled natural rubber. *Journal of Polymer Science Part B: Polymer Physics* **2019,** *57* (12), 780-793.
23. Huneau, B., Strain-induced crystallization of natural rubber: a review of X-ray diffraction investigations. *Rubber chemistry and technology* **2011,** *84* (3), 425-452.
24. Toki, S.; Sics, I.; Ran, S.; Liu, L.; Hsiao, B. S., Molecular orientation and structural development in vulcanized polyisoprene rubbers during uniaxial deformation by in situ synchrotron X-ray diffraction. *Polymer* **2003,** *44* (19), 6003-6011.
25. Tosaka, M.; Murakami, S.; Poompradub, S.; Kohjiya, S.; Ikeda, Y.; Toki, S.; Sics, I.; Hsiao, B. S., Orientation and crystallization of natural rubber network as revealed by WAXD using synchrotron radiation. *Macromolecules* **2004,** *37* (9), 3299-3309.
26. Toki, S.; Che, J.; Rong, L.; Hsiao, B. S.; Amnuaypornsri, S.; Nimpaiboon, A.; Sakdapipanich, J., Entanglements and networks to strain-induced crystallization and stress–strain relations in natural rubber and synthetic polyisoprene at various temperatures. *Macromolecules* **2013,** *46* (13), 5238-5248.
27. Toki, S.; Sics, I.; Ran, S.; Liu, L.; Hsiao, B. S.; Murakami, S.; Senoo, K.; Kohjiya, S., New insights into structural development in natural rubber during uniaxial deformation by in situ synchrotron X-ray diffraction. *Macromolecules* **2002,** *35* (17), 6578-6584.
28. Lee, S.; Pharr, M., Sideways and stable crack propagation in a silicone elastomer. *Proceedings of the National Academy of Sciences* **2019,** *116* (19), 9251-9256.
29. Marano, C.; Calabrò, R.; Rink, M., Effect of molecular orientation on the fracture behavior of carbon black-filled natural rubber compounds. *Journal of Polymer Science Part B: Polymer Physics* **2010,** *48* (13), 1509-1515.
30. Liu, C.; Morimoto, N.; Jiang, L.; Kawahara, S.; Noritomi, T.; Yokoyama, H.; Mayumi, K.; Ito, K., Tough hydrogels with rapid self-reinforcement. *Science* **2021,** *372* (6546), 1078-1081.
31. Xu, X.; Jagota, A.; Peng, S.; Luo, D.; Wu, M.; Hui, C.-Y., Gravity and surface tension effects on the shape change of soft materials. *Langmuir* **2013,** *29* (27), 8665-8674.
32. Ewoldt, R. H.; Hosoi, A.; McKinley, G. H., New measures for characterizing nonlinear viscoelasticity in large amplitude oscillatory shear. *Journal of Rheology* **2008,** *52* (6), 1427-1458.
33. Kurniawan, N. A.; Wong, L. H.; Rajagopalan, R., Early stiffening and softening of collagen: interplay of deformation mechanisms in biopolymer networks. *Biomacromolecules* **2012,** *13* (3), 691-698.
34. Fakhouri, S.; Hutchens, S. B.; Crosby, A. J., Puncture mechanics of soft solids. *Soft Matter* **2015,** *11* (23), 4723-4730.

35. Barney, C. W.; Zheng, Y.; Wu, S.; Cai, S.; Crosby, A. J., Residual strain effects in needle-induced cavitation. *Soft Matter* **2019,** *15* (37), 7390-7397.
36. Fakhouri, S. M. Cavitation and Puncture for Mechanical Measurement of Soft Solids. University of Massachusetts Amherst, 2015.
37. Barney, C. W.; Chen, C.; Crosby, A. J., Deep indentation and puncture of a rigid cylinder inserted into a soft solid. *Soft Matter* **2021,** *17* (22), 5574-5580.
38. Schütz, A. K.; Soragni, A.; Hornemann, S.; Aguzzi, A.; Ernst, M.; Böckmann, A.; Meier, B. H., The amyloid–Congo red interface at atomic resolution. *Angewandte Chemie International Edition* **2011,** *50* (26), 5956-5960.
39. Diani, J.; Fayolle, B.; Gilormini, P., A review on the Mullins effect. *European Polymer Journal* **2009,** *45* (3), 601-612.
40. Webber, R. E.; Creton, C.; Brown, H. R.; Gong, J. P., Large strain hysteresis and mullins effect of tough double-network hydrogels. *Macromolecules* **2007,** *40* (8), 2919-2927.
41. Blanchard, A.; Parkinson, D., Breakage of carbon-rubber networks by applied stress. *Rubber Chemistry Technology* **1952,** *25* (4), 808-842.
42. Suzuki, N.; Ito, M.; Yatsuyanagi, F., Effects of rubber/filler interactions on deformation behavior of silica filled SBR systems. *Polymer* **2005,** *46* (1), 193-201.
43. Houwink, R., Slipping of molecules during the deformation of reinforced rubber. *Rubber Chemistry Technology* **1956,** *29* (3), 888-893.
44. Hanson, D. E.; Hawley, M.; Houlton, R.; Chitanvis, K.; Rae, P.; Orler, E. B.; Wrobleski, D. A., Stress softening experiments in silica-filled polydimethylsiloxane provide insight into a mechanism for the Mullins effect. *Polymer* **2005,** *46* (24), 10989-10995.
45. Toki, S.; Fujimaki, T.; Okuyama, M., Strain-induced crystallization of natural rubber as detected real-time by wide-angle X-ray diffraction technique. *Polymer* **2000,** *41* (14), 5423-5429.
46. Heinrich, G.; Klüppel, M.; Vilgis, T. A., Reinforcement of elastomers. *Current opinion in solid state and materials science* **2002,** *6* (3), 195-203.
47. Ito, K., Novel cross-linking concept of polymer network: synthesis, structure, and properties of slide-ring gels with freely movable junctions. *Polymer journal* **2007,** *39* (6), 489-499.

5. Chapter 5: Enhancing puncture resistance by increasing molecular weight and involving surface-active agent

5.1. Introduction

In the previous chapter, we have shown that the PVA hydrogel with 99% hydrolysis degree presents unexpected strain-induced crystallization behavior upon deep indentation, whereas that made of the PVA with a lower hydrolysis degree (DH = 88%) shows no crystallization. Association between PVA chains via hydrogen bonding plays a great role in crystallization behavior and mechanical properties. Besides the hydrolysis degree, the molecular weight, which is linked to the entanglement of the polymer chain, may also contribute to the network association and thus affect its mechanical response. In addition, the surface state of the sample and the indenter was reported to largely affect its fracture behavior as the puncture is a very localized and surface energy/friction-related process[1].

In this Chapter, we compare PVA hydrogel with different hydrolysis degrees and molecular weights to reveal the structure-property relation - distinct mechanical properties and fracture response. The surface tension of PVA hydrogel was also varied by adding surfactant to investigate the role of surface tension in its fracture resistance.

5.2. Experimental section

5.2.1. Material

PVA99 (degree of hydrolysis 99 %) with molecular weight M_w = 89,000 g/mol and M_w = 130,000 g/mol; PVA88 (degree of hydrolysis 88 %) molecular weight M_w = 67,000 g/mol and M_w = 150,000 g/mol, were purchased from Sigma-Aldrich. Surfactant Pentadecafluorooctanoic acid, PFOA, was purchased from Tokyo Chemical Industry (TCI).

5.2.2. Gel preparation

PVA stock solution in a concentration of 8.8 wt% (or 2 M for repeating unit) was prepared by dissolving the PVA powder in deionized water at 90 °C and stirring vigorously over four hours. Chemically cross-linked PVA hydrogel was prepared by mixing PVA stock solution (adjusted to 6.6 wt%, 1.5 M) and cross-linker GA with various concentrations in the presence of HCl (0.05 mM). To tune the surface tension of the PVA, the surfactant PFOA at a concentration of 0.25 g/L was added to the above-mentioned gel mixture solution. We waited at least for 12 h to finish gelation before measurements.

5.2.3. Methods

Puncture and rheology test was performed in the same manner as presented in the previous chapter.

5.3. Results and discussion

5.3.1. Elasticity

We compare the mechanical properties of hydrogels made of four PVA of different hydrolysis degrees (DH) and molecular weights (M_w):

- PVA88 (DH = 88%) with M_w = 67,000 and 130,000 g/mol,

- PVA99 (DH = 99%) with M_w = 89,000 and 150,000 g/mol.

PVA chemical gels of these PVA were prepared at a constant PVA concentration (6.6 wt%, or 1.5 M of the monomer units) with varied chemical crosslinker (glutaraldehyde, GA) concentrations, and by shear rheology measurements, we obtained the elastic plateau modulus. In **Figure 5.1**, the elastic modulus was plotted as a function of GA concentration. We found that the plateau modulus increases with the GA concentration for all the samples as expected, while we see strong effects of the molecular weight and hydrolysis degree. For both PVA99 and PVA88, the sample with the higher molecular weight exhibits higher elastic modulus compared to the sample with the lower molecular weight at the same crosslinker concentration. For the effect of DH, although the values of the molecular weight are different for the two values of DH, one can see that PVA99 with the higher DH has higher modulus than PVA88.

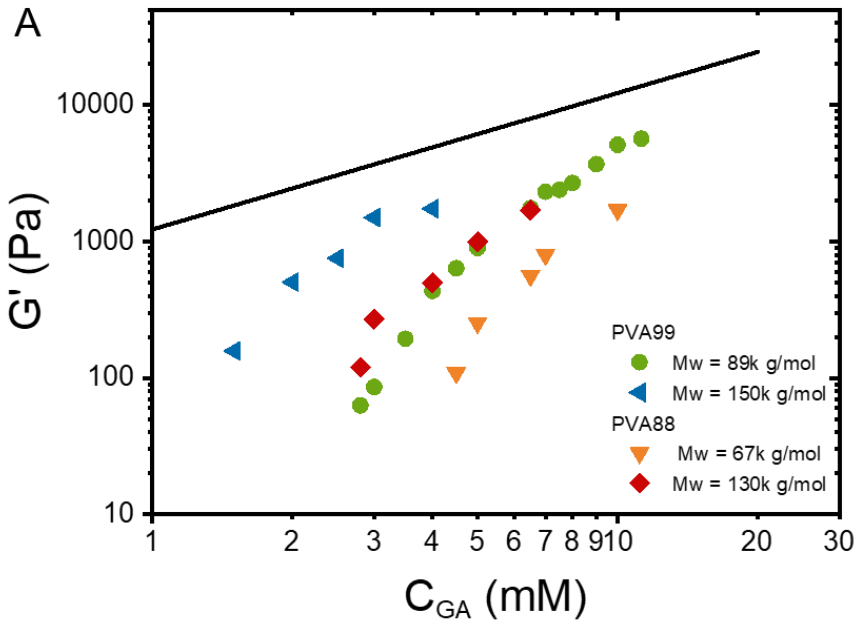
A
10000
1000
100
10
G' (Pa)
1
2
3
4
5
6
7
8
9
10
20
30
C_{GA} (mM)
PVA99
Mw = 89k g/mol
Mw = 150k g/mol
PVA88
Mw = 67k g/mol
Mw = 130k g/mol

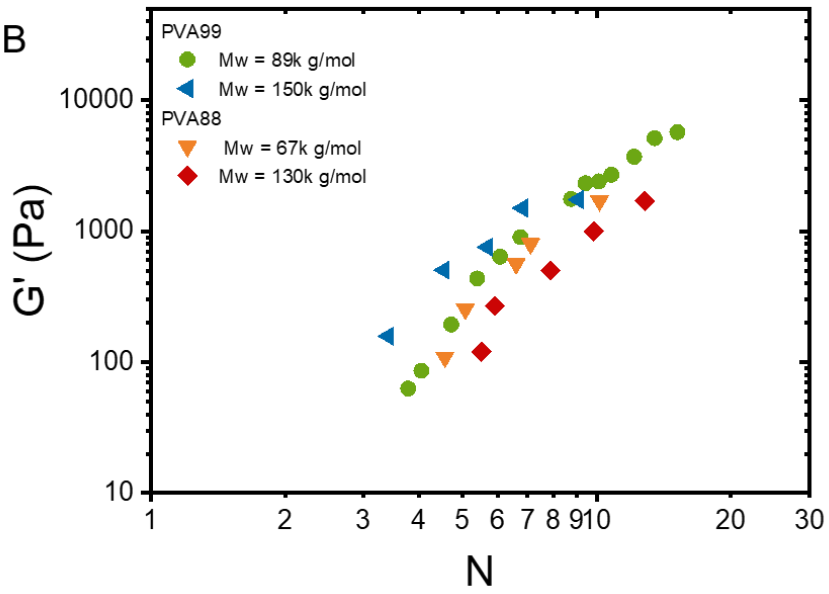
B
PVA99
Mw = 89k g/mol
Mw = 150k g/mol
PVA88
Mw = 67k g/mol
Mw = 130k g/mol
10000
1000
100
10
G' (Pa)
1
2
3
4
5
6
7
8
9
10
20
30
N

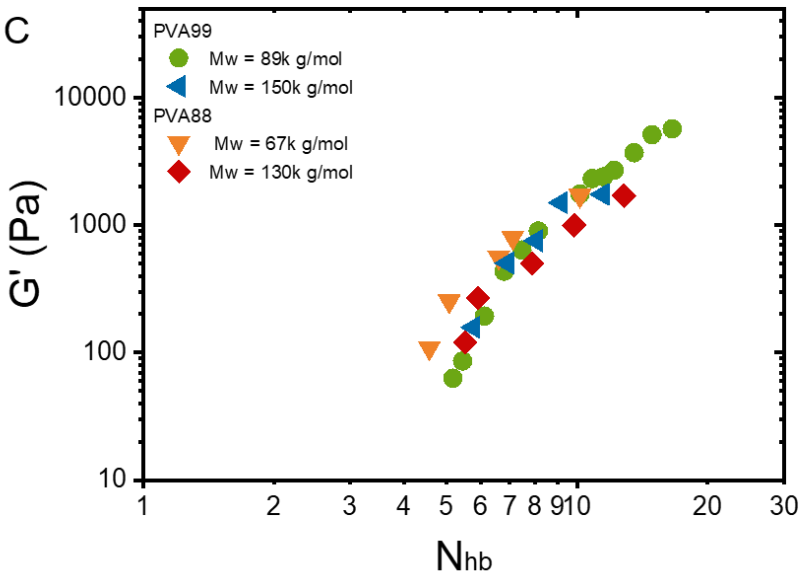

Figure 5.1. (A) Elastic modulus as a function of crosslinker GA concentration for PVA hydrogel. The black solid line indicates the maximum theoretical elastic modulus G_m. (B) Elastic modulus as a function of the molar ratio of the crosslinker to the polymer chain, $N = C_{GA}/C_p$. (C) Elastic modulus as a function of N_{hb} by considering the hydrogen bonding association as additional physical cross-linking.

It should be noted that the chemical crosslinker concentration C_{GA} is in the feed, and that the effective elastically active crosslinker concentration should be lower than C_{GA}, since there are always elastically inactive crosslinks (intra-chain crosslinks) and unreacted crosslinkers. Assuming that all the crosslinkers in the feed are incorporated in the percolated network and serve as elastically active crosslinks, the maximum theoretical elastic modulus G_m is estimated as follows. The molar concentration of the crosslinker C_{GA} (mM) can be converted into the number concentration of it as $1000C_{GA}N_{av}$ ($1/m^3$), where N_{av} is the Avogadro number (1/mol), and 1000 is used to convert L into m^3 (1 L = 10^{-3} m^3). The inverse of the number concentration gives volume per crosslinker ξ^3, and with a structure factor of 2, the elastic modulus can be estimated as $G_m = kT/(2\ \xi^3)$. The value of G_m is plotted

in **Figure 5.1A** as the black solid line. The measured values of modulus are lower than the theoretical value, especially at low crosslinker concentration, indicating that the crosslinking is inefficient close to the percolation limit.

Here we attempt to interpret this M_w- and DH-dependences of modulus by the amount of crosslinks per chain. First, the molar concentration of the chain C_p was calculated from the weight concentration of the PVA (6.6 wt%) and the molecular weight of each PVA tested. The number of crosslinks per chain was then estimated as the molar ratio of the crosslinker to polymer chain, $N = C_{GA}/C_p$. The values of elastic modulus are plotted as a function of N in **Figure 5.1B**. In order to have a percolated network of polymer chains by crosslinking, it is necessary to have at least two crosslinkers per chain ($N \geq 2$). For each PVA, the lowest value of N, close to the percolation limit is found about 4 – 5. Considering the inefficient crosslinking, this lowest limit of N seems reasonable. The curves for the different PVA samples approach each other, while one can still observe that the gels of PVA99 have higher modulus than those of PVA88.

The higher modulus of the PVA99 hydrogel than that of PVA88 hydrogels could be linked to the chemical structure of PVA and the physical crosslinking of hydrogen bonding. As shown in **Figure 5.2**, the dense -OH groups in the polymer chains for PVA 99 provide substantial hydrogen bonding associations serving as the additional physical crosslinking contributing to the elasticity of the hydrogel. On the contrary, the presence of the acetate groups (12% mol) in the polymer chains for PVA 88 largely impedes the association of the neighbor chains due to the steric-hindrances effect and therefore less effective to the elasticity of the sample.[2]

Assuming that physical crosslinks by hydrogen bonding for PVA99 additively contribute to the elasticity with the chemical crosslinks by glutaraldehyde, we roughly estimate its amount per chain N_{hb}, by adjusting the curves in Figure 1b. We

can reasonably suppose that the value of N_{hb} is proportional to the PVA molecular weight and that there is no association for PVA88. We found that N_{hb} = 1.4 for PVA99 M_w = 89 kg/mol (correspondingly N_{hb} = 2.4 for PVA99 M_w = 150 kg/mol) gives satisfactory superposition of the four curves, as shown **Figure 5.1C**. The values of N_{hb} are too small to percolate the chain and are smaller than the values of N.

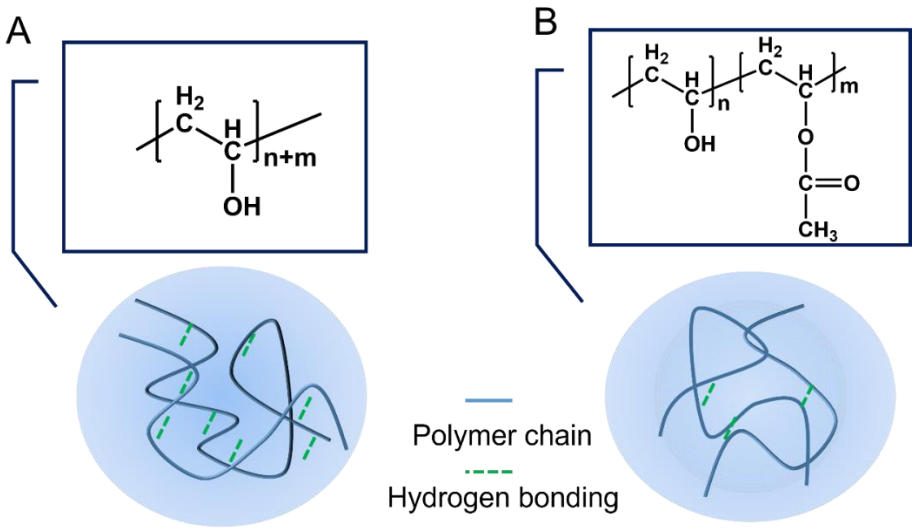

Figure 5.2. Schematic chemical structure of polymer solution for (A) PVA with 99% hydrolysis degree and (B) PVA with 88% hydrolysis degree. The higher content of -OH group in polymer chain endows PVA higher hydrogen bonding association in solution.

5.3.2. Cyclic loading-unloading test

To investigate the structural evolution of PVA hydrogel with different hydrolysis degrees during puncture, the cyclic loading-unloading test was also performed for PVA88 hydrogel. **Figure 5.3** shows the loading-unloading curve for PVA88 hydrogel (G' ~ 800 Pa, M_w = 67,000 g/mol) at the maximum applied displacement D_m = 10 mm, 15 mm, and 25 mm, respectively. Same as the tests performed for the PVA99 hydrogel shown in Chapter 4, two loading-unloading cycles were applied at

each maximum displacement, in order to explore the possible Mullin's effect. In **Figure 5.3A** two force curves at D_m = 10 mm are shown. the first loading and unloading curve exhibits no hysteresis, and the second cycle perfectly overlaps with the first cycle. When the applied displacement was increased to D_m = 15 mm, a similar behavior was observed (**Figure 5.3B**). That is to say, no Mullin effect was observed in this system. As shown in **Figure 5.3C**, when the maximum displacement is further increased to D_m = 30 mm, a sharp decrease of the force is observed at D = 21 mm, and a big hysteresis loop was observed for this loading-unloading cycle. It needs to be noted that all the loading-unloading curves prior to fracture with the incrementally applied displacement superpose well without any hysteresis loop for PVA hydrogel with DH = 88%, in contrast to that for PVA99 hydrogel in Chapter 4 where distinct hysteresis loop happens in the loading-unloading process. While we reported the permanent birefringence pattern during the cyclic loading test for PVA99 hydrogel, there is no visible birefringence pattern for PVA88 hydrogel.

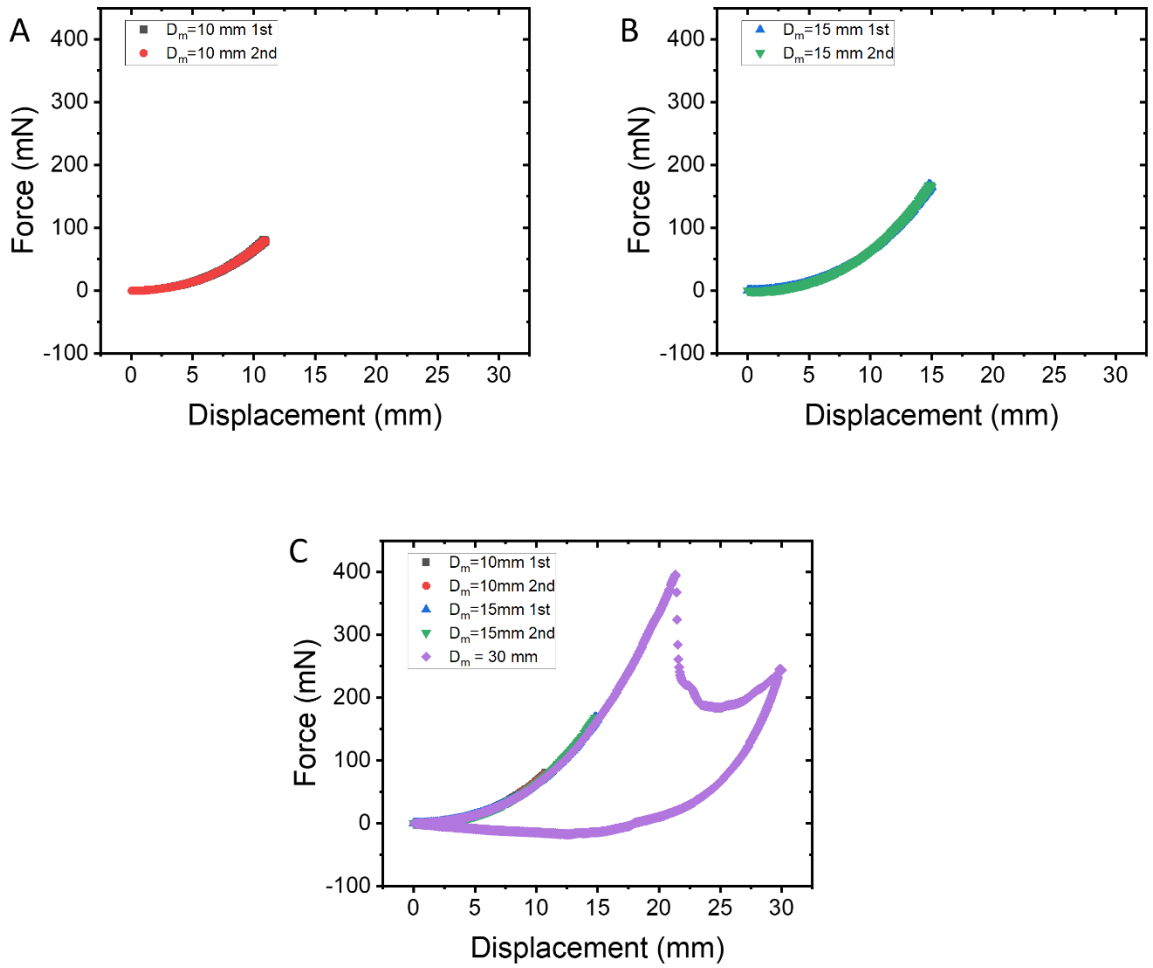

Figure 5.3. Cyclic loading and unloading test of puncture process for PVA88 hydrogel with M_W= 67,000 g/mol. (G' ~ 800 Pa, R= 0.23 mm)

The after-puncture birefringence morphology of PVA hydrogel with different hydrolysis degrees and the molecular weight is shown in **Figure 5.4**. It is evident that only the PVA with high hydrolysis degree DH = 99% shows a V-shaped permanent birefringence pattern while no sign of permanent anisotropic structure is observed for PVA88 no matter the molecular weight. The intensity of the birefringence is enhanced for the PVA99 with higher molecular weight presumably due to the stronger hydrogen bonding association that is fixed around the needle tip during the deep indentation process as discussed in Chapter 4. Correspondingly, the

above-needle-tip fracture behavior is also noted in the PVA99 with M_w = 150,000 g/mol where the permanent birefringence pattern or crystallization is observed after puncture. This result further confirmed our assumption in Chapter 4 that the highly hydrolyzed PVA hydrogel presents strain-induced crystallization upon the large puncture indentation.

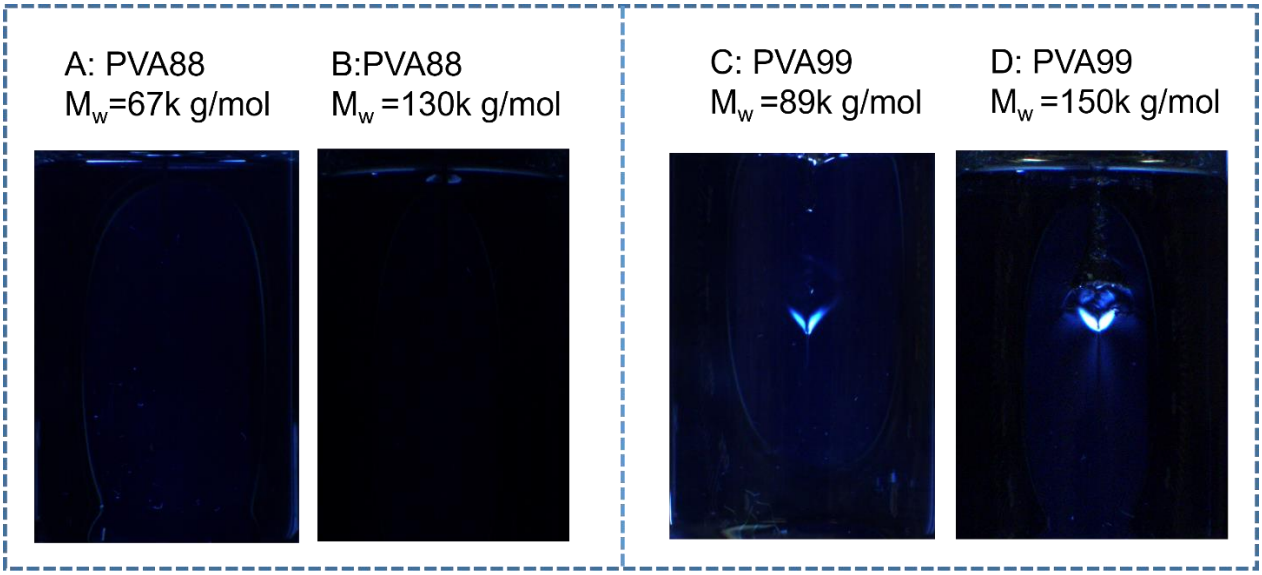

Figure 5.4. The birefringence observation of sample after puncture process. (A) PVA88 with M_w = 67,000 g/mol. (B) PVA88 with M_w = 130,000 g/mol. (C) PVA99 with M_w = 89,000 g/mol. (D) PVA99 with M_w = 150,000/mol. Elastic modulus is about 400 Pa for all the samples.

5.3.3. Fracture resistance

5.3.3.1. Effect of molecular weight

As has been declared by some literatures[3, 4], the fracture energy of material increases with M_w, which is generally recognized as the increase of entanglements among the molecular chains. Prentice studied the influence of molecular weight on the fracture of poly(methyl methacrylate) and reported that the fracture energy Γ scales with the molecular weight by $\Gamma \sim M_w^2$ until a critical value of M_w, above which Γ is constant.

To reveal the impact of molecular weight on the fracture properties of the PVA chemical gels, we plot the fracture resistance σ_c/G' as a function of indenter radius R normalized by elastocapillary length γ/G'. **Figure 5.5A** presents the fracture resistance of PVA99 with M_w = 89 kg/mol (same data in Figure14B of chapter 4) and M_w = 150 kg/mol, respectively. PVA with higher molecular weight yields higher fracture resistance, the values of σ_c/G' for M_w = 150 kg/mol are about twice larger than those for M_w = 89 kg/mol. It is interesting to note that there is a clear boundary when $RG'/\gamma \sim 2$, above which the fracture resistance is constant and below that value σ_c/G' increases significantly with scaling relation $\sigma_c/G' \sim (RG'/\gamma)^{-2/3}$ for PVA99 with two different molecular weight. Taking into consideration the crystallization in PVA99, we think that the sharp increase of the fracture resistance below elasto-capillary length scale is mainly owing to the reinforcement of the crystals formed during the deep indentation as discussed previously. For softer hydrogel, the marked chain extensibility facilitates the strain-induced crystallization and thus allows more crystals and a pronounced toughing effect.

In **Figure 5.5B**, the fracture resistance for PVA88 was found to increase with the molecular weight as well (data for PVA88 with M_w = 89 kg/mol here is the same with Path 1 gel from Figure 17 in chapter 3). Contrary to PVA99, the improvement of the fracture resistance below the elastocapillary length is small when considering the capillary effect for PVA88.

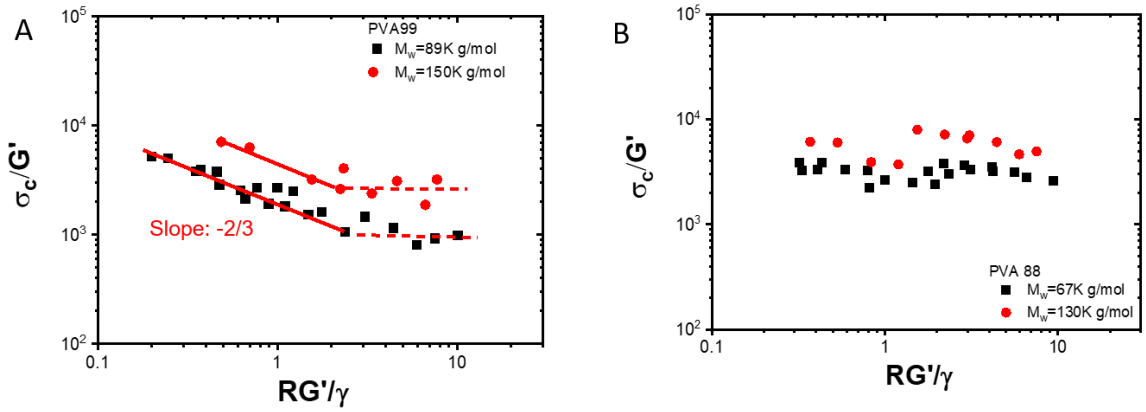

Figure 5.5. Critical nominal stress normalized by modulus, σ_c/G', as a function of indenter radius R normalized by elastocapillary length γ/G' for (A) PVA99 (molecular weight M_w = 89,000 g/mol and M_w = 150,000 g/mol), and (B) PVA 88 (M_w = 67,000 g/mol and M_w = 130,000 g/mol).

5.3.3.2. Effect of surface-active agent

The indentation-induced fracture behavior of hydrogel could be significantly influenced by the surface property of the sample itself such as surface energy, surface defect, and the interface properties of the sample and indenter, such as the friction condition.

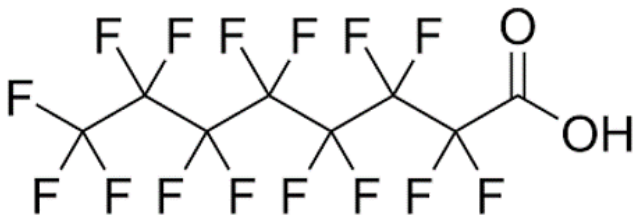

Figure 5.6. Chemical structure of pentadecafluorooctanoic acid, PFOA.

In an attempt to investigate the role of surface tension to the puncture behavior of PVA hydrogel, we lower the surface tension of the sample by adding non-ionic surfactant - PFOA in the pre-gel solution. The chemical structure of PFOA is shown in **Figure 5.6**. The strong C−F bond and hydrophobic interactions give excellent

properties of PFOA, including high surface wetting ability, strong surface activity, and high chemical and thermal stability compared to hydrocarbon surfactants.[5] Subsequently, the surface tension of the PVA99 solution (6.6 wt%) was reduced from γ = 52 mN/m to γ = 32 mN/m with the addition of a small amount of PFOA (0.25 g/L) measured by the tensiometer. Before performing puncture test, we first evaluated the rheological response to the addition of the surfactant into PVA99 hydrogel (**Figure 5.7**). The elastic and viscous modulus for PVA99 hydrogel with the absence and presence of surfactant perfectly superpose, either from strain sweep test or frequency sweep test. This result indicates that the presence of the surfactant does not change the elasticity and dynamics of the hydrogel.

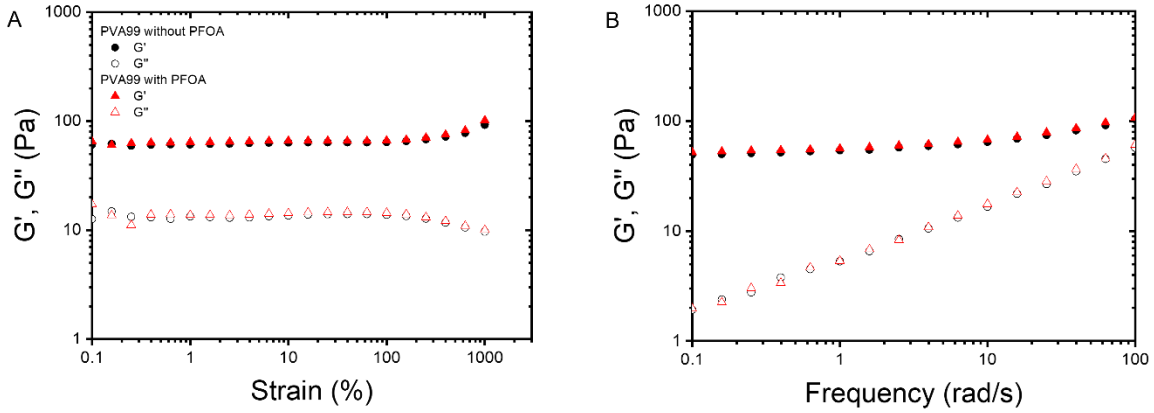

Figure 5.7. Representative rheological properties for PVA99 hydrogel with G' = 60 Pa (A) Modulus as a function of strain; (B) Modulus as a function of frequency for PVA99 hydrogel without surfactant (γ=52 mN/m), and with surfactant PFOA (γ=32mN/m).

Then we performed puncture tests and compared the large deformation mechanical response and fracture behavior of the PVA99 hydrogel with and without the surfactant. **Figure 5.8A** shows the representative loading curve for PVA99 hydrogel in the presence and absence of surfactant (G' = 250 Pa and R = 0.19 mm). Three

repeated tests were conducted with separately fresh specimens for both PVA99 without the surfactant and with the surfactant to ensure reproducibility. Before fracture occurs, the loading curve of the indentation process for all the specimens perfectly falls into the same path. Since the elastic modulus could be determined by the small contact region of the loading curve, this result further confirms that the modulus of the hydrogel with different surface tension values is the same. Nevertheless, while the gel without the surfactant reaches the fracture point at D_c ~ 15 mm and F_c ~ 50 mN, the gel with the surfactant displays unexpected much higher critical displacement D_c ~ 23 mm and critical force F_c ~ 110 mN at the fracture point, exhibiting considerably large fracture resistance. The morphology of gel with different surface tension is shown in **Figure 5.8B** where the D_c is larger for a gel with a lower surface tension value, indicating the larger deformability. The significant variation in terms of F_c suggests that a much larger puncture force is necessary to fracture the sample with lower surface tension. Considering force balance, it looks like a paradox where the smaller surface tension acting as an inverse force to prevent the indentation is supposed to facilitate the fracture initiation in the material; conversely, it improves fracture resistance allowing a large deformation prior to penetration of gel surface.

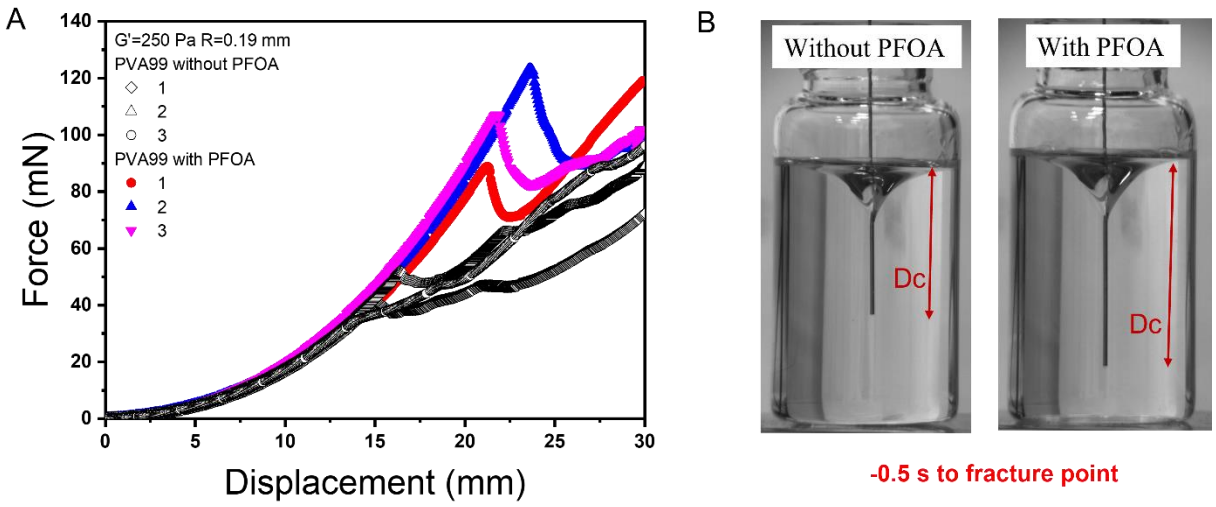

Figure 5.8. (A) Loading curve of PVA99 hydrogel (M_w = 89,000 g/mol) in the absence of surfactant (γ=52 mN/m) and the presence of surfactant PFOA (γ=32 mN/m) (G' = 250 Pa and R = 0.19 mm). (B) Pictures of hydrogel near fracture point where the critical displacement D_c for pure PVA hydrogel is smaller than that for PVA hydrogel with lower surface tension.

We then systematically vary the modulus of the gel by altering the crosslinker concentration in the presence of the surfactant PFOA. The fracture resistance σ_c/G', versus normalized length scale RG'/γ for two gels with different surface tension, are shown in **Figure 5.9**. We observed the similar deviation behavior of σ_c/G' for both samples when it is below the specific length scale $R<G'/\gamma\sim2$, with identical scaling relation $\sigma_c/G'\sim (RG'/\gamma)^{-2/3}$. Notably, the fracture initiation resistance σ_c/G' for gels with lower surface tension γ=32 mN/m is systematically higher than that value for gels with surface tension γ=52 mN/m.

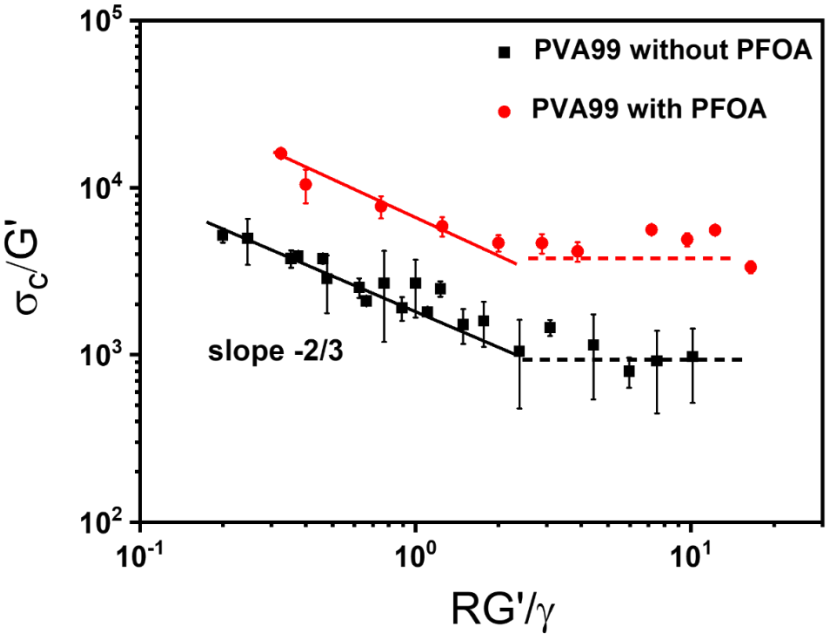

Figure 5.9. The nominal stress over modulus σ_c/G', versus normalized length scale RG'/Υ for PVA99 hydrogel (M_w = 89,000 g/mol) in the presence and absence of surfactant PFOA.

To further verify this phenomenon, we also performed the tensile test for PVA99 hydrogel with higher modulus G' = 3000 Pa in the presence and absence of surfactant PFOA. Interestingly, gels with PFOA or lower surface tension value present higher fracture stress and stretch ratio compared to that without surfactant. This result reflects that the addition of surfactant also improves the tensile performance of the sample, in good agreement with the result from puncture test. We assume that this behavior is probably because the presence of the surfactant in the gel sample delays the initiation of the crack and therefore allows for larger deformation prior to fracture.

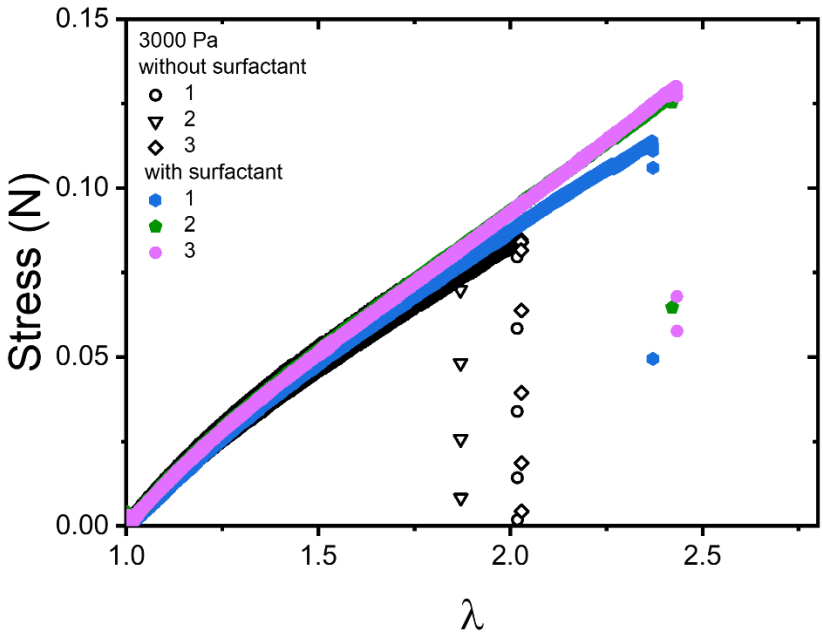

Figure 5.10. Stress as a function of stretch ratio from the tensile test for PVA99 hydrogel G' = 3000 Pa, with and without surfactant PFOA. The loading rate is 0.01 mm/s.

Some investigations were conducted to determine the influence of surfactants on the mechanical behavior of materials. Although mechanisms associated with the role of surfactant additives are not completely understood, it is proposed as a lubrication process in the presence of the surfactant in which the deformation of the material is markedly affected by surface conditions[6, 7]. Buckley studied the influence of the surfactant on deformation and friction coefficient of lithium fluoride crystals in sliding friction experiments[8]. The results indicated that the friction coefficient decreased significantly when a critical surfactant concentration was reached, and the presence of surfactant favored the plastic deformation and thereby reduced the tendency for fracture. This phenomenon is also known as Rehbinder effect[9]. Based on these studies, it is hypothesized that the presence of the surfactant PFOA serves

as the lubrication agent acting in the interface of the PVA hydrogel and indenter which facilitates the elastic deformation by homogeneously distributing the applied stress and thus effectively prevents the occurrence of the crack initiation.

To complete the comparison for both types of PVA, we conducted as well the puncture test for PVA88 hydrogel with varying surface tension by the addition of PFOA. The surface tension of PVA88 was decreased from γ = 42 mN/m to γ = 32 mN/m with PFOA (c = 0.25g/L) measured by the tensiometer. Similar to PVA99, the fracture resistance σ_c/G' was improved with the presence of the surfactant. Very interestingly, while the critical fracture force F_c is independent of the indentation velocity for pure PVA88 hydrogel as demonstrated in Chapter 3, the F_c for PVA88 gel in the presence of the surfactant relies on the applied velocity. Below v = 1 mm/s, F_c is almost constant and higher than that for pure PVA hydrogel; then it starts to drop when v >1 mm/s until to a comparable F_c plateau value as that for pure PVA. This result implies that the role of improvement of the fracture resistance is only accessible when the applied velocity is not significantly large, which may be associated with the migration rate of surfactant to move from the bulk to the interface generated by the deformation of the gel. The time scale for the transport of the surfactant to a clean interface from bulk is estimated of the order of tens milliseconds and the stabilization of the surfactant at the interface is reported to take ~ 1 second.[10] We roughly calculate the time needed to complete the puncture process for PVA gel with the presence of PFOA when the applied v = 10 mm/s: t = D_c/v ~ 2 s (here D_c ~ 20 mm estimated from the loading curve). This timescale is comparable to that needed to stabilize the surfactant in the gel surface. Therefore, we reasonably conclude that this velocity dependence of fracture property is due to the surfactant dynamics.

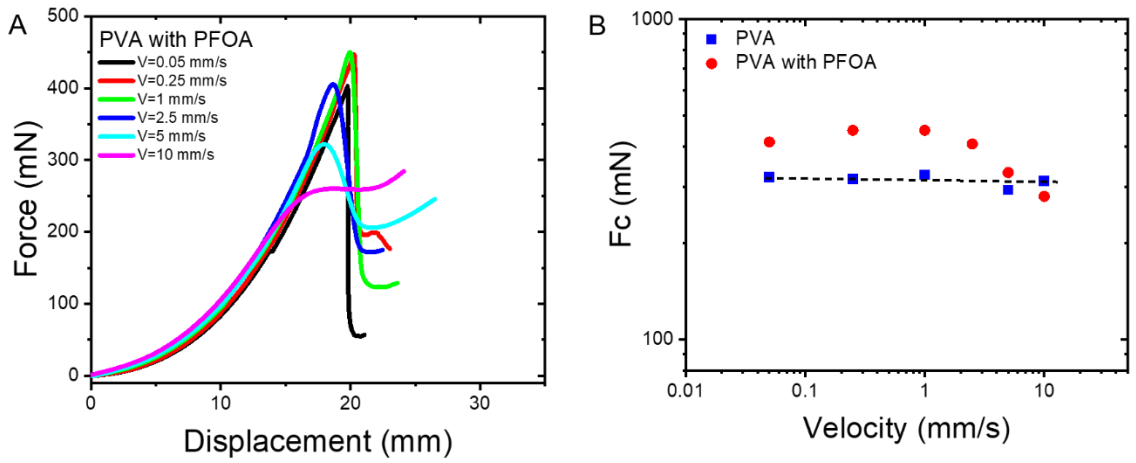

Figure 5.11. (A) Loading curve for PVA with surfactant PFOA under various indentation velocities (2) The critical fracture force as a function of applied indentation velocity for PVA88 hydrogel (M_w = 67,000 g/mol, G' ~ 600 Pa).

The lubricant solutions have been used to decrease the frictional coefficient, thus reducing abrasion and minimizing the energy loss in the operation of the bearing. An alternatively commonly used method to lower friction coefficient and assess lubrication condition is to involve oil. A thin layer of silicon oil was "smeared" on the contact surface with a thickness of ~3 mm. Typical loading curves of PVA99 hydrogel with different modulus in the presence and absence of the oil layer are shown in **Figure 5.12**. For gel with G' ~ 80 Pa (**Figure 5.12A**), the loading curve of the sample in the absence and presence of an oil layer overlaps in the linear contact region but the gel without oil layer fractures at lower critical force F_c. A similar result is found to gel with G' ~ 900 Pa (**Figure 5.12B**). Both the F_c and D_c are found to significantly increase for gel in the presence of the oil layer compared to the pure hydrogel. In this case, the loading curve for gel with/without oil layer superpose very well before fracture point, consistent with that found in **Figure 5.8A** when the surfactant is added to the system. Notably, the addition of surfactant in gel bulk and oil layer on gel surface both aides in markedly improving the puncture resistance of

the PVA hydrogel. A better lubrication condition between the indenter and gel surface is expected in these cases which facilitates the deformation and delays the initiation of the fracture.

A very similar phenomenon was reported by Wang et al.[1] They studied the effect of the coating surface on the penetration behavior of the laminar structure and concluded that the graphene oxide solution, grease, and oil on the sample surface could favor in increasing the puncture strength, improving the failure extension and dissipating additional energy. Connecting with our result, we thus conclude that the addition of surfactant and oil on the surface enables to improve the fracture resistance of PVA hydrogel by ensuing a favorable lubrication condition. This finding will be of interest to meet the requirements of the protection of material under transverse impact loadings by altering the surface state with these media.

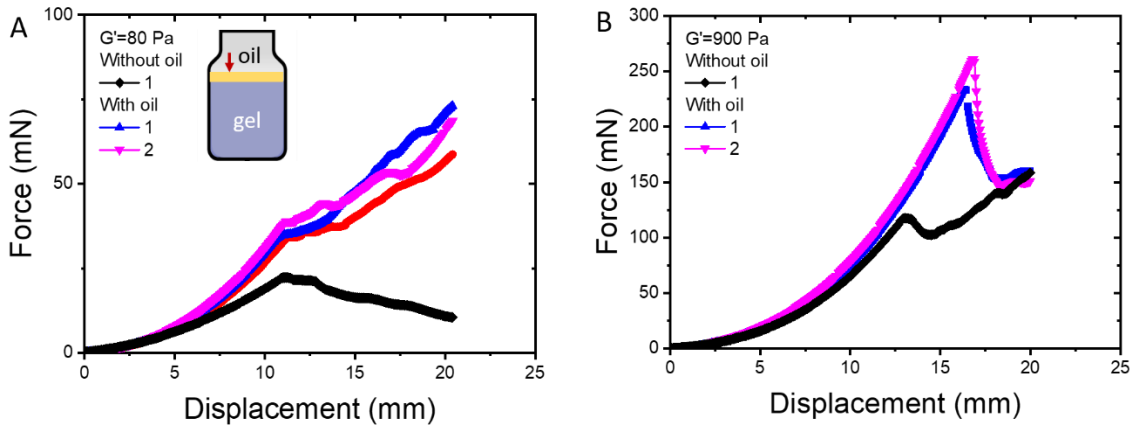

Figure 5.12. The loading curve of PVA99 hydrogel (M_w = 89,000 g/mol) in the presence and absence of silicon oil on the gel surface. (A) Gel with G' ~ 80 Pa; (B) Gel with G' ~ 900 Pa;

5.4. Conclusions

In this Chapter, we have investigated the effect of the molecular weight on the elasticity and fracture resistance of PVA chemical gels with different hydrolysis degrees, with particularity to reveal the role of surfactant in the fracture resistance of PVA. The conclusions of this study are summarized as follows:

1. The increased hydrolysis degree and molecular weight of PVA enhance its crosslinking efficiency and elasticity at the fixed crosslinker concentration attributed to the improved hydrogen bonding associations.
2. PVA with DH = 88% displays no hysteresis behavior under the cyclic loading-unloading test, and no permanent birefringence is observed after the puncture process. Higher molecular weight enables higher fracture resistance for both PVA with DH = 88% and DH = 99%.
3. The addition of surfactant in PVA hydrogel significantly improves its fracture resistance while the elasticity is kept the same, and this fracture-resistance enhancing effect relies on the applied indentation velocity given the surfactant dynamics acting on the gel surface.
4. Similar to the role of surfactant, the addition of silicon oil on the gel surface also improves fracture resistance. This result confirmed our assumption that a better lubrication condition between the gel surface and indenter in both cases favors the large deformation of gel and delays the initiation of the fracture, thus improving the fracture resistance.

5.5. References

1. Wang, P.; Yang, J.; Li, X.; Liu, M.; Zhang, X.; Sun, D.; Bao, C.; Gao, G.; Yahya, M. Y.; Xu, S., Modification of the contact surfaces for improving the puncture resistance of laminar structures. *Scientific reports* **2017,** *7* (1), 1-10.
2. Ilyin, S. O.; Malkin, A. Y.; Kulichikhin, V. G.; Denisova, Y. I.; Krentsel, L. B.; Shandryuk, G. A.; Litmanovich, A. D.; Litmanovich, E. A.; Bondarenko, G. N.; Kudryavtsev, Y. V., Effect of chain structure on the rheological properties of vinyl acetate–vinyl alcohol copolymers in solution and bulk. *Macromolecules* **2014,** *47* (14), 4790-4804.
3. Jawaid, M.; Bouhfid, R., *Functionalized graphene nanocomposites and their derivatives: Synthesis, processing and applications*. Elsevier: 2018.
4. Wang, X.; Li, R.; Cao, Y.; Meng, Y., Essential work of fracture analysis of poly (propylene carbonate) with varying molecular weight. *Polymer testing* **2005,** *24* (6), 699-703.
5. Kancharla, S.; Dong, D.; Bedrov, D.; Alexandridis, P.; Tsianou, M., Binding of Perfluorooctanoate to Poly (ethylene oxide). *Macromolecules* **2022**.
6. Shchukin, E. D., The influence of surface-active media on the mechanical properties of materials. *Advances in colloid interface science* **2006,** *123*, 33-47.
7. Gilman, J., The mechanism of surface effects in crystal plasticity. *Philosophical Magazine* **1961,** *6* (61), 159-161.
8. Buckley, D. H., *Influence of Surface Active Agents on Friction, Deformation, and Fracture of Lithium Fluoride*. National Aeronautics and Space Administration: 1968.
9. Malkin, A., Regularities and mechanisms of the Rehbinder's effect. *Colloid Journal* **2012,** *74* (2), 223-238.
10. Riechers, B.; Maes, F.; Akoury, E.; Semin, B.; Gruner, P.; Baret, J.-C., Surfactant adsorption kinetics in microfluidics. *Proceedings of the National Academy of Sciences* **2016,** *113* (41), 11465-11470.

6. Chapter 6: Visualization of 3D deformation during the puncture of soft materials

6.1. Introduction

Breaking the surface of soft materials or tissues with sharp tools are common events that take place everywhere including biting[1], medical needle insertion, and mechanical characterization[2]. In the case of protection, strength needs to be increased; for other cases, such as needle puncture, it is ideal to puncture under small depth to ease the pain. Understanding the fracture mechanism of such surface breaking process is crucial to realize material design or failure prediction in practical applications.

Failure under puncture or cutting, classified as active failure here, differs from the common passive failure that takes place at a localized crack under a known remote load. In passive failure, the fracture energy can be related to the strain energy release rate [3-5], which can be directly calculated from the load history of the homogeneously deformed bulk and sample/crack geometry. Oppositely, in active failure, the bulk of the material remains un-deformed while only the region around the crack is under a highly localized load. The advancing nature of the drive of the failure (needle or blade) decides that the singularized cannot be blunted[6] by large deformation but only sharpened. Furthermore, failure in soft matters under active failure happens almost always via subcritical transition: catastrophic fracture suddenly takes place with no steady propagation period [7]. As a result, it is difficult to cut/puncture through the surface (extremely high critical stress σ_c of failure) but much easier to break through the bulk material later. In puncture with well-defined needle geometry, reported σ_c is typically in the scale of 0.1~10 MPa for elastomers [8-9] and hydrogels [10-11], several orders higher than their modulus E. On the hand, σ_c/E is only in the order of one for passive failure in elastomers, measurable by non-scission mechanophore[12]. This distinct difference comes from either significant strain hardening when approaching very close chain extensibility or extremely large deformation over 100, which are

both unlikely for polymer networks commonly with defects and structural heterogeneity. The missing factor lays potentially in the local interaction and load transfer around the needle tip, but is difficult to analyze due to complex 3D geometry and non-equilibrium nature, where high enough spatial and temporal resolution are both required.

As the combination of the mechanical testing with birefringence imaging[13] and digital image correlation (DIC)[9, 14] have been explored, the visualization of the large-scale deformation is limited by the detection resolution, especially for soft hydrogels with a high amount of water content and large deformation at failure[15]. Digital image correlation (DIC) is a powerful tool that identifies the displacement of speckles, typically generated by spray painting, to calculate the spatially resolved deformation by full-field imaging. Instead of spray painting, laser speckle image technologies are particularly suitable for large strain measurement, as the speckles are normally homogeneously distributed all over the image even at large deformation. For conventional spray-painted speckles, the speckles can be high apart with increasing strain or even detach from the surface[15-16]. In this work, we use a laser sheet as the light source to generate laser speckles to achieve strain mapping with the 3D resolution, with an excellent spatial resolution of 0.3 mm, around the size of the needle tip. With the measurement, we discovered that there is a large-scale attachment along the needle between needle and gel, which contributes shear stress to the total measured force, resulting in the overestimated fracture stress.

6.2. Experimental section

6.2.1. Materials

PVA88 and PVA99 hydrogel samples are prepared as described in the previous chapter. Differently, instead of a cylindrical glass vial with a diameter of ~ 25 mm, in this PCI test, we poured the pre-gel solution into a transparent cuboid cuvette (in Polystyrene) with a dimension of 1 cm × 1 cm × 5 cm to finish the gelation process and perform the puncture test.

6.2.2. Methods

PCI measurements are conducted using a custom-made setup (the schematic is shown in **Figure 6.1A**). A uniform vertical laser line generated by the laser (λ = 480 nm) passes through a Powell lens and a cylindrical lens forming a laser and then is focused on the sample. The laser sheet width in z is 5 cm, tunable by the distance to the focusing lens, after which the laser sheet becomes parallel along x but focused in y. Samples are prepared in the cuboid vessel (inner size 1 cm × 1 cm × 5 cm) and positioned in a way where the central axis is at the focal length of the incident laser sheet. In this way, although in y laser sheet is focused before the central axis and divergent after, the width is small compared to the size of the sample, so that is ignored in the analysis. A CMOS camera collects time-resolved images with a framerate of 0.2 s/frame along y, so that the scattering angle is around 90 degrees. This is advantageous for the measurement by PCI applying single scattering, as the q value ($q = \frac{2\pi sin\theta}{\lambda}$, $\theta = 90°$) is the least sensitive to the angle dispersed in space. A linear polarizer is placed between the camera and the sample to block the multiply scattered light.

An image collected during puncture (puncture depth d = 10 mm) is shown in **Figure 6.1B**. It can be discovered that the laser sheet is blocked by the inserted needle so

that we can analyze the right side of the image above the needle tip and the whole width underneath. Very close to the needle (< 0.5 mm), the speckle quality is influenced by the strong reflection around the needle. An enlarged image is an inset in **Figure 6.1B**, where the existence of the speckles can be observed, on a scale around 50 μm (2.5 pixels).

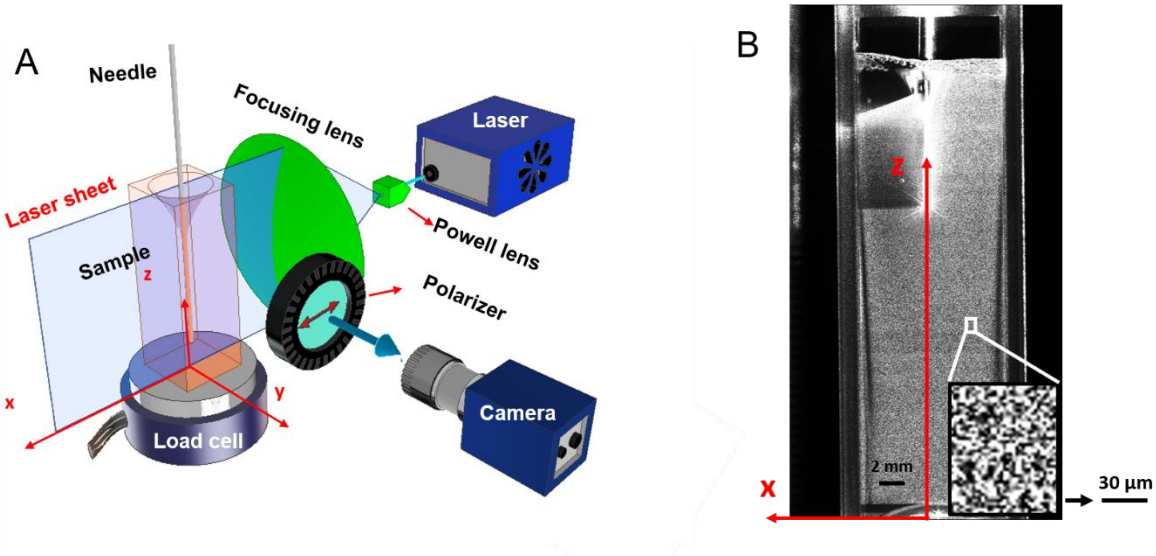

Figure 6.1. (A) Schematic of PCI measurement for puncture process. (B) An image during puncture (d=10 mm). Inset: an enlarged image showing the speckles generated by laser illumination.

6.3. Results and discussion

6.3.1. Principal of PCI

Laser speckles are generated by the illumination of a laser sheet generated by the Powell lens, where the incident laser is expanded along z (x, y, z coordinates are indicated in **Figure 6.1A**), the puncture direction. Ideally, only singly scattered light can be collected so that the cross-section in the laser sheet plane can be measured, which contains the full information in the 3D field.

The key idea of the measurement is to track the speckle displacement by comparing images from the scattered light intensity. In polymer networks, the decorrelation of the speckles generated from the local refractive index fluctuations will take place with the aging of the sample. After the substantial decorrelation of the speckle, the position of the speckle is not accessible by image correlation. The interference of aging kinetics with displacement tracking can be quantified by the comparison of the dynamics of the scatters in a static sample (only aging) and a displaced sample (displacement and aging). Dynamics can be quantified by the autocorrelation function of the scattered light intensity [17-21]:

$$\mathrm{C}(t,\tau) = \frac{\langle I(t)I(t+\tau)\rangle}{\langle I(t)\rangle\langle I(t+\tau)\rangle} - 1 \qquad 6.1$$

where t is the experimental time and τ is the time delay to calculate the correlation value. At a fixed time, a slower decorrelation of $C(\tau)$ with τ corresponds to slower dynamics [22]. $C(\tau)$ of the static and displaced sample are shown in **Figure 6.2A**. It can be discovered that for sample displaced with a smaller velocity v, the decorrelation is also slower in $C(\tau)$. However, even for the slowest v = 0.003125 mm/s, the decorrelation is still three orders slower than that of a static sample, where 30% of decorrelation is observed at 10^4 s. With aging-related dynamics being much slower than that from displacement, $C(\tau)$ for diplaced samples can be considered only contributed by displacement velocity. As a result, the decorrelation level should be related only to displaced distance (τv). $C(\tau v)$ for all the diplaced samples are plotted in **Figure 6.2B**, where all results overlap well with each other. With the measurement, we can estimate the minimal scale of velocity measurable by the method, where dynamics due to displacement are in the same order with aging, around 1~10 nm/s. The spatially resolved velocity can be mapped by tracking the displacement of the speckle at a fixed time interval, chosen to be 0.2 s for a puncture

velocity of 0.05 mm/s. The maximal velocity is presumably not larger than puncture velocity so that the correlation value at 0.5 s is always larger than 30% of the total range (**Figure 6.2A**) and the speckle 0.2 s later is still considerably correlated to the previous location. Displacement tracking by DIC is performed with an open source program pyDIC, developed by Damien André [23]. The spatial resolution, defined by the mesh size of 0.3 mm in DIC processing and time resolution is 0.2 s (5 images/s).

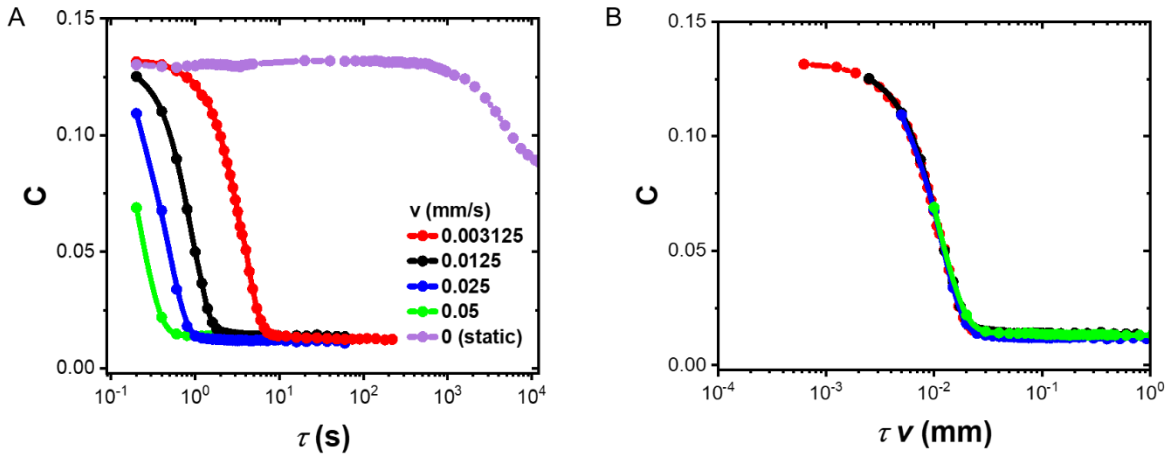

Figure 6.2. (A) Time-correlation value C as the function of time delay τ. (B) Spatial-correlation value C for displaced samples as the function of τv.

6.3.2. Validation of 3D deformation by laser slicing

Results for PVA88 hydrogel with G' = 550 Pa are shown in **Figure 6.3**. As the velocity mapping is measured in xz plane, to validate the y resolution, we illumintate the sample with a laser sheet at different y to visualize the 3D velocity distribution, which should be axisymmetric. y resolution in the applied geometry depends on the single scattering quality, which says if there is a substantial amount of multiply scattered collected, the measured velocity field will be an averaging in the whole illuminated volume in the sample. The velocity maps for y = 0 mm and y = -2 mm are shown in **Figure 6.3B**. With y = 0 mm, a vortex pattern can be observed

at around 4 mm higher than the needle tip. Closely to the needle, the velocity of the needle (0.05 mm/s) can be observed (orange arrow). As discussed, even though the speckle dynamics are not accessible around the crack tip, the position of the needle is still trackable by DIC. Remarkably, the vortex pattern is absent for velocity mapping at y = -2 mm but only upwards motion can be visualized with faster velocity. The 3D distribution of the vortex pattern is schematically shown in **Figure 6.3C** (red arrows). The shearing of the hydrogel by the puncture of the needle results in tension towards the needle and the sample far away is stretched by the tension, forming a 3D flow field shown as a vortex in 2D slicing. The faster velocity at y = -2 mm should be due to the larger distance ($r = \sqrt{x^2 + y^2}$) from the needle, which results in a different boundry condition. The velocity distribution at different validates the y-resolution by laser sheet illumination, but a more quantitative investigation required a vessel with large enough size to ensure universal boundary conditions at the different radial directions. Below the needle tip plane, is a large region with velocity pointing outwards from the needle tip. The 3D distribution for this motion is indicated by blue arrows in **Figure 6.3C**.

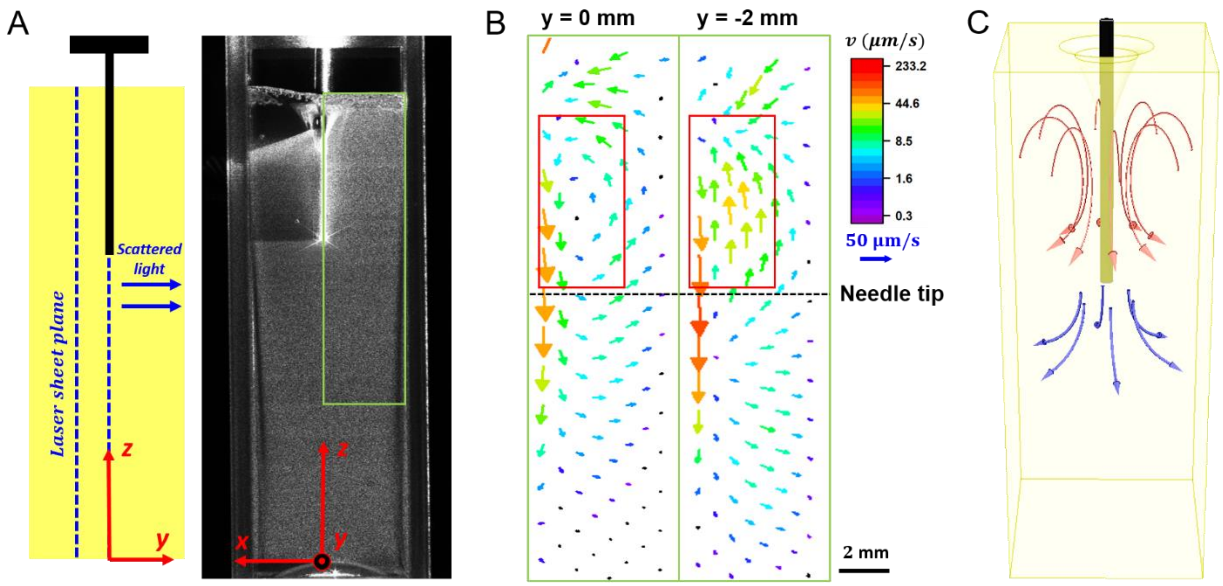

Figure 6.3. (A) Measurement with laser sheet illumination at different y. (B) Velocity maps at y = 0 mm and -2 mm, respectively, in the region indicated in (A). The velocity values are coded in both color and length (blue arrow). The regions containing vortex patterns are marked by the red square. (C) Schematic drawing of 3D velocity distribution interpreted from (B).

6.3.3. Strain mapping from the increment velocity field

Previous studies on puncture problems have shown the qualitative picture of the strain field around an indenter during deep indentation in which a compressible strain field below the indenter and shear strain field on the sides of the indenter is infered[24]. Very recently, Barney et al[25] quantitatively reported the strain distribution around the needle during the indentation process for a rigid PDMS sample (~ 500 kPa). While the compression strain below the needle tip is discovered, the above-needle-tip compression phenomenon is still missing and remains exclusive. This would be very important to understand the strain distribution for the soft hydrogel, where very large deformation is usually observed in practical applications. However, the fracture strain for ultra-soft material could be extremely large, for example, the fracture displacement in puncture could surpass the needle radius by $D_c/R \sim 100$. In this case, the strain mapping by DIC is inaccessible as the initially defined grid can be largely deformed at a later stage and thus easily lose the tracking resolution.

Here we extract the strain from the increment velocity field after validation of the visualization of 3D motion by laser sheet. With potentially ultrahigh strain including both tension/compression and shear around the needle, the initially tracked points tend to be blurred. To avoid the massive error generated during the accumulated strain by tracking one single point, we performed separate displacement tracking in an increment period T = 2 s. For each increment displacement field, we used a grid size of 15 pixels × 15 pixels. An imaginary grid is predefined with a grid size of 8

pixels along the puncture direction and 12 pixels in the perpendicular direction, as $(y(t=0), z(t=0))$ at the initial experimental time. The displacement field at a certain experimental time t' is calculated by selecting the closest 20 points around the coordinates $(y(t'-T), z(t'-T))$ in the imaginary grid and averaging their weighted displacement.

6.3.3.1. True strain ε_{zz}

The true strain ε_{zz} along the puncture direction for PVA88 hydrogel with G' = 550 Pa and G' = 1700 Pa are plotted in **Figure 6.4A** and **Figure 6.4B**, respectively, where the vertical positions of the needle tip are indicated by the dashed line. For the gel with G' = 550 Pa (D_c = 18 mm), at d = 5 mm, a extension region (strain $\varepsilon_{zz} > 0$) is observed above the needle tip whereas a compression region ($\varepsilon_{zz} > 0$) well below the needle tip is discovered as shown in **Figure 6.4A** i. At d = 7 mm, the extension strain above the needle tip is enhanced and surprisingly the compression strain starts to be visible even above the needle tip (**Figure 6.4A** ii). When d = 17.5 mm (approaching to fracture point), a very strong extension area occurs on the top part of the material as shown in the red color (**Figure 6.4A** iii). Remarkably, the length of the compression region along the tip reaches around 6 mm, almost 1/3 of d = 17.5 mm as indicated by the rectangular area in **Figure 6.4A** iii. The high compression above the needle tip indicates that there is an attachment between the wall of the needle and the gel. Even though the local interface between the gel and the needle is below the resolution of the optical images, we can characterize the interaction by further analyzing the resultant strain field.

In **Figure 6.4B**, the results for PVA88 hydrogel with G' = 1700 Pa (D_c = 11 mm) are shown, and similar patterns can be observed: at small d, there is extension ($\varepsilon_{zz} > 0$) above needle tip and compression underneath; with increasing d, there is a region along the needle above the tip with a compression field. It needs to be noted that

while the strain mapping for a gel with the different modulus (G' = 550 Pa and G' = 1700 Pa) at d = 5 mm and d = 7 mm is comparable when it is approaching the fracture point, their compression strain distribution is quite different. In **Figure 6.4B** iii, the compression area is concentrated in the needle tip with a short vertical length. This difference could be attributed to the deformability of gel with different modulus as discussed in the previous chapter. Lower modulus enables larger chain extensibility and thus a long area of gel is attached to the needle contributing to a long compression area in **Figure 6.4A** iii, but high modulus displays limited deformability prior to fracture in which the attachment between gel and needle surface is small and compression is highly concentrated at the needle tip.

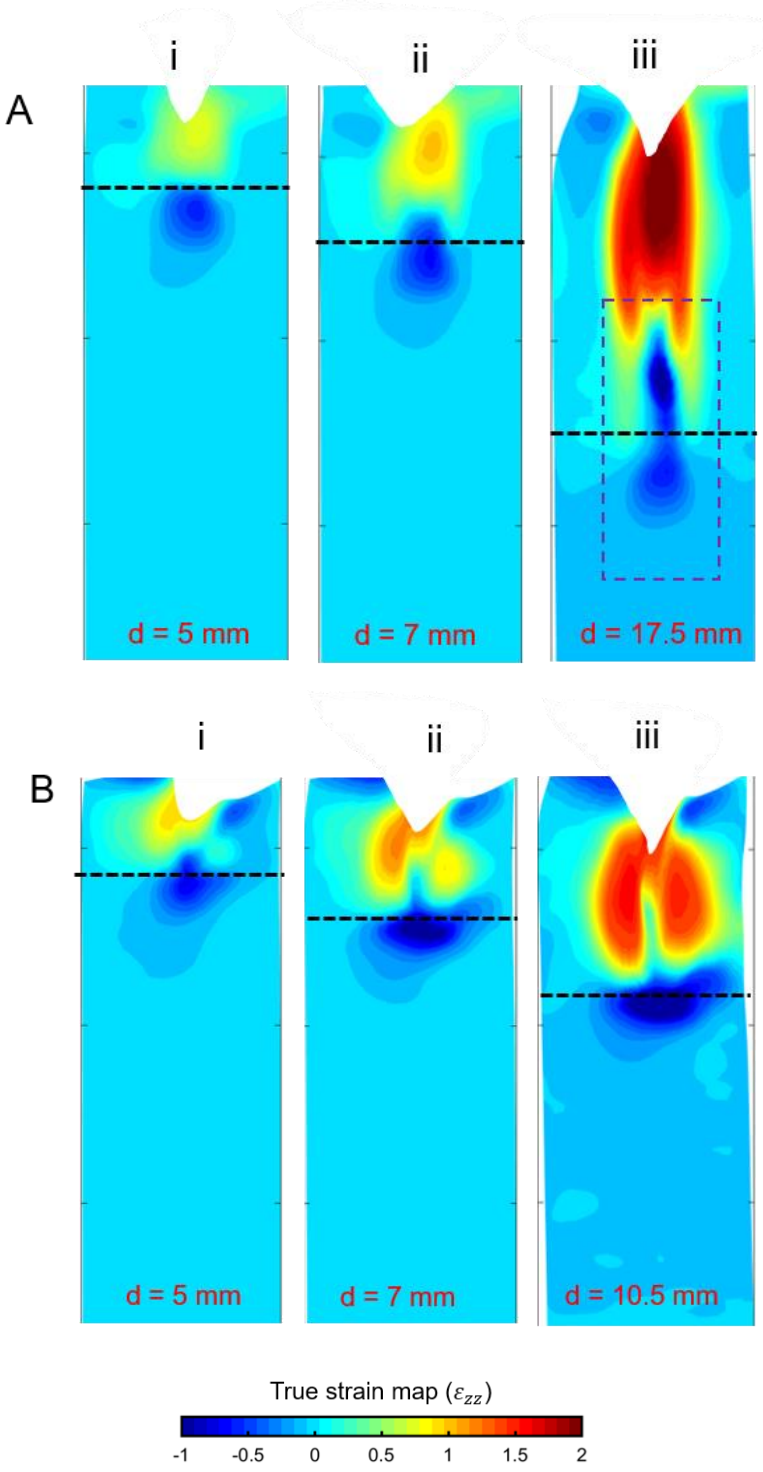

Figure 6.4. Strain mapping of indentation process for PVA88 hydrogel with different elastic modulus: true strain ε_{zz} along the puncture direction at various displacements. (A) G' = 550 Pa; (B) G' = 1700 Pa. The dashed line indicates the needle tip position.

6.3.3.2. Comparison between ε_{zz}, ε_{xx}, and ε_{xz}

In addition, we compare the tensor components ε_{zz}, ε_{xx}, and ε_{xz} at d = 17.5 mm for PVA88 hydrogel with G' = 550 Pa (**Figure 6.5**). As the region in ε_{zz} is compressed/extended, it is oppositely extended/compressed in ε_{xx}, indicating the incompressibility of the gel (**Figure 6.5A** and **Figure 6.5B**). Surprisingly, only in the region where strong compression along the needle is generated above the needle tip, strong shear is observed, reaching $|\varepsilon_{xz}|\sim1.3$ as shown in **Figure 6.5C**. This clearly indicates that there is a bonding between the gel and the needle, where the gel is pulled down along the needle with puncture, resulting in strong compression and shear.

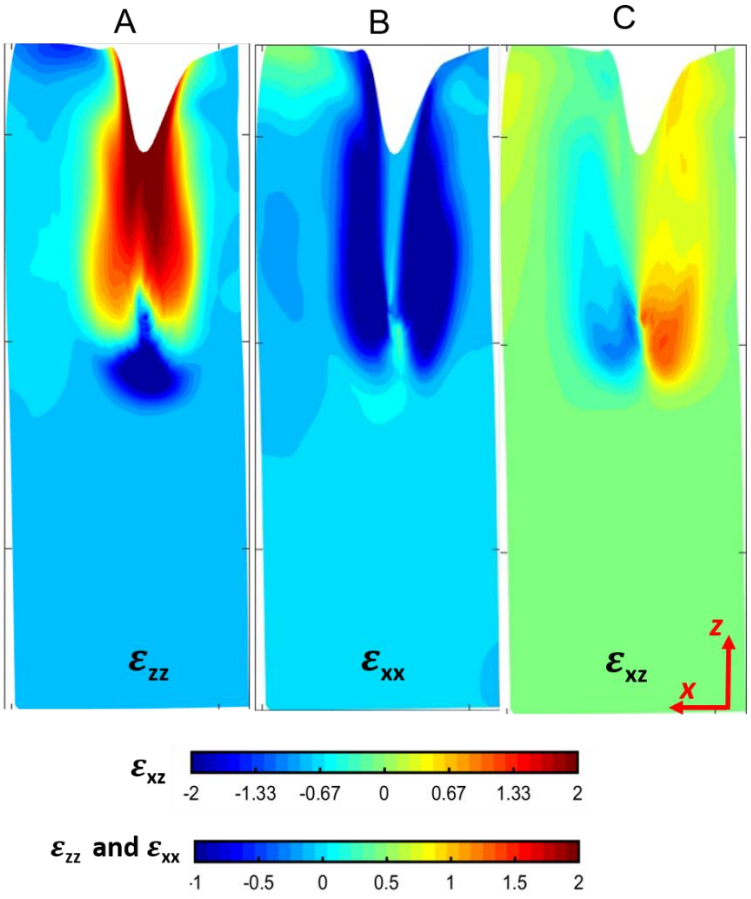

Figure 6.5. Components in true strain tensor of PVA hydrogel with G' = 550 Pa at d = 17.5 mm (A) ε_{zz}, (B) ε_{xx}, and (C) ε_{xz}.

6.3.4. Linking the strain mapping with macroscopic property

We attempt to link the strain mapping of PVA hydrogel to its macroscopic mechanical properties. The loading curve for PVA88 hydrogel with G' = 550 Pa is shown in **Figure 6.6**. As the sheared area increases with d, the measured force as the sum of compression and shear should increase significantly. Before d = 5 mm, the force-displacement curve is almost linear and no compression can be observed above the needle tip. From d > 5 mm, obvious strain hardening is observed with increasing compression above the needle tip. Note that fracture happens around d = 17.6 mm, so that at this early stage, the significant strain hardening should not be due to the local damage at the needle tip. Our measurements contrast the common assumption regarding deep indentation that only the gel under the needle tip can be compressed and damaged [7, 26]. More importantly, as it is traditionally to employ stress $\sigma = F/\pi R^2$ to estimate the fracture mechanics and damage scale in gel [7], our discovery shows that the actual σ can be largely overestimated without considering bonding with the needle. Qualitatively, the critical stress σ_c at fracture (either compression or shear) around the needle tip should be:

$$\sigma_c \sim \frac{F_c}{\pi R^2 + 6\pi R L_c} \qquad 6.2$$

where critical stress before fracture is considered to be the same for compression and shear. L_c is the critical contact length along the needle and the shear modulus G' is set to be $3E$, Young's modulus. Using eq. 6.2 in the measurement shown in Fig. 4 where L_c~ 6 mm and R = 0.45 mm, σ_c is on the scale of 10 kPa. The critical stress is around one order larger than the modulus (G' = 550 Pa), consistent with the measurements in compression [27] and single edge notched tensile experiments [12, 28].

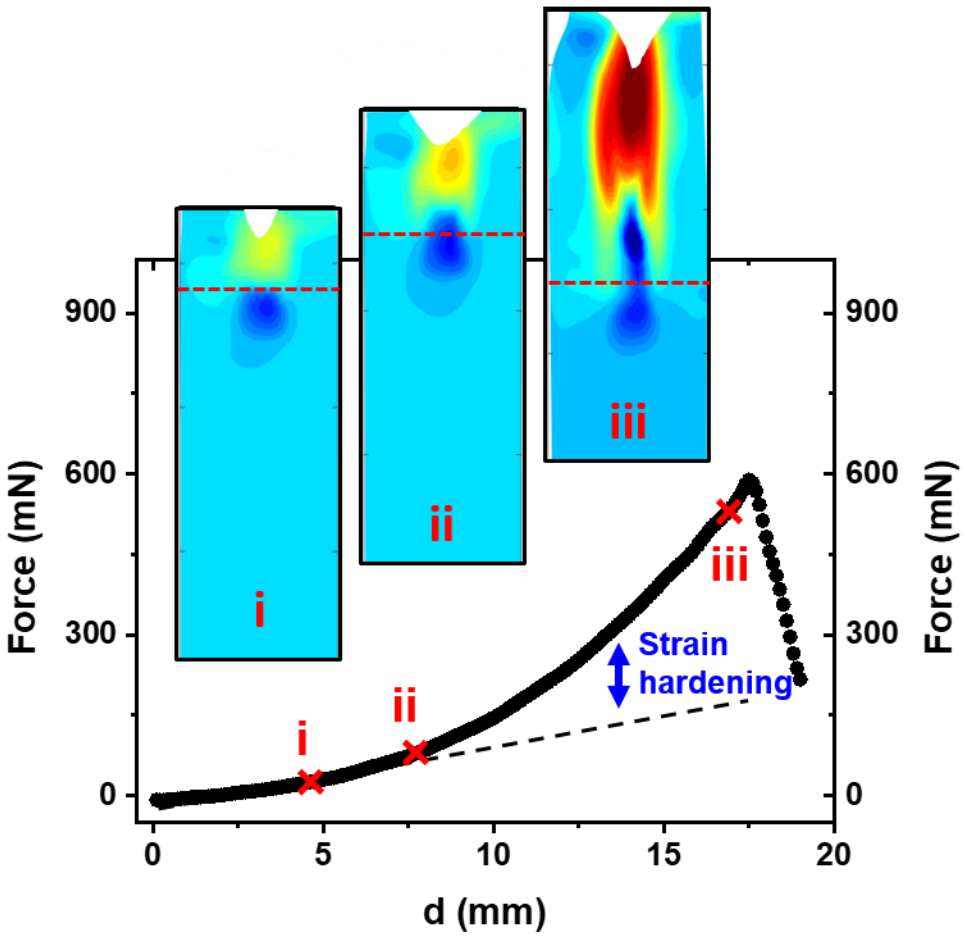

Figure 6.6. Force-displacement curve of PVA88 hydrogel with G' = 550 Pa showing strain hardening behavior at large deformation. Inset: ε_{zz} map at different displacement.

To confirm this finding, we also performed the PCI measurement for PVA99 hydrogel with various gel modulus. The mapping of strain ε_{zz} along the puncture, the direction is shown in **Figure 6.7**. For both of PVA99 hydrogel with G' = 250 Pa and G' = 1000 Pa, there is extension ($\varepsilon_{zz} > 0$) above needle tip and compression below the needle at a small d value; with increasing d, there is a region above the tip showing compression strain. Similar to the results for PVA88 hydrogel, we think that the above-needle-tip compression may originate from the attachment of gel and

needle surface as the modulus is quite low. It is worth noting that the strain mapping here analyzed is based on the indentation response right prior to the fracture point so the fracture behavior or catastrophic failure of these two PVA gels is not included in this analysis. This work will be further expanded by stress reconstruction based on the strain mapping of the puncture process, aiming to infer the fracture energy release rate in extreme geometry.

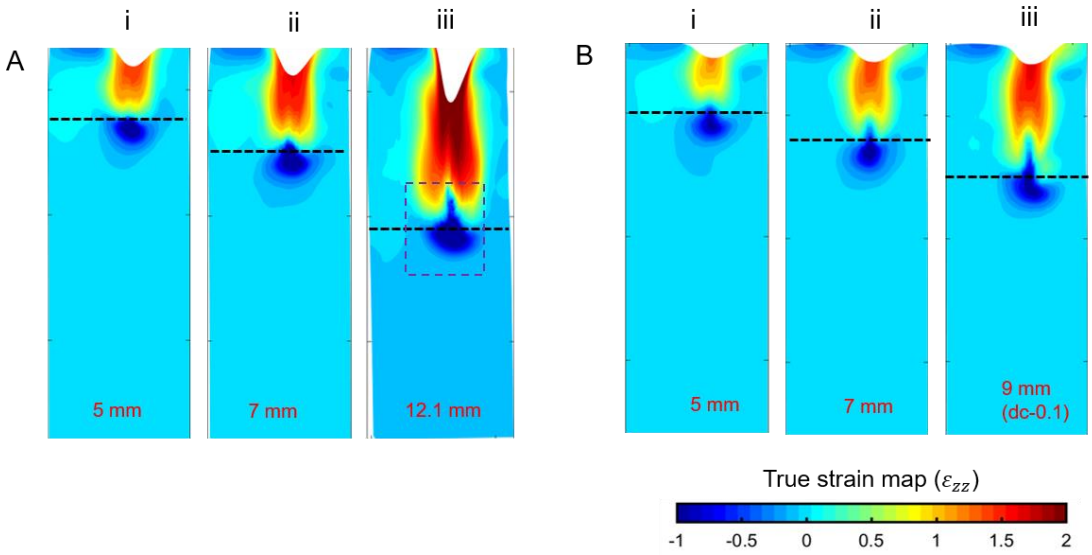

Figure 6.7. Strain mapping of indentation process for PVA99 hydrogel with different elastic modulus: true strain ε_{zz} along the puncture direction at various displacements. (A) G' = 250 Pa (D_c = 13 mm); (B) G' = 1000 Pa (D_c = 10 mm). The dashed line indicates the needle tip position.

6.4. Conclusions

In this chapter, we developed a novel technique to precisely measure the 3D deformation field, which combines photon correlation imaging (PCI) and DIC. Owing to this method, we successfully observed the deformation distribution of the puncture process with excellent resolution ~ 0.3 mm. Our measurements quantitatively demonstrate that there exists a strong compressed and the sheared region above the needle tip, resulting in the overestimated critical nominal stress (surpassing the elastic modulus by several orders of magnitude), which is absent in previous studies. This finding sheds new light on the understanding of how ultra-soft gel deforms and fractures under extreme indentation conditions, and would contribute to the prediction of injury and damage in biological tissues.

6.5. References

1. Santana, S. E.; Dumont, E. R.; Davis, J. L., Mechanics of bite force production and its relationship to diet in bats. *Functional Ecology* **2010,** *24* (4), 776-784.
2. Duncan, T. T.; Sarapas, J. M.; Defante, A. P.; Beers, K. L.; Chan, E. P., Cutting to measure the elasticity and fracture of soft gels. *Soft Matter* **2020,** *16* (38), 8826-8831.
3. Griffith, A. A., The phenomenon of rupture and flow in solids. *Phil. Trans. Royal Soc. London, A* **1920,** *221*, 163-198.
4. Wang, S.; Panyukov, S.; Rubinstein, M.; Craig, S. L., Quantitative adjustment to the molecular energy parameter in the Lake–Thomas theory of polymer fracture energy. *Macromolecules* **2019,** *52* (7), 2772-2777.
5. Lake, G. J.; Thomas, A. G., The Strength of Highly Elastic Materials. *Proceedings of the Royal Society A: Mathematical, Physical and Engineering Sciences* **1967,** *300* (1460), 108-119.
6. Hui, C.-Y.; Bennison, S.; Londono, J., Crack blunting and the strength of soft elastic solids. *Proceedings of the Royal Society of London. Series A: Mathematical, Physical and Engineering Sciences* **2003,** *459* (2034), 1489-1516.
7. Fakhouri, S.; Hutchens, S. B.; Crosby, A. J., Puncture mechanics of soft solids. *Soft Matter* **2015,** *11* (23), 4723-30.
8. Liu, J.; Chen, Z.; Liang, X.; Huang, X.; Mao, G.; Hong, W.; Yu, H.; Qu, S., Puncture mechanics of soft elastomeric membrane with large deformation by rigid cylindrical indenter. *Journal of the Mechanics and Physics of Solids* **2018,** *112*, 458-471.
9. Barney, C. W.; Chen, C.; Crosby, A. J., Deep indentation and puncture of a rigid cylinder inserted into a soft solid. *Soft Matter* **2021,** *17* (22), 5574-5580.
10. Muthukumar, M.; Bobji, M.; Simha, K., Needle insertion-induced quasiperiodic cone cracks in hydrogel. *Soft Matter* **2021,** *17* (10), 2823-2831.
11. Rattan, S.; Crosby, A. J., Effect of polymer volume fraction on fracture initiation in soft gels at small length scales. *ACS Macro Letters* **2019,** *8* (5), 492-498.
12. Chen, Y.; Yeh, C. J.; Qi, Y.; Long, R.; Creton, C., From force-responsive molecules to quantifying and mapping stresses in soft materials. *Science advances* **2020,** *6* (20), eaaz5093.
13. Fakhouri, S.; Hutchens, S. B.; Crosby, A. J., Puncture mechanics of soft solids. *Soft Matter* **2015,** *11* (23), 4723-4730.
14. Spagnoli, A.; Terzano, M.; Brighenti, R.; Artoni, F.; Ståhle, P., The fracture mechanics in cutting: a comparative study on hard and soft polymeric materials. *International Journal of Mechanical Sciences* **2018,** *148*, 554-564.
15. Liu, M.; Guo, J.; Hui, C. Y.; Zehnder, A. T., Application of Digital Image Correlation (DIC) to the Measurement of Strain Concentration of a PVA Dual-Crosslink Hydrogel Under Large Deformation. *Experimental Mechanics* **2019**.
16. Nagazi, M.-Y.; Brambilla, G.; Meunier, G.; Marguerès, P.; Périé, J.-N.; Cipelletti, L., Space-resolved diffusing wave spectroscopy measurements of the macroscopic deformation and the microscopic dynamics in tensile strain tests. *Optics and Lasers in Engineering* **2017,** *88*, 5-12.
17. Pine, D. J.; Weitz, D. A.; Chaikin, P. M.; Herbolzheimer, E., Diffusing wave spectroscopy. *Phys Rev Lett* **1988,** *60* (12), 1134-1137.
18. Pine, D. J.; Weitz, D. A.; Zhu, J. X.; Herbolzheimer, E., Diffusing-wave spectroscopy: dynamic light scattering in the multiple scattering limit. *Journal de Physique* **1990,** *51* (18), 2101-2127.

19. Weitz, D.; Pine, D., Diffusing-wave spectroscopy. In *Dynamic light scattering: The method and some applications*, Oxford University Press: 1993; pp 652-720.
20. Duri, A.; Sessoms, D. A.; Trappe, V.; Cipelletti, L., Resolving long-range spatial correlations in jammed colloidal systems using photon correlation imaging. *Physical review letters* **2009,** *102* (8), 085702.
21. Viasnoff, V.; Lequeux, F.; Pine, D., Multispeckle diffusing-wave spectroscopy: A tool to study slow relaxation and time-dependent dynamics. *Review of scientific instruments* **2002,** *73* (6), 2336-2344.
22. Ballesta, P.; Duri, A.; Cipelletti, L., Unexpected drop of dynamical heterogeneities in colloidal suspensions approaching the jamming transition. *Nature Physics* **2008,** *4* (7), 550.
23. André, D., pydic. **2018**, https://gitlab.com/damien.andre/pydic
.
24. Fakhouri, S. M. Cavitation and Puncture for Mechanical Measurement of Soft Solids. University of Massachusetts Amherst, 2015.
25. Barney, C. W.; Zheng, Y.; Wu, S.; Cai, S.; Crosby, A. J., Residual strain effects in needle-induced cavitation. *Soft Matter* **2019,** *15* (37), 7390-7397.
26. Fregonese, S.; Bacca, M., Piercing soft solids: A mechanical theory for needle insertion. *Journal of the Mechanics and Physics of Solids* **2021,** *154*, 104497.
27. Cristiano, A.; Marcellan, A.; Long, R.; Hui, C. Y.; Stolk, J.; Creton, C., An experimental investigation of fracture by cavitation of model elastomeric networks. *Journal of Polymer Science Part B: Polymer Physics* **2010,** *48* (13), 1409-1422.
28. Chen, Y.; Yeh, C. J.; Guo, Q.; Qi, Y.; Long, R.; Creton, C., Fast reversible isomerization of merocyanine as a tool to quantify stress history in elastomers. *Chemical science* **2021,** *12* (5), 1693-1701.

7. Chapter 7: The role of strain-induced crystallization in needle insertion cavitation

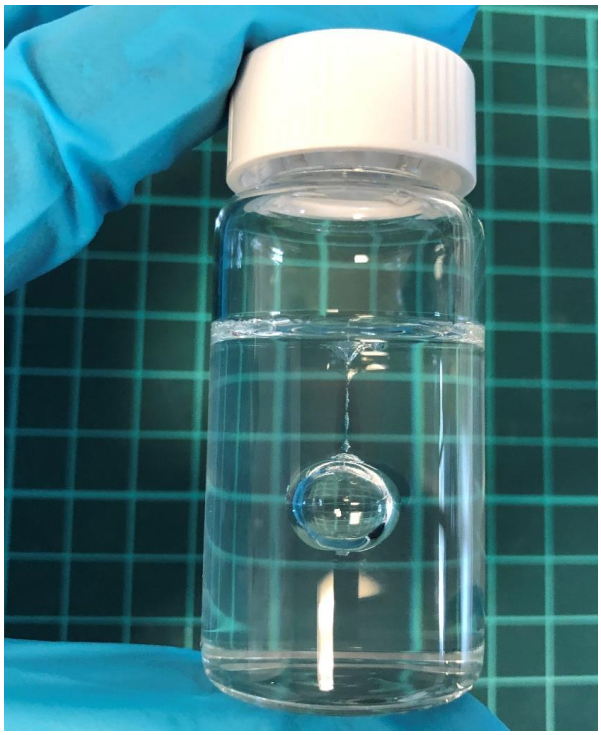

7.1. Introduction

Cavitation is the sudden, unstable growth of a defect inside the material when subjected to negative hydrostatic stress or internal pressure. There are commonly several types of cavitation that occurs according to the difference in driving mechanism: needle-induced cavitation (NIC)[1-2], laser-induced cavitation[3], acoustic-induced cavitation[4], shockwave-induced cavitation[5-6], confinement-induced cavitation[7-8], as well as supersaturation cavitation (explosive decompression)[9-10].

The cavitation rheology or NIC enables spatially localized probing of nonlinear elastic and fracture behavior for soft materials that are often difficult to manipulate with traditional mechanical characterization geometries. Recently, NIC has been extensively employed to measure the in vivo and ex vivo mechanical response of various polymer gels and biological networks such as brain tissue[11], eye lens[2, 12], bone marrow tissue in situ, and skin[13], exhibiting tremendous potential applications in the biomedical and biological field. Studies reported that the NIC method tends to overestimate the elastic modulus of soft solids when compared to traditional characterizations such as uniaxial extension and shear rheology. Bentz et al.[14] argued that this discrepancy should be attributed to the nature of the crosslinking bond in the material. Barney et al.[15] reported the residual strain effect at the needle tip that largely accounts for the overestimation of the critical pressure where the cavity initiates and thus results in the misinterpretation of the elasticity of the material. Therefore, they proposed an experimental protocol - retraction of the needle for a given distance before performing the cavitation experiment to release the indentation-induced residual strain providing reliable modulus measurement by cavitation rheology.

The NIC technique consists of two distinct steps: (1) needle inserting or indentation process and (2) subsequent air pressurizing or cavity growth process. While many

investigations have been focused either on the indentation[16-17] or on the cavitation process[18-19], separately, the impact of the needle insertion induced structural anisotropy in soft materials, and particularly of the strain-induced crystallization around the needle tip, on the subsequent cavitation response has never been established. Based on the results in Chapter 4, we have discovered a strain-induced crystallization (SIC) phenomenon at the needle tip for PVA with high DH during the deep indentation process, which could significantly influence the following cavitation process. To this end, in this chapter, we investigate the role of network structure variation induced by needle insertion (SIC) in its cavitation response using PVA hydrogel with different DH as a model gel system. The cavitation morphology with different needle retraction distances and fracture energy as estimated by cavitation would be revealed.

7.2. Experimental section

7.2.1. Materials

PVA hydrogel samples with different hydrolysis degrees and crosslinker GA concentrations were prepared by the same method described in previous chapters. In this work, PVA88 refers to PVA sample with DH = 88% and M_W = 67,000 g/mol; PVA99 refers to PVA sample with DH = 99% and M_W = 89,000 g/mol.

7.2.2. Methods

7.2.2.1. Indentation

A cylindrical flat-ended needle sourced from the Hamilton Company was used to perform the indentation test as detailed in previous chapters. The indentation velocity was kept at a constant value of v = 0.25 mm/s with the force and displacement being monitored using the force sensor with a 5 N load cell on the

bottom of the sample. The radius of the flat-ended needle varied from 0.23 – 0.45 mm according to the experimental requirement.

7.2.2.2. Needle-induced Cavitation (NIC)

The schematic of the cavitation setup is shown in **Figure 7.1.** Control of the pressure was achieved by a 1 mL glass Hamilton syringe in a pump purchased from KD scientific company (LEGATO®130 SYRINGE PUMP). The pressure was measured using a pressure sensor purchased from Omega Engineering (PXM409-070HGUSBH) and interfaced with a custom LabVIEW program.

The needle-induced cavitation test was performed following the indentation test where the needle was inserted to a maximum displacement d_{max} beyond the fracture point. The needle was then retracted by a given distance d_R before being held at a final displacement $d_{final} = d_{max} – d_R$, to release the possible residual strain around the needle tip as reported in the literature[15] to obtain a consistent critical cavitation pressure value (**Figure 7.1B**). Here the d_R for PVA88 and PVA99 hydrogel to measure the fracture energy in cavitation was set as ~ 10 mm. Then the cavitation (or the rapid expansion of a cavity in the sample at the needle tip) is induced by pressurizing the air with the pump and syringe into the gel at a constant rate v = 0.5 mL/min. The visualization of the initiation and the growth of the cavity was recorded by a camera with a frame rate of 50 fps (20 ms/frame). Particularly, instead of direct visualization of the sample, two polarizers were placed between the sample/camera and sample/light source as depicted in **Figure 7.1A** to explore the possible strain-induced crystallization and its effect on cavitation in the PVA sample with high hydrolysis degree.

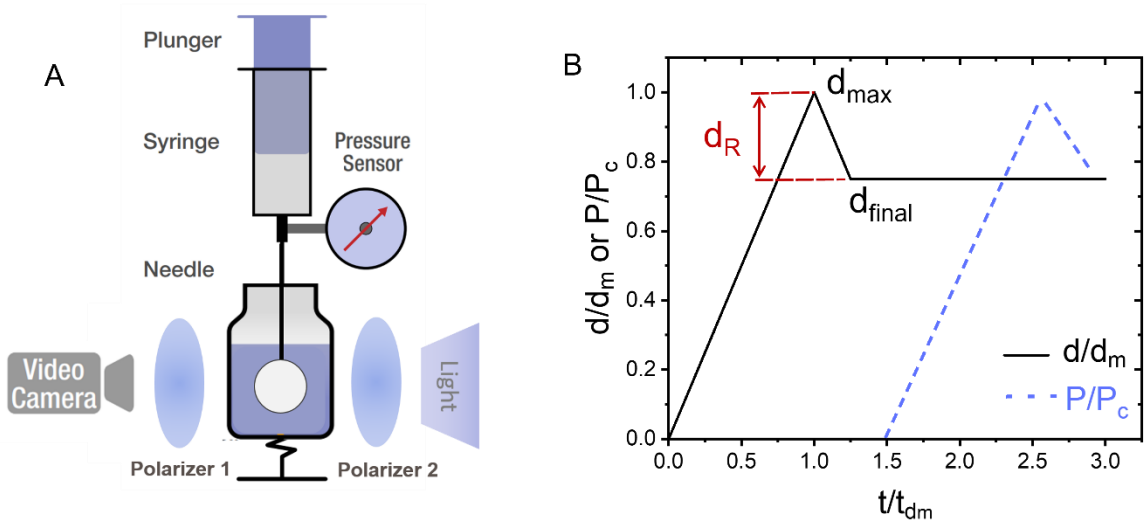

Figure 7.1. (A) Schematics of the cavitation setup which mainly consists of a syringe pump, a syringe, a pressure sensor, a needle, a light source, two polarizers and a video camera. (B) Normalized displacement and pressure against time for the needle insertion process. The needle is inserted into the gel at a constant velocity until a maximum displacement d_{max} after the penetration fracture point. Then the needle is retracted with a distance d_R and fixed at this final displacement d_{final} to perform the cavitation test by pressurizing the air with the syringe into the sample.

7.3. Results and discussion

7.3.1. Needle insertion cavitation

7.3.1.1. Determination of the initiation of elastic instability

In this section, we investigate how the cavity initiates at a critical pressure and grows. **Figure 7.2A** shows the critical cavitation pressure response as function of time for the PVA hydrogel (DH = 88%, G' = 600 Pa) with a needle with R = 0.31 mm. The morphology of the cavity at different stages in the pressure curve is also depicted in the pictures in **Figure 7.2B.** In the beginning, a very small tail (void) at the needle tip is visible because of the retraction of the needle, which is considered necessary for successfully obtaining the subsequent cavitation phenomenon (**Figure**

7.2B I). The pressure linearly increases as the increased volume of the pressurizing air by the syringe, in which the void at the needle tip starts to grow as shown in stage II. At t_c = 12 s a maximum pressure value P_c is reached and a bigger void in gel is observed as shown at the stage of III, indicating the initiation of the cavitation instability. After that, the pressure drops slightly and the cavity grows smoothly when keeping pressurizing the air at the stage IV and V.

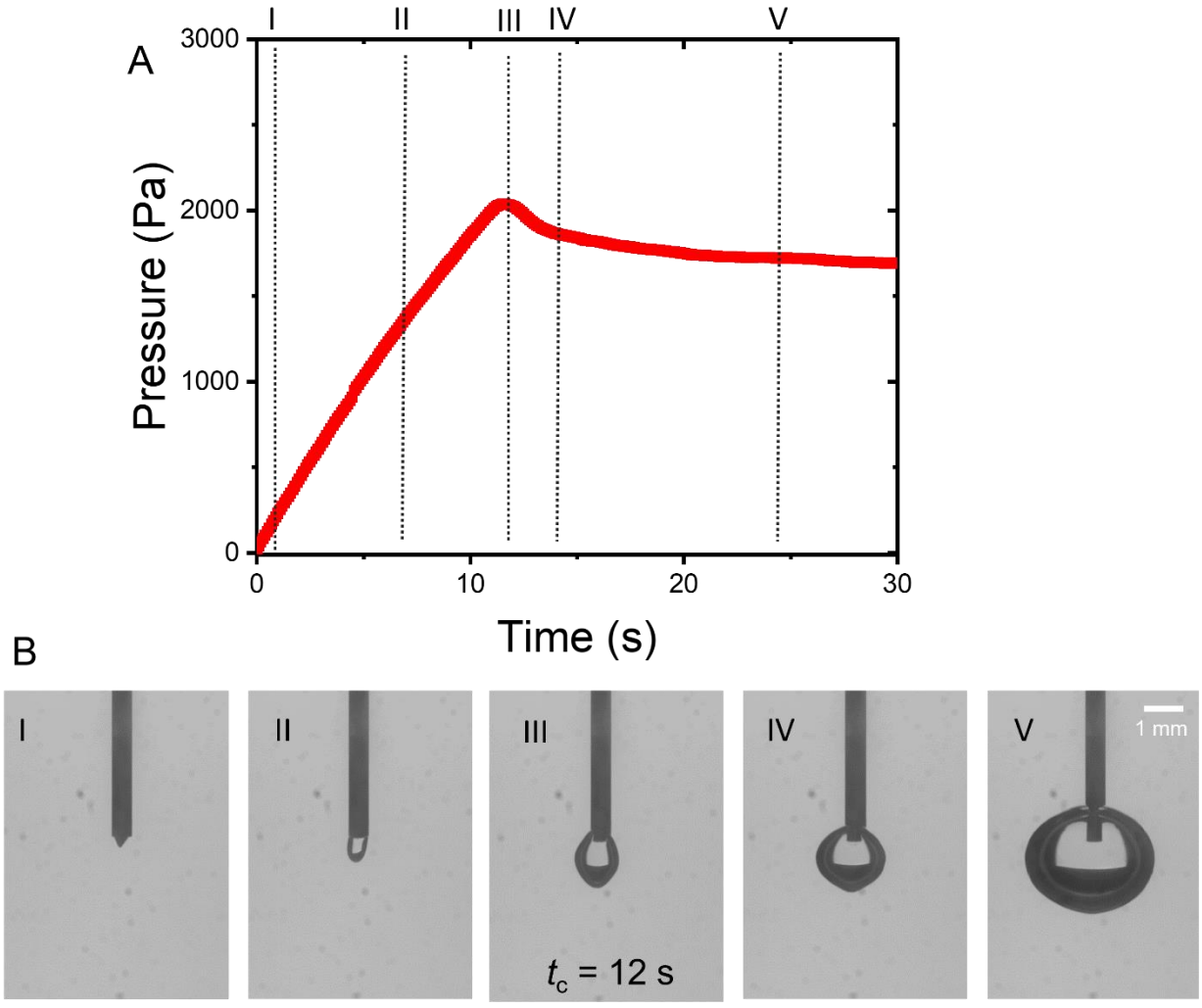

Figure 7.2. (A) Representative pressure response of the PVA hydrogel (DH = 88%, G' = 600 Pa) with a flat-end needle R = 0.31 mm. (B) Corresponding images of a needle in the gel at different stages of the cavitation process. The initiation of the instability or maximum pressure occurs at t_c = 12 s.

To better visualize and monitor the sudden expansion of the cavity at the critical pressure, we measure the projected area of the void at the needle tip during the cavitation process as shown in **Figure 7.3**. In **Figure 7.3A**, the moderate increase of the projected area corresponds to the linear increase of the pressure prior to the initiation of the instability. Then a very sharp rise of the area is observed at t_c = 12 s, perfectly consistent with the critical pressure value observed in the above pressure curve. The transition of growth rate is confirmed by the derivative of the projected area dS/dt in **Figure 7.3B** where the maximum value of dS/dt is observed at the same time t_c. This result demonstrates that initiation of the cavitation/elastic instability could be determined both from P_c in the loading curve as well as from the morphology variation of the cavity depicted as a sudden increase of volume (area) of the void or alternatively, the stretch ratio λ, ratio of the current void size to that in the reference state, R,

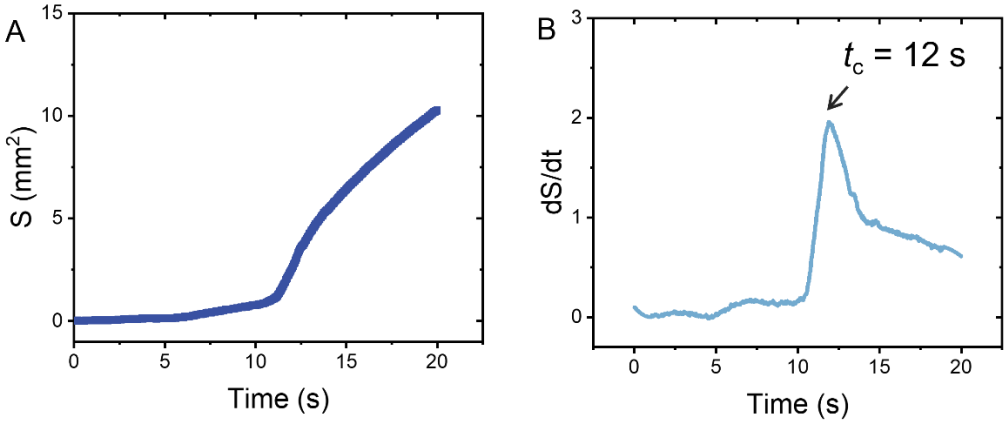

Figure 7.3. Growth of the cavitation. (A) The area of cavity as a function of time. (B) The derivative of cavitation area dS/dt as a function of time.

7.3.1.2. Driving mechanism

Needle insertion cavitation is induced by pressurizing air with a syringe into the gel. Once a critical pressure P_c is reached, the rapid expansion of a bubble is visible at

the end of the needle. The cavitation in soft materials can be elastic, reversible deformation, or it can be an irreversible process involving fracture of bonds[20-21]. In other words, the expansion of the material could be driven either by (1) elasticity or (2) fracture mechanism.

Assuming deformation of a spherical void by internal pressure, one need to consider two resistant forces: the elastic force of the soft solid, and the surface tension at the surface of the void. Taking into account of the Neo-Hookean strain energy and the Laplace pressure, the internal pressure can be written as: [22-24]

$$P = \frac{2\gamma}{R} \cdot \lambda^{-1} + E\left(\frac{5}{6} - \frac{2}{3} \cdot \lambda^{-1} - \frac{1}{6} \cdot \lambda^{-4}\right) \quad (7.1)$$

where γ is the interfacial tension of the injected fluid and sample (here γ = 52 mN/m for the surface tension of the PVA hydrogel). *R* is the void radius in the reference state (here we take the needle radius). λ is the stretch. *E* is the elastic modulus. The strain energy contribution is zero in the undeformed reference state (λ = 1), and it monotonously increases with λ. While the surface force is the maximum in the undeformed reference state and continues to decrease with λ. When the ratio of the initial void size to elasto-capillary length, *RE*/γ, is smaller than 1, the total pressure is its maximum, thus a peak of the pressure can be measured.

It is reported that the critical pressure is linked to the gel modulus in the case of elastic cavitation and the gel modulus/toughness in the case of irreversible fracture[1]. For the former, the critical pressure response related to the elastic deformation of cavitation can be represented by the eq. 7.2,[23]

$$P_c = \frac{C_1\gamma}{R} + C_2E \quad (7.2)$$

Where γ is the interfacial tension of the injected fluid and sample. R is the needle radius. C_1 and C_2 are constant values where C_1=2 and C_2=5/6 are assumed for an initially spherical void in an infinite, incompressible solid[25-26].

For the latter, the critical pressure of fracture-driven cavitation is described with the linear elastic solution for a penny-shaped crack of radius R in eq. 7.3,[24-25]

$$P_f = \left(\frac{\pi E G_c}{3}\right)^{1/2} \left(\frac{1}{R}\right)^{1/2} \quad 7.3$$

7.3.2. Fracture energy G_c estimated by cavitation

7.3.2.1. Effect of needle size and gel modulus

The effect of needle size and gel modulus on the cavitation behavior of PVA88 hydrogels with different moduli was studied as shown in **Figure 7.4**. In **Figure 7.4A** the pressure curves for gels with different moduli before cavitation overlap perfectly, while the P_c values are found to increase with gel modulus when the needle radius R = 0.45 mm. The dependence of P_c on gel modulus is then plotted in **Figure 7.4B**, from which a scaling relation $P_c \sim G'^{0.75}$ is observed.

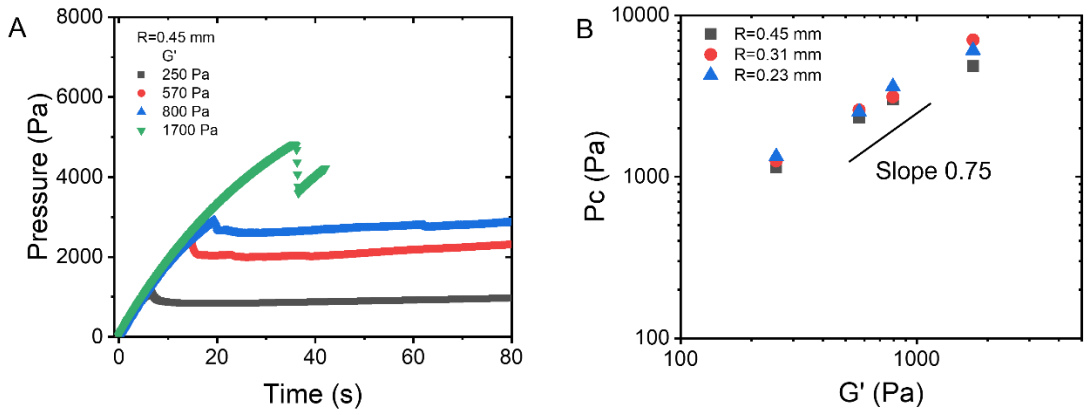

Figure 7.4. (A) Pressure response of cavitation process for PVA88 hydrogel with varying elastic modulus: R = 0.45 mm. (B) Critical pressure P_c as a function of gel modulus with various needle size.

7.3.2.2. G_c for PVA88 and PVA99

In an attempt to compute the fracture energy by assuming a fracture-driven cavitation mechanism from a penny-shaped crack of radius R, (since an irreversible cavity is observed after the cavitation process) P_c against $1/R$ is shown for PVA88 and PVA99 hydrogel, separately, in **Figure 7.5A** and **Figure 7.5B**. Note that the initial flaw size of the cavity is approximately considered the needle size R since a small defect is induced by the needle before the cavitation process. Apparently, it shows that a cavity growing from a smaller initial defect requires a higher critical pressure to grow.

A fit of data with $P_f = \left(\frac{\pi E G_c}{3}\right)^{1/2}\left(\frac{1}{R}\right)^{1/2}$ (eq. 7.3) was realized as indicated in the dashed line from which the fracture energy G_c is calculated. The fracture energy G_c estimated from the critical cavitation pressure is plotted against the gel modulus in **Figure 7.5C**. For PVA88 hydrogel, G_c is ranging from 1.7 ~ 5.2 J/m^2 when the gel modulus is increasing from 250 Pa to 1700 Pa. The fracture energy of chemically cross-linked PVA hydrogels was reported to be around ~10 J/m^2 by Zhao et al.[27], indicating that the cavitation method provides a very reliable and practical measurement of fracture energy in ultra-soft materials.

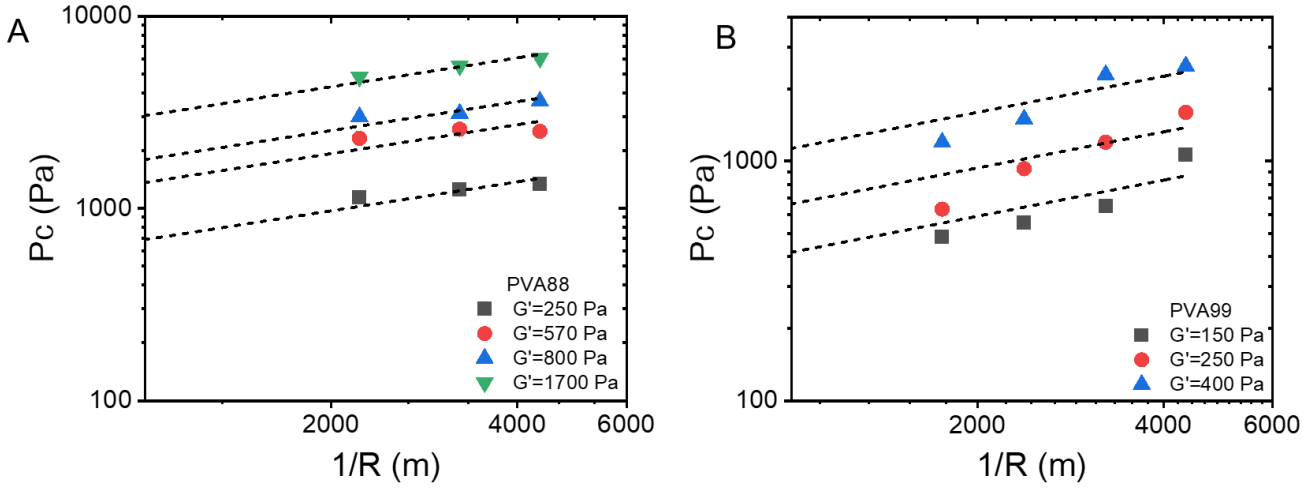

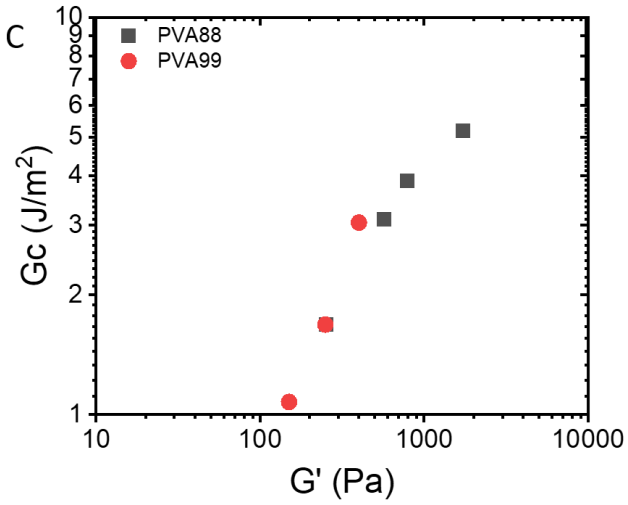

Figure 7.5. (A) Critical pressure P_c as a function of radius $1/R$ for PVA88 hydrogel. (B) Critical pressure P_c as a function of radius $1/R$ for PVA99 hydrogel. The solid line indicates the fit with the equation $P_f = \left(\frac{\pi E G_c}{3}\right)^{1/2}\left(\frac{1}{R}\right)^{1/2}$ by assuming the fracture-driven cavitation mechanism. (C) Estimated values of fracture energy G_c as a function of modulus for PVA88 hydrogel.

Very surprisingly, G_c for PVA99 hydrogels is found almost identical to that for PVA88 hydrogels with the comparable elastic modulus (**Figure 7.5C**).

Note that according to the Lake and Thomas theory, the fracture energy predicted from simple molecular arguments, G_c scales with the crosslinking density v as $G_c \sim v^{-1/2}$. [28] Thus, G_c is predicted to scale with the inverse square root of the elastic modulus $G_c \sim G'^{-1/2}$ in elastomers and gels if the chains in the network are Gaussian and the crosslinking level is homogeneous and not too low.[29] However, a strikingly different dependence of fracture energy on crosslinking ratio of polybutadiene elastomers was reported by Ahagon and Gent for low degrees of crosslinking.[30] They pointed out that G_c could increase as the degree of crosslinking increases for lightly cross-linked sample, i.e., as the molecular weight M_c of chains between points of crosslinking decreases. Connecting with our result, we assume that this phenomenon

could be associated with the structural heterogeneity of the poorly crosslinked gels. As discussed in the previous chapters, the low crosslinking ratio of PVA hydrogel results in strong structural heterogeneities, in which the fracture energy G_c maybe reduced by the imperfection network structure for a gel with low modulus.

7.3.3. The comparison of G_c from cavitation and pure shear

To compare the fracture energy estimated from cavitation and conventional mechanical measurement method, we performed the pure shear test for PVA99 hydrogel with a high modulus. The representative stress-stretch curve for gel with notch and without notch (G' = 5000 Pa) is shown in **Figure 7.6A**. The critical stretch value λ_c ~1.7 is determined from the notched sample and the fracture energy density $W(\lambda)$ is calculated by integrating the enclosed area from $\lambda = 1$ to λ_c in stress-stretch curve for un-notched sample. Thus the fracture energy $G_c = 8.8$ J/m^2 is obtained by the equation $G_c = W(\lambda)H_0$ (sample initial height $H_0 = 8.7$ mm) for G' = 5000 Pa. Similarly, $G_c = 11.3$ J/m^2 and $G_c = 14.1$ J/m^2 is calculated for PVA99 hydrogel with G' = 2900 Pa and G' = 2200 Pa, respectively, from pure shear test.

The fracture energy estimated from cavitation and pure shear as a function of gel modulus is plotted in **Figure 7.6B**. While the G_c increases with G' for PVA99 hydrogel at the low crosslinking level observed by cavitation, the fracture energy $G_c \sim G'^{-1/2}$ is found for PVA99 hydrogel at the high crosslinking level obtained from the pure shear test which agrees with the Lake and Thomas theory[29] and Gent's work[30] as discussed above. The great consistency of fracture energy value estimated from the NIC method and notched test in Tetrafunctional poly(ethylene glycol) (PEG) gels was also reported recently by Barney et.al[31].

This result indicates that (1) the cavitation method itself gives a reliable measurement of fracture energy for ultra-soft materials that are often difficult to manipulate with conventional mechanical measurement geometry. (2) the fracture

energy could be largely affected by the structural heterogeneity of ultra-soft materials at the low crosslinking level.

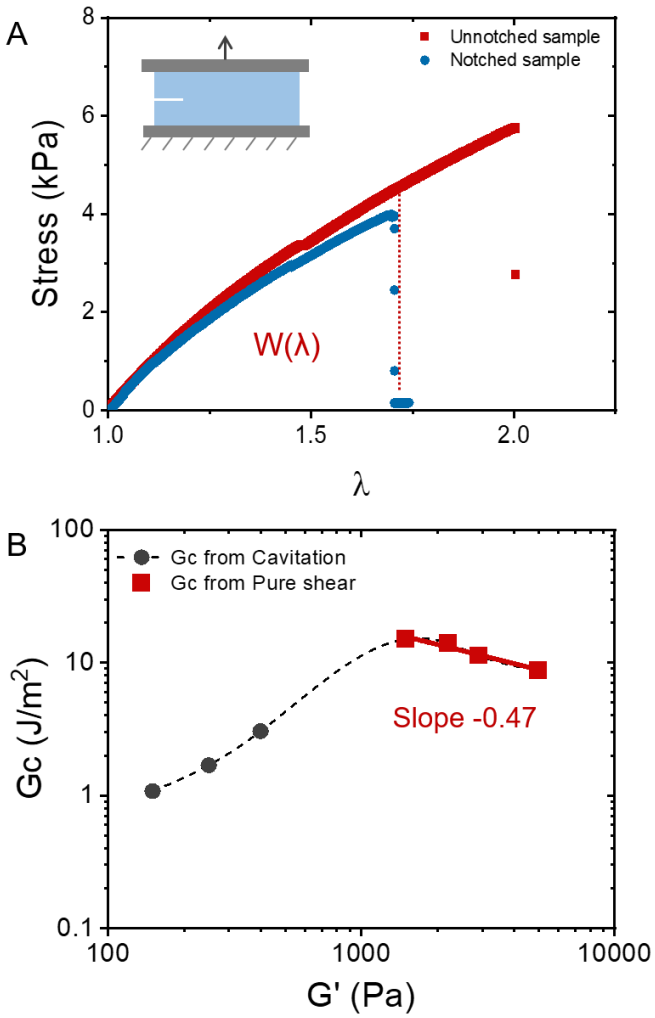

Figure 7.6. (A) Pure shear test for PVA99 hydrogel (G' = 5000 Pa). The critical stretch λ_c is determined from the notched sample and fracture energy density $W(\lambda)$ is the area enclosed by the stress-stretch curve from λ = 1 to λ_c for un-notched sample. Fracture energy $G_c = W(\lambda)H_0$ is obtained (the sample height H_0 = 8.7 mm). (B) The fracture energy measured from cavitation and pure shear test as a function of gel modulus.

7.3.4. Effect of needle-insertion-induced crystallization

The cavitation morphology for PVA hydrogels is shown in **Figure 7.7**. While a spherical cavity is always anticipated in hydrogel as shown in **Figure 7.7A**, we observed a very irregular "droplet"- shaped cavity in the PVA hydrogel with a high hydrolysis degree (**Figure 7.7B)**. What determines the morphology of the cavitation in an apparently transparent hydrogel?

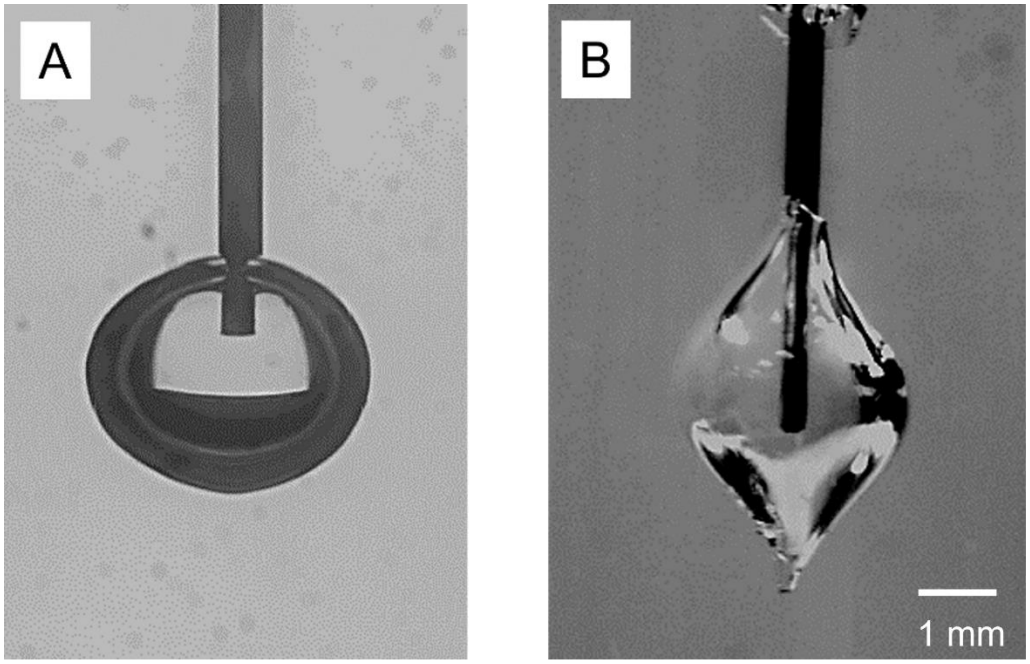

Figure 7.7. The cavitation morphology for PVA88 hydrogel (DH =88%, G' ~ 600 Pa) and PVA99 hydrogel (DH = 99%, G' ~ 400 Pa). The picture was captured by the camera directly without incorporation in the polarizers.

In Chapter 4, we noted that strain-induced crystallization occurred near the needle tip during the deep indentation process for PVA99. This permanent anisotropic structure is considered to originate from the localized strong hydrogen bonding association due to the increased polymer concentration around the needle tip. In this section, we will study how this localized reinforced structure introduced by the needle indentation affects the subsequent initiation of the cavity.

7.3.4.1. How crystallization affects the cavitation morphology

The cavitation morphology of the PVA99 hydrogel (G' = 150 Pa) with different needle retraction distances d_R (R = 0.31 mm) is shown in **Figure 7.8**. Here, all the pictures were captured by incorporating polarizers as depicted in **Figure 7.1A** to visualize the possible birefringence structure. At d_R = 0 (**Figure 7.8** I), a bright crystalline zone is observed through birefringence at the needle tip due to the SIC as has been discussed in Chapter 4. In this case, the material is reinforced locally and is impossible to deform and fracture by the pressurized air at the given experimental conditions.

Interestingly, when d_R is increased to 1.5 mm and the crystalline domain is left behind the needle tip a little bit, the cavity occurs at $t = t_c$ but its expansion is strongly restricted by the crystalline domain and an irregular droplet shape is observed instead of a spherical void (**Figure 7.8** II). The void continues to grow upwards along the needle to avoid the crystals at $t > t_c$. This answers the question that put forward in **Figure 7.7**. We further increase the retraction distance of the needle to d_R = 10 mm (**Figure 7.8** III). In this case, the needle is far away from the crystalline zone and that is invisible from the region of interest in pictures in which we assume the crystalline domain does not influence the cavitation that much. Thus, a regular spherical bubble is observed, and a much smaller critical pressure is obtained. Presumably, the gel is already fractured in that region by the insertion of the needle.

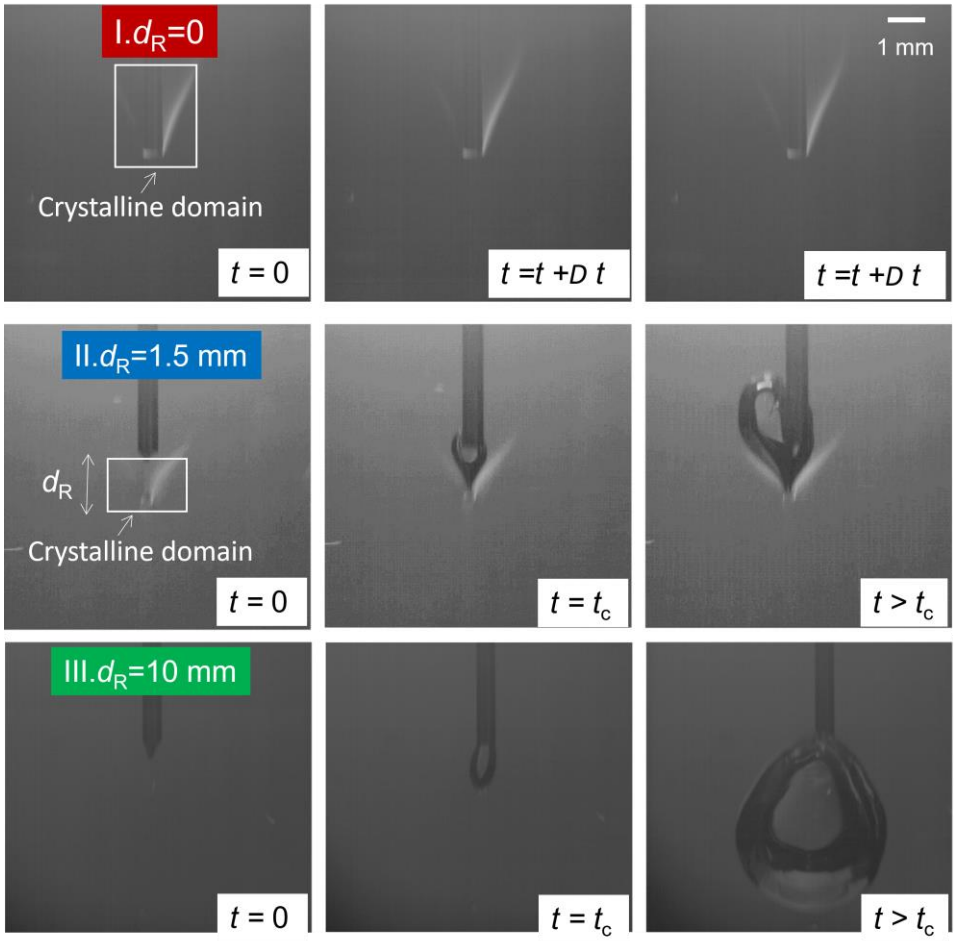

Figure 7.8. Corresponding morphology of cavitation for PVA99 hydrogel with varying retraction distance d_R at different moments, among which t_c indicates the time where critical pressure or cavitation occurs. (G' = 150 Pa, R = 0.31 mm)

Figure 7.9 shows the cavitation pressure response of the PVA99 hydrogel. While it is expected that the critical pressure should only scale with the gel elasticity and needle size according to eq. 7.3, big variations of P_c are observed when the needle retraction distance differs. Particularly, at d_R = 0 (no retraction of the needle before performing the cavitation), the pressure linearly increases to the maximum value that can be applied by the apparatus, and no cavitation phenomenon is observed. At d_R = 1.5 mm, P_c is ~ 2000 Pa and P_c decreases to ~ 900 Pa when d_R = 10 mm.

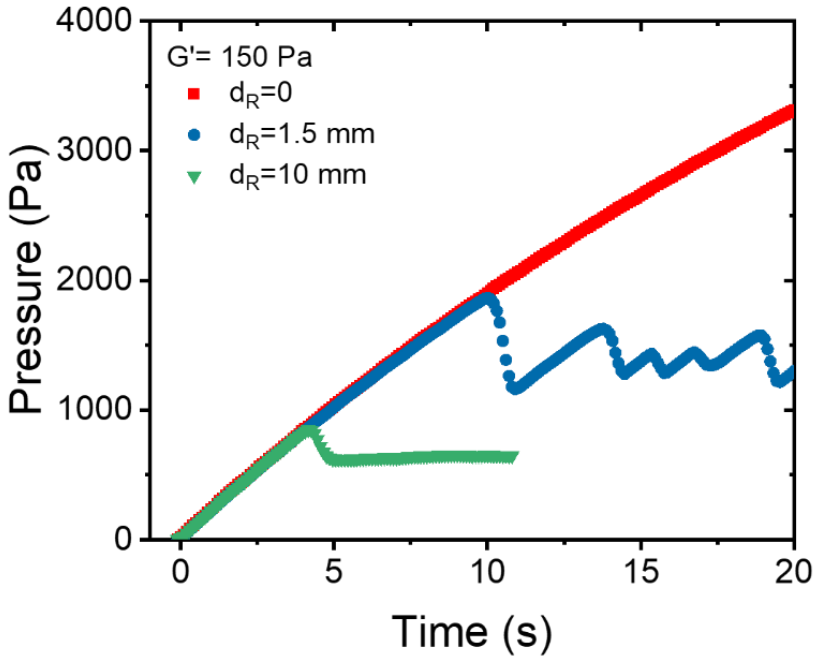

Figure 7.9. Pressure response of cavitation process for PVA99 hydrogel with varying retraction distance d_R. (G' = 150 Pa, R = 0.31 mm)

To confirm this phenomenon, we then performed the same cavitation test for PVA99 hydrogel with G' = 250 Pa. As shown in **Figure 7.10A**, the maximum critical pressure P_c ~3500 Pa is observed for d_R = 1.5 mm. As expected, a crystalline zone is visibly behind the needle tip in **Figure 7.10B I**. Consequently, the cavity chooses to expand upwards to avoid the reinforced network area and an irregular shape is observed. In this case, the critical pressure value to expand a cavity is increased by the existence of crystalline domains, where we could consider the elastic modulus of the gel is significantly increased around this area. When d_R is 8 or10 mm (no influence from the crystalline zone), the P_c is comparable (~1000 Pa). Correspondingly, a spherical and symmetric bubble occurs as seen in **Figure 7.10B II.**

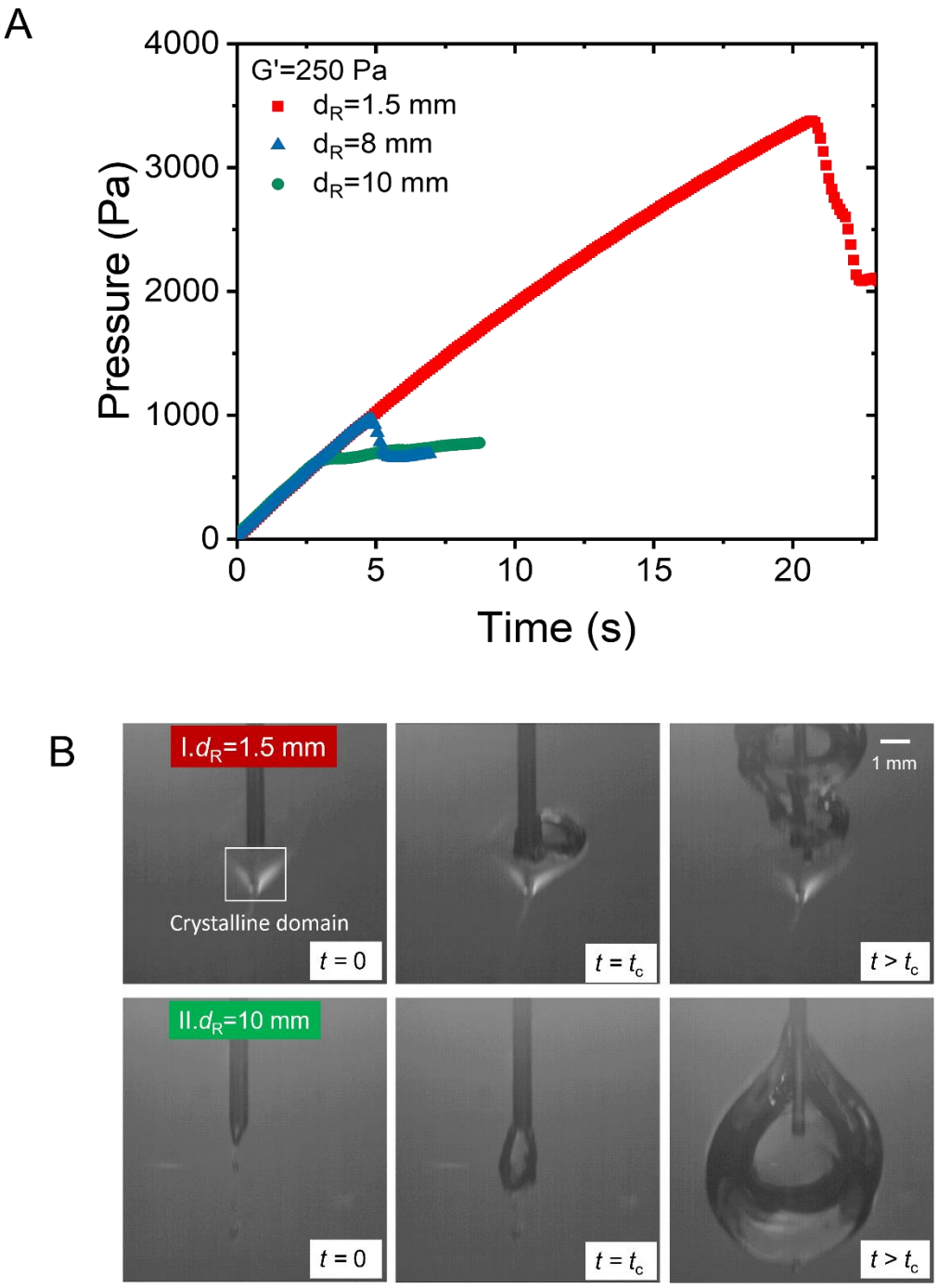

Figure 7.10. (A) Pressure response of cavitation process for PVA99 hydrogel with varying retraction distance d_R. (G' = 250 Pa, R = 0.31 mm) (B) Representative morphology of cavitation with varying retraction distance d_R at different moments.

We also tested a gel with a higher modulus G' = 400 Pa to investigate the possible birefringence morphology effect on the cavitation response. As shown in **Figure 7.11A,** the cavitation is inaccessible when d_R=1.5 mm, while this d_R value works for gels with G' = 150 Pa and G' = 250 Pa. When d_R=3.5 mm, the critical pressure value P_c occurs. This result indicates the presence of a bigger-size crystalline zone below the needle. Indeed, a less visible sub-crystalline zone emerges between needle tip and the bright v shape birefringence pattern (**Figure 7.11B I**), which displaces the pathway of the cavity expansion upwards. This structure is developed during the needle retraction process as discussed in Chapter 4. When d_R=10 mm (in the amorphous domain), the spherical cavity occurs as expected in **Figure 7.11B II** and P_c ~1800 Pa in this case.

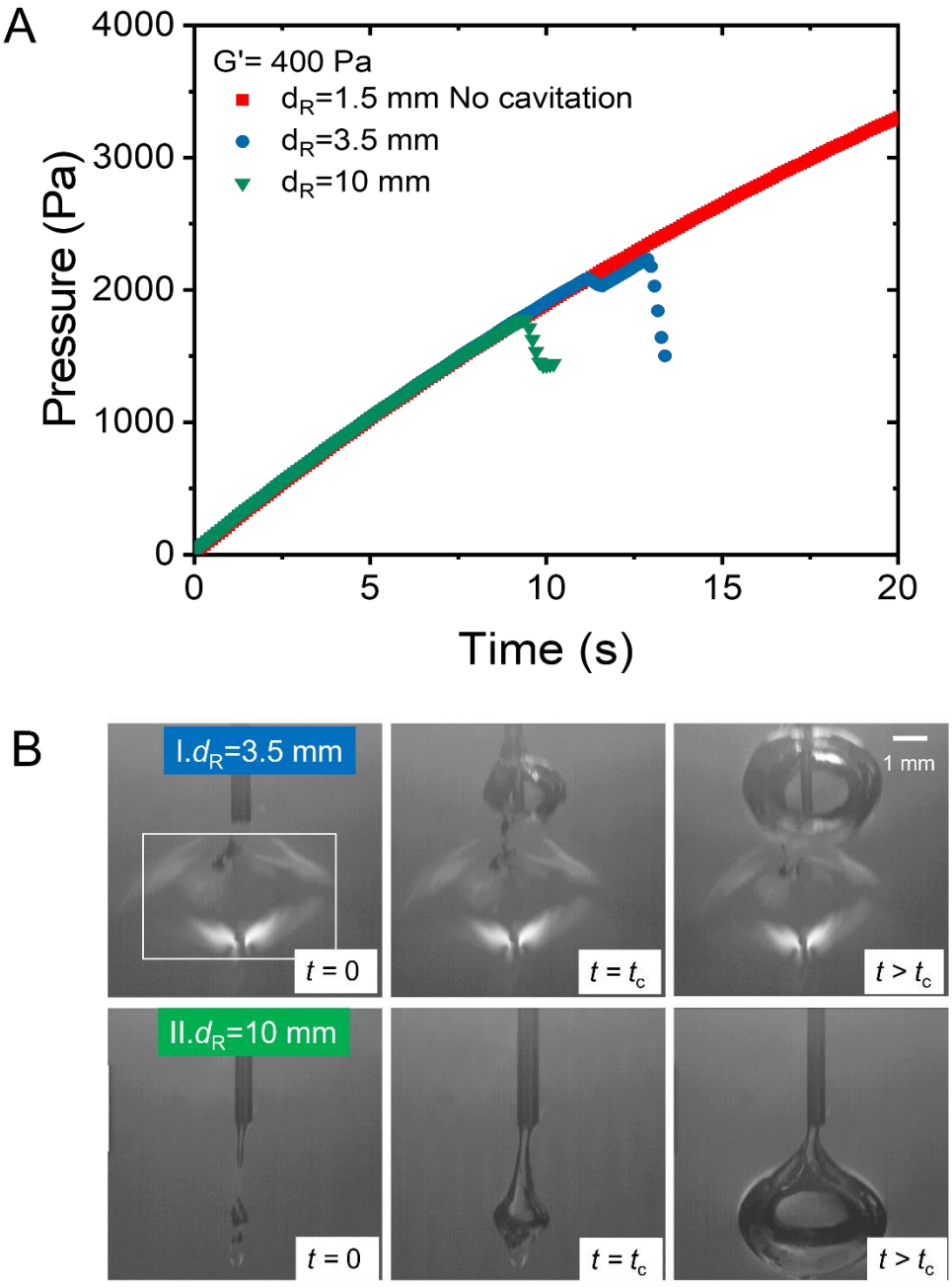

Figure 7.11. (A) Pressure response of cavitation process for PVA99 hydrogel with varying retraction distance d_R. (G' = 400 Pa, R = 0.31 mm) (B) Representative morphology of cavitation with varying retraction distance d_R at different moments.

7.3.4.2. The effect of the retraction distance

In order to further characterize the effect of the crystallization on the cavitation response, d_R dependence of the fracture energy G_c was further systematically studied. Here the G_c is calculated according to the eq. 7.4 since a fracture-driven mechanism fits well into the cavitation process as shown in **Figure 7.5**.

$$G_c \approx \frac{3P_f^2 R}{\pi G'} \qquad 7.4$$

For the PVA99 hydrogel showing strain-induced crystallization behavior in deep indentation, the values of G_c were plotted as a function of d_R in **Figure 7.12**. We discovered that the presence of the crystalline domains at the needle tip significantly affects the initiation of cavitation. Three regions can be identified. Without retraction of the needle (d_R = 0 mm), we did not observe cavitation under the given experimental conditions. As seen in the birefringence image (**Figure 7.12 (a)**), the needle tip is inside the crystalline zone. The minimum value of d_R that results in cavitation (d_R ~ 1 mm for gel with G' = 150 Pa and G' = 250 Pa; and d_R ~ 3 mm for G' = 400 Pa), roughly corresponds to the size of the crystalline zone of the sample. Thus, region I roughly represent the crystalline domain where the cavitation behavior is dominated by the crystallization behavior of the PVA hydrogel.

In region II, G_c is found to decrease with the applied d_R. In other words, the fracture energy is increased due to the near-field influence of crystallization. Although the main anisotropic structure has been left below the needle, the gel near that area serving as a reinforced network increases the critical pressure. Meanwhile, the pathway of the cavitation expansion is displaced upwards, and an irregular shape of the cavity is formed to avoid expansion into the crystalline domain (**Figure 7.12 (b) and (c)**).

Finally, when the needle tip is far away from the crystalline zone (d_R > 7 mm), we consider the material in an amorphous state represented by region III, and a spherical cavity is observed (**Figure 7.12 (d)**). In this region, G_c stabilizes at a plateau, insensitive to the applied d_R. Note that the cavitation analysis in 3.2.2 is based on the data in this region.

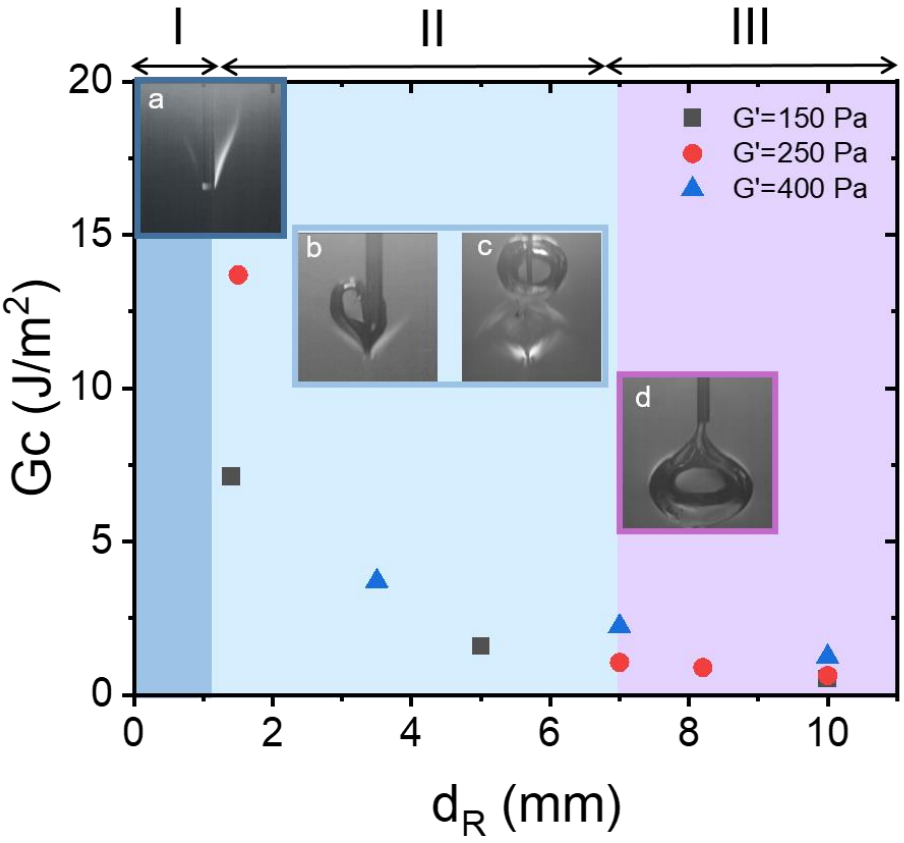

Figure 7.12. Plots of fracture energy G_c against retraction distance d_R for PVA99 hydrogels. Region I represents the crystalline domain where the crystallization prevents the occurrence of the cavitation; Region II is the case where the cavitation and fracture initiation energy are affected by the near-field influence of the crystalline zone; Region III is the amorphous domain where the critical value is insensitive to the d_R and displays great consistency with the theoretical value.

It is worth noting that the fracture energy G_c also decreases with the applied retraction distance d_R for PVA88 hydrogels at d_R < 7 mm and stabilizes at d_R > 7 mm.

Since there is lack of visible crystallization in PVA88 hydrogels (always spherical cavity), we attributed this phenomenon as the possible residual strain effect. Barney et al.[15] reported that the residual strain effect at the needle tip could lead to an overestimation of the critical cavitation pressure for PDMS and acrylic triblock gels. By retraction of the needle, the residual strain is released and thus a reliable and consistent critical pressure is obtained. Interestingly, at the same gel modulus level, G_c for PVA88 can be even smaller than that for PVA99 hydrogel at $d_R < 7$ mm. We assume that there exists a polymer concentration gradient around the needle tip for PVA99 hydrogel: around needle tip, the hydrogen bonding associations bind the polymer chains in the polymer-concentrated region (crystalline domain); above which the polymer chains are thus diluted (as shown in **Figure 7.13A**). Although spherical cavities are both visible in the amorphous domain for PVA88 and PVA99 hydrogels, the polymer-diluted region in PVA99 presents somehow softening effect that facilitates the growth of the cavity, resulting in the lower fracture initiation energy compared to PVA88 hydrogel where a homogenous structure is expected. However, when the retraction distance is long enough ($d_R > 7$ mm), where the hardening and softening effect are ignorable for PVA99, the ultimate fracture energy G_c of PVA99 and PVA88 with similar modulus is substantially the same.

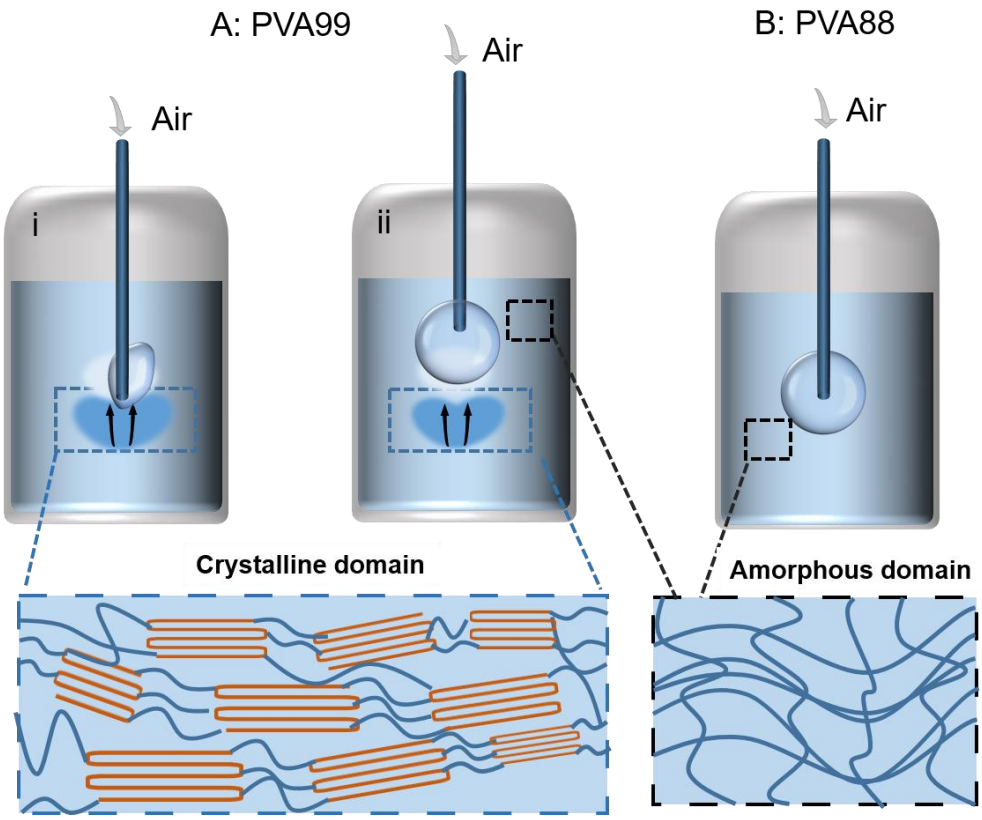

Figure 7.13. The schematic of cavitation nucleation in PVA99 and PVA88 hydrogel. (A) PVA99 hydrogel showing crystallization phenomenon below the needle tip: (i) the cavity grows upward to avoid the reinforced network area displaying an irregular spherical shape. (ii) the needle is retracted to be far away from the crystalline domain and the cavity initiates in the amorphous domain. (B) PVA88 hydrogel without crystallization behavior where the cavity initiates in the amorphous domain. The blue shallow in (A) indicates the crystalline domain due to the increased polymer concentration, above which the white zone represents the possible softening effect due to the resultant diluted polymer chains.

7.4. Conclusions

This chapter sets out to investigate the needle-insertion-induced cavitation in soft hydrogels with particularity to determine the role of the strain-induced crystallization in the initiation of the cavitation response (morphology and fracture energy). The main conclusions are summarized below:

1. The initiation of the elastic instability of cavitation could be determined by monitoring the pressure response depicted as the maximum value P_c in the curve, as well as by capturing the growth of the cavity where an explosion of the cavity is observed.
2. Fracture energy G_c increases with G' for PVA hydrogels at the low crosslinking level from cavitation while $G_c \sim G'^{-1/2}$ is found at high crosslinking level, consistent with Lake-Thomas theory, indicating that the structural heterogeneity governs the fracture initiation of ultra-soft materials.
3. The strain-induced crystallization significantly influences the initiation of cavitation for PVA hydrogel with DH = 99%, in which three regions can be identified: (I) the cavitation is prevented by the crystalline domain when needle retraction $d_R = 0$. (II) G_c is increased due to the near-field effect of the crystalline domain and decreases with d_R, in which the bubble expands upwards with an irregular droplet shape. (III) G_c is insensitive to the applied d_R when the needle tip is far away from the anisotropic structure and a spherical bubble is observed.
4. The ultimate G_c for PVA with DH = 88% and DH = 99% is comparable once the needle retraction is large enough to ensure the cavitation initiated in the amorphous domain of the gel.

This is the first study reporting the indentation-induced crystallization at the needle tip which largely increases the fracture energy. As this anisotropic structure has never been discovered and considered in the previous studies on cavitation, it would shed new light on the understanding of cavitation mechanics and damage in biological tissues as well as polymeric material. Given this novel finding, it helps to improve needle-induced injury detection, prevention, and the

localization of accurate drug injection in tissues. It would also contribute to the design of more sustainable and reinforced materials to mitigate or prevent damage in practical applications.

7.5. References

1. Kundu, S.; Crosby, A. J., Cavitation and fracture behavior of polyacrylamide hydrogels. *Soft Matter* **2009,** *5* (20), 3963-3968.
2. Cui, J.; Lee, C. H.; Delbos, A.; McManus, J. J.; Crosby, A. J., Cavitation rheology of the eye lens. *Soft Matter* **2011,** *7* (17), 7827-7831.
3. Estrada, J. B.; Barajas, C.; Henann, D. L.; Johnsen, E.; Franck, C., High strain-rate soft material characterization via inertial cavitation. *Journal of the Mechanics Physics of Solids* **2018,** *112*, 291-317.
4. Khokhlova, V. A.; Bailey, M. R.; Reed, J. A.; Cunitz, B. W.; Kaczkowski, P. J.; Crum, L. A., Effects of nonlinear propagation, cavitation, and boiling in lesion formation by high intensity focused ultrasound in a gel phantom. *The Journal of the Acoustical Society of America* **2006,** *119* (3), 1834-1848.
5. Hong, Y.; Sarntinoranont, M.; Subhash, G.; Canchi, S.; King, M., Localized tissue surrogate deformation due to controlled single bubble cavitation. *Experimental Mechanics* **2016,** *56* (1), 97-109.
6. Kang, W.; Adnan, A.; O'Shaughnessy, T.; Bagchi, A., Cavitation nucleation in gelatin: Experiment and mechanism. *Acta Biomaterialia* **2018,** *67*, 295-306.
7. Crosby, A. J.; Shull, K. R.; Lakrout, H.; Creton, C., Deformation and failure modes of adhesively bonded elastic layers. *Journal of Applied Physics* **2000,** *88* (5), 2956-2966.
8. Lin, S.; Mao, Y.; Radovitzky, R.; Zhao, X., Instabilities in confined elastic layers under tension: Fringe, fingering and cavitation. *Journal of the Mechanics Physics of Solids* **2017,** *106*, 229-256.
9. Morelle, X. P.; Sanoja, G. E.; Castagnet, S.; Creton, C., 3D fluorescent mapping of invisible molecular damage after cavitation in hydrogen exposed elastomers. *Soft Matter* **2021,** *17* (16), 4266-4274.
10. Gent, A.; Tompkins, D., Nucleation and growth of gas bubbles in elastomers. *Journal of applied physics* **1969,** *40* (6), 2520-2525.
11. Mijailovic, A. S.; Galarza, S.; Raayai-Ardakani, S.; Birch, N. P.; Schiffman, J. D.; Crosby, A. J.; Cohen, T.; Peyton, S. R.; Van Vliet, K. J., Localized characterization of brain tissue mechanical properties by needle induced cavitation rheology and volume controlled cavity expansion. *Journal of the Mechanical Behavior of Biomedical Materials* **2021,** *114*, 104168.
12. Zimberlin, J. A.; McManus, J. J.; Crosby, A. J., Cavitation rheology of the vitreous: mechanical properties of biological tissue. *Soft Matter* **2010,** *6* (15), 3632-3635.
13. Jansen, L. E.; Birch, N. P.; Schiffman, J. D.; Crosby, A. J.; Peyton, S. R., Mechanics of intact bone marrow. *Journal of the mechanical behavior of biomedical materials* **2015,** *50*, 299-307.
14. Bentz, K. C.; Sultan, N.; Savin, D. A., Quantitative relationship between cavitation and shear rheology. *Soft Matter* **2018,** *14* (41), 8395-8400.
15. Barney, C. W.; Zheng, Y.; Wu, S.; Cai, S.; Crosby, A. J., Residual strain effects in needle-induced cavitation. *Soft Matter* **2019,** *15* (37), 7390-7397.
16. Fakhouri, S.; Hutchens, S. B.; Crosby, A. J., Puncture mechanics of soft solids. *Soft Matter* **2015,** *11* (23), 4723-4730.
17. Barney, C. W.; Chen, C.; Crosby, A. J., Deep indentation and puncture of a rigid cylinder inserted into a soft solid. *Soft Matter* **2021,** *17* (22), 5574-5580.

18. Cristiano, A.; Marcellan, A.; Long, R.; Hui, C. Y.; Stolk, J.; Creton, C., An experimental investigation of fracture by cavitation of model elastomeric networks. *Journal of Polymer Science Part B: Polymer Physics* **2010,** *48* (13), 1409-1422.
19. Gent, A.; Lindley, P., Internal rupture of bonded rubber cylinders in tension. *Proceedings of the Royal Society of London. Series A. Mathematical and Physical Sciences* **1959,** *249* (1257), 195-205.
20. Raayai-Ardakani, S.; Earl, D. R.; Cohen, T., The intimate relationship between cavitation and fracture. *Soft matter* **2019,** *15* (25), 4999-5005.
21. Kim, J. Y.; Liu, Z.; Weon, B. M.; Cohen, T.; Hui, C.-Y.; Dufresne, E. R.; Style, R. W., Extreme cavity expansion in soft solids: Damage without fracture. *Science advances* **2020,** *6* (13), eaaz0418.
22. Chiche, A.; Dollhofer, J.; Creton, C., Cavity growth in soft adhesives. *The European Physical Journal E* **2005,** *17* (4), 389-401.
23. Dollhofer, J.; Chiche, A.; Muralidharan, V.; Creton, C.; Hui, C., Surface energy effects for cavity growth and nucleation in an incompressible neo-Hookean material—modeling and experiment. *International Journal of Solids and Structures* **2004,** *41* (22-23), 6111-6127.
24. Lin, Y.-Y.; Hui, C.-Y., Cavity growth from crack-like defects in soft materials. *International journal of fracture* **2004,** *126* (3), 205-221.
25. Zimberlin, J. A.; Sanabria-DeLong, N.; Tew, G. N.; Crosby, A. J., Cavitation rheology for soft materials. *Soft Matter* **2007,** *3* (6), 763-767.
26. Gent, A.; Tompkins, D., Surface energy effects for small holes or particles in elastomers. *Rubber Chemistry and Technology* **1970,** *43* (4), 873-877.
27. Lin, S.; Liu, X.; Liu, J.; Yuk, H.; Loh, H.-C.; Parada, G. A.; Settens, C.; Song, J.; Masic, A.; McKinley, G. H., Anti-fatigue-fracture hydrogels. *Science advances* **2019,** *5* (1), eaau8528.
28. Lake, G.; Thomas, A., The strength of highly elastic materials. *Proceedings of the Royal Society of London. Series A. Mathematical and Physical Sciences* **1967,** *300* (1460), 108-119.
29. Creton, C.; Ciccotti, M., Fracture and adhesion of soft materials: a review. *Reports on Progress in Physics* **2016,** *79* (4), 046601.
30. Ahagon, A.; Gent, A., Threshold fracture energies for elastomers. *Journal of Polymer Science: Polymer Physics Edition* **1975,** *13* (10), 1903-1911.
31. Barney, C. W.; Sacligil, I.; Tew, G. N.; Crosby, A. J., Linking cavitation and fracture to molecular scale structural damage of model networks. *Soft Matter* **2022**.

8. General conclusion

The fracture process of ultra-soft materials is significantly distinct and complicated compared to common soft materials, as it could be affected by the anticipated surface tension and structural heterogeneity, and may involve different dimensional scales (mesh size, elasto-capillary size, elasto-adhesive size, flaw size, etc.). The structural evolution of material during large deformation, such as chain orientation, strain-induced crystallization, or structural anisotropy, is also directly related to fracture.

In this work, systematic studies have been conducted on different ultra-soft hydrogel systems, in order to investigate the effect of structural heterogeneity, surface tension, and strain-induced crystallization on their (small and large) deformation and localized fracture properties at small length scale.

First, the deformation and puncture behavior of ultrasoft gels of (chemically crosslinked) polyacrylamide (PAAM), PDMS, and (physically crosslinked) carrageenan were investigated. Using the puncture test at small indentation depth, the low strain elastic modulus of the gels could be estimated by the Neo-Hookean model, consistent with that from the shear rheometer. The fracture resistance for PAAM and PDMS is one order of magnitude larger than that of carrageenan. Below the elasto-capillary length scale, fracture resistance is improved at smaller length scales since capillarity must play a role in the onset of fracture by puncture; Above the elasto-capillary length scale, fracture resistance is dominated by the nonlinear elasticity.

Then we investigated the impact of the structural heterogeneity of Poly (vinyl alcohol) hydrogels (PVA) with hydrolysis degree DH = 88% on their deformation and fracture behavior at the elasto-capillary length scale. PVA hydrogels (DH = 88%) with modulus ranging from 80 – 1700 Pa (comparable elasticity) were synthesized by varying the chemical crosslinker, glutaraldehyde, concentration at fixed PVA content (Path 1) and by varying the PVA fraction with a fixed crosslinker

concentration (Path 2). By dynamic light scattering, the contribution of structural heterogeneities to the scattered light for gels from Path 2 was found to be significantly larger compared to that from Path 1 at the low modulus range. As a consequence, the fracture strain and fracture resistance σ_c/G' were reduced for gel from Path 2 indicating that the strong structural heterogeneity favors crack nucleation at lower average stress.

For PVA hydrogels with DH = 99%, surprisingly, we found the critical strain (the ratio of fracture displacement to needle size D_c/R) could reach 5,000 – 10,000%, and fracture resistance σ_c/G' for softer gels was improved relative to the stiffer ones, where the critical nominal stress could surpass modulus by 3–4 orders of magnitude. Combining real-time birefringence observation, we discovered the failure initiates several millimeters above the needle tip and there is always a permanent birefringence pattern remaining after removing the needle from the hydrogel. This anisotropic structure was confirmed to be the strain-induced crystallization (SIC) zone that occurs around the needle tip during the indentation. The SIC displaces the crack initiation point from the needle tip to the edge as the network around the needle tip was physically reinforced by the crystals. Consequently, the loosely cross-linked sample demonstrates higher fracture resistance compared to the densely cross-linked one, contributing to its high deformability and the resultant larger area of crystalline domain.

Following the work on PVA hydrogels with different hydrolysis degrees, we found that the increase in molecular weight could increase their fracture resistance which is considered attributed to the stronger hydrogen bonding association serving as additional physical cross-linkings. In addition, by adding surfactant in PVA hydrogel (lower surface tension) and oil on the gel surface, the fracture resistance was also

significantly improved explained by favoring the large deformation of gel and delaying the initiation of the fracture.

To quantitatively visualize the 3D deformation field during the puncture process and better understand the related fracture behavior, we developed a novel technique that combines photon correlation imaging (PCI) and DIC. With this method, we successfully observed the deformation distribution of the puncture process at an extremely large indentation depth with an excellent resolution of ~ 0.3 mm. Our measurements quantitatively demonstrate that there exists a strong compressed and the sheared region above the needle tip, resulting in the overestimated critical nominal stress (surpassing the elastic modulus by several orders of magnitude), which is absent in previous studies.

Finally, we investigated the effect of strain-induced crystallization (SIC) on the cavitation response in PVA hydrogels. We discovered that an irregular-spherical cavity happens in PVA hydrogel with DH = 99 % due to the crystalline domain in the needle tip in which the fracture initiation energy G_c is highly improved. By retracting the needle far away from this anisotropic structure, a spherical cavity occurs, in which G_c for PVA with DH = 99 % and PVA with DH = 88 % is comparable. In the amorphous domain, G_c increases with the modulus at a low crosslinking level while $G_c \sim G'^{-1/2}$ is found at a high crosslinking level, consistent with Lake-Thomas theory, indicating that the structural heterogeneity governs the fracture initiation of ultra-soft materials.

This work demonstrates that while the surface tension is expected to govern the fracture behavior of ultra-soft hydrogel at the elasto-capillary length scale, the structural heterogeneity introduced by crosslinking, and structural anisotropy induced by SIC play a significant role in the fracture behavior of soft materials. This study provides very novel insight into the interplay of material physical chemistry,

structural evolution, and mechanical properties under extremely large strain conditions. The findings will be of interest to understanding the mechanical response of soft organs in the human body to medical invasive devices, aiding in predicting/preventing the injury (fracture) locations, and realizing material design and medical assistant instrument development.

RÉSUMÉ

Les matériaux ultra-mous présentent des caractéristiques de déformation et de fracture différentes de celles des matériaux mous ordinaires, en raison des effets anticipés de leur tension superficielle et de leur hétérogénéité de structure. Dans ce contexte, nous avons systématiquement étudié les propriétés de fracture d'hydrogels ultra-mous en utilisant des méthodes de ponction et de cavitation. Pour le polyacrylamide, le PDMS et le carraghénane, la résistance à la fracture est dominée par l'élasticité non linéaire au-dessus de l'échelle de longueur élasto-capillaire. En-dessous cette échelle spécifique, la résistance à la fracture augmente puisque la capillarité joue un rôle dans le début de la fracture. En synthétisant des hydrogels de poly(alcool vinylique) (PVA) à faible degré d'hydrolyse à partir de deux voies de percolation (percolation de liens et percolation de site), nous avons découvert que les gels formés par percolation de site, étudiés par diffusion dynamique de la lumière, possèdent une plus forte hétérogénéité de structure et entraînent une plus faible résistance à la fracture. Étonnamment, une cristallisation extrême induite par déformation pendant la ponction a été observée dans l'hydrogel de PVA avec un degré d'hydrolyse élevé. En effet, le réseau de cet hydrogel est renforcé localement autour de la pointe de l'aiguille et déplace le point d'initiation de la fissure de la pointe de l'aiguille vers le bord. Cette structure anisotrope donne lieu à une cavité sphérique irrégulière dans la méthode de cavitation et augmente significativement son énergie de fracture. En outre, nous avons constaté que l'augmentation de la masse moléculaire, l'ajout d'un tensioactif ou le dépôt d'une couche d'huile en surface augmentent chacun la résistance à la fracture de l'hydrogel. Enfin, nous avons mis au point une nouvelle technique optique : l'imagerie par corrélation de photons, qui permet de déterminer quantitativement la distribution des déformations en compression et en tension autour de l'aiguille. Ces nouvelles connaissances et avancées méthodologiques fourniront des informations utiles pour la conception de matériaux souples mais résistants aux fractures, et de robots assistant chirurgicaux dans les applications médicales.

MOTS CLÉS

Hydrogel ultra-mou, Fracture, Longueur élasto-capillaire, Hétérogénéité de structure, Cristallisation induite par déformation

ABSTRACT

Ultra-soft material exhibits different deformation and fracture characteristics compared to common soft material due to anticipated surface tension effects and structural heterogeneity. To this end, we systematically investigated fracture properties of ultra-soft hydrogels using puncture and cavitation methods. For soft polyacrylamide, PDMS, and carrageenan, fracture resistance is dominated by the non-linear elasticity above the elasto-capillary length scale. Below this particular scale, fracture resistance is improved since capillarity must play a role in the onset of fracture. By synthesizing poly(vinyl alcohol) (PVA) hydrogels with low hydrolysis degree from two percolation paths (bond-percolation and site percolation), we discovered that gels formed by site-percolation possess stronger structural heterogeneity studied via dynamic light scattering and thus result in lower fracture resistance. Surprisingly, an extremely large strain-induced crystallization during puncture was discovered in PVA hydrogel with high hydrolysis degree, which locally reinforces the network around the needle tip and displaces the crack initiation point from the needle tip to the edge. This anisotropic structure results in an irregular spherical cavity in the cavitation experiment and largely improves its fracture energy. In addition, we found that increasing the molecular weight, adding surfactant, and placing an oil layer on hydrogel surfaces could each increase their fracture resistance. In the end, we developed a novel optical technique - photon correlation imaging - in which compression and tension strain distribution around the needle is quantitatively revealed. These new insights and methodological advances will provide useful information to design soft but fracture-resistant materials and surgical assistant robots in medical applications.

KEYWORDS

Ultra-soft hydrogel, Fracture, Elasto-capillary length, Structural heterogeneity, Strain-induced crystallization